Micromechanical simulation and experimental investigation of the creep damage of stainless austenitic steels

Liang Huang

Université Pierre et Marie Curie

Ecole doctorale Science mécanique, acoustique, électronique & robotique

CEA SACLAY/DEN/DANS/DMN/SRMA/LC2M

Simulation micromécanique et étude expérimentale de l'endommagement par fluage des aciers austénitiques inoxydables

Par Liang HUANG

Thèse de doctorat de l'Université Pierre et Marie Curie

Dirigée par Maxime SAUZAY

Présentée et soutenue publiquement le 06 Décembre 2017

Devant un jury composé de :

Mr. Alan Cocks, Professeur, University of Oxford	Rapporteur
Mr. Rolf Sandström, Professeur, KTH Royal Institute of Technology	Rapporteur
Mr. Olivier Castelnau, Directeur de Recherche CNRS, Arts et Métiers ParisTech	Examinateur
Mr. Dominique Leguillon, Directeur de Recherche CNRS, UPMC	Examinateur
Mme. Sophie Dubiez-Le Goff, Docteur-Ingénieur, AREVA NP	Examinatrice
Mr. Adrien Guery, Ingénieur de recherche, EDF	Examinateur
Mr. Maxime Sauzay, Chercheur, CEA	Examinateur

Contents

List of notations

$\frac{a}{b}$	inclusion shape factor $(-)$
b	Burgers vector (m)
d_0	interface thickness (m)
d_g	grain size (m)
e	Euler constant $(-)$
$h(\alpha)$	cavity volume divided by a volume of a sphere of same radius $(-)$
k_b	Boltzmann constant (JK^{-1})
r	cavity radius (m)
r_c	critical radius of a stable nucleus (m)
r_{orient}	a stress ratio characterize crystal orientations effect $(-)$
r_{sf}	a stress ratio characterize shape factor effect $(-)$
r_{sym}	a stress ratio characterize symmetric inclusion tip angle effect $(-)$
r_{asym}	a stress ratio characterize asymmetric inclusion tip angle effect $(-)$
$\dot{r}$	cavity growth rate (m)
t_f	time to fracture (h or s)
t_i	incubation time required to reach the steady-state nucleation rate (s)
t_{min}	creep time at which $\dot{\varepsilon}_{min}$ is reached (s)
C_{11}, C_{12}, C_{44}	cubic elasticity constant (MPa)
D_b	bulk diffusion coefficient $(m^2 s^{-1})$
$D_{gb}\delta$	diffusion coefficient in grain boundaries times the grain boundary thickness, δ $(m^3 s{-}1)$
δD_r	initial variation in specimen diameter relative to the initial average diameter, $\bar{D}$ (m)
E	Young's modulus (GPa)
ΔG	variation in Gibbs free energy (J)
L	half distance between two cavities (m)
L_R	Rice length (m)

N_0^{max}	total number of possible cavitation sites (m^{-2})
N_a	number of cavities per unit grain boundary area (m^{-2})
N_m	number of cavities per unit polished longitudinal section area (m^{-2})
(O_i^1, O_i^2)	i^{th} set of random crystal orientations of the two grains in which inclusion is embedded ($-$)
$\dot{N}_0$	cavity nucleation rate ($m^{-2}s$)
Q	activation energy for dislocation motion (eV)
T	temperature ($^\circ C$ or K)
T_m	temperature at melting point ($^\circ C$ or K)
V	activation volume for dislocation motion (m^3)
Z	reduction in cross-section area at fracture ($-$)
α'	prefactor of the Dyson law (m^{-2})
α_{GB}	angle between grain boundary plan and tensile axis ($^\circ$)
γ_i	energy per unit area of surface i or interface i (Jm^{-2})
γ_{frac}	interface fracture surface energy (Jm^{-2})
$\dot{\gamma}^i$	viscoplastic slip rate of slip system i (s^{-1})
ε	strain ($-$)
$(E^{vp}$	macroscopic viscoplastic strain ($-$) used only in Chapters 2 to 4)
ε_c	critical cavity nucleation initiation strain ($-$)
ε_{min}	strain level at which $\dot{\varepsilon}_{min}$ is reached ($-$)
$\dot{\varepsilon}_{min}$	minimum strain rate (s^{-1})
μ	elastic shear modulus (MPa)
ν	Poisson's ratio ($-$)
ρ	dislocation density (m^{-2})
σ	tensile stress (MPa)
$(\Sigma$	macroscopic tensile stress (MPa) used only in Chapters 2 to 4)
σ_c	critical interface fracture stress (GPa)
σ_{nn}	interface normal stress (GPa)
τ_c	critical shear stress to activate plastic slip (MPa)
τ^i	resolved shear stress applied on slip system i (MPa)
τ_{nm}	interface shear stress (GPa)
φ	tip angle of symmetric or asymmetric precipitate ($^\circ$)
ω_f	critical area porosity of cavities ($-$)
$\bar{\omega}(t)$	average area fraction of cavities at time t ($-$)
Ω	atomic volume (m^3)

list of abbreviations

BCC	Body-centered cubic
FCC	Face-centered cubic
EBSD	Electron backscatter diffraction
EDX(EDS)	Energy-dispersive X-ray spectroscopy
FEG	Field emission gun
SEM	Scanning electron microscope
TEM	Transmission electron microscopy
TKD	Transmission Kikuchi Diffraction
GBS	Grain boundary sliding
CZM	Cohesive zone model
DFT	Density functional theory
MD	Molecular dynamics
FEM	Finite element method

Context

To answer its energy needs and guarantee its independence, France opted in the 1970s for the development of nuclear energy. Today, almost 76% of electricity is provided by from nuclear power plants in France, mostly from Pressurized Water Reactors (PWRs).

Since 2001, a number of countries, including France, have been working on the design of different types of reactors which would ultimately replace the Generation II reactors at the end of operation . The objectives of the Generation 4 International Forum are:

- improving nuclear safety;
- limiting nuclear proliferation by burning plutonium stocks;
- minimizing nuclear waste;
- optimizing the use of natural resources;
- reducing the costs of construction and operation of nuclear reactors.

Six concepts were selected at the end of the first research and development phase. Among the six chosen concepts, Direction de l'Energie Nucléaire (DEN) (French Alternative Energies and Atomic Energy Commission (CEA)) has devoted much of its research effects to the development of a Sodium-cooled Fast Reactor (SFR). Two reactors of this type were built in France, Superphenix, built in Creys-Malville, currently stopped, and Phenix in Marcoule. The design of an industrial prototype, ASTRID (Advanced Sodium Technological Reactor for Industrial Demonstration), is on going

In this context, the long term creep resistance properties of the austenitic stainless steels of the AISI 316 family are intensely studied, in the MASNA project launched by CEA. The 316 stainless steels has better resisting corrosion at high temperature than the 304 stainless steels. Contrarily to the family of 9-12%Cr tempered martensitic steel, the austenitic steels of type 316 are not subjected to fatigue and creep softening.

Incoloy 800 has also been studied in the MASNA project. Incoloy 800 is well-known for its ability to maintain a stable microstructure during prolonged exposure to high temperature. Incoloy 800 is used for steam generator tubing in nuclear power plants (Superphenix) and other heat exchangers at temperature up to $550°C$.

The SFR has the peculiarity of operating at higher temperatures than PWRs.

The heat is transfered by means of a liquid sodium. It is transfered from the primary to the secondary circuit. In these circuits, the temperature can reach $550°C$. The lifetime of the IV generation nuclear reactors, including the ASTRID prototype, is wished be extended to 60 years at temperatures close to $550°C$. Then, the long term creep resistance becomes a major factor for the safety of reactors. Obviously, it is impossible to reproduce such experimental tests at the laboratory. It appears risky to design the structures on the basis of short-term creep test results only. Such extrapolations are usually uncertain, if they are based on macroscopic mechanical tests alone. The only way to make the predictions more reliable is to base them on the physical mechanisms involved during long term creep. That requires the understanding, the modeling and the simulation of creep damage evolution, depending on temperature, stress and time.

Thus, the manuscript is based on the following general methodology:

- First, the study of the macroscopic results obtained by creep tests makes it possible to highlight the main fracture mechanisms and to formulate the first hypotheses;
- In a second step, the physical phenomena responsible for the macroscopic properties measured are identified by coupling various observation techniques (SEM, EBSD, TEM);
- Based on both macroscopic and microscopic information, a modeling based on the physical damage mechanisms is proposed. Finally, the comparison between the modeling results with the available experimental data and observations. The predictions are discussed with respect to other models usually referenced in literature.

This manuscript includes six chapters.

Chapter 1 consists in a state of art concerning material microstructure and basic creep properties.

In Chapter **??**, either necking damage (short term creep tests) or intergranular creep damage (long term creep tests) are observed in five batches of Incoloy 800 depending on stress and temperature. Then, short and long term creep lifetimes are well predicted at temperature ranging between 500 and $760°C$, using the combination of the combination of necking and Riedel intergranular damage models. The Riedel model is based on the Dyson cavity nucleation law which assumes that the cavity density is proportional to the remote creep strain. The Dyson law prefactor, α', is the only parameter measured experimentally. In agreement with literature observations, we conclude that cavities nucleate at the interface of grain boundary particles.

In Chapter 2, the prefactor of the Dyson law, α', is computed for 316L(N), based on the calculated interface stress distribution and a stress criterion. By crystal viscoplasticity Finite Element computations, distributions of interface stress fields around an ellipse-like inclusions are provided, accounting the random

crystal orientations of the neighbor grains, and the grain boundary orientation with respect to the tensile axis are evaluated.

In chapter 3, the interface stress fields and distributions and distributions are calculated for different inclusion morphologies, including inclusion aspect ratio, and inclusion tip geometry.

In chapter 4, the Raj model is discussed by coupling it with our calculated stress distribution. Other classical stress concentrator sources, such as slip bands and grain boundary sliding, are also discussed. Then, the Dyson law prefactor, α', is reevaluated and compared to measured values. And creep lifetimes are predicted in large range of temperatures and stress. They are carefully compared to the existing experimental data, up to 30 years.

The creep lifetimes of Incoloy 800 and 316L(N) are well predicted using the necking and Riedel models for large ranges of temperatures and remote stresses. The cavity nucleation rate is can be either measured or predicted. Our work leads to theoretical explanation of the well-known phenomenological Dyson law, based on the random nature of microstructure.

Chapter 5 consists in general conclusion and perspectives proposed to improve further the long term lifetime prediction.

Chapter 1

Introduction

This chapter provides the state of the art concerning the microstructure and creep properties of 316L(N) stainless steel and Incoloy 800 alloy. Then, some classical models of the creep deformation and damage are highlighted.

Since the mechanical properties and the fracture behavior depend strongly on microstructure, the first section provides some basic elements concerning the metallurgy of these materials. And particularly, the microstructure evolutions during long term ageing and under creep condition are highlighted. The second section provides some classical phenomenological laws concerning creep deformation and damage. The third section describes the mechanisms of creep deformation. Finally, several damage mechanisms and lifetime prediction models are discussed in the forth section.

1.1 Materials under study

1.1.1 Chemical composition

Generally, austenitic stainless steels and Incoloy 800 alloy sustain relatively high strength and high corrosion resistance at high temperature, which leads them to be used frequently for high temperature applications.

The materials under study are AISI 316L(N) steel and Incoloy 800 alloy. Table 1.1 provides the chemical compositions of various grades of austenitic stainless steels and the specification of Incoloy 800 alloy. The historical development in austenitic materials is presented in Fig. 1.1. The AISI 316 steel differs from the AISI 304 steel by the addition of 2.5%wt molybdenum. This addition makes it possible to increase the mechanical characteristics as well as the resistance to corrosion. Subtype 'L' means 'low carbon' and indicates that the steel contains less than 0.04%wt carbon. The subtype 'N' means the nitrogen content is controlled and therefore the nitrogen content is higher than the one of low carbon steels (AISI 316L). Nitrogen is provided to compensate the decrease in C content, with respect to the resistance to dislocation motion specifically. As opposed to low-carbon steels, a high carbon steel, specified by 'H', has a carbon content in the $0.4 - 1.0$%wt range.

The chemical composition of Incoloy 800 alloys will be discussed in the Chapter **??**.

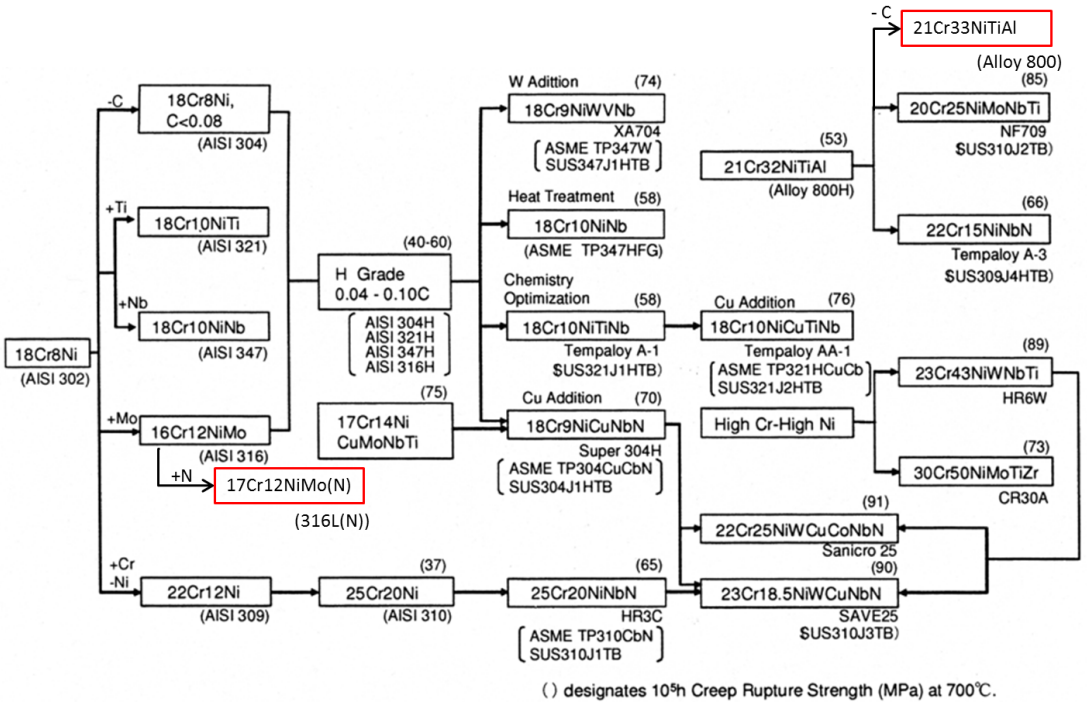

Figure 1.1: Historical development of the family of austenitic stainless steels [4].

Element	304	316	316L	316L(N)	316H TB	Incoloy 800
Fe	bal	bal	bal	bal	bal	bal
C	0.08	0.08	0.03	0.035	0.07	0.10
Cr	17-20	16-19	16-19	17-18.2	16.6	19-23
Ni	9-12	10-14	10-14	11.5-12.5	13.6	30-35
Mn	2	2	2	2	1.65	1.5
S	0.03	0.03	0.03	0.03	0.007	0.015
Si	1	1	1	0.61	1	
Mo		2.25-2.75	2.25-2.75	2.25-2.75	2.33	
Ti						0.15-0.6
Al					0.0017	0.16-0.6
N				0.08	0.025	0.03

Table 1.1: Chemical composition of different austenitic stainless steels ($wt\%$) (RCC-MR Code, 2007 [1], 316H TB [2]) and Incoloy 800 alloys [3].

The 316L(N) stainless steel and Incoloy 800 alloy contain both high chromium content to give them strong corrosion resistance. Since, high chromium content stabilizes the ferrite structure, it should be balanced by austenite stabilizing elements. The ferrite stabilizing elements, called as ferrite stabilizers, are chromium (Cr) (at high content $> 8\%$), molybdenum (Mo), silicon (Si), titanium (Ti) and niobium (Nb), etc. Elements stabilizing the austenite structure are called austenite stabilizers, as nickel (Ni), manganese (Mn), carbon (C) and nitrogen (N), etc.

The notion of equivalent chromium and nickel content can be used to predict the existing phases in phase diagrams for Fe-Cr-Ni based alloys (Fig. 1.2a). Harries [5] proposed the following formulas to calculate the equivalent chromium and nickel contents:

$$Ni_{eq} = [Ni] + [Co] + 0.5[Mn] + 30[C] + 0.3[Cu] + 25[N](wt\%) \quad (1.1a)$$

$$Cr_{eq} = [Cr] + 2[Si] + 1.5[Mo] + 5.5[Al] + 1.75[Nb] + 1.5[Ti] + 0.75[W](wt\%) \quad (1.1b)$$

Since each chemical element affects differently the materials properties, the effect of the main chemical elements will be discussed in the following.

1.1.2 Effect of the main chemical elements.

The mechanical properties and corrosion resistance of stainless steels depend strongly on their chemical composition. Some effects of the main alloying el-

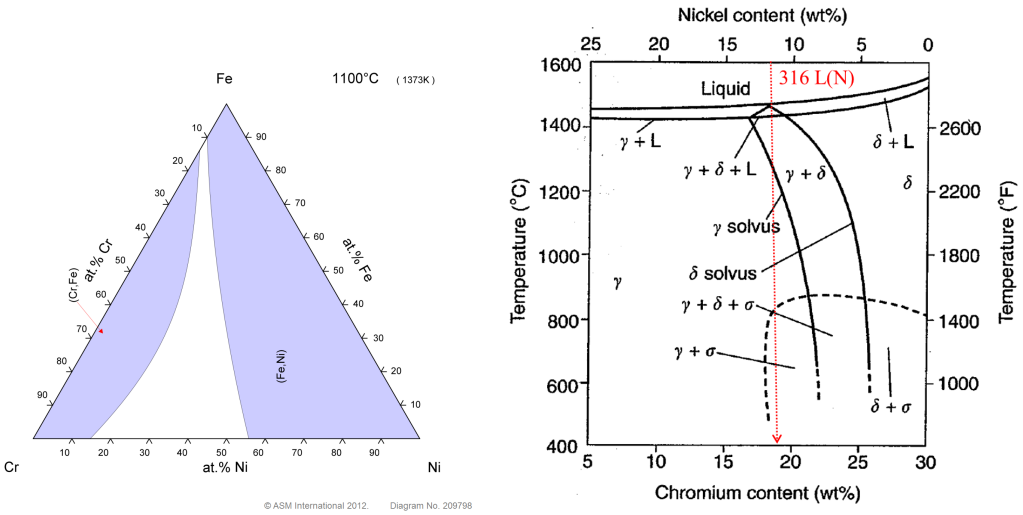

(a) (b)

Figure 1.2: Phase diagrams of Fe-Cr-Ni alloy; (a) isothermal section of ternary Fe–Cr–Ni phase diagram at 1100°C [6]; (b) pseudo-binary section of the Fe-Cr-Ni ternary system at 70% Fe [7].

ements of austenitic stainless steels, as C, Cr, Ni, Mo and N, are described below.

Carbon C

Carbon is generally considered to be one of the most important elements in steels. The C atoms located at the interstitial sites of the crystallographic cell. This improves the mechanical strength of iron. Moreover, carbon is more soluble in austenite than in ferrite, therefore stabilizes the austenitic domain of steels [8]. Low carbon content makes it possible to improve the tenacity and the ductility and thus the cold working behavior [9]. However, with the addition of chromium, carbon is likely to be incorporated in chromium carbide precipitates, particularly at grain boundaries, favoring intergranular corrosion. That leads to the attempts of decreasing the cabon content and the 'L' austenitic stainless steel subtype discussed in subsection 1.1.1.

Chromium Cr

Chromium is an influent element in stainless steels, since it allows the formation of a passive film, which provides high corrosion resistance. The passive film is thicker as the chromium content is higher. However, chromium has a body-centered cubic structure (BCC), such as ferrite. Therefore, it is a ferrite stabilizer.

The higher the chromium content, the larger the risk of intermetallic phase formation. During high temperature operation, the chromium-rich intermetallic phases (such as σ phase) are described in the equilibrium diagram of the pseudo-binary section of the Fe-Cr-Ni ternary system (Fig. 1.2b) [7].

Nickel Ni

As an austenite stabilizer, the addition of nickel in sufficient quantity in Fe-Cr steel makes it possible to obtain an austenitic steel (Face-centered cubic (FCC) structure). Nickel is also known to improve corrosion resistance in chloride environments [10].

Molybdenum Mo

The addition of molybdenum improves significantly the resistance to uniform and localized corrosion in austenitic stainless steels. Nevertheless, molybdenum promotes the precipitation of carbides and intermetallics, such as $M_{23}C_6$ and σ phase.

Nitrogen N

Nitrogen is an austenite stabilizer. Similarly to carbon, nitrogen is located at the interstitial sites of austenite cells. The increase in nitrogen content leads to an increase in twinning in austenite by decreasing the stacking fault energy, especially for steels with low nickel content [11]. This effect could explain that the nitrogen-containing steels display better mechanical properties, as 316L(N).

In addition, nitrogen is more soluble than carbon in solid solution in austenite and ferrite, which reduces the risk of nitride precipitation compared to carbide precipitation. Elements such as chromium and manganese are known to increase the solubility of nitrogen in iron, whereas nickel decreases it [12].

1.1.3 Grain size

Grain boundaries play an important effect in creep properties, through grain boundary sliding, grain boundary diffusion and grain boundary cavitation. Therefore, the creep resistance is strongly influenced by grain size. However, no clear conclusion arises from by experimental results [13, 14]. Creep can be decomposed into intergranular creep and intragranular creep. Intergranular creep is expected to be affected by changing the grain size.

The grain size is controlled by the heat-treatment. For the AISI 316L(N) and Incoloy 800, the grain sizes are 15-30μm and 50-150μm, respectively.

It should be noticed that two Incoloy 800 grades differ by their respective heat-treatments: 'Grade 1', corresponds to anneal at approximately 980°C (grain

size 10-20μm) and 'Grade 2', to anneal at approximately 1150°C (grain size 50-250μm) [15]. In this study, only Grade 1 is considered.

1.1.4 Secondary phases

It is observed on isothermal section of ternary Fe–Cr–Ni phase diagram at 1100°C [6] (Fig. 1.2a) and pseudo-binary section of the Fe-Cr-Ni ternary system at 70% Fe [7] (Fig. 1.2b), that 316L(N) is concentration range for which both austenite and ferrite phases co-exist. Since they are obtained by quenching from temperature range $1000 - 1200°C$, it is thus understood why austenitic steels often contain a small percentage of ferrite.

When a stainless steel is subjected to a heat-treatment at a temperature T_1, the element contents are higher than the solubility thereof at temperature T_2 (work condition) ($T_2 < T_1$). Then, during further ageing at high temperature or creep, atoms can diffuse and more stable second phases[1] are produced. Their nature depends on temperature, the previous heat-treatment and the cooling conditions. The main precipitates and intermetallics observed in AISI 316L(N) and Incoloy 800 are presented in Table 1.2.

Hence, the second phases observed in 316L(N) stainless steels and Incoloy 800 alloy in the as-received state or formed during creep are described in the following subsection.

1.1.4.1 Carbides

The most frequently observed carbides in austenitic steels and Incoloy 800 during heat-treatments are $M_{23}C_6$, where M accounts mainly for mainly chromium, partially substituted by Fe, Mo or Ni [18]. The $M_{23}C_6$ particles are known to nucleate generally first at grain boundaries, resulting in a significant decrease in intergranular corrosion resistance [8]. However, the $M_{23}C_6$ particles could also be observed at the twin boundary and in the matrix [24, 28, 29]. Hong et al. [17] and Padilha and Rios [9] studied the relationship between carbide germination and grain boundary disorientation. They showed that the increase in grain disorientation leads to a change of $M_{23}C_6$ geometry, from a platelet geometry to triangular one [9]. The size of the intergranular $M_{23}C_6$ particles is generally below 0.5μm [29–31].

The $M_{23}C_6$ particles are generally the first type of second phases to be nucleated in austenitic stainless steels because they may be coherent or semi-coherent with the austenite crystal. Indeed, the mesh parameter of the face-centered cubic $M_{23}C_6$ is approximately 3 times that of austenite. And these two phases are

[1]The precipitates and intermetallic phases are all considered as secondary phases in this manuscript.

Phase	Chemical composition	Crystallographic Structure[1]	Formation Temperature ($°C$)	Crystallographic group	Lattice constant (nm)	location	Material	Reference
$M_{23}C_6$	$Cr_{23}C_6$	FCC	500-950	$Fm\bar{3}m$	1.056-1.065	bulk GB[2]	316L(N) Incoloy 800	[16, 17]
G	$Ni_{16}Si_7Ti_6$	FCC	300-750	$Fm\bar{3}m$	1.14	GB	316L(N) Incoloy 800	[2, 15, 18]
σ	Fe, Cr, Mo, Ni	tetragonal	600-1000	$P4_2/mnm$	a=0.879-0.883 c=0.454-0.459	bulk GB	316L(N)	[19, 20]
χ	$Fe_{36}Cr_{12}Mo_{10}$	BCC	700-900	$I\bar{4}3m$	0.878±0.005	bulk GB	316L(N)	[21]
Laves	Fe_2Mo	hexagonal	550-850	$P6_3/mmc$	a=0.473 c=0.772	bulk GB	316L(N)	[22, 23]
Ferrite (δ)		BCC		$Im\bar{3}m$	0.286		316L(N)	[24, 25]
γ'	$Ni_3(Ti, Al)$	FCC			0.3607	bulk	Incoloy 800	[15, 26]
$Ti(C, N)$	$Ti(C, N)$	FCC		$Fm\bar{3}m$	0.424-0.433	bulk	Incoloy 800	[27]

Table 1.2: Details of the main precipitates and intermetallics observed in 316L(N) and Incoloy 800. [1] BCC: Body-centered cubic and FCC: Face-centered cubic, [2] GB: grain boundary

approximately in a cube on cube orientation relationship, [16, 18]:

$$\{110\}_{M_{23}C_6} \| \{110\}_{\gamma} \qquad \langle 001 \rangle_{M_{23}C_6} \| \langle 001 \rangle_{\gamma} \tag{1.2}$$

Other types of carbides such as M_7C_3, M_6C and MC have also been observed during ageing of austenitic stainless steels. Precipitation of M_7C_3 occurs only in high-carbon austenitic steels, or in processes such as carburization [8]. The M_6C precipitates, with a diamond FCC structure, are generally much rarer than other carbides and are favored by the addition of molybdenum and nitrogen [9, 21]. The MC carbides have a FCC structure of NaCl type. Finally, the introduction of elements such as V, Nb, Ti, Zr, Al, Hf and Ta, are known to lead to the nucleation of highly stable MC-type intragranular carbides. That is generally used to hinder $M_{23}C_6$ precipitation [9].

1.1.4.2 G Phase

The G phase is a silicide, formed in austenitic steels stabilized with titanium and niobium [18]. It is also observed when decomposing ferrite at temperatures below $500°C$ [9]. The G phase is particularly rich in nickel and silicon and its stoichiometric composition is $Ni_{16}Si_7Ti_6$ (Table 1.2).

In the case of G phase nucleated during the decomposition of ferrite, the particle size is very law, in order of the one to the ten nanometers. And they are dispersed in the metallic matrix [32].

In AISI 316 and Incoloy 800 alloys, the G phase is observed after short term ageing $(1000h, 600°C)$. Under such conditions, the G phase particles are located along grain boundaries and at triple points, with a size up to $500nm$ [2, 15].

1.1.4.3 σ Phase

The σ phase is known to be hard and brittle, rich in chromium and molybdenum, resulting in a drastic reduction of the mechanical properties and corrosion resistance [33–35].

Nilsson [33] pointed out that high chromium and molybdenum contents accelerate the precipitation kinetics and increase the volume fraction of σ phase, whereas nickel increases the kinetics of precipitation but decreases the volume fraction of σ phase.

It is generally believed that σ phase particles nucleate lately in AISI 316 steels. However, once the nucleation of σ phase has occurred, the size of σ phase particles may rapidly reach $1\mu m$ [2]. Nevertheless, the precipitation mechanisms are still not fully clear.

1.1.4.4 χ Phase

The lattice parameter of the intermetallic χ phase is about three times that of ferrite, allowing χ growth in a cube on cube orientation relationship with ferrite,

where the {111} planes and ⟨001⟩ directions of the two phases are parallel. Since the strong crystallographic coherence of the two phases, the energy required for the nucleation of the χ phase in ferrite is low. Therefore, the χ phase formation kinetics is faster than the σ phase one. The χ phase is, however, less stable than the σ phase and could be absorbed by the σ phase for longer ageing times [36]. The χ phase is richer in molybdenum than the σ phase and its formation is triggered by an increase in the molybdenum content [21].

1.1.4.5 Laves phase η

Laves phase particles could be observed in the matrix and at grain boundaries. The laves phase (η) is a minor constituent of stainless steels containing Mo (such as AISI 316). Its chemical composition is Fe_2Mo. Theoretically, laves phases do not exist in the material in its as-received state. They can appear after a in-service time over $100h$ [2].

1.1.4.6 γ' ($Ni_3(Ti, Al)$)

This precipitate is observed in Incoloy 800 after a few hundred hours of service at temperatures between 500 and $650°C$. Contrarily to carbides formed at grain boundaries, the γ' phase nucleates homogeneously in the matrix. The γ' phase particles are spheroidal. Their size and density are controlled by the chemical composition, the heat-treatment conditions and creep conditions. However, the size of γ' is generally below $100nm$.

The long-term elevated-temperature strength of Incoloy 800 is affected by the strengthening effects of γ' particles. Unfortunately, this phase may also cause decrease in long term ductility [26].

During creep, the γ' particles could be either sheared or circumvented by dislocation gliding. Consequently, parameters, such as precipitate size, inter particle distance and volume fraction in matrix, affect the creep resistance of Incoloy 800 after long term service at high temperature. That affects the evolution of its creep ductility, with temperature and time.

1.1.4.7 Ti(C,N)

The $Ti(C, N)$ particles are generally rectangular large precipitates ($1 - 5\mu m$), embedded in the grains of Incoloy 800 alloys [15]. The affinity of titanium to carbon is higher than the Cr one, thus $Ti(C, N)$ precipitates are much more stable than $M_{23}C_6$ precipitates [27]. Therefore, the presence of $Ti(C, N)$ could inhibit $M_{23}C_6$ precipitation. However, $M_{23}C_6$ particles nucleate preferentially at in-service temperatures because $M_{23}C_6$ is more stable at high temperature [27].

1.1.4.8 δ Ferrite

The residual δ ferrite has a higher chromium concentration than the austenitic matrix, and because of its structure, the diffusion rate of these elements is faster. During annealing, this phase can be decomposed into thermodynamically stable austenite and into a wide variety of second phases, according genetic decomposition:

$$\delta \longrightarrow \gamma + precipitate \tag{1.3}$$

These precipitates are mainly $M_{23}C_6$ carbides. Depending on temperature, the intermetallics may also be formed, but in smaller quantities because their precipitation kinetics are slower.

Fig. 1.3 shows the microstructure in one sheet of as-received AISI 316L(N). Some ferrite bands are observed. Villanueva et al. [37] observed that the initial δ ferrite bands arise from the solidification. They are indeed elongated and parallel to the rolling direction. This observation agrees with the observations of Rieth et al. [38], Padilha et al. [20], Slattery et al. [23] and Odnobokova et al. [39].

Figure 1.3: Microstructure of the as-received material, 1/2 of the plate thickness, observed by optical microscopy (×100) [40].

1.1.5 Microstructure evolution at high temperature

At high temperature, the microstructure of austenitic steels is unstable. The microstructure changes in function of temperature, time, stress and strain.

Villanueva et al. [37] studied the precipitation of σ phase in AISI 316L. Their observations show that, during creep, the formation of σ phase occurs at grain

boundaries and at triple points. And no σ phase was detected in the metallic matrix.

The microstructural evolution of 316H TB in function of time and temperature is shown in Fig. 1.4a. At $550°C$, the $M_{23}C_6$ precipitate appears after almost $2000h$. And no σ phase particle is observed even after 10^5h. However, this TTP diagram is established only based on the observation of the microstructure of the specimen head portions. Hence, the stress and viscoplastic strain effect is not included in this TTP diagram. Fig. 1.4b is based on the analysis of the data provided by the NIMS data sheet [2]. It illustrates that, under stress and viscoplastic strain, the σ phase particles could be observed after $100h$ (at $700°C$), which is much earlier than under the unloaded condition (specimen heads, pure ageing). Therefore, it can be concluded that the stress and viscoplastic strain has a strong effect on precipitation at high temperature.

As shown in Fig. 1.5, the NIMS data sheet provides the size evolution of $M_{23}C_6$ and σ phase particles during creep in AISI 316H TB [2]. In the head portion, the size of $M_{23}C_6$ is lower than 250nm. Unfortunately, no specific information about the size of $M_{23}C_6$ carbides in the gauge portion is given. From SEM or TEM image in literature [17, 41], we deduce that the size of $M_{23}C_6$ is generally lower than $0.5\mu m$, which is much lower than the size of σ phase. Moreover, once σ phases are observed, their size reaches 1 or $2\mu m$ [2]. This holds in both in the head and gauge portions.

The kinetics of precipitation during creep depends on many factors, including temperature, stress, chemical composition, crystallographic structure, grain size and heat-treatment. Therefore, these precipitation phenomena are difficult to be studied either experimentally or theoretically. Nevertheless, CALPHAD computations [42] demonstrated that the G phase is not stable at high temperature. The χ phase appears only at high temperature ($> 700°C$) as shown in Fig. 1.4a. Furthermore, along grain boundaries, the $M_{23}C_6$ precipitates and the σ phase particles are generally observed compare to others. Consequently, only the $M_{23}C_6$ precipitates and the σ phase particles are considered in Chapters 2, 3 and 4.

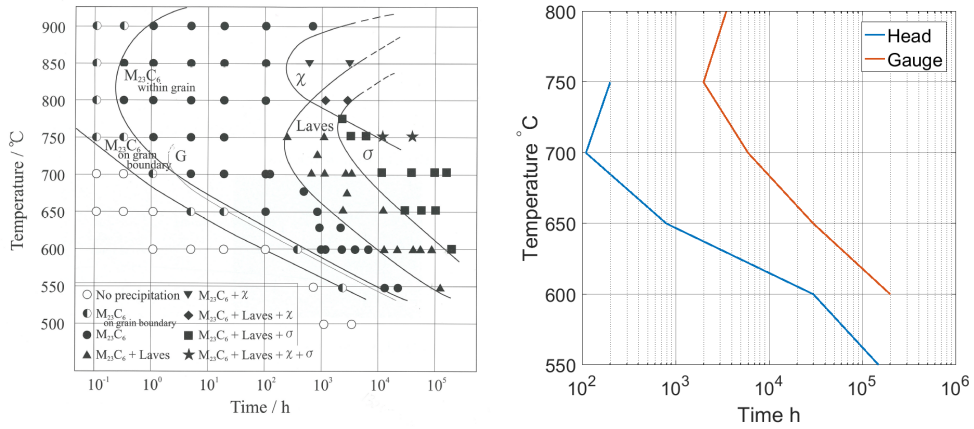

(a) (b)

Figure 1.4: Time-temperature-precipitation (TTP) diagram (a) for specimen head portions of 316H TB [2]; (b) of σ phase for both specimen head and gauge portions of 316H TB obtained by analyzing NIMS data sheet [2].

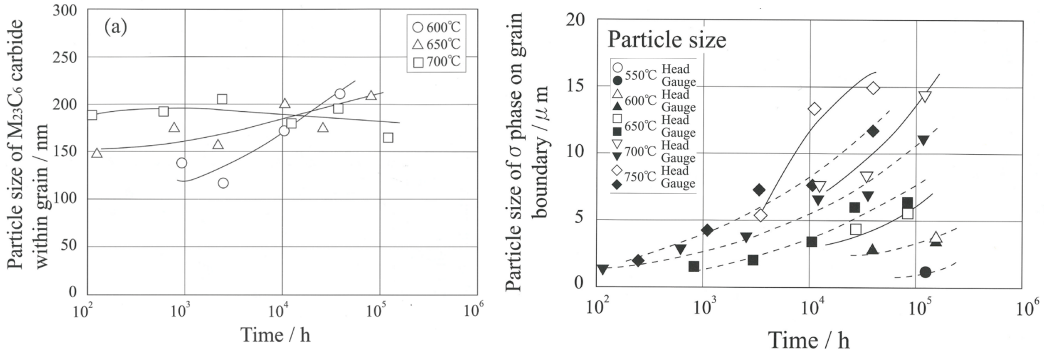

(a) (b)

Figure 1.5: Change in particle size of (a) $M_{23}C_6$ particles in specimen head portion in function of time and (b) σ phase particles in specimen head and gauge portions in function of time for 316H TB [2].

1.2 Creep background

Viscoplastic materials deform continuously when subjected to a constant load and temperature. This phenomenon is called creep.

Creep deformation is thermally activated, i.e. relatively small variations in temperature cause considerable variations in strain rate. Creep is possible at all temperatures above absolute zero. However, for metallic alloys, creep occurs generally significantly only at temperatures close to or higher than about $0.4T_m$, with T_m the melting temperature. Thus, creep deformation is most often negligible for alloys used in the construction of structures such as bridges or ships. This is not the case for many materials which may be used in the nuclear power plants of Generation IV, which will be subjected to temperatures above $500°C$ during several decades. The short and long term creep behaviors of AISI 316L(N) and Incoloy 800 alloys, are therefore, studied in the present work.

1.2.1 Creep deformation

Creep is a deformation process observed when applying a constant engineering stress, σ^{eng}, to a specimen at high temperature. A few authors impose a constant true stress, σ^{true}. A typical creep curve for metals and alloys is shown in Fig. 1.6.

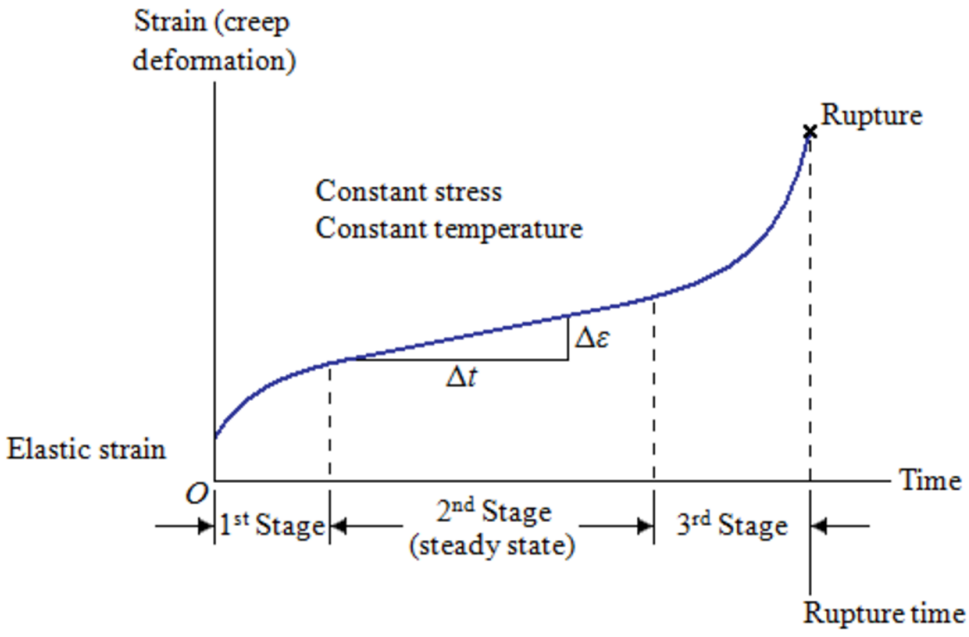

Figure 1.6: Typical creep curve in metals and alloys.

Three stages are delineated in the creep curve:

- the primary stage (first stage), the deformation rate decreases due to the increasing of dislocation and low angle boundary densities and the effect of intergranular viscoplastic strain incompatibilities and resulting internal stress;
- the steady-state creep stage (or secondary stage), during which the strain rate is approximately constant. This strain rate is generally called as the minimum strain rate, $\dot{\varepsilon}_{min}$. The constant strain rate is caused by a balance between dislocation annihilation and deformation hardening. Then, the dislocation density is almost constant during this stage. This is a dynamic equilibrium.
- the tertiary stage. The strain rate accelerates up to fracture, due to necking, internal cracks or voids, and the decrease in cross-section area of the specimen in case of constant force lading.

The relationships between engineering and true strains and stresses are the followings:

$$\varepsilon^{true} = ln(1 + \varepsilon^{eng}) \tag{1.4a}$$

$$\sigma^{true} = \sigma^{eng} \cdot (1 + \varepsilon^{eng}) \tag{1.4b}$$

The minimum true strain rate, $\dot{\varepsilon}^{true}_{min}$, could be determined by plotting the evolution of true strain rate in function of the true strain or time.

A significant indicator of the involved creep fracture mechanisms is the reduction in fracture area, Z. The area of fractured surface, S_f, is generally used to calculate the reduction in area, Z. The reduction in area is the ratio between the variation of transversal section, $S_0 - S_f$, and the initial section area, S_0:

$$Z(\%) = \frac{S_0 - S_f}{S_0} \cdot 100\% \tag{1.5}$$

Creep deformation and fracture have been studied phenomenologically for almost hundred years.

1.2.2 Phenomenological viscoplasticity laws

The phenomenological creep deformation and fracture laws are presented in this subsection.

1.2.2.1 Phenomenological creep laws

Andrade's Law

In 1910, a mathematical law ruling the viscoplastic strain during the primary stage (Fig.1.6) was proposed by Andrade [43]:

$$\varepsilon(t, \sigma, T) = C_1 \cdot t^{C_2} \cdot \sigma^{n_1} \tag{1.6}$$

where the coefficients C_1, C_2 and n_1 are temperature-dependent.

The strain rate during the primary stage is calculated using Eq. 1.7, which assumes deformation hardening.

$$\dot{\varepsilon} = C_3 \cdot \varepsilon^{C_4} \cdot \sigma^{n_2} \tag{1.7}$$

In this equation, $\dot{\varepsilon}$ (% h^{-1} or s^{-1}) denotes the strain rate for a given creep strain, ε(%), under stress σ (MPa or Pa) and at temperature T ($^{\circ}C$).

The coefficients C_1, C_2, n_1, C_3, C_4 and n_2 are adjusted using experimental creep curves. The values of the coefficients of 316L(N) are provided by the RCC-MR design code [1], and more recently, reevaluated by Cui [44] for the materials under study. In Chapters 2 and 3, these parameters will be used for Finite Element simulations. For Incoloy 800, these parameters are not provided by the MCC-MR code [1].

Norton's Law

In 1929, Norton [45] proposed a phenomenological law which links the minimum strain rate to the stress.

$$\dot{\varepsilon}_{min}^{true} = C \cdot (\sigma^{eng})^n \tag{1.8}$$

where $C(MPa^{-n}h^{-1}$ or $Pa^{-n}s^{-1})$ and $n(T)$ are temperature dependent material constants, $\dot{\epsilon}_{min}^{true}$ (h^{-1} or s^{-1}) is the minimum true strain rate and σ^{eng} (MPa or Pa) is the engineering stress. The values of coefficients C and n are provided in Chapter **??** (Incoloy 800) and Chapter 2 (316L(N)).

For describing the thermally-activation of creep deformation, the temperature dependence can be expressed as an Arrhenius-type expression as proposed by Sherby and Burke [46]:

$$\dot{\varepsilon}_{min} = A_{SB} \cdot exp(-\frac{Q}{RT}) \tag{1.9}$$

where R is the gas constant ($8.314 Jmol^{-1}K^{-1}$), A_{SB} is a constant, and Q is the activation energy for creep deformation ($Jmol^{-1}$).

Webster and Ainsworth [47] combined Eq. 1.8 and Eq. 1.9, proposed Eq. 1.10. This equation takes into account the effect of stress and temperature.

$$\dot{\varepsilon}_{min} = A_{WA} \cdot \sigma^n \cdot exp(-\frac{Q}{RT}) \tag{1.10}$$

1.2.2.2 Phenomenological lifetime predictions

Using conventional uniaxial creep tests to estimate long term creep lifetime of structural materials may require impractically long testing times. In fact, the laboratory creep test duration is generally less than one year, which is very short compared to the in-service condition (duration up to 60 years). Few laboratory,

as NIMS [2], ORNL [48, 49], have long term test up to 25 years, which is always shorter than the in-service ones.

Therefore, over the past decades, many studies aimed to develop predictive models, based on short term test results, to estimate long term lifetime. Firstly, creep lifetimes are predicted by phenomenological laws, especially the Monkman-Grant relationship and the Larson-Miller relationship. Both laws make it possible to extrapolate from the available experimental test lifetimes at different temperatures and/or lower stresses.

Monkman-Grant relationship

The Monkman-Grant relationship [50] has been shown to be valid for a wide range of metals and alloys. The strain rate is assumed to be constant during the creep test and equal to the minimum strain rate. The well-known Monkman-Grant law describes the relationship between minimum strain rate ($\dot{\varepsilon}_{min}$) and fracture lifetime (t_f) [50].

$$\dot{\varepsilon}_{min}^{m_{MG}} \cdot t_f = C_{MG} \tag{1.11}$$

where m_{MG} is a constant that is originally evaluated by Monkman and Grant to be between 0.8 and 1 for metals and alloys and C_{MG} is the Monkmann-Grant constant. Therefore, considering $m_{MG} = 1$, the product of minimum strain rate and fracture time is constant and independent of test temperature (Fig. 1.7) [51].

Based on this equation, results of short term, high stress creep tests can be extrapolated to long term low stress creep conditions. The value of m_{MG} depends on each material microstructure, and small values of m_{MG} is associated with large grain materials [51, 52].

The Larson-Miller relationship

In Larson-Miller approach, a constant parameter called C_{LM} is defined as a function of test temperature, fracture time and materials constant. Knowing this material constant, the fracture time can be extrapolated from short term laboratory tests result at temperature/stress higher than the in-service ones.

The Larson-Miller parameter is defined by the following relationship:

$$P(\sigma) = T(C_{LM} + logt_f) \tag{1.12}$$

From the results of tests carried out under different stresses, the Larson-Miller function of the stress, $P(\sigma)$, can be deduced. $P(\sigma)$ determines the time to reach a given strain with different couples of (σ, T).

Fig. 1.8 shows experimental creep failure results for various alloys, which justifies the use of a value of C_{LM} of almost 20 [54]. Nevertheless, the Larson-Miller relationship is only a phenomenological law used to predict long term creep fracture properties without a well defined physical basis.

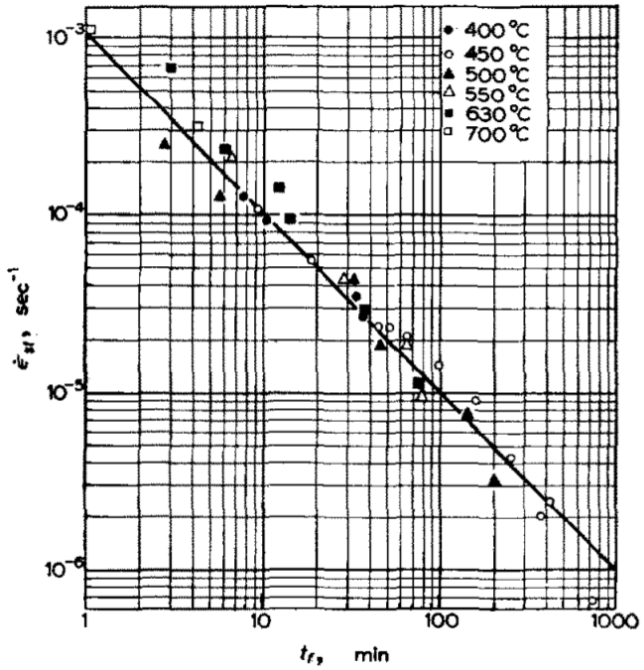

Figure 1.7: Minimum strain rate in function of lifetime in copper (Eq. 1.11) [53].

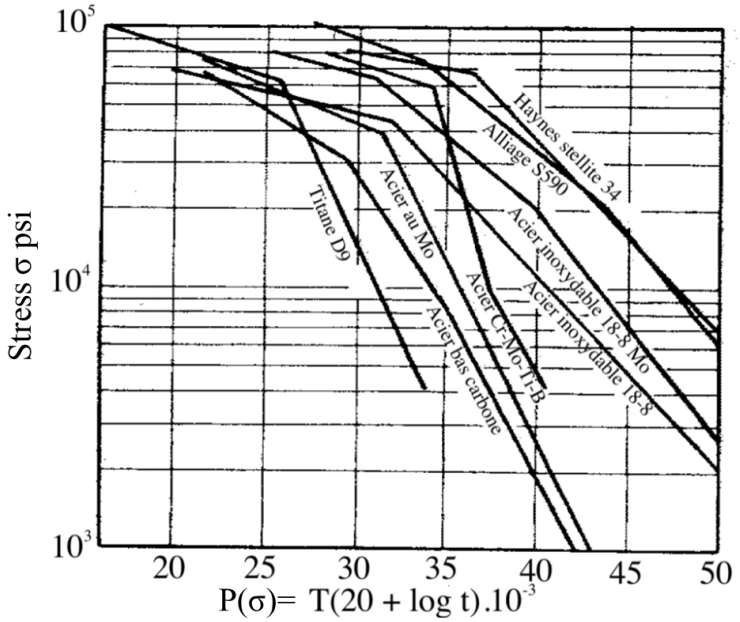

Figure 1.8: Larson Miller representation of experimental creep lifetimes, t, for various alloys [54] (Psi = pound per square inch).

The extrapolations carried out based on phenomenological models may lead to a large over- or underestimations of long term creep lifetime. Therefore, the understanding of the physical deformation and damage mechanisms are necessary to predict more reliable long term creep lifetimes.

1.3 Creep deformation mechanisms

The minimum strain rate has been shown to be well predicted by the Mukherjee-Bird-Dorn equation [55], which expresses the creep rate in terms of stress, temperature and grain size, as:

$$\dot{\varepsilon}_{min} = \frac{A_{MBD}\mu b}{k_b T} D_b(T)(\frac{b}{d_g})^p(\frac{\sigma}{\mu(T)})^n \tag{1.13}$$

where A_{MBD} is a dimensionless constant, $D_b(T)$ is the bulk self-diffusion coefficient, d_g is the grain size, $\mu(T)$ is the elastic shear modulus, n is the stress exponent.

More precisely, several mechanisms are known to contribute to the creep deformation of steels, such as diffusion, grain boundary sliding and climb/glide of dislocations. Each mechanism of deformation depends on stress, temperature and metallurgical structure.

A first classification of the mechanisms is proposed by Cannon and Langdon [56] in function of the value of p. If the crystal deformation mechanism is dominant and the grain boundary sliding plays a negligible role, then, $p = 0$. If the grain boundaries contribute to the deformation process, p takes values from 1 to 3.

In the following, the main mechanisms of pure diffusion creep are described and then those involving dislocation.

1.3.1 Diffusion creep

At high temperature and low stress, a almost linear relationship between the minimum strain rate and the tensile stress is generally observed [52, 57]. Such a deformation may not caused by dislocation glide, but by pure diffusion.

In fact, the vacancy chemical potential in grain boundaries is affected by the grain boundary normal stress direction. Therefore, atoms diffuse from boundaries oriented parallel to the tensile axis to the perpendicular ones. Then, the creep deformation may occur. The flow may take place either through the crystalline lattice (Nabarro and Herring diffusion creep [14, 58]) or along grain boundaries (Coble diffusion creep) [13].

The Nabarro-Herring creep

Nabarro [14] and Herring [58] proposed that, during creep deformation, the matter is transported by extraction of atoms from the inside of a crystal through its surface. The vacancy and atom flows are in the opposite directions through the volume of each grain (Fig. 1.9a). Atoms move from the compressed surface to the ones loaded in tension. And vacancies are transported along the reverse path. In pure tension loading, this phenomenon results in grain elongated in the tensile direction.

Assuming the bulk diffusion dominant, Herring[58] deduced the following strain rate:

$$\dot{\varepsilon}_{min} = A_{NH}\frac{D_b\sigma\Omega}{d_g^2 k_b T} \tag{1.14}$$

where A_{NH} is a constant D_b is the bulk self-diffusion coefficient, Ω is the atomic volume. This equation should be more suitable at very high temperature.

The important characteristics of this model appear as:

- creep-diffusion results in a behavioral behavior of the Newtonian viscous type;
- the creep strain rate is faster at high temperature;
- the strain rate is faster with a small grain size.

The Coble creep

The Coble model [13] proposed a polycrystalline creep law, for which the flow velocity is controlled by the diffusion along the grain boundaries (Fig. 1.9b) which is generally be faster than the bulk one. In fact, the intergranular self-diffusion energy is, generally, about twice as low as the bulk one [59]. Coble [13] proposed:

$$\dot{\varepsilon}_{min} = A_{Co}\frac{D_{gb}\delta\sigma\Omega}{d_g^3 k_b T} \tag{1.15}$$

where D_{gb} is the vacancy self-diffusion coefficient along grain boundaries and δ is the grain boundary thickness.

The difference between the Herring-Nabarro model and that of Coble relates to the influence of the grain size and the activation energy. The experimental tests carried out on copper have clearly shown a variation in the rate of creep proportional to $1/d^3$ at low temperature ($550°C$) and $1/d^2$ at higher temperature ($840°C$) [57].

1.3.2 Grain Boundary Sliding

The two previous diffusion models are based on simplified hypotheses, such as identical grain shapes and homogeneous grain deformation. Moreover, the grains must remain in contact during the deformation process, provided intergranular

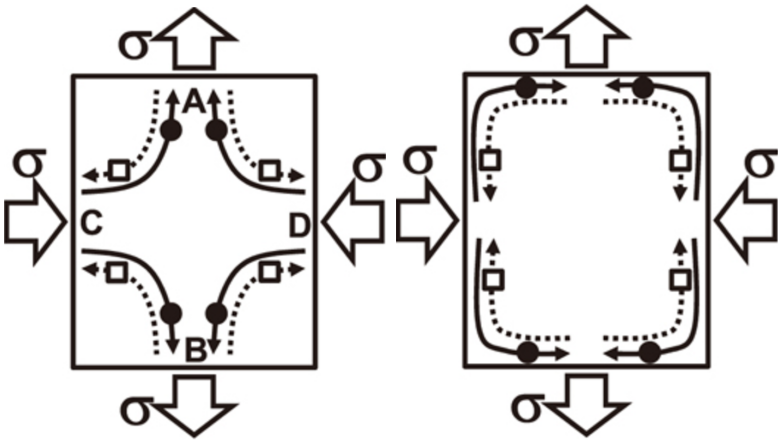

(a) (b)

Figure 1.9: a) The Nabarro-Herring creep: vacancy diffusion from the free surface loaded in tension and the ones loaded compression, b) The Coble creep: diffusion occurs through the grain boundaries (•: atom, □: vacancy) [60].

damage has not taken place. However, at high temperature, grains may glide along their grain boundaries because of differences in crystallographic orientations. This phenomenon is called grain boundary sliding.

Grain boundary sliding and diffusional creep are related as studied in details by Raj and Ashby [61]. Considering a polycrystal as a compact set of hexagons, they proposed that grain boundary sliding or flow induce diffusion create the deformation incompatibilities.

Assuming that diffusion takes place both in volume and along the grain boundaries, Raj and Ashby [61] calculated the minimum strain:

$$\dot{\varepsilon}_{min} = C_{RA}\frac{\sigma\Omega}{k_bT}\frac{1}{d^2}D_b[1+\frac{\pi\delta}{\lambda}\frac{D_{gb}}{D_b}] \tag{1.16}$$

where λ is the basic periodicity of the grain boundary, for a perfect hexagonal arrangement microstructure, $\lambda = d_g$.

Diffusion creep and grain boundary sliding creep lead to a linear viscous creep: $\dot{\varepsilon}_{min} \propto \sigma^1$. These models can not explain the creep deformation mechanism at high stress, for which the stress exponent is much higher than 1. Then, dislocation climb and glide usually considered at higher stress.

1.3.3 Dislocation creep

Dislocations glide during creep may be controlled by self-diffusion. Because of the similarity in the activation energy, vacancies are expected the motion of dislocations to overcome obstacles on their slip planes.

At high temperature, the dislocation motion has two degrees of freedom: climb and glide. Both mechanisms allow dislocations to bypass the obstacles with different activation energy and volume. The obstacles against dislocation movement decrease the creep rate.

Weertman [62] proposed a steady-state dislocation theory based on the climb of edge dislocations. This theory assumes that work-hardening occurs when dislocation are arranged as pile-ups against existing barriers such as grain boundaries, precipitates, other dislocations or solid solution atom clusters. A stress exponent of three is obtained.

Then, Sherby and Weertman [63] proposed a more general power creep law equation as:

$$\dot{\varepsilon}_{min} = A_{SW}(\frac{\sigma}{\mu})^{n-1}\frac{\sigma\Omega}{k_bT}exp(-\frac{Q}{RT})exp(-\frac{P\Delta V}{RT}) \tag{1.17}$$

where A_{SW} is a dimensionless constant, P is hydrostatic pressure, R is the gas constant, Q is activation energy (considered as the activation energy of self-diffusion through the bulk [63]) and ΔV is the activation volume.

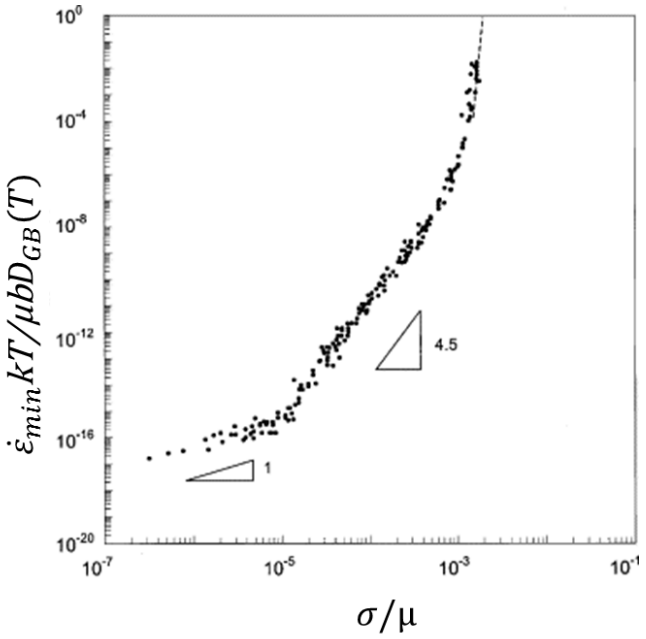

Figure 1.10: The normalized minimum creep rate versus the modulus-compensated steady-state stress for 99.999 pure Al [52].

Fig. 1.10 illustrates the typical creep deformation behavior of a metal. This figure can be divided into three regions. The fist region covers very low stress levels. It could be explained by diffusion creep and/or grain boundary sliding. The second region covers intermediate stress levels. This is the dislocation creep domain corresponding to motion of dislocations by combined glide and climb.

The third region show a stronger deviation from linearity observed at very high stress/ low temperature and is referred to the power-law breakdown [52].

1.3.4 Deformation map

For a given microstructure, the activated creep deformation mechanism depends on the applied stress and temperature. It is useful to couple the experimental results and theoretical models concerning viscoplastic deformation mechanisms in the form of diagrams or maps, as was carried out systematically by Ashby [59]. The deformation mechanism maps for AISI 316L(N) [59] and Incoloy 800 [64] are plotted in Fig. 1.11.

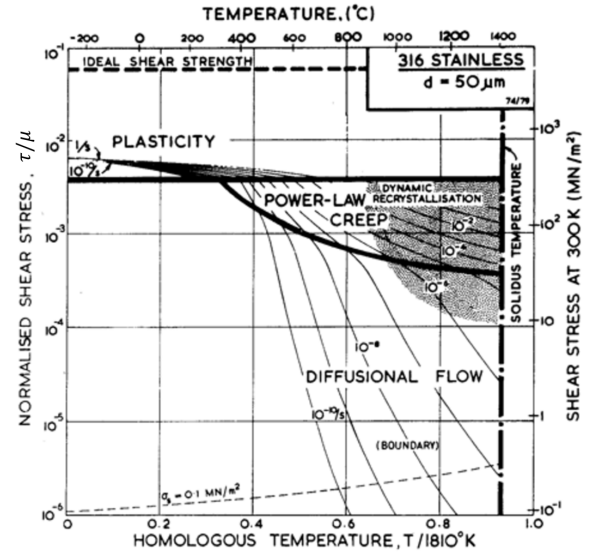

(a)

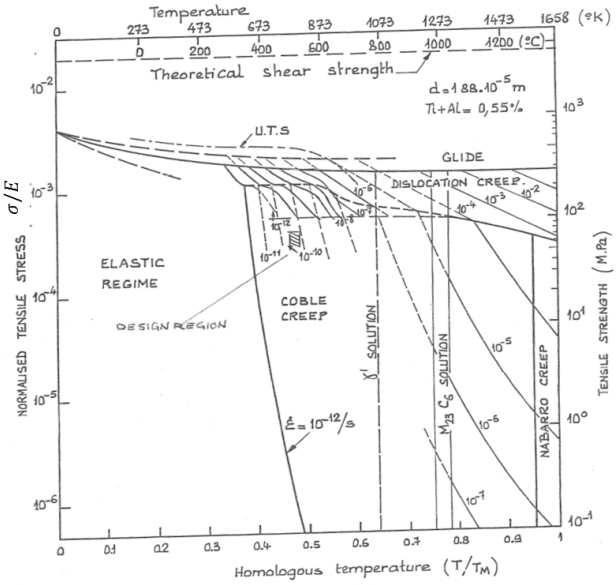

(b)

Figure 1.11: Stress-temperature deformation mechanism maps for (a) AISI 316 with a grain size of 50 μm [59], (b) Incoloy 800 with a grain size of 18.8μm (Grade 1) [64].

1.4 Damage mechanisms

Fractography is generally used to determine the fracture mode. The microstructure observations of the fracture surface are generally carried out by Scanning Electron Microscope (SEM). It consists in comparing the observed fracture surfaces with those which are classically reported in literature for well-determined loading conditions.

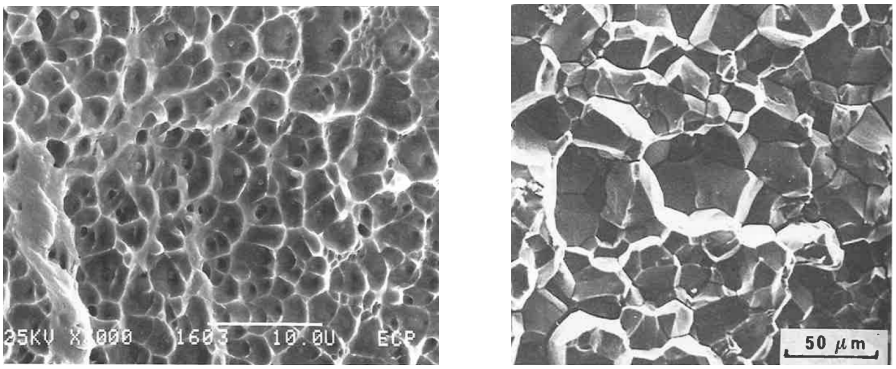

(a) (b)

Figure 1.12: Fractographies of (a) ductile fracture of 316L steel (b) intergranular fracture at $650°C$ of Inconel 718 [57].

Two different types of fracture surface are generally observed after creep failure (Fig. 1.12):

- Ductile fracture surfaces (Fig. 1.12a) are generally characterized by the presence of a plastically deformed zone, as induced by necking for uniaxial creep. There is no clear cleavage or crack propagation. Such fracture surfaces show dimples with possibly second phase particles inside. This type of fracture is a transgranular fracture. Ductile fracture surfaces are generally observed after short term creep one;

- Intergranular fracture surfaces (Fig. 1.12b) result from another creep damage, specifically intergranular cavitation. At the microscopic scale, grain boundaries are observed on the fracture surfaces. Such damage mechanism is usually observed after tests hold at high temperature and low stress. Intergranular cavitation leads to a kind of 'embrittlement' of the grain boundaries. Thus, cracks propagate along the grain boundaries leading to coalescence and final fracture. Specimen elongation and reduction in fracture area are much lower than for ductile damage.

SEM observation concerning Incoloy 800 are shown in Chapter **??**.

1.4.1 Necking

Based on the homogeneous reduction in cross-section, Hoff [65] deduced that the creep lifetime is inversely proportional to the minimum strain rate:

$$t_f = \frac{1}{n\dot{\varepsilon}_{min}} \tag{1.18}$$

However, this model assumes the fracture takes place when the specimen strain tends to infinity, and the cross-section reduces to zero, because of volume conservation. Therefore, generally, this model overestimates the creep lifetime [66].

In ductile polycrystalline materials, the overall plastic deformation may become instable. The instability phenomenon leads to localized necking, which is characterized by a localized reduction in the specimen cross-section which may occur during creep deformation. In fact, the decrease in cross-section leads to an increase in local true stress. When the applied stress is no longer compensated by hardening, necking occurs. It should be noticed that not only the stress, but also the sensitivity to strain rate affect necking process. Necking is the result of the appearance of a deformation heterogeneity at the macroscopic scale which can lead to a ductile fracture occurring in the corresponding zone. In the necking zone, the increase in strain results generally into hardening which has a stabilizing effect [67].

Among the numerous mechanical analyzes of the instability phenomenon, a simple model, the Hart criterion, is presented hereafter. It allows a reasonable prediction for a uniaxial tensile creep test of an axisymmetric sample. The Hart criterion [67] assumes that the specimen has a cross-section defect: the gauge part of specimen, with a cross-section S, has a reduced area $S + \delta S$ ($\delta S < 0$).

Because of equilibrium, the tensile force is uniform and identical in the necking and no necking specimen parts:

$$F = \sigma \cdot S = \sigma_{necking} \cdot (S + \delta S) \tag{1.19}$$

Further, for a viscoplastic material, Hart proposed that the necking part is instable because the reduction in area in the necking part evolutes faster than in the remaining parts of the specimen. From these assumptions, Hart deduced the instability condition as:

$$\frac{\delta\dot{S}/\dot{S}}{\delta S/S} < 0 \tag{1.20}$$

Recently, based on the Hart criterion, Lim et al. [68] proposed a model to predict the deformation of the necking specimen part. The short term creep lifetime is deduced. That approach will be applied to Incoloy 800 in Chapter **??**.

For ductile creep fracture, assuming that the secondary stage is predominant compared to the first and tertiary stages, He and Sandström [69] proposed

that the specimen will be fractured when the strain reaches a critical value, $varepsilon_{crit}$, equal to 0.2.

$$t_f = \frac{\varepsilon_{crit}}{\dot{\varepsilon}_{min}} \tag{1.21}$$

In their work, the minimum strain rate, $\dot{\varepsilon}_{min}$, is calculated using a deformation model based on creep precipitation hardening, dislocation glide and climb properties and stacking fault energy [70, 71]. This creep rate model predicts that the minimum strain rate is proportional to the power three of tensile stress, $\dot{\varepsilon}_{min} \propto \sigma^3$.

1.4.2 Intergranular fracture

For long term creep fracture, intergranular cavitation becomes dominant, which includes cavity nucleation, growth and coalescence.

1.4.2.1 Cavity nucleation

Similarly to ductile cavitation, two types of cavity formation mechanisms were proposed in the past, either inclusion fracture or cavities nucleate at the inclusion-matrix interface, as shown in Chapter **??**. However, in our work, inclusion fracture is only observed in intergranular Ti(C,N) in Incoloy 800, and has no impact on further damage. Therefore, the fragmentation of inclusion is not considered as a main long term creep damage initiation mechanism in this study.

It is generally believed that cavity nucleation[2] along grain boundaries in metals and alloys occurs due to high local stress concentrations. At high temperature, vacancies diffuse along grain boundaries. Therefore, grain boundaries act as effective sources of vacancies for cavity nucleation.

In pure metals, cavities are often initiated at the intersections of slip bands and grain boundaries (Fig. 1.13c), or at the triple junction (Figs. 1.13a and 1.13b). In commercial high temperature steels, the second phase particles located along grain boundaries are the most observed locations for cavity nucleation (Fig. 1.13d). The materials under study, AISI 316L(N) and Incoloy 800 alloys contain intergranular second phases particles. Therefore cavitation starts from these intergranular particles, which will be studied in Chapters **??**, 2 and 3.

When a material containing second-phase particles is subjected to tensile loading, it deforms heterogeneously because of the mismatch in Young's modulus and viscoplasticity behavior of the grains with different crystallographic orientations are different. In particular, the ones of the matrix and second phase particles are usually different. Inhomogeneous deformation leads to high stress concentrations close to particle-matrix interfaces. Further, it should be noticed

[2]The 'cavity nucleation' is the conventional nomenclature of this process. It should be noticed that the Raj and Ashby model considers that cavities nucleate by agglomeration of vacancies. And the others consider the decohesion of interfaces or particle fracture.

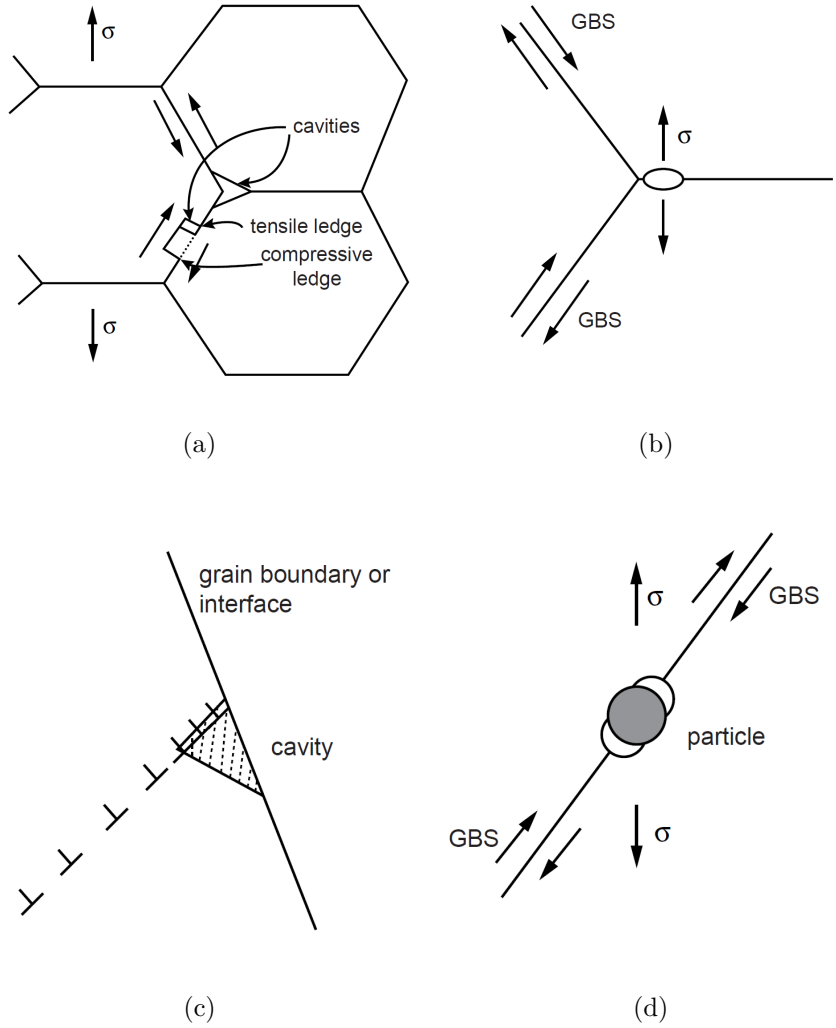

Figure 1.13: Cavity nucleation mechanism. (a) sliding leading to cavitation at triple points ledges, (b) cavity nucleation from vacancy condensation at a high stress region. (c) cavity nucleation from thea Zener-Stroh mechanism. (d) The formation of a cavity from a particle-obstacle in conjunction with the mechanisms described in (a-c) [52].

that such the stress concentrations may relax by diffusional flow along the interfaces [72, 73].

It is generally observed that large cavities located along grain boundaries perpendicular to tensile axis [74–76]. And small cavities are observed along grain boundaries parallel to tensile axis. This point will be explained in Chapter 4.

During last fifty years, two main mechanisms were proposed to the responsible for cavity nucleation, either thermally-activated vacancy clustering (Fig. 1.13a) or interface fracture. Usually both mechanisms require high local stresses to occur. Stress concentrations may be induced by grain boundary sliding (Fig. 1.13b), pile-up (Fig. 1.13c) and intergranular particle (Fig. 1.13d). The two main nucleation mechanisms are now described.

1.4.2.1.1 Thermally-activated nucleation of cavities

Intergranular cavity nucleation is provided from the formation of a stable cluster of vacancies. The surface of cavities is constituted by a lenticular segment shape [77] (explain in details subsection **??** in Chapter **??**). This cavity geometry requires both a fairly quick superficial diffusion, in order to keep the constant curvature of cavities during growth, and an isotropic superficial energy.

The creep nucleation mechanism was initially proposed by Greenwood et al. [78]. This mechanism assumes that the cavities nucleate preferentially by condensation of the vacancies under the effect of the normal local stress acting on the grain boundaries. Finally, Raj and Ashby [77] showed that this cavity nucleation mechanism occurs more quickly if the normal stress to the grain boundary is high and the surface energy of the cavity is low. Then, they deduce that it is easier to generate cavities at the multiple junction joints where the local stresses are higher (Figs. 1.13a and 1.13b). From the thermodynamic point of view, Raj and Ashby [77] proposed an energy barrier based on the variation of the Gibbs free energy, ΔG.

ΔG is given by [77]:

$$\Delta G = -\sigma_n V + \gamma^{free} S^{free} - \gamma^{interface} S^{interface} \tag{1.22}$$

Three terms contribute to the energy variation:

1) the work induced by the application of a remote tensile stress on an elastic medium containing a cavity of volume V;

2) the energy to be supplied for the creation of the cavity free surface, S^{free};

3) the loss of the energy of the grain boundary due to the reduction of its surface, consumed by the cavity growth, $S^{interface}$.

By derivating ΔG with respect to r, the critical value of the cavity radius, r_c, is deduced. The maximum value of $\Delta G(r)$ is reached (unstable equilibrium). Neglecting interface energy term allows the evaluation of:

$$r_c = \frac{2\gamma_s}{\sigma_n} \tag{1.23}$$

The incubation time required to reach the steady-state nucleation rate t_i is equal to:

$$t_i = \frac{r_c^3 F_v}{4 D_{gb}\delta} \tag{1.24}$$

where $D_{gb}\delta$ is the self-diffusion coefficient along grain boundaries multiplied by the grain boundary thickness and F_v is the geometrical function describing the cavity geometry as proposed by Raj and Ashby [77]. The incubation time, t_i, is generally very short, as few μs. So that, the cavity nucleation could be considered as instantaneous and continuous, once the stress and energy criteria are satisfied, during creep.

This model is limited by the fact that nucleation governed by the applied stress, with the definition of a threshold stress, because of the exponential dependence with stress. However, according to Yoo and Trinkaus [79], the experimental data show that cavity nucleation is controlled by the rate of deformation, but not the tensile stress, in agreement with the numerous proofs of the Dyson law.

Once ΔG is calculated, it is possible to deduce the cavity nucleation rate. The expression of the steady-state nucleation rate proposed by Raj and Ashby [77] is:

$$\dot{N}_0 = \frac{4\pi\gamma_s D_{gb}\delta}{\Omega^{4/3}\sigma_n} N_0^{max} exp(-\frac{4\gamma_s^3 F_v}{\sigma_n^2 k_b T}) exp(\frac{\sigma_n \Omega}{k_b T}) \tag{1.25}$$

where σ_n is the normal stress acting on the grain boundary. The grain boundary stress is generally believed to be higher than the tensile stress [80, 81].

Arnaud [82] plotted the variation of the germination rate as a function of the normal local stress for AISI 316 at $650°C$ based on the Raj model (Eq. 1.25, Fig. 1.14). His plot shows that, for a tensile stress lower than $\sigma_n/E = 4.3 \cdot 10^{-3}$, the nucleation rate is lower than $1m^{-2}s^{-1}$, this result does not agree with experimental measurements [44]. Further, this model predicts that a small variation in the applied stress induces a exponential variation in cavity nucleation rate (Fig. 1.14). This does not agree with experimental observations [44, 74, 83]. Further, the nucleation of the defects is only possible if the normal stress exerted on the grain boundaries is approximately ten times higher than the applied stress. This point will be discussed in Chapters 2 and 3. And numerical application of Eq. 1.25 for the material under study is presented in Chapter 4.

1.4.2.1.2 Particle matrix interface fracture

Thermally-activated vacancy clustering theory could not predict correctly the

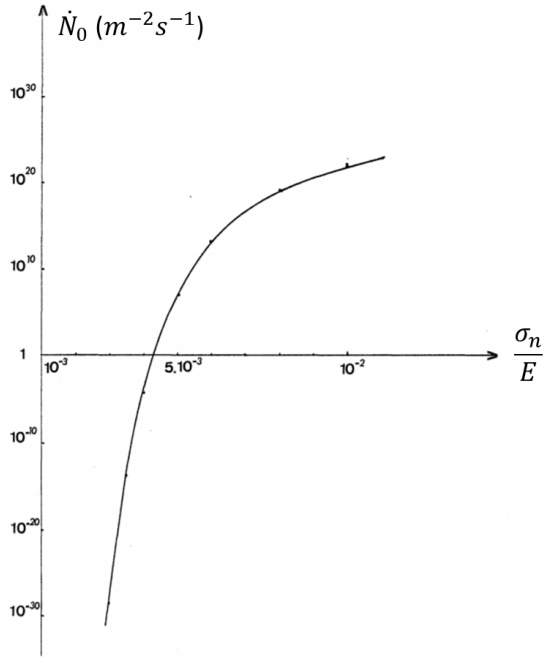

Figure 1.14: Variation of the cavity nucleation rate as a function of the remote tensile stress for a 316 steel at $650°C$ [82].

cavity nucleation rate. Therefore, it is proposed that cavities nucleate due to intergranular particle-matrix interface fracture. It is well known that interface fracture requires high local stresses. Then, several mechanisms leading to stress concentration have been proposed in literature. Grain boundary sliding and pile-up effects are described in the following.

1.4.2.1.3 Stress concentrator

Grain boundary sliding

Chen and Machlin [84] proposed that the interaction between the grain boundary ledges and grain boundary sliding leads to high local stress. The grain boundary ledges may exist initially or result from grain boundary sliding. Chen and Machlin [84] expected these interactions lead to a high local stresses at the ledges, which may be high enough for interface fracture to occur.

However, following Harris [5] and Fleck et al. [85], such local stresses induced by the grain boundary sliding should insufficient for the interface fracture.

Recently, Barkia et al. [86] carried out in-situ test in titanium at room temperature. Their observations show a strong link between grain boundary sliding and grain boundary decohesion. However, these observations were carried out at a strain rate of $2 \cdot 10^{-4} s^{-1}$, which is very high compared to standard creep

test strain rate.

Further, if grain boundary sliding is predominant, it should be expected that the maximum damage occurring during a uniaxial test should be observed along the grain boundaries oriented at $\pm 45^\circ$ with respect to the tensile axis [57]. In practice, it is considered that large cavities is most observed on the grain boundaries which are perpendicular to the tensile axis [52, 57, 75, 79, 87]. And small cavities is mostly observed on the grain boundaries which are parallel to the tensile axis. Therefore, the grain boundary sliding may not be predominant for cavity nucleation at least in the considered materials. However, the microscopic observations do not make it possible to observe the cavities at the nucleation stage (in order of 20nm), but in the more advanced stage of growth.

Dislocation pile-ups

Dyson [74] showed that cavities are observed in creep specimens prestrained at room temperature, Nimonic 80A. He suggested that the mechanism of cavity nucleation at ambient temperature may influence or induce cavity nucleation at high temperature. The thermally-activated nucleation would hardly occur at room temperature. Then, the Zener-Stroh mechanism [88] (Fig. 1.13c) was proposed to explain this phenomenon.

In the Zener-Stroh mechanism, cavity nucleation is controlled by localized plasticity. And interface fracture is caused by the stress field induced by dislocations pile-ups against a hard particle.

Kassner et al. [89] carried out creep tests on high purity silver at ambient temperature. Their observations show that cavity nucleation occurs continuously and is also believed to be due to the Zener-Stroh mechanism [52].

1.4.2.1.4 Conclusion about cavity nucleation

Various mechanisms were proposed to justify the occurrence of an important stress concentrations at certain sites along the grain boundaries, to cause cavity nucleation. Existing cavity nucleation models require indeed high local stress concentrations, for both thermally-activated cavity nucleation and particle-matrix interface fracture, as already noticed in literature.

Recently, Lim [80] calculated the stress concentration at triple points using Crystal Viscoplasticity Finite Element computations. The calculated stress could reach twice of the tensile stress, but it is obviously not enough for either thermally-activated cavity nucleation or interface fracture.

The effect of slip bands is not described in this part. Sufficiently high stress may be reached [90], but they are rarely observed during creep deformation, except for nickel-based alloys. it will be discussed in Chapter 4.

In the following, we focus on the stress concentration induced by second phase particles located at grain boundaries in accordance with all experimental observations. The Eshelby inclusion theory [91] is the simplest method to calculate

inclusion stress because of its thermo-elastic assumption. However, it leads to an overestimation of the local stress. The Eshelby theory will be applied in Chapter 3 to discuss the effect of inclusion aspect ratio.

In Chapters 2 and 3, the effect of intergranular particle morphology on interface stresses will be calculated by crystal viscoplasticity Finite Element computation. Then, the distribution of interface stresses is used to calculate cavity nucleation rate in Chapters 2 and 4.

It should be noticed that local stresses may be relaxed during creep deformation. However, this is a very complex problem, involving the transport of matter along grain boundaries (the Coble creep) and the creep of the grains themselves. Only approximate solutions exist. It firstly relies on the fact that, only the intergranular particles constitute sites where the stress does not relax in a very short time.

In conclusion, concerning cavity nucleation, it is generally believed that the effects of the interface normal stress and the grain boundary sliding may more important compared to other mechanisms.

1.4.2.2 Cavity growth

Cavity growth may occur by different coupled or uncoupled mechanisms. First, several kinetics and mechanisms are coexisting, as lattice diffusion, grain boundary diffusion, constrained growth and viscoplastic growth. Second, the grain orientations and the surrounding of each grain boundary is different, which could influence cavity growth rate, so as grain boundary coherency, second phase effect, etc. Such microstructure effects are rarely studied.

In the following, some models describing the most well-known cavity growth mechanisms are presented:

-the diffusion-controlled cavity growth model proposed by the Hull-Rimmer [92]. The constrained diffusion growth initially proposed by Dyson [93], was then developed by Rice [94];

-the plasticity-controlled growth is proposed by Riedel [51] and Nix [95].

- the model coupling between diffusion and viscoplasticity proposed by Chen and Argon [96] is also discussed.

1.4.2.2.1 Diffusion growth

Cavity diffusion growth is a mechanism of interest for creep damage. It may occur at low strain rate. This means that it may play an important role in the structure components loaded at low stress and for long term. Such low stresses and long durations may be out of the scope of laboratory tests, which are often using

The cavity growth by vacancy diffusion was initially highlighted by Hull and Rimmer [92]. They assumed that, during creep, cavities grow by vacancy diffusion along grain boundaries.

This model requires several conditions. The vacancy diffusion along the cavity surface is quick enough to keep te equilibrium geometry of cavity (spherical geometry), at all time. Cavities are periodically located along grain boundaries, for each perpendicular facet, with the same spacing $2L$ (Fig. 1.15a). The density of vacancies in the grain boundary is assumed to be constant to keep the diffusion growth for all creep lifetime. Finally, grains are assumed to be rigid, without viscoplastic deformation around the cavity surface.

Accounting for all these hypotheses, Hull and Rimmer deduced the cavity growth rate, as:

$$\dot{r} = \frac{D_{gb/v}\delta\sigma_n\Omega}{k_bT} \cdot \frac{1}{2Lr} \tag{1.26}$$

where L is one half the average distance between cavities in grain boundaries.

Thereafter, Raj and Ashby [77] improved this model. They proposed that the vacancy diffusion flux is induced by the normal stress acting on the grain boundaries, but not the hydrostatic pressure. This model will be explained in details, applied and discussed in Chapter **??**.

The described model assumed that intergranular cavitation occurs in a homogeneous way over all grain boundaries (Fig. 1.15a). In fact, experience shows that this is not the case, and that the Fig. (1.15b) is closer to the observations in many cases, especially in alloys that contain precipitates at grain boundaries. In facet, the surrounding material creeps restricting cavity growth.

Therefore, the damaged grain boundaries may need to be considered as relatively isolated. This was described by Dyson [93], as constrained cavity growth.

During creep, the damaged grain boundaries tend to deform faster, due to cavity growth, than the surrounding matrix. In order to fulfill strain accommodation, the stress acting on these grain boundaries is reduced by internal stress. And the diffusion cavity growth rate is then decreased because of this reduction in normal stress.

Then, Rice [94] developed further this idea, based on the compatibility between the strain rate induced by diffusion cavity growth and the remote strain rate. Then, this model was improved by Riedel [51]. The constrained cavity growth rate proposed by Riedel will be applied and discussed in Chapter **??**.

1.4.2.2.2 Viscoplastic growth

For a large cavity radius, when the local strain rate is sufficiently large, the diffusion phenomenon does not have time to be efficient enough. This viscoplasticity-controlled cavity growth model was initially proposed by Hancock [97]. This model proposed that the cavity growth is a result of creep deformation of the matrix surrounding cavities, provided the vacancy fluxes is low enough.

However, this model requires a high creep strain rate, which explains that viscoplasticity-induced cavity growth is less important for typically low stress creep fracture conditions.

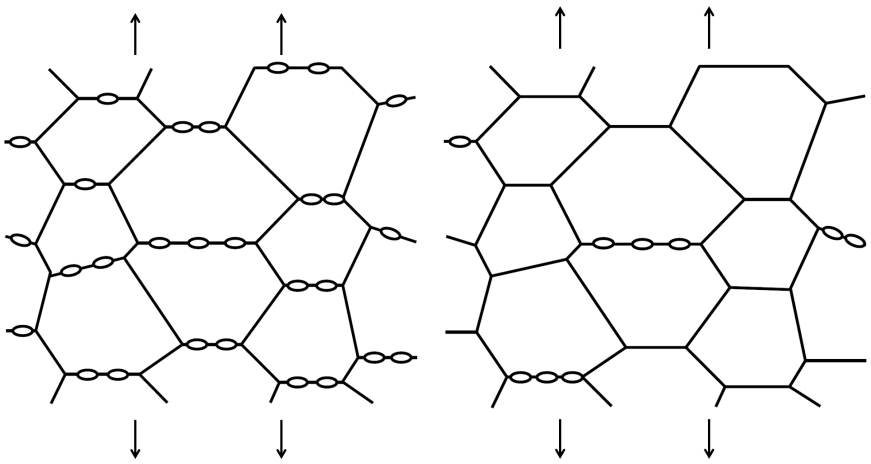

(a) (b)

Figure 1.15: (a) The homogeneous and (b) the heterogeneous cavitation at grain boundaries under vertical loading [52].

1.4.2.2.3 Coupling between diffusion and viscoplasticity

In diffusion growth models, the creep deformation of the surrounding grains is neglected. The atoms coming from the cavities deposit all along grain boundaries. In fact, the vacancies necessary for cavity growth, diffuse only from the area near to the cavities. In this case the diffusion distance, is quite short. This will increase the cavity growth rate. This problem was studied by several authors [95, 96, 98–100]. These models assume that the deformation away from the cavities takes place by grain creep deformation. A schematic presentation of the coupling of grain boundary diffusion and viscoplastic deformation is illustrated in Fig. 1.16.

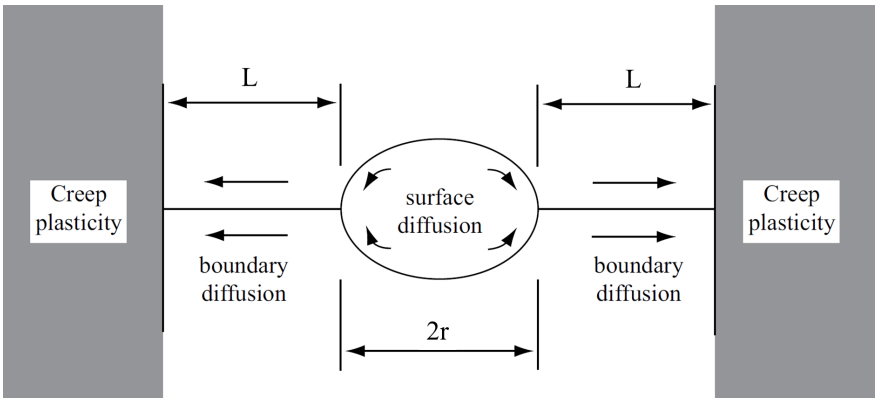

Figure 1.16: Intergranular cavity growth model with a coupling between grain boundary diffusion and viscoplasticity [100].

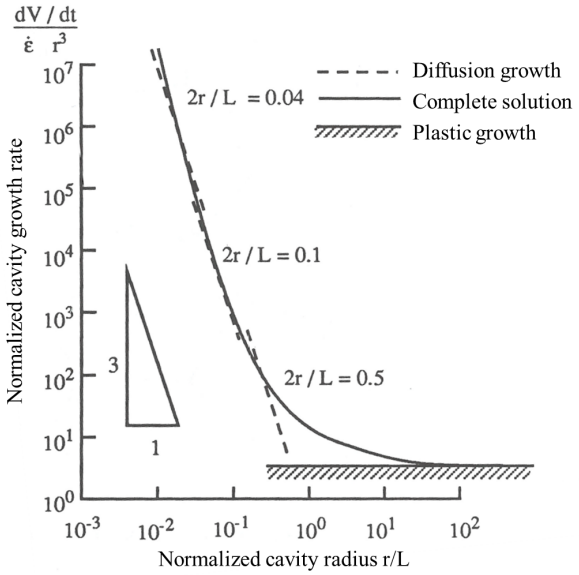

Figure 1.17: Growth rate of the cavities normalized by $\dot{\varepsilon}r^3$ as a function of the cavity size normalized by the diffusion distance L [57].

In the area close to the cavities, the vacancies are produced uniformly and diffuse to the cavity surface, which induces stresses relaxation. In this are, deformation results mainly from the formation of the vacancies. In the area far from the cavities, no vacancy is produced and the deformation is ensured by crystal creep.

The diffusion length L, is the characteristic length computed by Needleman and Rice [100], as:

$$L = (\frac{D_{gb}\delta\Omega\sigma_n}{kT\dot{\varepsilon}})^{1/3} \tag{1.27}$$

This diffusion length is also called as 'the Rice length'. This characteristic length allows the deviation of a criterion to determine if the viscoplasticity-controlled cavity growth takes place or not. The Rice length and derived criterion will be used in Chapter **??**.

Chen and Argon [96] studied in details this problem, taking into account the reduction in the diffusion distance, they deduced the coupled cavity growth:

$$\frac{dV}{dt} = \frac{2\pi\dot{\varepsilon}L^3}{ln(\frac{r+L}{r}) + (\frac{r}{r+L})^2(1 - \frac{1}{4}(\frac{r+L}{r})^2) - \frac{3}{4}} \tag{1.28}$$

Fig. 1.17 presents the normalized cavity growth rate $(dV/dt)/(\varepsilon\dot{r^3})$, as a function of the normalized radius $\frac{r}{L}$. The dotted lines correspond to the rigid grain

model, for various values of the area fraction of cavities. This approximation is quite correct, especially for the low values of $\frac{r}{L}$. The horizontal asymptote plotted for the large values of the $\frac{r}{L}$ ratio corresponds to the pure viscoplastic regime.

1.4.2.3 Cavity coalescence

The cavity coalescence process is well-known in ductile deformation. In this case, the coalescence can be decomposed into several stages, as shown by the observations of Weck and Wilkinson [101] (Fig. 1.18). These experimental observations confirm the coalescence mechanism proposed by Thomson [102]. These figures show a steel containing two preexisting cavities and subjected to mechanical loading.

It is generally believed that the evolution of the plastic deformation leads to a nucleation step, with cavities produce by the decohesion of inclusion-matrix interface. Then plasticity-induced growth occurs (Fig. 1.18b) In the experiment carried out by Weck and Wilkinson, the holes were produced by laser drill and are considered as preexisting cavities (Fig. 1.18a).

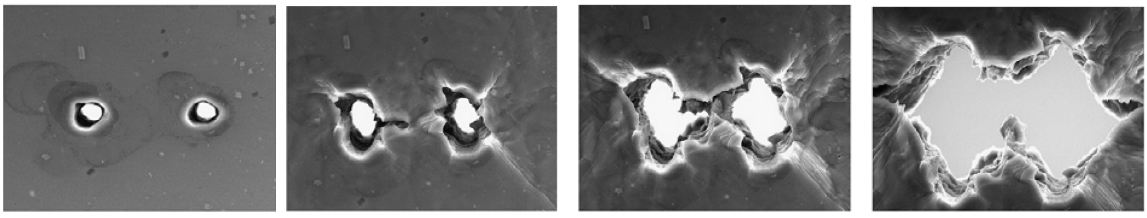

(a) (b) (c) (d)

Figure 1.18: in-situ SEM images of the deformation of Alloy 5052 containing two holes oriented at 90° with respect to the tensile direction, in function of the macroscopic strain, (a): $\varepsilon = 0$, (b): $\varepsilon = 0.204$, (c): $\varepsilon = 0.220$ (d): $\varepsilon = 0.223$ [101].

The next two steps concern specifically coalescence. This involves a collective and rapid phenomenon of plastic instabilities inducing a local constriction of the ligament between the two cavities (Fig. 1.18c). These ligaments are experimentally observed on each of the fracture surfaces. It may also be accelerated by the presence of defects.

Therefore, the ultimate stage of ductile fracture is the coalescence of the cavities (1.18d). It is caused by plastic instability. The simplest coalescence condition consists in assuming that the ratio of the cavity size r to their average distance L_0 reaches a critical value ω_f.

For coalescence, Thomason [103] considered a square prism containing a prismatic cavity and a cylinder containing a cylindrical cavity. He assumed that the

coalescence is reached when the ligament area between the cavities reaches its load limit while the horizontal layers on either side of the cavity remain rigid. He thus estimated the instability limit and obtained an estimation of the coalescence onset caused by a multi-axial loading. However, in ductile damage, the effect of grain boundaries most often be neglected, because cavities are generally located inside grains.

During creep deformation, the coalescence process begins when the cavities and the associated deformation fields start to interact with each other, typically when the cavity size is of the order of magnitude of their spacing. This final stage of damage leads more or less rapidly to fracture. The complete process is particularly complex.

First, the cavity distribution at the end of the growth stage is very heterogeneous, whereas most models consider only the average cavity volume or surface fraction, $\bar{\omega}$. For ductile fracture, the critical value ω_f is generally lower than 0.06 [104–106]. For creep fracture, it was experimentally estimated to be 0.028 for a 25Cr–35Ni–0.4C austenitic steel [107], 0.06 for a 18Cr-8Ni steel [108] and 0.04 for AISI 316 steels [109].

Second, cavities are usually assumed to be spherical, but this is no longer valid in such a strongly deformed area and damage volume (Fig. 1.18d). Indeed, the cavities will grow anisotropically and tend to join each other, either by localized bands containing small cavities, or by micro-necking of the ligaments which separate them, to form a macro-crack.

Finally, the fracture mechanisms are dependent on the deformation path and the loading condition, but also on the flow stress and the strain hardening of the matrix.

1.4.3 Physically-based lifetime prediction

1.4.3.1 The Riedel model

Two different fracture model were proposed by Riedel [51], either constrained cavity growth or unconstrained cavity growth. For continuous cavity nucleation and unconstrained diffusive cavity growth, Riedel [51] proposed a lower bound for creep lifetime:

$$t_f = 0.33\left(\frac{h(\alpha)kT}{\Omega D_{gb}\delta\sigma}\right)^{2/5}\left(\frac{\omega_f}{\dot{N}_0}\right)^{3/5} \tag{1.29}$$

where ω_f is the critical cavitated area fraction and $\dot{N}_0$ is the cavity nucleation rate used in the Dyson law [74]. Dyson assumed that cavities nucleate continuously and cavity density increases linearly with the viscoplastic strain. In the restrictive from of the Dyson law, the cavity nucleation rate depends only on $\dot{\varepsilon}_{min}$. The Dyson law is expressed as:

$$\dot{N}_0 = \alpha' \cdot \dot{\varepsilon}_{min} \tag{1.30}$$

where α' is a material dependent constant. More details about the Dyson are provided in Chapter **??**, where will be used to predict creep lifetime of Incoloy 800.

Thereafter, the upper and lower bounds of $q(\omega)$ were used to predict the upper and lower bounds of t_f [51]:

$$0.301(\frac{h(\alpha)kT}{\Omega D_{gb}\delta\sigma})^{2/5}\frac{(\omega_f)^{0.5164}}{(\dot{N}_0)^{2/5}} \leqslant t_f \leqslant 0.354(\frac{h(\alpha)kT}{\Omega D_{gb}\delta\sigma})^{2/5}(\frac{\omega_f}{\dot{N}_0})^{2/5} \tag{1.31}$$

Eq. 1.31 was, then, modified and improved by Lim [80]. The lower bound derived by Lim will be applied to predict long term creep lifetime in Chapters **??** and 4.

Finally, in case of constrained cavity growth, the lower and upper bounds are more difficult to derive. However, there is a very good agreement between the time for coalescence on isolated facets, t_c, and the time to fracture [52], which means $t_c = t_f$. Moreover, Riedel [51] derived the time for coalescence in case of constrained growth:

$$t_f = 0.38[\frac{\pi(1+(3/2))}{\dot{N}_0}]^{1/3}\frac{\omega_f}{(\dot{\varepsilon}_{min}d_g)^{2/3}} \tag{1.32}$$

1.4.3.2 Recent Models

Recently, Sandström and co-workers [69, 70, 110–112] proposed two models for transgranular fracture and intergranular fracture.

For intergranular fracture, the Sandstöm model [111] includes cavitation by grain boundary sliding and constrained cavity growth. This model assumes that the intergranular creep fracture occurs when the cavitated area fraction reaches a critical value, ω_f, taken as 0.25.

$$\omega_f = \int_{t_i}^{t} N_0(t_1)\pi r^2(t_1,t)dt_1 \tag{1.33}$$

where t_i is the incubation time, $N_0(t_1)$ is the number of cavities at time t_1, r is the cavity radius at time t, of which produced at time t_1. $N_0(t_1)$ is determined using Eq. 1.34. The cavity radius could be calculated using a modified constrained cavity growth rate expression [113]. By accounting for the distribution of sub-boundary corners and particles, He and Sandstöm [114] proposed a cavity nucleation rate (Eq. 1.34) of the same type of Dyson law [74].

$$\dot{N}_0 = A_s\dot{\varepsilon}_{min} \tag{1.34}$$

where A_s is a constant depending on sub-grain size, particle spacing in grain boundaries and grain boundary displacement rate.

1.5 Conclusion and summary of the manuscript

In this chapter, we briefly presented the chemical element effects and precipitation in AISI 316 and Incoloy 800.

Then, reference creep phenomenological laws were described, especially for creep deformation, minimum strain rate and lifetime predictions.

In order to better understand creep deformation and damage mechanisms, some physically based models of creep deformation were summarized, as diffusion creep, dislocation climb/glide and grain boundary sliding. Concerning damage and failure, necking and intergranular cavitation damage were separately studied. The two most cited cavity nucleation mechanisms were presented: the thermally-activated law proposed by Raj and particle-matrix interface fracture.

Two laws allow the evaluation of the the cavity nucleation rate under creep condition: the Dyson law and the Raj law. The Dyson law assumes that, for a given material, the cavity nucleation rate depends only on the minimum strain rate. This means that $\dot{N}_0 \propto \sigma^n$, n is the Norton law exponent. On the contrary, the Raj model predicts that the cavity nucleation rate depends exponentially on the applied stress, $\dot{N}_0 \propto \sigma^{-1} \cdot exp(\frac{A}{\sigma^2})$. The predictions of both theories will be discussed in details in Chapter 4.

Finally, the physically-based models allowing long term lifetime prediction were presented, in particular, the Riedel model and Sandstöm's models.

Lim [80] predicted the short term creep lifetimes of Grade 91 using the necking model. And long term creep lifetimes were predicted using the Riedel model with experimentally measured prefactor of Dyson law, α'. Using a similar combined model, both short and long term lifetimes of AISI 316L(N) and other austenitic stainless steels were well predicted by Cui et al. [115]. Creep lifetimes of Grade 91 and 316L(N) were well predicted up to 25 years in a large range of temperature.

These results leads us to predict lifetime of Incoloy 800 alloys in Chapter **??**. Once more, The predicted lifetimes agree well with experimental data at temperatures ranging between 500 and 760°C. Further, the effect of Ti+Al content is well predicted using the combination of both the necking and Riedel models.

No adjusted parameter is used as applying the Riedel model. Only the measurement of the Dyson law prefactor, α', is necessary to predict long term lifetimes. Further, as explained in section 1.4.2, the cavity nucleation mechanism has not been well established yet. The random features of local microstructure have been rarely introduced in the computation of stresses, such as crystalline orientations of the grains, elasticity coefficients of second phase particles, grain boundary plane orientation with respect the tensile axis and geometry of the second phase particles.

In Chapters 2 and 3, the crystal viscoplasticity Finite Element computations are carried out, to evaluate all these effects, using the Cast3m software. Calculations are carried out for 316L(N), because there are many creep data and

experimental observations concerning 316L(N) published in literature or available at our laboratory. The effects of the random crystalline orientations of the grains and grain boundary plane orientation with respect the tensile axis are investigated in Chapter 2. And precipitate shape factor and tip geometry effects are investigated in Chapter 3.

Next, in Chapter 4, the local stresses induced by grain boundary sliding (GBS) are calculated based on reference models. These stresses are shown to be too low for inducing interface fracture. Further, the Raj model is applied using the interface stress distributions computed by DEM and accounting for the random nature of microstructure. The particle size effect is roughly introduced using an energy balance equation. Thereafter, our calculated stress distributions are used to evaluate the prefactor of the Dyson law, α'. Results show that the magnitude of the computed prefactor value, of α' is similar to the magnitude of the measured values in 316L(N). Further, the prefactor, α', is almost stress- and temperature-independent, but it depends linearly on the density of large intergranular precipitate.

Chapter 4 is finished with long term lifetime predictions of 316L(N) at temperature ranging between 525-700$°C$ based on our computed value of the Dyson law prefactor, α'. Creep lifetimes are rather well predicted, up to 25 years, compared to experimental data.

Finally conclusions are drawn in Chapter 5. Work in progress and perspectives required to enhance the physically-based prediction of cavity nucleation and long term creep lifetimes are highlighted.

Chapter 2

Theoretical and experimental study of creep damage in Incoloy 800

To be submitted to Materials Science and Engineering A

Depending on stress, temperature and material, transition in creep fracture mechanism are extensively observed in metals and alloys. To investigate such transition, Incoloy 800 alloys are subjected to numerous creep tests at temperatures ranging from 500 up to 760°C.

At first, experimental observations show two failure mechanisms: necking fracture for short term testing and intergranular fracture for long term testing.

Then, the onset of necking is firstly analyzed using the Hart criterion of viscoplastic instability. The necking evolution with strain is then predicted which allows us to provide lifetime prediction.

The proportionality between the cavity nucleation rate and the creep strain rate is assumed following the well-known Dyson law. The Riedel model assumes cavity growth by grain boundary diffusion coupled with continuous nucleation. This model is used to predict long term lifetime.

The results show that lifetimes are accurately predicted by the combination of the necking model and the Riedel model whatever the chemical composition, stress and temperature.

Furthermore, the comparison between the experimental data obtained from different batches of Incoloy 800 alloy shows that the higher the Ti+Al content the stronger the creep resistance. This seems due to the differences in γ' precipitation and its influence on creep strain rate. Such effect is well predicted through the combination of the necking and intergranular fracture models, which are strain rate dependent.

Finally, the measured and the predicted cavity size distributions are compared and the applicability of such combined modeling to various metals and alloys is

discussed.

2.1 Introduction

The first Incoloy 800 alloy was developed by the International Nickel Company in 1949 in response for a heater element material for electrical appliances [**?**]. Several modified Incoloy 800 alloys have been later developed for special service requirements. The first application of Incoloy 800 alloys in nuclear power plant corresponds to replace some of the stainless steel components in the HTGR High Temperature Gas-cooled Reactor[**?**].

Due to its high strength and high corrosion resistance at high-temperature in water and steam environments, the Incoloy 800 alloy was used as the steam generator (SG) tube material for Superphénix. Its properties and historical applications for the nuclear industry [**?** **?** **?** **?**] make it one of the potential candidates for steam generator tubes of the Generation IV nuclear reactor ASTRID (Advanced Sodium Technological Reactor for Industrial Demonstration).

The in-service lifetime of the generation IV nuclear power reactors is wished to reach 60 years. For that reason, it is necessary to study the mechanical properties evolution of the Incoloy 800 alloy with the in-service time, particularly during creep at high temperature and for long term lifetimes.

The creep properties and microstructure evolutions in Incoloy 800 alloys at high temperature were studied mainly experimentally. Wickens and Grover [**?**] observed $M_{23}C_6$ precipitation at grain boundaries during creep testing of Incoloy 800 alloys at temperature ranging from 500 to 600°C. By transmission electron microscopy (TEM) observations, Malfa and Quaranta [**?**] showed that the γ' phase precipitates are distributed homogeneously in the Incoloy 800 matrix after creep deformation. Cozar and Rouby [26] observed that the creep strain rate decreases in alloys when γ' precipitation occurs.

Several creep lifetime prediction models have been proposed in the past. Creep lifetime may be predicted by the phenomenological Monkman-Grant relationship [50], which relates the failure time to the minimum strain rate. Larson-Miller relationship [54] makes the link between tensile stress, temperature and lifetime. These two relationships are phenomenological ones, and their parameters are adjusted based on short experimental data. However, the extrapolation of the prediction of these models to long term creep may lead to an incorrect lifetime prediction.

The physically-based fracture models and experimental observations highlight two main fracture mechanisms: necking fracture [51, 67, 68, 202] and intergranular cavitation fracture [51, 57, 77, 80, 81, 109, 115].

Based on the necking theory, Hart [67] deduced a flow instability criterion which can be used for viscoplastic materials obeying the Norton power-law relationship. Extending the Hart criterion to creep loading, Lim et al. [68] showed that necking starts just after the minimum creep rate, $\dot{\varepsilon}_{min}$, is reached. Predicting both necking onset and necking cross-section evolution, Lim et al. [68] deduced a lifetime prediction model for necking fracture.

For intergranular fracture, experimental observations [51, 74, 94, 100**?**] show that, under low stress and high temperature, cavities nucleate continuously [51, 68, 74] and grow by intergranular diffusion of vacancies [51, 77, 92]. This phenomenon causes later the coalescence of cavities. Finally, the fracture of specimens takes place when the area fraction of cavities and cracks along grain boundaries reaches a critical value, ω_f, of about a few percent following experimental measurements [80, 109, 115].

The change in damage mechanisms leads to slope change in stress-lifetime curve. Therefore, the lifetime prediction from the extrapolation of short term creep data may could not predict correctly long term creep lifetime. Then, the physically-based lifetime predictions are performed in this study.

In this chapter, experimental results from numerous creep tests carried out at CEA/EDF on four batches of Incoloy 800 alloy are studied. Sixty creep tests are considered with temperature ranging from 500 to 550 $°C$.

Section **??** presents the experimental observations which show that two different fracture mechanisms may occur. Sections **??** an **??** present creep lifetime prediction using the combination of the Necking model and the Riedel model to predict creep lifetime. Our predictions agree well experimental data for various Incoloy 800 batches for lifetimes ranging in 100-30 000h, and temperatures between 500°C and 760°C (with data of ORNL [48]).

Additionally, in section **??** the analysis of the creep experimental results of the four batches of the Incoloy 800 alloys (CEA&EDF) shows the influence of the Ti+Al content on strain rate and then on creep lifetime. Higher Ti+Al content leads to stronger creep resistance. It is due to the differences in γ' precipitation and its influence on strain rate. Such trends are quantitatively well predicted by the combination of the two models which are strain rate-dependent.

Finally, in section **??**, the cavity size distribution is predicted and compared with the experimental one.

2.2 Experimental methods and results

2.2.1 Materials and experimental methods

'Incoloy 800' is the generic name of a family of austenitic alloys, which are basically Fe-Ni-Cr alloys containing minor but influent amounts of carbon, aluminum and titanium. Table **??** displays the specification on chemical composition currently used for Incoloy 800 alloys (ASTM, 2004 [3]) and the measured compositions of the batches under study.

The high fraction of Ni is necessary to get an austenitic matrix and to provide strong mechanical properties, whereas Cr improves the oxidation resistance. The low carbon content leads to a better intergranular corrosion resistance. The Ti atoms can stabilize carbon which increases the intergranular corrosion resistance.

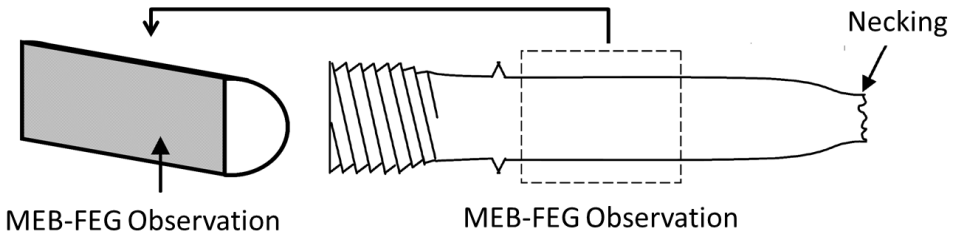

Figure 2.1: Schematic pictures showing the fracture surface and the longitudinal section observed by FEG-SEM.

Because the addition of Ti atoms leads to the precipitation of γ' precipitation. The Si solid solution increases the chromium equivalent of the alloy [**?**].

The mechanical properties of Incoloy 800 alloys are also strongly influenced by the annealing procedure applied to each batch. All the products have undergone a heat-treatment process very close to the industrial one applied to steam generator tubes. That includes

- hot forming;
- intermediate heat-treatment between 980 and 1025°C;
- cold-rolling;
- final heat-treatment at 980°C.

This heat-treatment leads to a grain size ranging between 50-100μm.

Experimental creep tests were carried out at CEA and EDF, at constant temperature (between 500 and 550°C) and constant load. And tests at high temperature (649 and 760°C) carried out by ORNL [48] are also considered in this study. Depending upon precise chemical composition and heat treatment condition, the considered alloys of these different batches can exhibit a number of desirable properties which are attractive for a wide variety of industrial applications.

Area reductions of the fracture surfaces are measured using a Laser Scan Micrometer and a binocular microscope using the LAS Core software. FEG-SEM observations are carried out to characterize the intergranular damage occurring during creep tests. A schematic presentation of the observed fracture surfaces and the longitudinal section of the specimens is shown in Fig. **??**. The longitudinal sections of the specimens is polished with polish paper grade 1200, followed by polishing with diamond spray 3μm and 1μm.

2.2.2 Analysis of experimental data

The creep data of the five Incoloy 800 alloys at temperatures ranging from 500 to 760°C are now analyzed.

A classical analysis of the creep curves is first carried out. Creep curves can be divided into three stages: primary, secondary (or steady-state) and tertiary

Element	ASTM [3]	HB 647	75193	HN 823	HH3283	7686A [48]
Fe	bal	bal	bal	bal	bal	bal
C	≤0.10	0.033	0.044	0.054	0.061	0.007
Cr	19-23	21.6	21.8	21.4	19.8	21.26
Ni	30-35	34.6	34.2	33.9	32.9	30.94
Mn	≤1.5	0.94	0.56	0.89	0.82	0.97
S	≤0.015	0.003	0.005	0.001	0.006	0.007
Si	≤0.70	0.35	0.30	0.47	0.45	0.41
N	≤0.03	0.026	0.021	0.018	0.013	
Ti	0.15-0.6	0.12	0.11	0.13	0.40	0.39
Al	0.16-0.6	0.12	0.11	0.13	0.40	0.39
Ti+Al	0.45-0.75	0.32	0.56	0.63	0.83	0.88

Table 2.1: Chemical composition of different batches of Incoloy 800 alloys and ASTM specification [3] (wt%). 7686A is reported in [48].

creep stage. The secondary stage is characterized by a almost constant strain rate, known as minimum strain rate.

A general relationship between the minimum stain rate and the tensile stress, called Norton power law, is expressed in Eq. **??**:

$$\dot{\varepsilon}_{min}^{true} = C(\sigma^{eng})^{n(T)} \tag{2.1}$$

where $C(MPa^{-n}s^{-1})$ and $n(T)$ are temperature dependent material constants, $\dot{\varepsilon}_{min}^{true}$ is the minimum true strain rate (h^{-1}) and σ^{eng} is the engineering stress (MPa).

The engineering stress, σ^{eng}, is computed using the initial cross section and the engineering strain is denoted as ε^{eng} (%), which is measured continuously during each test.

The relationships between engineering and true values are:

$$\varepsilon^{true} = ln(1 + \varepsilon^{eng}) \tag{2.2}$$

$$\sigma^{true} = \sigma^{eng}(1 + \varepsilon^{eng}) \tag{2.3}$$

The minimum true strain rate, $\dot{\varepsilon}_{min}^{true}$, is determined by plotting the evolution of the true strain rate in function of the true strain or time, and evaluating the minimum value.

For each temperature, the values of C and n are determined by plotting the evolution of the minimum true strain rate in function of the engineering stress as shown in Fig. **??**. The parameters values are given in Table **??**.

Fig. **??** shows that, for a given stress, a higher Ti+Al content leads to a lower minimum strain rate. For example, at 550°C and under 300MPa, the minimum strain rate of the HB 647 batch (with the lowest Ti+Al content) is $2.4 \cdot 10^{-8}$ s^{-1}, but it is only $6.7 \cdot 10^{-10}$ s^{-1} for the HH 3283 batch (with the highest Ti+Al content) (table **??**). The first material deforms 35 times faster than the second one. Besides, the stress-lifetime curves show that the higher Ti+Al content, the better creep resistance. It means that under the same stress, a higher Ti+Al content leads to a longer lifetime. Such effect needs to be better understood on the quantitative point of view, and will be discussed in section **??**.

Following literature [**? ? ? ?**], γ' precipitates are observed in crept Incoloy 800 alloys, which influence creep properties. And Ni, Ti and Al are the major elements in the composition of the γ' precipitates, $Ni_3(Ti, Al)$. The precipitate size is about 100nm, that is why they can hardly be observed by FEG-SEM. A higher Ti+Al content leads to a higher number of γ' precipitates, which increases the material hardness, because of dislocation-precipitate interactions. As a consequence, the minimum strain rate is lower. That may explain qualitatively why, the creep resistance of materials with high Ti+Al content is better than the with low Ti+Al content. But the quantitative relationship linking the Ti+Al content and lifetime is still missing at this stage, particularly depending on the fracture mode.

Batch	Temperature (°C)	n	C ($MPa^{-n}s^{-1}$)
HB 647	550	8.05	$1.74 \cdot 10^{-23}$
75193	500	10.33	$1.17 \cdot 10^{-31}$
	525	10.80	$1.17 \cdot 10^{-31}$
	550	12.87	$1.80 \cdot 10^{-35}$
HN 823	500	22.67	$2.56 \cdot 10^{-62}$
	525	19.30	$1.06 \cdot 10^{-52}$
	550	16.42	$6.09 \cdot 10^{-45}$
HH 3283	550	13.41	$1.29 \cdot 10^{-38}$
7686A(ONRL)	649	8.81	$4.72 \cdot 10^{-23}$
	760	11.68	$2.92 \cdot 10^{-26}$

Table 2.2: The Norton parameters (Eq. **??**) of the Incoloy 800 alloys under study at $500°C$, $525°C$ and $550°C$.

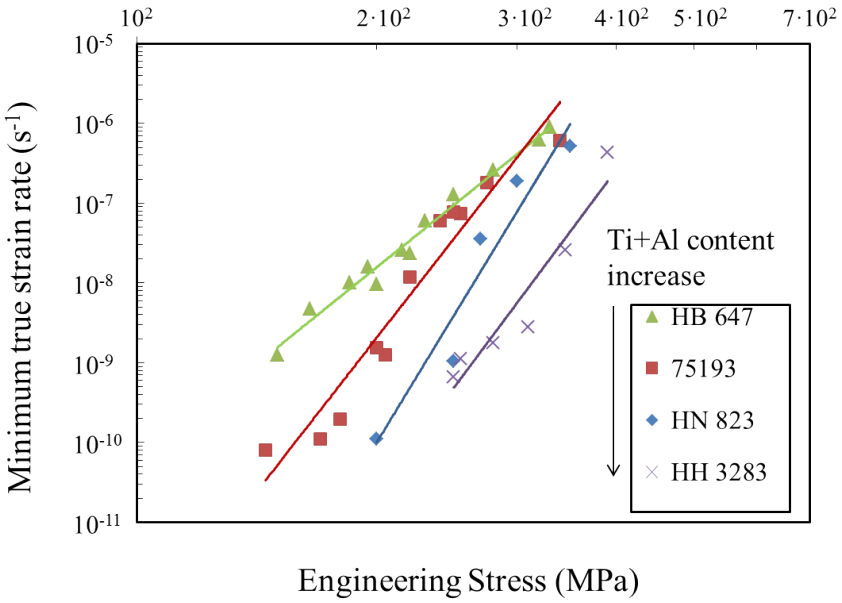

Figure 2.2: Adjustment of the coefficients of the Norton Law at 550°C (CEA&EDF).

2.2.3 Measurement of the reduction in fracture area and observations of the fractured Specimens

The FEG-SEM observations of fracture surfaces (Fig. **??**), show two different types of fracture surface, either necking fracture (Fig. **??**) or intergranular fracture (Fig. **??**).

The necking fracture surface is characterized by voids and dimples (Fig. **??**). Dimples are generally observed on the ductile fracture surface [57]. On the contrary, grain boundaries can be clearly observed on the intergranular fracture surfaces (Fig. **??**).

The measured reduction in area at fracture (Z):

$$Z = \frac{S_0 - S_f}{S_0} \cdot 100\% \tag{2.4}$$

with S_0 the original area and S_f the area after fracture, Z varies between 10% and 70% (Fig. **??**).

Generally, necking fracture, short term tests, is accompanied by a higher area reduction ($Z\% > 40\%$) and high failure strain in comparison to intergranular fracture. For intergranular fracture, long term tests, the reduction in fracture surface areas is lower than 30% based on our FEG-SEM observations of the fracture surfaces as shown in Fig. **??**.

Fig. **??** shows the area reduction versus the minimum creep rate in the 500-550°C temperature range. The mean curve (blue line) shows that a high

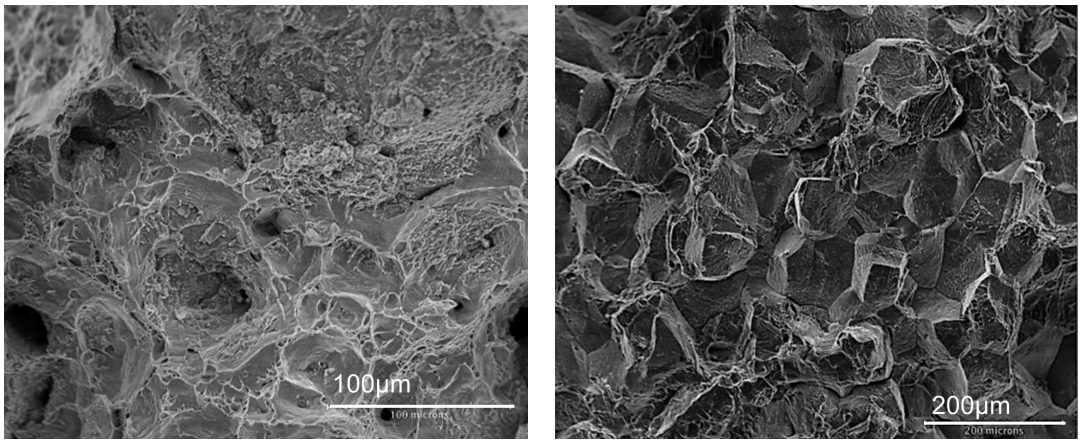

(a) (b)

Figure 2.3: FEG-SEM observations of the fracture surfaces of the HN 823 alloy for two different test conditions. (a) necking fracture 550°C, 280MPa, 332h, Z%=42%; (b) intergranular fracture 500°C, 310MPa, 5082h, Z%=10%.

minimum strain rate leads to a high area reduction. On the contrary, a low creep rate leads to a low area reduction. A high strain rate plateau is observed, with an area reduction of about 55%. A drastic decrease is observed between 10^{-8} and $10^{-7}s^{-1}$. Finally, the area reduction seems to decrease much slower down to $10^{-10}s^{-1}$ (Fig. **??**). A value of almost 15% is reached. No clear temperature effect can be observed.

According to our area reduction measurements and fracture surface observations, it can be concluded that a high minimum creep rate leads to necking fracture, and a low minimum creep rate leads to intergranular fracture.

2.2.4 Observations of the longitudinal sections

The observations of the polished longitudinal sections by FEG-SEM are focused on precipitates, cavities and short cracks. In all specimens, two types of precipitates are observed chromium carbides, $M_{23}C_6$, and titanium carbonitrides, $Ti(C,N)$. The $M_{23}C_6$ precipitates, generally $Cr_{23}C_6$ precipitates, appear at grain boundaries and triple junctions. The $Ti(C,N)$ particles are generally rectangular precipitates observed in the matrix. The affinity of titanium to carbon is higher than the Cr one. Thus, $Ti(C,N)$ precipitates are more stable than $M_{23}C_6$ precipitates. But, in comparison to the $Ti(C,N)$ carbonitrides, the $M_{23}C_6$ precipitates are produced preferentially at in service temperatures ranging from 500 to 550°C [**?**].

For a few carbonitrides, short cracks ($\sim 1\mu m$) can be observed (as shown in Fig. **??**) at the interfaces with the metallic matrix. But the crack sizes remain always similar to the precipitate size. And neither propagation nor coalescence

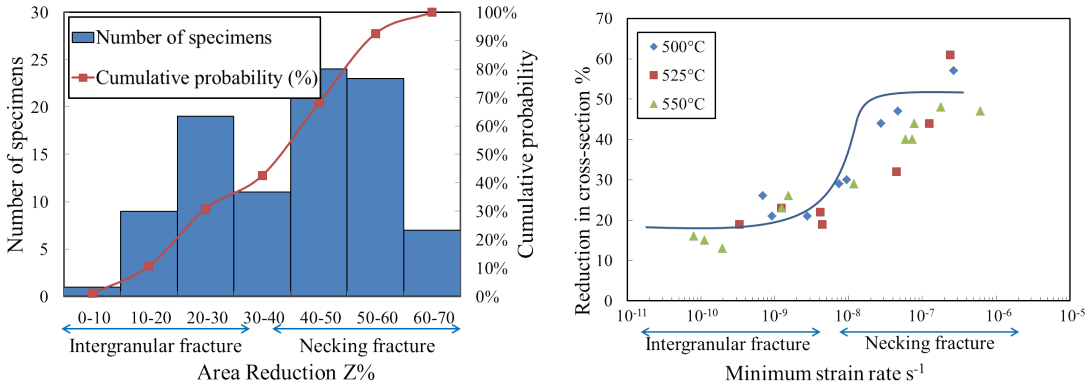

Figure 2.4: (a) Histogram and cumulative probability of the area reduction measured on the fracture surfaces, $Z\%$ (HN 823 alloy). The two fracture domains distinguished thanks to FEG-SEM observations (Figs. **??** and **??**) are highlighted; (b) Area reduction measured after fracture as a function of the minimum creep rate (75193 alloy).

is observed. Consequently, such micro cracks are not considered in the creep damage modeling presented in section **??**.

Intergranular cavities can be observed in specimens which failed due to intergranular damage, but not observed in the ones fractured by necking. Intergranular cavities are initiated at the interfaces of $M_{23}C_6$ precipitates and matrix as shown in Fig. **??**. Then, cavities grow along grain boundaries and triple points. This is why long term creep damage is also called intergranular cavitation damage. Furthermore, growth and coalescence of cavities lead to intergranular cracks. Cracks propagate along the grain boundaries perpendicularly to the tensile axis as shown in Fig. **??**, which agrees with many observations reported in literature.

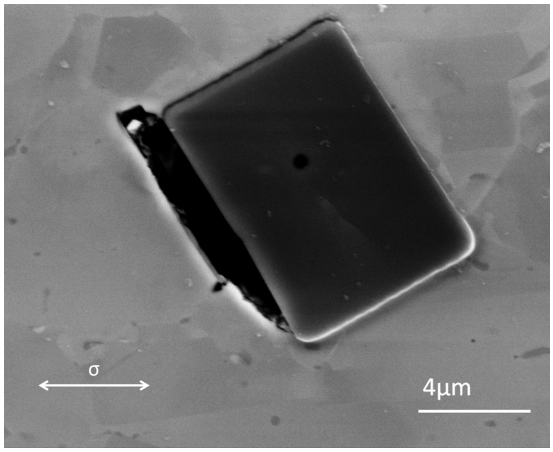

Figure 2.5: $Ti(C, N)$ precipitate in the matrix, with a microcrack at the interface between the alloy matrix and the precipitate (525°C, 270MPa, 2720h, HN 823).

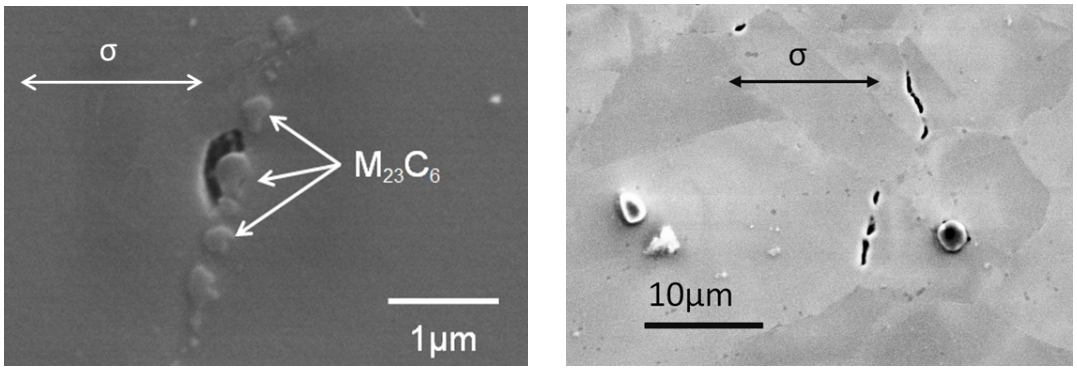

(a) (b)

Figure 2.6: FEG-SEM observations of cavities and short crack longitudinal sections (525°C, 270MPa, 2720h, HN 823). (a) a cavity initiated at the interface between a $M_{23}C_6$ carbide and the matrix, along a grain boundary; (b) short cracks resulting from the coalescence of intergranular cavities.

2.3 Lifetime prediction models

Two different damage mechanisms are observed. Therefore, at least two damage models should be used to predict lifetimes for both short and long term regimes.

2.3.1 Necking model

As shown in the previous section, short term creep specimens are characterized by relatively high fracture area reduction and high elongation at fracture. Generally, short term creep specimens are fractured due to viscoplastic instability (necking) which is simulated in the following.

At any given time, a portion of the gauge length is assumed to be characterized by a small reduction in cross section, $\mid \delta S \mid$. The remaining gauge length is assumed to display a homogeneous cross section, S, as shown in Fig. **??**.

The onset of necking is defined by arising of the viscoplastic deformation instability. This means that the difference in cross section increases with time. The corresponding time is assumed to be the onset of necking. This phenomenon is analyzed referring to the Hart criterion [67]. Using this criterion and the volume conservation assumption, Eq. **??** was deduced by Lim et al. [68]:

$$\frac{\ddot{\varepsilon}^{eng}}{\dot{\varepsilon}^{eng}} - 2 \cdot \frac{\dot{\varepsilon}^{eng}}{1 + \varepsilon^{eng}} > 0 \tag{2.5}$$

Using this equation, it is deduced that the necking onset occurs at a time very close to t_{min}, the time at which the strain rate reaches its minimum, $\dot{\varepsilon}_{min}$ [80]. This model assumes that after the necking onset, the deformation of the necking part is considered to be homogeneous with a initial cross section $S - \delta S$ (Fig. **??**). Only large curvatures radius allow such piecewise homogeneity based modeling to be accurate enough. Similarly, that allows us to adopt the assumption of uniaxial stress and strain in the necking volume (Fig. **??**).

Based on the Hart criterion, the volume conservation assumption and the Norton law, Lim et al. [68] deduced Eq. **??** which allows the creep lifetime prediction in case of fracture by necking.

$$t_f - t_{min} = \frac{1}{\dot{\varepsilon}_{min} n}[1 - \delta D_r(2 + \varepsilon_{min})]^n \tag{2.6}$$

where

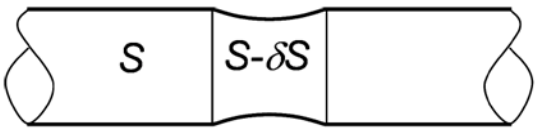

Figure 2.7: Sketch of a specimen at the onset of necking (initial inhomogeneity).

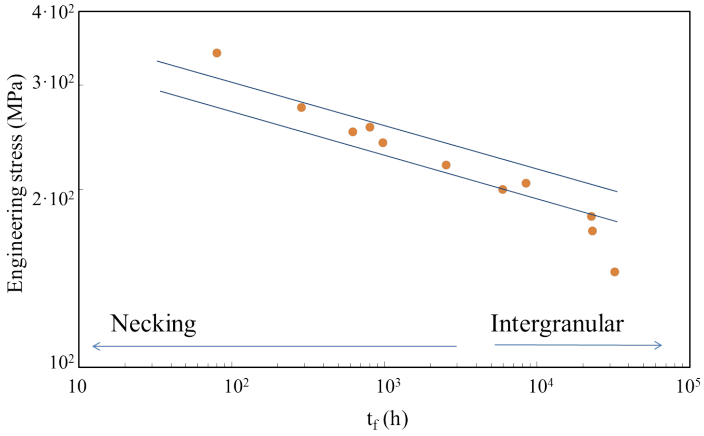

Figure 2.8: Experimental and predicted lifetimes (Necking model, upper and lower bounds, Eq. (**??**)) for the 75193 batch at 550°C.

- t_f is the time to failure by necking

- δD_r is the initial variation in diameter relative to the initial average diameter, $\bar{D}$, of the specimen: $\delta D_r = \delta D/\bar{D}$ (Fig. **??**).

Based on the measurement of the cross-section of the specimens and the creep test results for temperatures of 500, 525 and 550°C, the ranges of variation of the input parameters of Eq. **??** can be measured experimentally.

The variation in the initial diameter is measured experimentally by laser scan micrometer on the machined specimens ($|\delta D_r| \in [10^{-4}, 10^{-3}]$).

Additionally, the ranges of variation of the other input parameters are: $\varepsilon_{min} \in [0.8\%, 8\%]$ and $\frac{t_{min}}{t_f} \in [0.1, 0.6]$, based on the analysis of our numerous creep curves. The Norton law parameters at different temperatures and for different batches are given in Table **??**, and the $\dot{\varepsilon}_{min}$ values are calculated using the Norton power law.

Lower and upper bound curves are deduced from the ranges of variation of the input parameters. Lifetime predictions agree well with short term experimental data (Fig. **??**), without using any adjusted parameter. The predictions agree well the creep lifetimes lower than $3 \cdot 10^3$h for 75193 alloy at 550°C (Fig. **??**). Above such lifetime, the Necking model overestimates the creep lifetime. The reduction in area of the tests, with lifetime lower than $3 \cdot 10^3$h, show large necking and ductile fracture ($Z \geqslant 40\%$). A clear slope change is observed at about 10^4h. That may be due to intergranular damage which might affect the time to fracture as shown in the section **??** (Fig. **??**). For the lifetimes range in $3 \cdot 10^3$ and 10^4h, it could be the coexisting of necking and intergranular damage $Z \in [30 - 40\%]$.

2.3.2 Modeling of intergranular fracture

Dyson observed that cavities do not nucleate at the same time but continuously one after another [74]. Cavity nucleation starts rather early and continues over the whole creep test [93, 185, 240]. Riedel [51] proposed a model to predict long term creep lifetimes. The Riedel model assumes that, under creep conditions, cavities nucleate continuously as shown by Dyson [74] and then grow by grain boundary vacancy diffusion. The nucleation and growth of intergranular cavities cause coalescence of cavities, and then microcracks form. The fracture of specimens takes place as the area fraction of cavities and short cracks reaches a critical value, ω_f [51]. So that, the values of the different input parameters such as the cavity nucleation rate, $\dot{N}_0$, the grain boundary vacancy self-diffusion coefficient, $D_{gb/v}$, and the critical damage, ω_f, should be evaluated. Their ranges of variation should be evaluated too, in order to assess the sensitivity of the predictions with respect to the uncertainties in the input parameter values.

2.3.2.1 Cavity geometry parameter

Particular cavity shapes (Fig. **??**) could reduce the nucleation energy barrier, which leads to earlier cavity nucleation at grain boundaries but not in the crystals [51]. In addition, voids along grain boundaries can display different shapes depending if they nucleate at grain boundaries, triple points, quadruple points or at the interfaces with precipitates located at grain boundaries [77]. In the following, only grain boundary cavity nucleation is taken into account in agreement with our observations.

In Fig. **??**, the following notations are used:

- σ_b is the average normal stress acting on the grain boundary facet, in this study, σ_b is considered as applied stress, σ;
- L is the half distance between two cavities;
- r_b is the half-length of penny shape cavity (Fig. **??**);
- r is the radius of the corresponding spherical cavity (broken line) which has the same volume as the lenticular one ($\alpha < \frac{\pi}{2}$) of half-length r_b (Fig. **??**).

The cavity geometry is defined by the half-length of the lenticular cavity, r_b, and the angle α. This angle can be calculated by considering the balance of the surface tension. Eq. **??**, links the grain boundary surface energy, γ_{gb}, and the cavity free surface energy, γ_s [51].

$$\cos\alpha = \frac{\gamma_{gb}}{2\gamma_s} \tag{2.7}$$

Eq. **??** permits us to define a parameter $h(\alpha)$ which is the lenticular cavity volume divided by the volume of the spherical cavity [51].

$$h(\alpha) = \frac{1}{2}\frac{2 - 3\cos\alpha + \cos^2\alpha}{\sin^3\alpha} \tag{2.8}$$

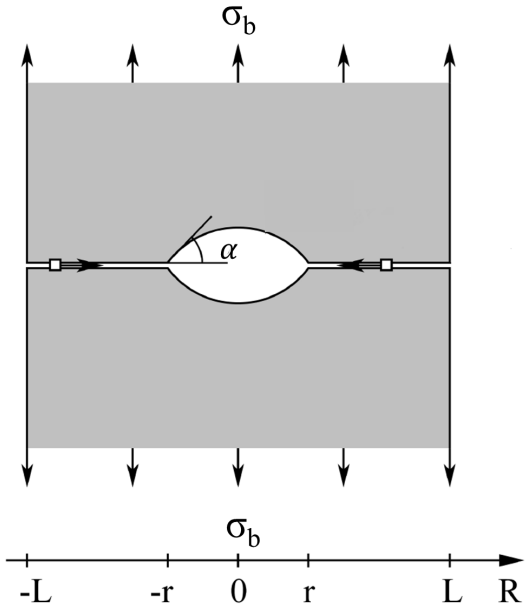

Figure 2.9: Schematic picture showing an isolated lenticular void and a simpler spherical void (broken line, $\alpha = \frac{\pi}{2}$) formed at a grain boundary without precipitate (axisymetry).

As $\gamma_b \in [0.8, 1.2] Jm^{-2}$ for general grain boundaries, $\gamma_s \in [2, 3] Jm^{-2}$ [51, 80, 83, 115], then, the value of $h(\alpha)$ is found to belong to $[0.70, 0.95]$.

2.3.2.2 Continuous nucleation law

It is observed experimentally that cavities do not nucleate instantaneously but one after one, particularity, during the secondary stage [74]. A phenomenological kinetic law of nucleation of intergranular cavities was proposed by Dyson [74], which is based on the results of many measurements carried out on different materials [15, 100]. The Dyson law links the nucleation rate with the minimum strain rate:

$$\dot{N}_0 = \alpha' \cdot \dot{\varepsilon}_{min} \tag{2.9}$$

where

- $\dot{N}_0$ is the cavity nucleation rate per grain boundary unit area (number of cavity$\cdot m^{-2} \cdot s^{-1}$)
- α' is a factor of proportionality depending on the material and loading conditions (m^{-2})

The α' factor is determined experimentally using the following equations:

$$\alpha' = \frac{N_a}{\varepsilon_f} \tag{2.10}$$

$$N_a = \frac{d_g \cdot N_m}{\pi \cdot d_H} \tag{2.11}$$

where

- N_a is the number of cavities per unit grain boundary area (m^{-2})
- N_m is the number of cavities per unit area of polished longitudinal section (m^{-2})
- ε_f is the axial strain in the homogeneous parts of the specimen (away from the necking volume), measured after fracture
- d_g is the grain size measured by the intercept line method (μm)
- d_H is the harmonic average of intersected cavity diameters (μm).

The parameter α' is evaluated using an image processing software. Fifteen FEG-SEM images are analyzed for each specimen, which allows us to measure N_m and d_g. Those parameters are measured focusing on the longitudinal sections located far away from the fracture surface. That allows us to negligent necking effect on cavity nucleation. The measured values of α' are provided in Table **??**. The measurement error is considered to be $\pm 30\%$. The evaluation of measurement error is shown in Appendix A. Our FEG-SEM cavity measurements take into account only cavities such as cavity size, $2r$, is larger than $0.4\mu m$.

T(°C)	Stress (MPa)	t_f(h)	α' 10^{11} (m^{-2})	d_g (μm)	$d_H(\mu m)$	ε_f (%)	$\dot{\varepsilon}_{min}$ $10^{-10}s^{-1}$
500	340	2246	5.10 ± 1.53	50	1	13.5	172.2
500	310	5082	9.44 ± 2.83	50	1	8.5	7.2
525	270	5082	4.40 ± 1.32	50	2	9.7	55
600	300	330	5.60 ± 1.68	100	1.5	3	27.3

Table 2.3: Measured values of the Dyson law prefactor, α', (Eq. **??**) for different creep specimens of the HN 823 alloy tested in different conditions.

As shown in Fig. **??**, the linear relationship between cavity nucleation rate and minimum strain rate shows that the α' factor seems almost stress and temperature independent between 500°C and 600°C and between 270 and 340MPa. But more data would be required to draw final conclusions. The similar measurements carried out by Lim [80] and Cui [44] show that creep specimens fractured at higher temperature and higher tensile stress may display slightly higher values of the α' factor compared to the others. Nevertheless, according to Needham and Gladman [177] and Dyson [74], this α' factor is rather independent of both tensile stress and temperature, which is in agreement with our current study.

Furthermore, differences in the α' factor values could be induced by the experimental uncertainties in the measurements. For instance, our measurements take account only cavities for which the effective diameter is larger than 0.4 μm.

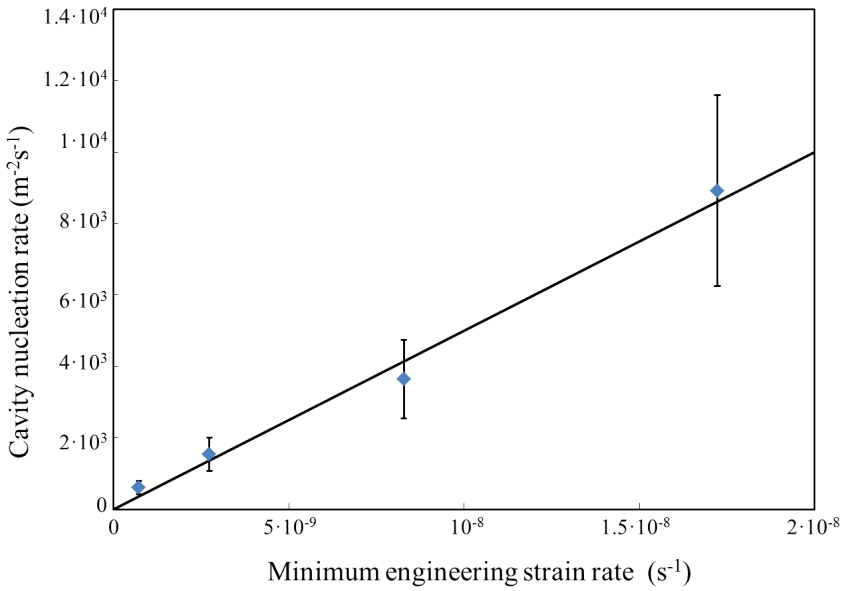

Figure 2.10: Plot of the measured cavity nucleation rate versus the minimum strain rate for different temperatures and stresses of HN 823 alloy (Table **??**).

Our measurements show that the α' factor is of the order of $6 \cdot 10^{11} m^{-2}$, which is similar to the 347 type stainless steel value [177], as shown in Table **??**. According to Table **??**, the values of α' are similar in the Grade 91, Nimoniac 80A and 316 L(N) alloys. However, their chemical composition, crystallographic structure and precipitation are completely different.

2.3.2.3 Vacancy self-diffusion coefficients

As mentioned previously, cavity growth (by vacancy diffusion) along grain boundaries is the most influent damage mechanism for long term tests. The predominant cause of intergranular cavity growth is grain boundary vacancy diffusion at elevated temperature, as shown in section **??**. Thus, the vacancy self-diffusion coefficient becomes an influent parameter to predict intergranular creep fracture. Atomic self-diffusion coefficients along grain boundaries D_{gb}, and in the bulk, D_b, of Incoloy 800 alloy were measured experimentally by Lindemann et al. [**?**], Paul et al. [**?** **?** **?**] and Guiraldenq [**?**]. The Arrhenius law parameters for atomic self-diffusion of the major atoms (Fe, Cr and Ni) are reported in Table **??**, for both in crystal bulk and along grain boundaries.

Fig. **??** shows the evolution of the diffusion coefficients of the Fe, Cr and Ni atoms, along grain boundaries and in the bulk, in function of temperature. The results show a large gap between bulk and grain boundary diffusion coefficients (around $\times 10^4$) in the interested temperature range. This means that bulk diffusion is negligible in comparison to the grain boundary one. That is in agreement

Material	T (°C)	Stress(MPa)	α' 10^{10} (m^{-2})	Reference
$\frac{1}{2}$Cr-$\frac{1}{2}$Mo-$\frac{1}{4}$V Steel	500	293-309	150	[83]
1Cr-1Mo-$\frac{1}{4}$ Steel	550	262-355	140	[83]
347 Stainless steel	550 and 650	92-385	80	[177]
Nimonic 80A (in tension)	Room temperature		4	[74]
Grade 91	500 600	230 90	7 0.1	[80]
316 L(N)	500-750	80-370	0.39-0.95	[44]
Incoloy 800	500-600	270-340	60	present work

Table 2.4: Values of the Dyson law prefactor, α', for various materials subjected to creep.

diffusing atom	$D_{gb0}\delta$ $(m^3 s^{-1})$	Q_{gb} $(kJ \cdot mol^{-1})$	D_{b0} $(m^2 s^{-1})$	Q_b $(kJ \cdot mol^{-1})$	T range (°C)
Fe [**?**]	$4.9 \cdot 10^{-11}$	216.0	$1.50 \cdot 10^{-6}$	241.0	800-1000
Fe [**?**]	$9.4 \cdot 10^{-15}$	160.7	$3.20 \cdot 10^{-5}$	259.6	477-827 (gb) 747-1227 (b)
Fe [**?**]	$2.2 \cdot 10^{-16}$	104.2	$6.30 \cdot 10^{-5}$	278.0	850-1050
Cr [**?**]	$2.9 \cdot 10^{-14}$	184.2	$3.24 \cdot 10^{-4}$	287.4	502-897 (gb) 787-1237 (b)
Ni [**?**]	$1.9 \cdot 10^{-14}$	156.4	$8.62 \cdot 10^{-5}$	255.9	477-807 (gb) 797-1227 (b)
Ni [**?**]	$1.4 \cdot 10^{-15}$	142.0	$1.50 \cdot 10^{-4}$	300.0	850-1050

Table 2.5: Arrhenius law parameters for atomic self-diffusion along grain boundaries (gb) and in bulk (b) for Incoloy 800 alloys.

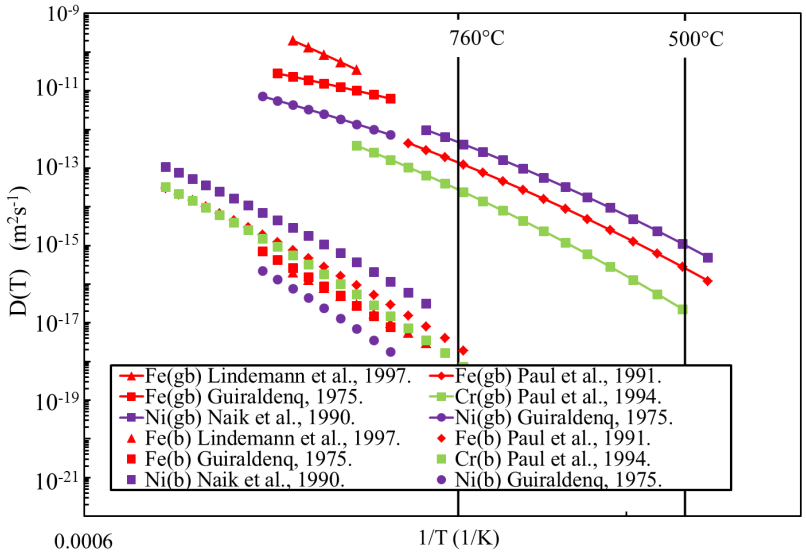

Figure 2.11: Grain boundary (gb) and bulk (b) self-diffusion coefficients of Fe, Cr and Ni in Incoloy 800 alloy depending on temperature. The range of temperature of interest is [500-760°C] (Table **??**).

with many observations showing that cavities are located on the grain boundaries instead of in the bulk. As choosing the grain boundary diffusion parameters, we should avoid a too large extrapolation of the diffusion coefficient values. This extrapolation out of the temperature range of measurement, could lead to errors in the values of self-diffusion coefficients. Since our temperature range of interest is 500−750°C, the values measured by Paul et al.[**?** **?** **?**] are used (Table **??**).

Furthermore, cavity growth occurs by vacancy diffusion along grain boundaries. The grain boundary vacancy self-diffusion coefficient, $D_{gb/\nu}(T)$ is estimated by Eq. **??** [**?**]:

$$\frac{1}{D_{gb/\nu}(T)} = \frac{N_{Fe}}{D_{gb/Fe}(T)} + \frac{N_{Cr}}{D_{gb/Cr}(T)} + \frac{N_{Ni}}{D_{gb/Ni}(T)} \tag{2.12}$$

where N_i is the mole fraction of the element i ($i = Fe,\ Cr\ or\ Ni$). The values are given in in Table **??**.

2.3.2.4 Evaluation of the Rice length

Two mechanisms can be considered for cavity growth, either viscoplastic deformation of the surrounding grains or grain boundary vacancy diffusion. The cavity growth mechanism can be assessed using a length parameter, L_R, given by Eq. **??**, and usually called the Rice length [100].

$$L_R = \left(\frac{D_{gb/\nu}\delta\Omega\sigma}{k_b T}\frac{1}{\dot{\varepsilon}_{min}}\right)^{\frac{1}{3}} \tag{2.13}$$

T (°C)	$D_{gb/Fe}$ m^2s^{-1}	$D_{gb/Cr}$ m^2s^{-1}	$D_{gb/Ni}$ m^2s^{-1}	$D_{gb/\nu}$ m^2s^{-1}	$D_{gb/\nu}\delta$ m^3s^{-1}
500	$2.60 \cdot 10^{-16}$	$2.07 \cdot 10^{-17}$	$1.03 \cdot 10^{-15}$	$8.46 \cdot 10^{-17}$	$4.23 \cdot 10^{-26}$
525	$5.70 \cdot 10^{-16}$	$5.08 \cdot 10^{-17}$	$2.21 \cdot 10^{-15}$	$2.03 \cdot 10^{-16}$	$1.02 \cdot 10^{-25}$
550	$1.19 \cdot 10^{-16}$	$1.18 \cdot 10^{-17}$	$4.52 \cdot 10^{-15}$	$4.61 \cdot 10^{-16}$	$2.31 \cdot 10^{-25}$
600	$4.56 \cdot 10^{-15}$	$5.52 \cdot 10^{-16}$	$1.67 \cdot 10^{-14}$	$2.05 \cdot 10^{-15}$	$1.03 \cdot 10^{-24}$
650	$1.51 \cdot 10^{-14}$	$4.11 \cdot 10^{-15}$	$5.38 \cdot 10^{-14}$	$7.73 \cdot 10^{-15}$	$3.87 \cdot 10^{-24}$
700	$4.43 \cdot 10^{-14}$	$7.49 \cdot 10^{-15}$	$1.53 \cdot 10^{-13}$	$2.52 \cdot 10^{-14}$	$1.26 \cdot 10^{-23}$
760	$1.41 \cdot 10^{-13}$	$2.81 \cdot 10^{-14}$	$4.71 \cdot 10^{-13}$	$8.92 \cdot 10^{-14}$	$4.46 \cdot 10^{-23}$
δ is the typical grain boundary thickness ($0.5 \cdot 10^{-9}$ m)					

Table 2.6: Grain boundary self-diffusion coefficients at $500 - 760$°C.

where

- Ω is the atomic volume ($1.21 \cdot 10^{-29} m^{-3}$)
- k_b is the Boltzmann constant ($1.38 \cdot 10^{-23} JK^{-1}$)

The ratio between the cavity growth rate by grain boundary diffusion and the one induced by the viscoplastic flow is approximately equal to $(r/L_R)^3$ for a round cavity of radius r.

Needleman and Rice [100] showed that cavity growth is controlled by diffusion alone if $r/L_R \leqslant 0.2$ (with negligible viscoplasticity effect). The diffusion and viscoplasticity processes combine together to produce growth in excess if $0.2 < r/L_R \leqslant 20$, which differs from each mechanism considered individually. Finally the viscoplasticity process is the dominant cavity growth mechanism if $r/L_R > 20$.

The Rice length is now evaluated. The cavities are observed far away from the fracture surfaces. Based on the measured cavity sizes, the ratio $\bar{r}/L_R$ computed for the four specimens are generally lower than 0.2, as shown in Table **??**. For the test at 500°C under 340MPa, this value is 0.25, but it is still close to 0.2. Thus, the cavity growth by viscoplasticity can be neglected for all the considered tests, except in the necking volume close to failure.

2.3.2.5 Cavity growth rate induced by vacancy diffusion

Raj and Ashby [77] assumed that when steady-state is established, all parts of the grain boundary or gain must release in the same amount of matter [77]. Accounting for the condition of mechanical equilibrium of a disk of radius L (Fig. **??**), and the number of atoms added along the grain boundary located around a cavity because of the cavity growth per unit time, the cavity growth rate can

T °C	Stress (MPa)	$\dot{\varepsilon}_{min}$ 10^{-10} (s^{-1})	L_R (μm)	$\bar{r}$ (μm)	$\bar{r}/L_R$	r_{max} (μm)	r_{max}/L_R
500	340	172.2	2.02	0.5	0.25	1.2	0.59
500	310	7.2	2.74	0.5	0.18	1.3	0.47
525	270	55	5.75	1	0.17	2.0	0.35
600	300	27.3	4.84	0.75	0.15	1.5	0.31

Table 2.7: The Rice length (Eq. **??**), the $\bar{r}/L_R$ ratio and the r_{max}/L_R for different fractured specimens of the HN 823 alloy.

be obtained as the following [80]:

$$\dot{r} = \frac{2\Omega D_b \delta}{h(\alpha) k_b T} (\frac{1}{r})^2 \frac{\sigma_b - \sigma_0(1-\omega)}{q(\omega)} \tag{2.14}$$

where

- ω is the area fraction of cavities: $\omega = (\frac{r}{L})^2$, which characterizes the intergranular damage
- $q(\omega) = -2ln(\omega) - (1-\omega)(3-\omega)$
- σ_0 is the sintering stress, $\sigma_0 = \frac{2\gamma_s}{r}$. If the applied stress, σ, is lower than this stress, no growth occurs

The area fraction of cavities increases over time up to the specimen fracture. The critical average value of the area fraction of cavities along grain boundaries is denoted as ω_f. This parameter is measured experimentally based on SEM observations and measurements carried out on longitudinal sections. The value of $\bar{\omega}_f$ is 0.041 for Incoloy 800 alloys. This value is similar to one measured by Auzoux [109], 0.04 for 316 SS. Dyson and Mclean[**?**] assumed that ω_f should lower than 0.1. Lim [80] used the $\omega_f = 0.1 \pm 0.05$ to predict the creep lifetime of Grad 91. Simulations of the viscoplastic deformation of homogeneous porous material show that the strain rate increases very quickly as soon as porosity reaches 5-10% is reached. According to our experimental observations, in the following a critical porosity value of 0.04 ± 0.01 is then used predict the creep lifetime of Incoloy 800.

The Raj and Ashby equation [77] assumes that the diffusion flux of vacancies is induced by the normal stress acting on grain boundaries, and not by the hydrostatic pressure. The rate of growth is only driven by the synergistic effect of grain boundary diffusion and normal stress.

Considering that cavities are heterogeneously distributed along grain boundaries, Dyson [74] suggested that the cavity growth should be constrained by the matrix viscoplastic deformation. Due to intergranular cavitation and matter redistribution along the grain boundaries, the strain compatibility between the cavitated grain boundary and the surrounding non damaged matrix should be

fulfilled ensured. This induces a decrease of stress through the damaged grain boundary. Additionally the volume surrounding the damaged grain boundary may then deform faster than the viscoplastic matrix to ensure strain compatibility [94]. A reduction in cavity growth rate is induced by the reduction of local stress. Rice [94] proposed Eq. (**??**) to calculate the constrained cavity growth rate.

$$\dot{r} = \frac{2\Omega D_b \delta}{h(\alpha) k_b T} (\frac{1}{r_b})^2 \frac{\sigma_b - \sigma_0(1-\omega)}{\frac{8{L_R}^3}{\xi L^2 d_g} + q(\omega)} \tag{2.15}$$

where

- $\xi = \frac{4}{\pi^2 (1+\frac{3}{n})^{1/2}}$ with n the exponent of the Norton law

It should be noticed that the ω function: $q(\omega) = -2ln(\omega) - (1-\omega)(3-\omega)$ is monotonically decreasing with ω from zero up to ω_f, so that, $[q(\omega)]_{min} = q(\omega_f)$. From the fracture criterion, it drives that $\omega_{max} = \omega_f$, with ω_f the critical area fraction of cavities. Considering that at fracture:

$$\omega_{max} = (\frac{\bar{r}}{L(t_f)})^2 = \omega_f \simeq 0.04 \tag{2.16}$$

it derives that:

$$L(t_f) \simeq 5\bar{r} \quad whereas \quad [q(\omega)]_{min} = 3.7 \tag{2.17}$$

Further, L decreasing with time down to $L(t_f)$. Besides, $\frac{8{L_R}^3}{\xi L^2 d_g}$ is monotonically increasing with L decreasing. Using the mean value of n ($n = 15$ Table **??**), ξ equals 0.37.

As shown in section **??**, the mean value of the cavity radius is $0.5\mu m$, so that: $\frac{\bar{r}}{L_R} = 0.19$ at fracture. Assuming that:

$$L_R = 5\bar{r} = L(t_f), \quad d_g = 100\mu m, \quad \bar{r} = 0.5\mu m = 0.5 \cdot 10^{-6} m \tag{2.18}$$

then, $(\frac{8{L_R}^3}{\xi L^2 d_g})_{max} = 0.54$. It can be deduced that $(\frac{8{L_R}^3}{\xi L^2 d_g})_{max} \ll [q(\omega)]_{min}$, so that, in the present work, the constrained cavity growth effect is negligible. The Raj and Ashby equation is therefore used in the following. It means that only grain boundary diffusion growth is considered (Eq. **??**). And the σ_b equals the applied stress, σ.

2.3.2.6 Prediction of long term creep lifetime

The Riedel model provided upper and lower bounds to predict long term creep lifetimes, derives from Eqs. **??** and **??**. In fact, in general, the set of equations cannot be solved analytically [51].

Furthermore, closer upper and lower bounds based on the Riedel set of equations were proposed by Lim [80]:

$$0.301 \left(\frac{h(\alpha) k_b T}{\Omega D_{gb/v} \delta \sigma} \right)^{\frac{2}{5}} \frac{\bar{\omega}_f^{0.516}}{\dot{N}_0^{\frac{3}{5}}} \leq t_f \leq 0.354 \left(\frac{h(\alpha) k_b T}{\Omega D_{gb/v} \delta \sigma} \right)^{\frac{2}{5}} \frac{\bar{\omega}_f^{\frac{2}{5}}}{\dot{N}_0^{\frac{3}{5}}} \tag{2.19}$$

Uncertainties in the material input parameters should be taken into account for the intergranular damage prediction. Then, the predicted upper and lower bound values differ by a factor of almost three. At same time, uncertainties in the necking modeling input parameter lead to the final upper and lower bound values differ by a factor of almost two.

2.4 Lifetime prediction

2.4.1 Stress lifetime plots

In this part, the combination of the necking and the Riedel models is used to predict the short and long term lifetimes.

The predictions are based on the Norton law parameters, which have been previously adjusted for each batch and at each temperature (Table **??**). That allows the evaluation of the minimum strain rate. The δD_r, t_{min} and ε_{min} values are measured experimentally. The prefactor of the Dyson law, α', and the critical damage area fraction, ω_f, measured for the HN 823 alloy are used for lifetime prediction for all the other batches. It is indeed assumed that that the $M_{23}C_6$ precipitates do not differ much from one batch to another in the same loading conditions. This assumption needs to be checked experimentally. The main difference between the batches consists in their dependence of minimum strain rates with respect to their chemical composition (Table **??**, Fig. **??**). That dependence is usually explained qualitatively by the difference in γ' intragranular precipitation linked to the Ti+Al content.

The combined model predicts lifetime up to $3 \cdot 10^4$h (3 years) (75193 550°C) with low stress (140MPa) in account of the change of creep damage mechanism (Fig. **??**).

As shown in Fig. **??**, the combination of the necking model and the Riedel model leads to predicted lifetimes in agreement with the experimental data for the 75193 alloy at 550°C. The evaluation of the experimental uncertainty in the input parameter values allows us to plot the lower and upper bound curves. This uncertainty could explain that the predicted lifetime is shorter than the experimental lifetime for the test at 340MPa, 80h. Further this may due to the uncertainty caused by the prediction of minimum strain rate. As shown in Fig. **??**, the experimental results of the 75193 alloy show changes of slope in $\dot{\varepsilon}_{min}$-stress curve, which is not taken into account for the Norton parameters evaluation. It could lead to a better lifetime prediction with the change in Norton parameters.

It should be noticed that the predicted fracture mode agrees well with the one evaluated through the area reduction measurements (Figs. **??** and **??**). That shows the consistency of the combination of the two models and damage mechanisms determined by FEG-SEM observations. Finally, the slope change caused by the change in damage mechanisms is well predicted through the combined

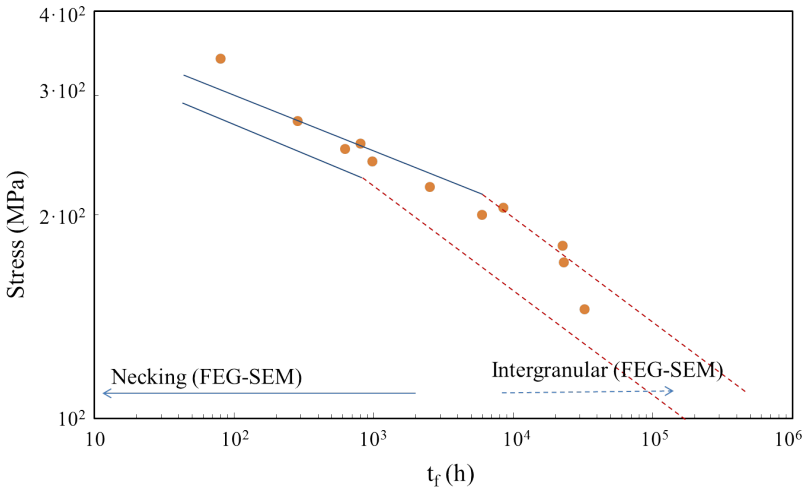

Figure 2.12: Lifetimes predicted by the Necking model (blue lines) and the Riedel model (red lines) compared with experimental data for the 75193 alloy at 550°C (orange points). The failure modes evaluated by the fractured area reduction measurements and the FEG-SEM observations are mentioned along the time axis.

model.

The predicted and experimental lifetime curves and data obtained for different batches (Table **??**) at 550°C are plotted in Fig. **??**. The effect of the Ti+Al content is well predicted through the difference in the Norton parameters only. The agreement between the experimental and the predicted lifetime holds whatever the Ti+Al content. That leads us to propose that the carbide formation may be weakly dependent on the Ti+Al content or affects not so strongly the cavity nucleation law. So that, the Ti+Al content would have little influent on the α' value (Eq. **??**). This should be confirmed by further experimental observations.

The predictions are also carried out for Incoloy 800 alloys tested at temperatures ranging from 500 to 760°C, as shown in Fig. **??** and **??**. The lifetimes of the 75193 alloy and the 7686A alloy at different temperatures are well predicted using the value of α' measured in the HN 823 alloy. This leads us to propose that the value of α' do not differ a lot in the temperature ranging in 500 and 760°C. Further, the value of α' should be independent on the tensile stress. These points agree well with the Dyson law, which propose that, for given material, the α' is a constant. Further, using same value of α', the lifetime of 7686A [48] are well predicted. Therefore, the value of α' may not differ or slightly differ for a small variation of chemical compositions.

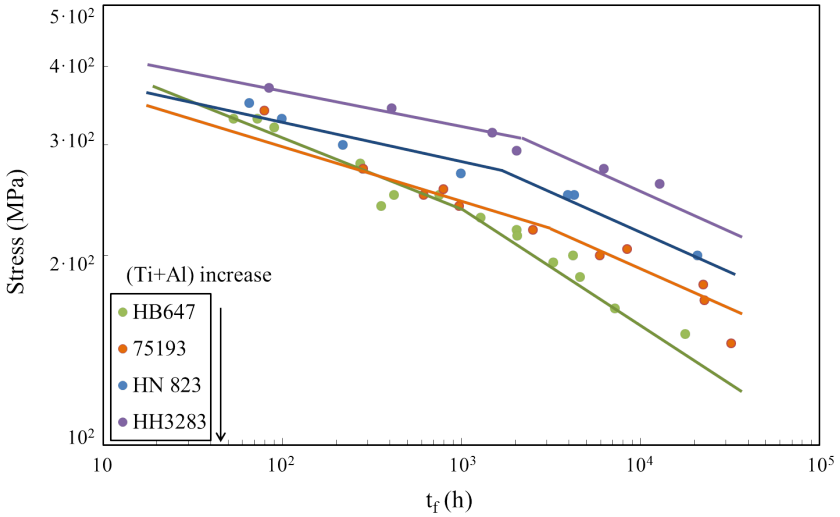

Figure 2.13: Experimental (points) and predicted (lines) lifetimes for various Incoloy 800 alloys, with different Ti+Al contents, at 550°C (Necking model and the Riedel model predictions).

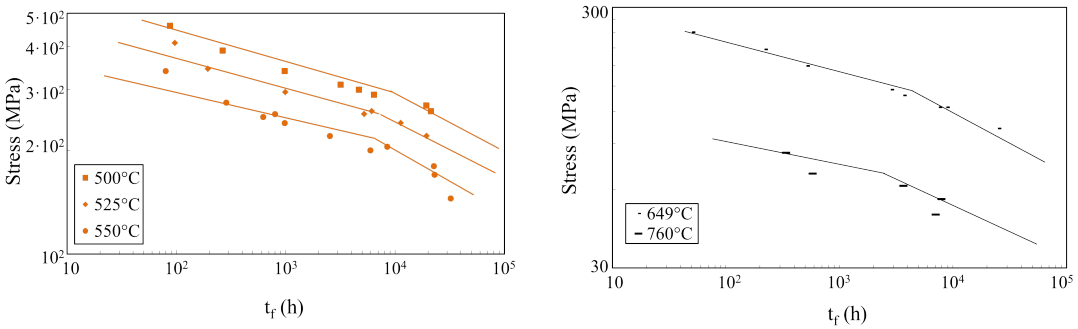

(a) (b)

Figure 2.14: Comparison between experimental and predicted lifetimes at temperatures ranging from 500 to 760°C (Necking model and the Riedel model predictions). (a) 75193 alloy at 500, 525 and 550°C; (b) 7686A alloy at 649 and 760°C (data of ORNL [48]).

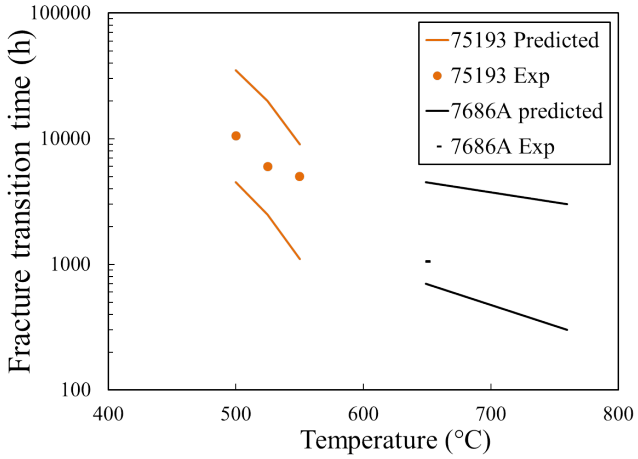

Figure 2.15: Transition times in fracture mechanisms predicted by the combined model for different temperatures (Necking model and the Riedel model predictions) compared with experimental results.

2.4.2 Prediction of the transition in fracture mechanism

The Monkman-Grant and the Larson-Miller laws are phenomenological relationships, whereas the combined model used previously is physically-based. The necking model is based on the prediction of both necking onset and necking cross-section evolution. And the Riedel model is based on continuous cavity nucleation and grain boundary diffusion growth, in agreement with observations.

From the observations of the fracture surfaces and the measured lifetimes, we can finally evaluate experimentally the transition times in damage mode depending on temperature and material. Using the combined model, the transition time between the two damage mechanisms can be predicted too. Fig. **??** shows the evaluation of transition time in function of temperature. It should be noticed that, with few experimental results of 7686A at $750°C$, the experimental transition time cannot be evaluated. Following the predictions, an increase in temperature leads to an earlier change in damage mechanisms, which agrees with experimental data. The dependence of the grain boundary self-diffusion coefficient temperature is may stronger than the creep strain rate one. That explains such a temperature dependence of the transition time.

2.5 Cavity size distribution

Riedel [51] proposed a cavity size statistical distribution function, $N(r, t, \sigma, T)$, which account for cavity nucleation and growth equations (Eq. **??** and **??**). The distribution is a function of time, temperature and stress, which gives more

insight into the cavitation mechanisms in the specimens.

The cavity size distribution should be updated during creep. Assuming that cavity nucleation is stress and temperature independent, the number of cavities growing from r to $r + \partial r$ is shown in Eq. **??**.

$$\dot{N} = -\frac{\partial(N \cdot \dot{r})}{\partial r} \tag{2.20}$$

Eq. **??** and Eq. **??** are proposed as test functions for, respectively, the cavity growth rate and cavity nucleation rate:

$$\dot{r} = A_1 \cdot r^{-\beta} \cdot t^{-k} \tag{2.21}$$

$$\dot{N}(t) = A_2 \cdot t^{\gamma} \tag{2.22}$$

Finally, Riedel deduced from Eq. **??** and Eq. **??**, a general solution for the cavity size statistical distribution function as [51]:

$$N(r,t) = \frac{A_2}{A_1} \cdot r^{\beta} \cdot t^{k+\gamma} \cdot (1 - \frac{1-\alpha}{1+\beta} \cdot \frac{r^{\beta+1}}{A_1 \cdot t^{1-\alpha}})^{\frac{k+\gamma}{1-k}} \tag{2.23}$$

where A_1, A_2, k, β and γ are parameters depending on stress and temperature via the cavity nucleation and growth law, but not on time or on cavity size.

To calculate the cavity size distribution, it is proposed that the cavity nucleation law is similar to the Dyson law (Eq. **??**), so that γ is equal to 0 and $\dot{N}(t) = A_2 = \dot{N}_0$.

And the A_1, k and β coefficients are evaluated using the cavity growth rate law proposed by the Raj and Ashby (Eq. **??**), which links cavity growth rate, cavity size and applied tensile stress.

$$\frac{1}{r^2} = r^{-\beta} \tag{2.24}$$

$$\frac{2\Omega D_b \delta}{h(\theta) k_b T} \frac{\sigma - \sigma_0(1-\omega)}{q(\omega)} = C' \cdot F(\omega, r) = A_1 t^{-k} \tag{2.25}$$

Eq. **??** contains two parts (Eq. **??** and Eq. **??**) as described in Eq. **??**. Using lower and upper bounds of the function $F(\omega, r_b)$ appearing in Eq. **??**, we can calculate analytically C'.

Assuming that $\sigma \frac{2\Omega D_b \delta}{h(\theta) k_b T} = C'$ and $F(\omega, r) = \frac{1 - \frac{\sigma_0}{\Sigma_n}(1-\omega)}{q(\omega)} = b\omega^a$, the lower and upper bounds of $F(\omega, r)$ are obtained using the minimum and the maximum measured radius values, respectively, r_{min} and r_{max}. The the minimum cavity radius, r_{min}, is assumed as critical radius, r_c [77]. Assuming that $r_c = r_{min} = \frac{2\gamma_s}{\sigma}$, then $r = r_c$, $\sigma_0 = \sigma$.

$$F(\omega, r_c) = \frac{1 - \frac{\sigma_0}{\sigma}(1-\omega)}{q(\omega)} = \frac{1 - \frac{\sigma}{\sigma}(1-\omega)}{q(\omega)} = \frac{\omega}{q(\omega)} \tag{2.26}$$

The maximum radius, r_{max}, is determined experimentally. The function $F(\omega, r_{max})$ can be rewritten as:

$$F(\omega, r_{max}) = \frac{1 - \frac{r_c}{r_{max}}(1-\omega)}{q(\omega)} \tag{2.27}$$

Experimental measurements show that ω_f is generally lower than 0.05 as explain in part 3.2, so that, the upper and lower bounds of the function $F(\omega, r)$ are obtained for 270MPa and $525°C$. And they are generally valid for $0 < \bar{\omega} < 0.05$ and $r_c < r < r_{max}$.

Under these conditions, the maximum cavity radius measured experimentally amounts to $r_{max} = 0.8\mu m$. And the minimum cavity radius is evaluated using $r_c = r_{min} = \frac{2\gamma_s}{\sigma}$. Then, we find $r_c = 18nm$. Under each loading conditions, the $F(\omega, r)$ function can bounded ω-power laws. For instance, at $525°C$ and $270MPa$, we deduce that $0.5\omega^{1.25} < F(\omega, r) < 6.1 \cdot 10^8 \omega^{0.5}$. The evolution of the average area fraction of cavities along grain boundaries, $\bar{\omega}(t)$, can be calculated by integrating the areas occupied by individual cavities times their density [51], and is given by:

$$\bar{\omega}(t) = I(k, \beta, \gamma) A_2 A_1^{\frac{2}{\beta+1}} t^{k+\gamma+\frac{(1-k)(\beta+3)}{\beta+1}} \tag{2.28}$$

where $I(k, \beta, \gamma)$ is defined by Eq. **??** [51]:

$$I(k, \beta, \gamma) = \pi(1+\beta)^{\frac{\beta+3}{\beta+1}} \int_0^u x^{\beta+2}[1-(1-k)x^{\beta+1}]^{\frac{k+\gamma}{1-k}} dx \tag{2.29}$$

if $k > 1$, $u = +\infty$ and if $k < 1$, $u = (1-k)^{-\frac{1}{\beta+1}}$

The combination of Eqs. **??**, **??**, **??**, **??** and **??** provides bounds valid for the considered loading parameters :

$$-12.6 < k < -0.5 \quad and \quad A_1 = [C \cdot b \cdot [I(k, \beta, \gamma) \cdot A_2]^k]^{\frac{1}{1-\frac{2}{3}k}} \tag{2.30}$$

With $(a, b) = (0.5, 6.1 \cdot 10^8)$ (upper bound) and $(a, b) = (1.25, 0.5)$ (lower bound), The analytical calculation leads to $\beta = 2$, $-12.6 < k < -0.5$ and A_1 is proportional to A_2, C and k. Fig. **??** shows the calculation results, with predicted curves bounding the experimental cavity size cumulative distribution.

This model combines the cavity growth rate and cavity nucleation rate equations. It allows the prediction of the cavity size distribution. This model was proposed by Riedel [51] and was used later by Lombard and Vehoff [129] and Lim [80]. The cavity growth rate equation used the Raj and Ashby one which is based on cavity growth by vacancy diffusion along grain boundaries. And the nucleation rate is calculated by the Dyson law, which is a phenomenological law, based on numerous cavity density measurements.

Assuming that $A_1 = A_2 = 1$, Riedel [51] proposed different combinations of parameters k, β and γ, which leads to various types of distribution curves.

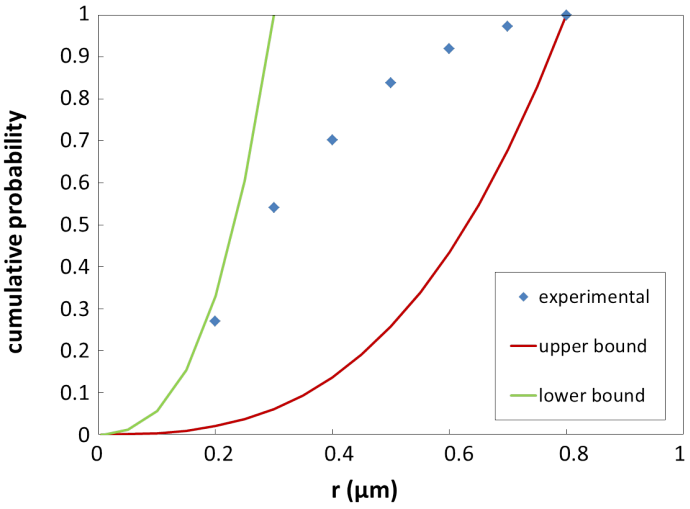

Figure 2.16: Comparisons between the predicted and measured cavity size distributions (550°C, 310MPa, 5082h).

He showed that using parameters such as $\beta = 2$, $\gamma = 0$ and $k = 2$, the cavity size distribution curves are obtained. Then, the choice of those parameter values allows the plot of cavity distribution curve form more similar to the experimental ones. However, the chosen parameters have no physical meaning [51]. Because A_1 and A_2 have physical meaning, specially, A_2 is the cavity nucleation rate, which is different to 1.

Lim [80] followed a similar approach as ours, but assuming $\beta = 2$, $\gamma = 0$ and $k = 1$. The cavity size distribution issue of these parameters is overestimated of a factor 2 or 3.

Lombard and Vehoff [129] proposed to fit the parameters from the measured cavity distributions, but the parameters, A_1, A_2, k, β and γ, should be fitted for each stress and each temperature. And that approach could not be predictive because the experimental cavity size distributions have been used in the parameter adjustments.

In this study, we can calculate analytically the cavity size distribution for each test conditions, the upper and lower bound curves of the $F(\omega, r)$ function. Each experimental cavity distribution curve is found to be bounded by the predicted upper and lower bounds curves. And predictions can be generally provided for different stress and temperature conditions after reevaluating the upper and lower bound power laws (Fig. **??**), without using any experimental distribution.

2.6 Discussion

As shown in section **??**, the short term and long term creep lifetimes are accurately predicted using the combination of Necking and the Riedel models. The effect of the Ti+Al content is also accounted for by both models through the differences in strain rate. Furthermore, the cavity size distribution is fairy well predicted.

Recent studies show that the combination of the both models using two bound curves, predicts efficiently 316L(N) [115], Grade 91 steel [80] and 347 alloy [44] creep lifetimes in large temperature and stress ranges. In the case of the Incoloy 800 alloys, the Norton law parameters differ from one batch to another due to strong differences in the volume fractions and sizes of the γ' precipitates. On the contrary, such large chemical composition effect is not observed in 316L(N) and Grade 91, at least not in such proportions. It is then of interest to valid this model for various materials, such as copper, Aluminum alloys, Ni-based alloys and other materials.

For the cavity growth mechanism, the constrained cavity growth model has been used by Eggeler et al. [**?**] and Sandström and Wu [110]. However, our numerical applications show that the constrained effect is negligible. And the plastic cavity growth is also negligible via the Rice length. Therefore, only grain boundaries diffusional cavity growth is taken into account in this paper.

Recently, He and Sandström [69] proposed a ductile creep fracture model based on dislocation creep, which predicts correctly short term creep lifetimes. However, this model does not take into account directly the viscoplastic instability. This leads the authors to assume that failure takes place when the total strain reaches a conventional value of 0.2 for all austenitic stainless steels, which do not valid for all temperature and stress. Moreover, the effect of the Ti+Al content may could not be correctly predicted by this model, due to the constant chosen parameters for one series of material.

Sandström and Wu [111] proposed a intergranular creep fracture model based on grain boundary sliding, which has been proved experimentally. This model predicts a Dyson-type cavity nucleation rate. Nevertheless, it should be noticed that grain boundary sliding model could not provide an explanation for cavity nucleation along the grain boundaries perpendicular or parallel to the tensile direction [52, 57, 79].

For the cavity nucleation, the Dyson law parameter, α', used previously is assumed to be independent of the Incoloy 800 batch, temperature and applied stress. This point needs to be further verified by SEM-FEG observations. Accounting for the measurement error bar, no clear dependence of the α' parameter with respect to temperature and stress shows can be highlighted (Table **??**, Fig. **??**).

Further, the cavity nucleation mechanism has not been well established yet. For alloys containing second phases, such as Incoloy 800 alloys, AISI 316, Ni-

based alloys and grade 91 steel, the cavities appear generally at the interfaces of the second phase particles located along grain boundaries [51, 52, 81, 117, 121, 128, 134, 150**?**]. Large cavities are more numerous along perpendicular grain boundaries. But if all cavities including the smallest ones ($r \simeq 20nm$), they are the most numerous along grain boundaries parallel to the tensile axis [93, 185].

Our work in progress focuses on computations by the Finite Element Method of the stress fields at precipitate-crystal interfaces, accounting for the crystal viscoplastic flow of the surrounding grains. Then local stress and energy criteria allow the prediction of interface fracture and the progressive nucleation of cavities through the polycristal. Such modeling may help to evaluate theoretically the Dyson law parameter value, α', and its dependence with respect to time, temperature, stress and material.

2.7 Conclusion

The creep properties of Incoloy 800 alloys were investigated experimentally at temperatures ranging between 500°C and 760°C, for lifetimes up to 33 000h. Two main fracture mechanisms were observed: necking and intergranular damage.

The onset of necking is first analyzed using the Hart criterion of viscoplastic instability and then the necking evolution is predicted up to failure. The used necking model was proposed by Lim based on the Hart theory of viscoplastic instability, the Norton law and the volume conservation.

Intergranular damage is predicted based on the Riedel model, which assumes that cavities nucleate continuously following the Dyson law. This well-known phenomenological law assumes that the cavity density is linearly proportional to the remote viscoplastic strain. Additionally, the Riedel model assumes that cavities grow by vacancy diffusion along grain boundaries. This leads us to predict lower and upper lifetime bounds. The Riedel bound curves are shown to be rather stable with respect to the experimental parameter uncertainties in the input parameter values, such as the cavity nucleation rate evaluated through cavity density measurements and grain boundary self-diffusion coefficient.

The comparison between predicted and experimental lifetimes shows that lifetime is accurately predicted by the combination of the necking and Riedel models. Predicted and measured lifetimes agree well whatever the chemical composition, the temperature (from 500 to 760°C) and the applied stress. That holds for lifetimes from a few ten hours up to 33000h.

The comparison between different batches of Incoloy 800 shows the strong influence of the Ti+Al content on strain rate and creep lifetime. A higher Ti+Al content leads to lower strain rate and better creep resistance. Such trends are quantitatively well predicted by the combination of the necking and Riedel models.

Our results confirm the validation of such modeling to predict creep lifetime

in both short and long term simulations in various steels, such as austenitic stainless steels [115] and tempered martenitic steels [68].

It should be noticed that the Dyson law is assumed to be valid and the experimental evaluation of its prefactor vale is needed when using the Riedel model. Cavity nucleation mechanisms should be studied experimentally, analytically or by numerical calculations to provide a reliable and comprehensive prediction of cavity nucleation. The following chapters aim to evaluate theoretically the cavity nucleation rate, $\dot{N}_0$.

The experimentally measured values of the prefactor of the Dyson law, α', introduced in the lifetime predictions lead predictions of creep lifetimes in fair agreement with experimental data up to 25 years. Further, only this α' parameter should be measured allowing long term creep lifetime predictions. Therefore, it is important to calculate this parameter, specially its dependence on stress and temperature. This leads us to calculate the stress fields around particles using the Finite Element method in Chapter 2. Further, there are more experimental data and microstructural observations in 316L(N) and more generally in austenitic stainless steels than in Incoloy 800. Therefore, our calculations focus on 316L(N) in Chapter 2 and 3.

The results will be discussed in details in Chapter 4 where the lifetime predictions using the predicted nucleation law will be compared to all existing lifetime data up to 30 years.

Chapter 3

Modeling of creep cavity nucleation in 316L(N)

To be submitted to J. Mech. Phys. Solids

Long-term creep fracture at high temperature is characterized by grain boundary cavitation. In the alloys contain second phase particles, cavities nucleate preferentially along the interfaces of these second phase particles and the surrounding matrix. However, the dominant cavity nucleation mechanism in creep has not been well established yet. It is generally believed that interface fracture is caused by high local stress fields. Therefore, the interface stress fields around second phase particles are computed to check if they may be high enough to allow fracture to occur.

By the finite element method, crystal elastoviscoplastic laws are used to calculate the stresses around second phase particles located along grain boundaries during creep deformation. Our calculations take into account the effect of the random neighbor grain crystallographic orientations, temperature, tensile stress and the orientation of grain boundaries with respect to the tensile axis. Further, cavitation is assumed to take place when the maximum interface normal stress reaches a critical fracture stress, which evaluation is based on atomistic theories.. Numerical results show that interface fracture occurs continuously and the cavity density increases linearly with macroscopic strain, in agreement with numerous experimental measurement data. In addition, the cavity nucleation rate is predicted by combining the intergranular second phase particle density and the evolution of the fraction of fractured interfaces with the remote strain.

Consequently, this work provides a theoretical explanation to the well-known Dyson law. And it shows that interface fracture may be the dominant cavity nucleation mechanism in alloys containing intergranular second phase particles.

3.1 Introduction

The austenitic stainless steel, 316L(N) is a suitable candidate for structural components of the Generation IV nuclear power plant, ASTRID (the Advanced Sodium Technological Reactor for Industrial Demonstration). Under high temperature and stress conditions, the lifetime of some components should reach 60 years. Therefore, the long term creep failure mechanisms occurring in 316L(N) need to be understood and predicted.

Long term creep failure is characterized by the nucleation, growth and coalescence of cavities along grain boundaries. Intergranular precipitates seem to be most observed cavity nucleation locations. This phenomenon is called intergranular creep fracture [51, 52, 77, 79, 87].

The cavity nucleation mechanism has not been well established yet. Two mechanisms were proposed to explain the cavity nucleation: vacancy-diffusion (thermally-activated nucleation) and interface fracture.

Based on vacancy diffusion, Raj [81] proposed a thermo-activated theory, which assumes that the agglomeration of vacancies may lead to a stable nuclei of critical size. And the cavities continue to growth. Raj [77] computed the variation of the Gibb's energy depending on cavity size and deduced the stable nuclei size. A constant cavity nucleation rate was derived by Raj too. However, the predicted cavity nucleation rate increases exponentially with the increase in the tensile stress. The critical conditions for cavity nucleation are proposed as a threshold stress drived from the exponential dependence and an incubation time [51, 77, 81]. However, Argon et al [116], Riedel [51] and Yoo and Trinkaus [79] suggested that this model requires a very high local stress, typically higher than $10^4 MPa$, which seems difficult to reach even close to particle interface.

Thereafter, several authors [117–119] proposed an alternative cavity initiation mechanism. It is considered that intergranular particle-matrix interface fracture may occur when the interfacial stress reaches a critical fracture value, which is in order of few GPa. Then, grain boundary sliding, pile-ups and other mechanisms were proposed to be responsible for such high local stresses.

Harries [5], Riedel [51] and others [70, 111, 120] proposed that grain boundary sliding (GBS) may lead to high stress concentrations at triple points and second phase particles at grain boundaries. Based on the work of Sandström [70, 111], He [121] proposed two GBS models, the shear sliding model and the shear crack model. Their predictions agree well with experimental results. However, the GBS models could not explain that the smallest cavities are observed mostly on the grain boundaries parallel to the principal tensile stress and the largest along the grain boundaries perpendicular to the loading axis [74, 75]. Smith and Barnby [122] proposed that dislocation pile-ups against second phase particles induce high local stress concentrations. But the local stress is often overestimated by pile up theory [90]. And pile-ups are not often observed at particle-matrix interface, particularly in high temperature creep condition.

The calculations based on the previous mechanisms could not leads to local stresses reaching the interface critical fracture stress [51]. Therefore, the interface stress need to be calculated to verifier the interface fracture mechanism. Some existing models [44, 91, 102, 123] provide the calculation of stress fields in the vicinity of inclusions embedded in an plastically deformed matrix. However, few studies focus on the effect of the crystallographic orientations of neighbor grains and other microstructure features. That is why such effects of the random microstructure effect will be investigated in details in our study.

In this chapter, the creep properties, the second phases and the grain boundary cavitation in the 316L(N) austenitic stainless steel under study are experimentally investigated in section 2.2. Section 2.3 presents the meshes and constitutive laws used in the Finite Element computations. The input parameters are adjusted using experimental macroscopic creep curves at difference temperatures and stresses. In section 2.4, based on the experimental observations, the influence of

- random grain orientations,
- stress,
- temperature,
- angle between the grain boundary plane and the tensile axis on the interface stress fields

are investigated in details. Our results show that the interface stress distributions are stress and temperature independent, which agrees well with experimental observations. This may explain the weak dependence of cavity nucleation rate with stress and temperaturee.

Finally, in section 2.5, the interface critical fracture stress is estimated using the Universal Bonding Energy Relationship (UBER) and literature data for coherent and incoherent interface. Applying this critical fracture stress to interface stress distribution, it is found that cavity density increases linearly with the remote strain. This agree well with the well known Dyson law [74] and many experimental measurements [75, 76]. The prefactor of the Dyson law is, then, evaluated analytically and it is found to be in the same order as the experimental one [115].

3.2 Experimental background and results

3.2.1 Material under study

The creep tests are conducted on a 316L(N) stainless steel. Its chemical composition is given in Table 2.1. To avoid the heterogeneity of mechanical properties, the as-received material had been annealed at $1070°C$ for 20 min, and then followed by water quenching. This heat treatment leads to grain size of 15-30μm.

Elements	C	S	P	Si	Mn	Ni	Cr	Mo	N	B
wt.%	0.028	0.0001	0.028	0.31	1.88	12.67	17.31	2.44	0.077	0.0012

Table 3.1: Chemical composition of the studied 316L(N) stainless steel (in wt.%)

Young's modulus (E) is given as a function of temperature T ($°C$), as $E(MPa) = 201660 - 84.4 \cdot T(°C)$ with $20 \leq T(°C) \leq 700$ [44]. Under the temperatures of interest, $600°C$ and $650°C$, the values of Young's modulus are, respectively, $151GPa$ and $149GPa$. Poisson's ratio ν is equal to 0.3 [57, 124, 125].

3.2.2 Microscopic observations

The SEM-FEG-EBSD observations are carried out on longitudinal sections of the specimens located far away from the fracture surfaces. The microscopic observations are carried out on the specimens after a test at $600°C$, under $220MPa$ and fractured at $7148h$.

The thin foil samples are observed by the TKD (Transmission Kikuchi Diffraction, sometimes referred as t-EBSD) observations. The thin films are taken from longitudinal sections of the specimens. Then, they are polished into thin slices with thickness in the order of $100\mu m$. From the prepared slices, discs with the desired diameter are cut by using a disc cutter. The preparation is finished by the electrolytic polish with a solution of 70% Ethanol absolute, 20% 2-Butoxyethanol and 10% perchloric acid at $5°C$, $30V$ until a hole is produced in the center of each disc.

The microscopic observations on the same material [44] show that the cavities are generally located close to the second phase particles along grain boundaries. But, small cavities with critical cavity size (around $20nm$) [126] are difficult to be observed along the longitudinal sections of the fractured specimens. Following experimental observations, we infer that the cavitation is associated with second phase particles. This assumption agrees with several experimental observations concerning materials containing particles [127–129].

There are generally two types of second phase particles along grain boundaries, the $M_{23}C_6$ carbides and the σ phase particles [18, 20, 21, 24, 37, 130–133]. The crystallographic structure, the lattice constant and the chemical composition are different between the $M_{23}C_6$ carbide and the σ phase. However, the Cr, Fe, Mo and Ni elements are the main elements in the composition of both the $M_{23}C_6$ carbide and the σ phase. As a consequence, it is difficult to distinguish between $M_{23}C_6$ carbide and σ phase by using only SEM-FEG-EDX. Therefore, we use the TKD observations to identify the observed second phases.

Fig. 2.1 shows the $M_{23}C_6$ carbides and the σ phase particles located along grain boundaries. Observations show that the σ phase particles are much larger

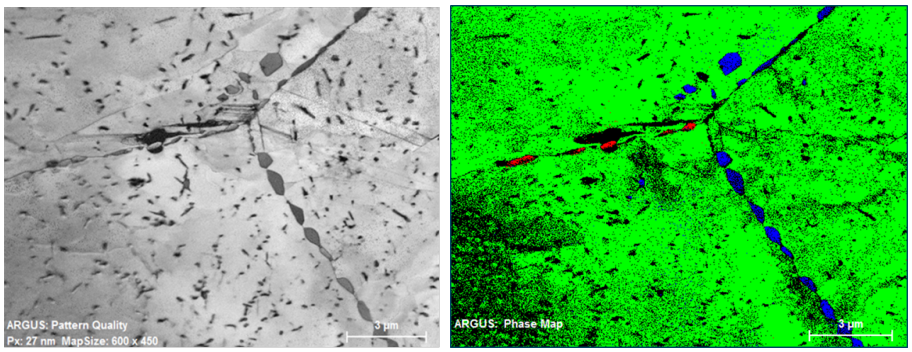

(a) (b)

Figure 3.1: (a) TKD pattern quality map of the thin foil; (b) TKD phase map with the austenitic matrix shown in green, $M_{23}C_6$ carbides in red and σ phase particles in blue. Creep test $600°C$, $220MPa$, $7148h$.

than the $M_{23}C_6$ carbides, which agrees with the observations of Kimura et al. [128] and Shin [134]. Based on the NIMS creep data sheets and our observations, it can be inferred that the creep cavities are generally located along the interfaces of the σ phase particles. It may be due to the size of σ phase particles which is larger than the $M_{23}C_6$ carbides, rather than weaker interfaces on the fracture point of view.

The time-temperature-precipitation (TTP) diagrams of long term aged 316 stainless steels [128, 135, 136] show that the $M_{23}C_6$ carbides are generally detected after only $100h$. And the σ phase appears after $1000h$ ($700°C$), or even $10000h$ ($600°C$). But, the σ phase appears earlier in the gauge portion than the head portion (or the aged specimens). This could explain that we observe that the size of σ phase particles is larger than the one of $M_{23}C_6$ carbides. And the cavity nucleation starts with the larger particles [117], this explains that the cavitation occurs on the interface of σ phases.

Recently, Bunett et al. [137] studied the creep cavitation in 316H steel. They observed that cavitation takes place into residual ferrite phase. But, according to our observations and others [20, 37, 130, 138, 139], the ferrite phase is generally observed as elongated bands. The cavitation could certainly appear in the ferrite bands. But, the size of such cavities is generally very small ($< 500nm$) and no coalescence is observed. So, this type of cavitation is not considered as playing an important role in damage evolution in this manuscript.

Thereafter, the interfacial stress fields are calculated to understand continuous nucleation and assessing of interface stresses may be high enough to induce fracture. We start with the creep curves predictions.

3.3 Macroscopic and crystalline constitutive laws

In this part, the creep curves are predicted using two different models, the isotropic creep flow rules and the polycrystalline modeling. These constitutive laws will be used to calculate the stress fields around inclusions, along grain boundary of a bicrystal (obey crystalline constitutive laws) embedded in a homogeneous matrix (obeys isotropic creep flow rules) (Fig. 2.5).

3.3.1 Macroscopic isotropic creep flow rules

The creep curves are firstly calculated using isotropic creep flow rules based on two well known creep laws: the Andrade law for the primary stage and the Norton law for the secondary stage [43].

The primary creep stains are calculated using Eq. 2.1. In this equation, $E_f^{vp}(t, \Sigma, T)$ is the creep deformation under a stress Σ (Pa) at the creep time t (s) and at temperature T $(^\circ C)$. The coefficients C_1, C_2, n_1 are independent of the stress Σ, but are a function of the temperature T, The time at the end of the primary creep is denoted as $t_{fp}(\Sigma)$. It is calculated by Eq. 2.2.

$$E_f^{vp}(t, \Sigma, T) = C_1 \cdot t^{C_2} \cdot \Sigma^{n_1} \tag{3.1}$$

$$t_{fp}(\Sigma) = C_3 \cdot \Sigma^{n_3} \tag{3.2}$$

At the end of the primary stage, the creep strain $E_{ffp}^{vp}(\Sigma)$ is calculated using the following equation:

$$E_{ffp}^{vp}(\Sigma) = C_1 \cdot t_{fp}^{C_2} \cdot \Sigma^{n_1} \tag{3.3}$$

The secondary stage begins after t_{fp}. The creep strain E_f^{vp} is calculated by the sum of primary strain, E_{ffp}^{vp}, and the secondary strain, $\dot{\varepsilon}_{min} \cdot (t - t_{fp})$, at time t:

$$E_f^{vp} = E_{ffp}^{vp} + \dot{\varepsilon}_{min} \cdot (t - t_{fp}) \tag{3.4}$$

The minimum strain rate, $\dot{\varepsilon}_{min}$, characterizes the secondary stage. The minimum strain rate is calculated by the Norton law, which is a phenomenological law (Eq. 2.5).

$$\dot{\varepsilon}_{min} = C \cdot \Sigma^n \tag{3.5}$$

The boundary conditions are set as shown in Fig. 2.2. Some of the displacement components at three summits of the vertexes are set to zero to block the six degrees of freedom (3 rotations and 3 translations), preventing any rigid body motion. The engineering stress, Σ^{eng}, is applied at the top and bottom surfaces shown in Fig. 2.2. These numerical calculations are obtained using a large strain and displacement finite element formulation

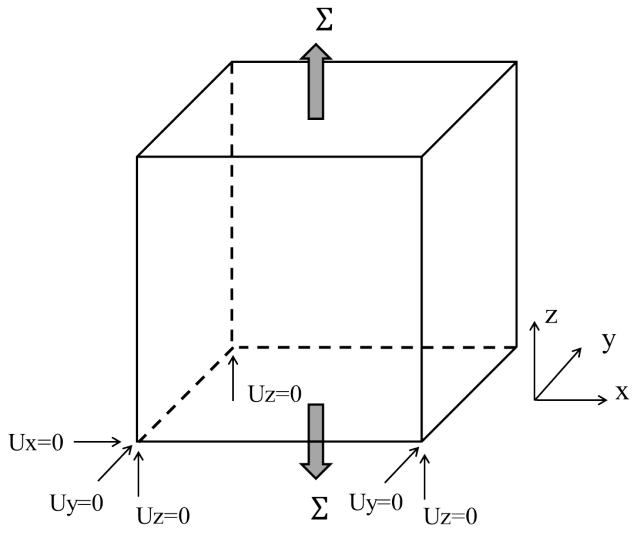

Figure 3.2: Boundary conditions, six degrees of freedom are blocked to avoid any rigid body motion.

For the 316L(N) stainless steel under study, parameters, $C_1, C_2, C_3, C, n_1, n_3$ and n are adjusted by Finite Element calculations. The adjusted parameters for different temperatures and tensile stresses are provided in Table 2.2.

Figs. 2.3a and 2.3b show the predicted engineering creep strain curves compared to the experimental ones. The results show that the creep curves are accurately predicted by the Andrade law and the Norton law with our adjusted parameters (Table 2.2). Even for the test at $600°C$, under $230MPa$, the secondary creep curve is not perfectly simulated, but the difference in minimum strain stress between the simulated and experimental results is only of 10%.

Temperature	C_1 $(Pa^{-n_1}s^{-C_2})$	C_2	C_3 $(Pa^{-n_2}s^{-1})$	C $(Pa^{-n}s^{-1})$	n_1	n_3	n
$600°C$ [44]	$6.23 \cdot 10^{-40}$	0.48	$1.53 \cdot 10^{84}$	$5.01 \cdot 10^{-84}$	4.13	-9.35	8.99
$650°C$	$2.70 \cdot 10^{-41}$	0.55	$8.39 \cdot 10^{71}$	$1.04 \cdot 10^{-73}$	4.37	-8.06	7.99

Table 3.2: Values of the parameters of the macroscopic creep laws of the 316L(N) steel at 600 and $650°C$ (Eqs. 2.1-2.5).

3.3.2 Crystal constitutive laws

3.3.2.1 Elasticity and visoplasticity laws

A crystalline elastoviscoplasticity law [140] devoted to the description of the crystal viscoplastic behavior of FCC steels is described in the present section.

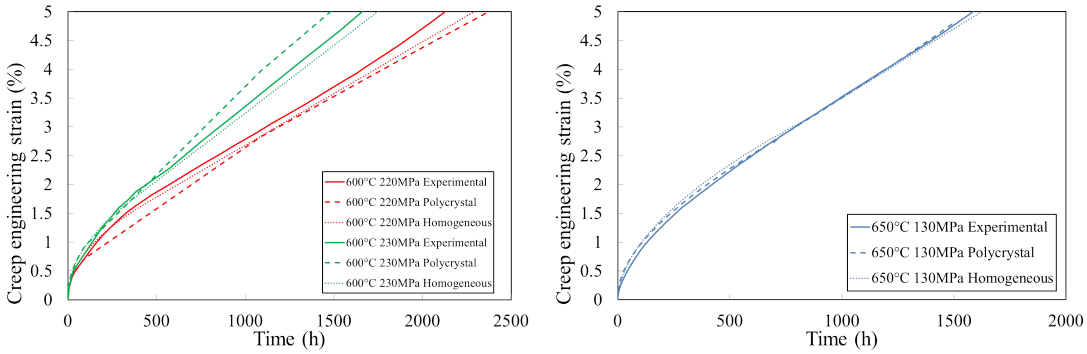

(a) (b)

Figure 3.3: Experimental and simulated creep curves (by polycrystalline model) of 316L(N) at (a) 600°C and (b) 650°C. The 'Homogeneous' label corresponds to the simulations carried out using isotropic creep laws (Eqs. 2.1 to 2.5), and the 'Polycrystal' label corresponds to the simulations carried out using the large scale aggregate (Fig. 2.4, Eq. 2.8).

The cubic elastic coefficients C_{11}, C_{12} and C_{44} were chosen as $222GPa$, $110GPa$ and $56GPa$ at 600°C, respectively [125].

This model considers a set of 12 $\{111\} < 110 >$ easy slip systems and are defined on each of them. Viscoplastic slips and dislocation densities are the main internal variables. No distinction is made between screw and edge dislocations. An identical thermally-activated flow rule affected to each slip system and a specific strain hardening relationship.

This model is implemented in the CAST3M Finite Element code in order to take into account lattice rotations that may be responsible for subsequent slip activation induced deformation.

When slip occurs on a slip system, the resolved shear stress τ^i on the slip system equals the contribution of two terms.

-The effective shear stress $\tau^i - \tau_c^i$ which corresponds to the value of the resolved shear stress necessary to overcome the lattice friction;

-The interaction of dislocations with precipitates which can be modeled by a critical shear stress τ_0

The slip glide on slip system i may be induced by the resolved shear stress τ^i which is applied on the slip system i and defined by.

$$\tau^i = \sigma : (\vec{m}^i \otimes \vec{n}^i) \tag{3.6}$$

where σ is the local stress tensor, $\vec{m}^i$ is the glide direction and $\vec{n}^i$ is the vector perpendicular to the slip plane.

Excessing the critical shear stress, τ_c, is required to activate plastic simplicity

slip. It is assumed to be the same for all 12 slip systems. Forest dislocations are indeed obstacles which can not be bypassed based on thermal activation. It is expressed as:

$$\tau_c = \tau_0 + \alpha\mu b\sqrt{\rho} \tag{3.7}$$

In Eq. 2.7, the Taylor factor, α is a constant equal to about 0.30 for FCC crystals [124]. The elasticity shear modulus, μ, equals $64GPa$ for 316L(N) at $600°C$. The burgers vector, b equals $2.56 \cdot 10^{-10}m$. And The total dislocation density is denoted as ρ. The initial critical shear stress, τ_0, is induced by soli solution effects, other obstacles than dislocations can be crossed by only thermal activation. The value of τ_0 is assumed to be very weak at high temperature [124, 141]. Solid solutions clusters and small matrix precipitates are assumed to be bypassed by thermal-activation.

The flow rule on a slip system is based on the thermally-activated glide of dislocations, through the small scale obstacles. The viscoplastic slip rate on slip system i is expressed by [140, 142]:

$$\begin{cases} \dot{\gamma}^i &= 2\nu_D b^2 \rho \exp(-\frac{Q}{k_b T}) \sinh(\frac{V}{k_b T}(\tau^i - \tau_c^i)) & \text{if} \quad \tau^i - \tau_c^i > 0 \\ \dot{\gamma}^i &= 0 & \text{if} \quad \tau^i - \tau_c^i \leq 0 \end{cases} \tag{3.8}$$

In Eq. 2.8, the Debye vibration frequency is denoted as ν_D, which is about $10^{13}s^{-1}$. The activation energy for dislocation motion, Q, equals $3eV$. This activation energy is close to the diffusion energies of carbon and nitrogen in the austenite [140]. The Boltzmann constant, k_b, equals $1.38 \cdot 10^{-23}J \cdot K^{-1}$. The activation volume, V, of dislocation glide by small obstacles will be adjusted in the following. This model has been applied to calculate the fatigue [141, 143–145], creep [80, 146, 147] and creep-relaxation [125] properties.

3.3.2.2 Adjustment of the Crystal Viscoplasticity Law Parameters

The previous part presents the crystal constitutive laws and values of most of the adopted parameter values. Only one of them, V, needs to be adjusted to predict the macroscopic creep curves as accurately as possible.

The polycrystalline aggregates, which grains are cubic, is used to adjust the value of V. The cubic polycrystalline aggregate contains 6^3 cubic grains with random crystallographic orientations. Each crystal contains 7^3 FEs (Fig. 2.4) to get stable predictions of the creep strain curves. Therefore, this polycrystalline aggregates is preferentially used for the identification of the activation volume.

Based on the measurements carried out on creep specimens of 304 stainless steel, Cuddy [148] proposed that between $704°C$ and $816°C$, the density is independent on temperature, but depends strongly on the tensile stress. The dislocation density increases during the primary stage, but can be considered as constant during the steady-state stage for each applied stress. Challenger and Moteff [149] have carried out creep tests and TEM observations to measure the

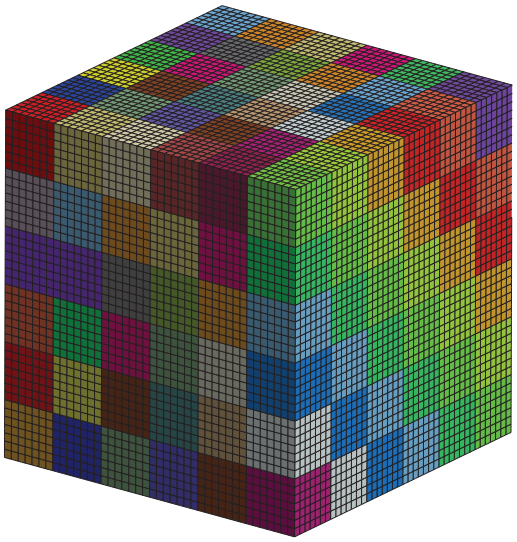

Figure 3.4: Polycrystalline aggregate containing 216 grains of random crystallographic orientations, the displayed colors of the different grains are independent of the random crystallographic orientations.

dislocation densities of 316 stainless steel under different creep conditions. Then, following their measurements, temperature has no effect on the dislocation density, we estimated that the dislocation density under $220MPa$ is $5.3 \cdot 10^{13} m^{-2}$, $5.8 \cdot 10^{13} m^{-2}$ under $230MPa$ and $1.81 \cdot 10^{13} m^{-2}$ under $130MPa$.

The adjusted value of the activation volume V should allow a reasonable agreement between the predicted macroscopic creep curves and the experimental ones at least up to few percents. At $600°C$, for $220MPa$ and $230MPa$, the adjustment of the V parameter leading to an activation volume equal to $120b^3$. The adjusted value amounts to $400b^3$ at $650°C$. Fig. 2.3a and 2.3b shows the predicted creep curves compared to the experimental ones. The adjusted activation volume is similar to the values found by Catalao ($\sim 100b^3$, $500-600°C$), and increases strongly for a higher temperature [146] (from Reference [143]). Further, the considered activation volume, may correspond to the interaction between the dislocation and the solid solution on one hand, and small matrix precipitates on the other hand [140].

3.4 Interfacial stress field calculations

Using the Finite Element simulation, the normal and shear stress fields along the interface of second phase particles are computed to quantify the influence of the microstructural heterogeneities. Most of the calculations correspond to a creep test applied on the 316L(N) steel, at $600°C$, and under $220MPa$. Stress and temperature effects are investigated in subsection 2.4.4.

In order to study the stress fields at interface of matrix and second phase, a quasi-2D (Fig. 2.5) stress plane analysis is carried out. The crystal elasto-viscoplasticity constitutive equations assigned to the two neighbor grains (green and cyan) are described in section 2.3.2. Two grains have independent random crystal orientations. And the homogeneous external matrix (blue) obeys the isotropic creep flow rules (Eqs. 2.1 and 2.5), with the parameters given in Table 2.2. No mesh refinement or computation time step affects the simulation results. The ratio of extern matrix size and the grain size was assumed amount to 7.5, to ensure that the size of the homogeneous matrix does not affect the interface stresses. An inclusion is located at grain boundaries parallel to the tensile axis. The inclusion shape factor is equal to three and the particle tip is assumed circular. The effect of grain boundary orientation with respect the tensile axis is investigated in details in subsection 2.4.5. Furthermore, for cavity nucleation to occur, a critical size of the second phase particle is often considered as necessary [44, 121, 134, 150]. That is why the largest second phase particles ($3\mu m$) observed in the grain of usual size $20\mu m$ are considered. Finally the size report between the inclusion and grain is then 3/20.

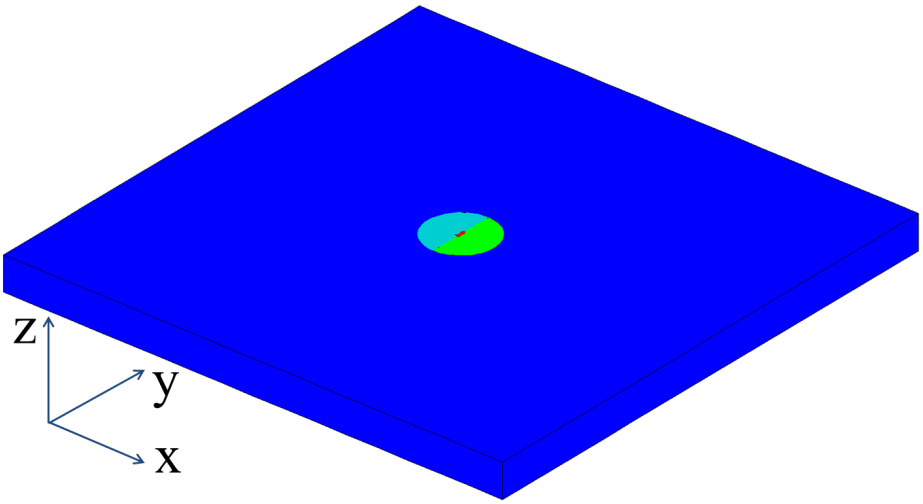

(a)

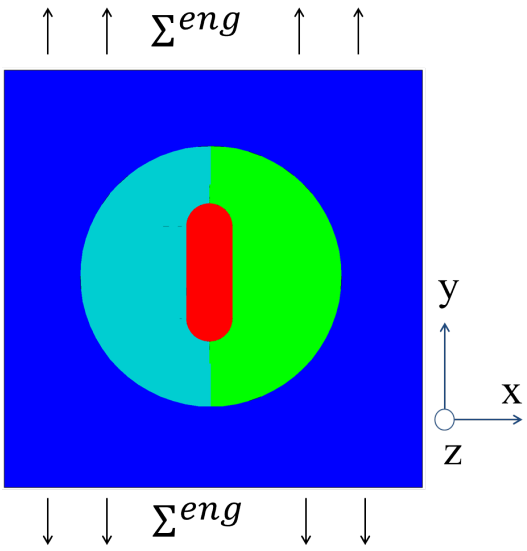

(b)

Figure 3.5: Quasi-2D mesh of the particle (red) located at a grain boundary, between two grains (green and cyan). The bicrystal is embedded in a homogeneous matrix (blue) a) large scale view; b) Zoom, note that the ratio between particle and grain size is largely increased.

3.4.1 Influence of the particle elasticity constants

As shown in section 2.2, two types of intergranular precipitates, $M_{23}C_6$ precipitates and σ phase particles are observed using various techniques, SEM-FEG-EBSD and TEM [18, 19, 44, 128]. The mechanical properties of both second phases are uneasy to be determined experimentally. DFT (Density Functional Theory) calculations were carried to study the properties of these second phases [22, 144, 151–153]. Some elasticity coefficients of the second phases of interest are given in Table 2.3.

Second phase	$E\ (GPa)$	Anisotropy factor	System	Reference
$M_{23}C_6$	282.3	1.02	$Cr_{23}C_6$	[151]
	348.4	0.93	$Cr_{23}C_6$	[152]
	343.2	1.01	$Cr_{11}Fe_{12}C_6$	
	336.2	1.06	$Cr_{23}C_6$	[144]
	315.2	1.13	$Fe_{23}C_6$	
Second phase	$B\ (GPa)$	$E^{(1)}\ (GPa)$	System	Reference
σ phase	217	260	$Fe-C$	[153]
	268	322	Fe_2Cr	[22]
	288	346	Fe_2Mo	
	238	286	Cr_2Fe	

$^{(1)}$ Calculated by $E = 3 \cdot (1 - 2\nu) \cdot B$, assuming $\nu = 0.3$.

Table 3.3: Values of Young's modulus (E) and Bulk modulus (B) for various $M_{23}C_6$ and σ phase particles provided by DFT calculations [22, 144, 151–153].

The $M_{23}C_6$ precipitates are shown to almost obey isotropic elasticity. From our knowledge, no information about the anisotropy of σ phase has been published. As the σ phases is tetragonal crystal system, it is probably elasticity anisotropy, which remains to be investigated. To investigate the influence of Young's Modulus, isotropic elasticity is considered. Further, by DFT calculations, Jiang [154] calculated the Poisson's ratio of $M_{23}C_6$ as 0.3, this value is used in our calculations. Taking into account values of Young's modulus varying from $100GPa$ to $400GPa$ (Table 2.3), the normal stress field along the interfaces between inclusion and the two grains are computed.

The results are plotted in Fig. 2.6b, which shows that the normal stress field is almost independent of the inclusion Young's modulus value. Our results agree well with the ones of Cui [44]. A Young's modulus value equals $350GPa$ is, then, used in the following subsections. Second, inclusions are assumed to obey still isotropic elasticity and Poisson's ratio ranges between 0.1 and 0.45. The interface stress fields are found to be once more independent of Poisson's ratio.

Therefore, our simulated interface stress fields are certainly representative of many different type of particles. Only the effect of cubic elastic remains to be investigated.

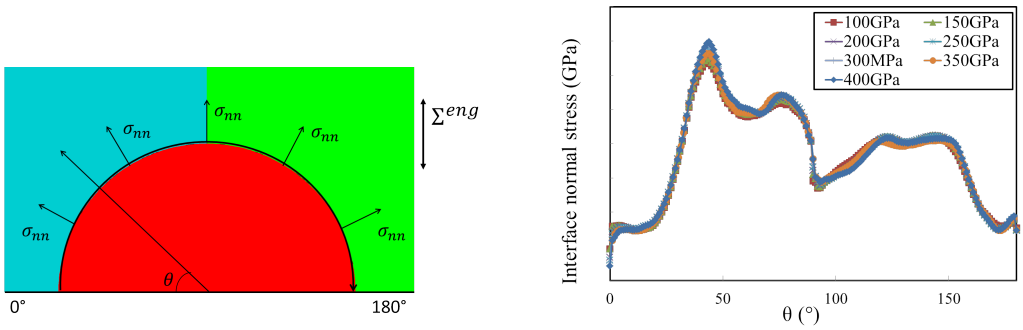

(a) (b)

Figure 3.6: Presentation of the normal stress along the interface in function of Young's modulus of the inclusion. a) sketch showing the normal stresses along the inclusion-grain interface, for the ϕ angle between 0° and 180°; b) Normal stress along the interface in function of θ for a macroscopic strain of $E^{vp} = 4\%$

3.4.2 Influence of the random orientations of the two neighbor grains

The normal stress fields at the interface between the inclusion and two surrounding grains are computed for a temperature of $600°C$ and under $220MPa$ (Fig. 2.5). The normal stress fields are obtained from thirty computations, using the same inclusion geometry (Fig. 2.5) and grain boundary parallel to tensile axis. Thirty sets of two random crystal orientations are selected for the two neighbor grains.

The normal stress field at each interface, $\sigma_{nn}(\theta)$ (Fig. 2.6a), computed from 30 sets of crystal orientations are plotted in function of θ in Fig. 2.7. The reference curve entitled 'Homogeneous' corresponds to the interface normal stress field computed for an inclusion embedded directly in the homogeneous matrix (which obeys the macroscopic isotropic creep flow rules, Eqs. 2.1 and 2.5).

The results obtained with the thirty sets of crystal orientations display a huge heterogeneity. The maximum interfacial normal stress, σ_{nn}^{max}, for the 30 sets are generally reached in the $45 - 130°$ range of variation of θ, except for set 3 and 25 (Fig. 2.7). However, in the 'Homogeneous' case, the stress distribution are smooth. And the maximum normal stress, σ_{nn}^{max}, are located at 60° and 120°, agree with Finite Element calculation results of [44, 155, 156]. Therefore, this heterogeneity is caused only by the crystalline orientations of the

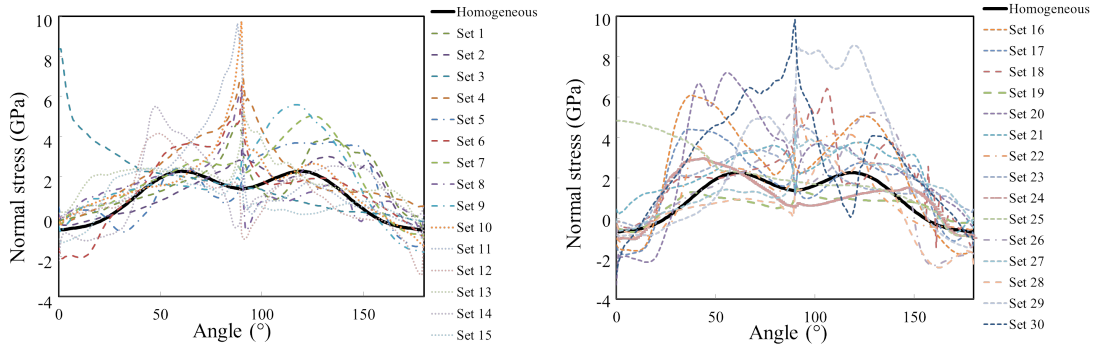

(a) (b)

Figure 3.7: Distributions of the normal stress along the interface between second phase particles and grains, plotted with respect to the θ angle (Fig. 2.6a). Thirty sets of random crystal orientations are taken into account. a) sets 1-15; b) sets 16-30. $T = 600°C$, $\sigma = 220MPa$, $E^{vp} = 4\%$.

two neighbor grains. A ratio characterizing the influence of the random crystallographic orientations, $r_{orient}(i)$, is deduced as the ratio between the maximum normal stress computed along the interface of an inclusion surrounded by two grains, $\sigma_{nn}^{max}(O_i^1, O_i^2)$, and embedded in the homogeneous matrix or two grains with crystalline orientations (O_i^1, O_i^2), $\sigma_{nn}^{max}(homogenous)$.

$$r_{orient}(i) = \frac{\sigma_{nn}^{max}(O_i^1, O_i^2)}{\sigma_{nn}^{max}(homogeneous)} \tag{3.9}$$

Considering the thirty sets of random orientations (i=1-30), the stress concentration ratio $r_{orient}(i)$ varies between 0.33 and 4.14, and the average ratio $\bar{r}_{orient}(i)$ amounts of 1.85. The values of $r_{orient}(i)$ may slightly changed in function of creep time or macroscopic strain, for a given set of orientations. However, the interval of $r_{orient}(i)$ and $\bar{r}_{orient}(i)$ remain almost constant.

Fig. 2.8 shows the cumulative probabilities of the maximum normal along the interface for fifteen and thirty sets of random crystal orientations. Surprisingly two normal stress distribution curves show very similar shape. The standard deviation for 30 sets is 1.66GPa, which is 1.74GPa for 15 sets. Therefore, a series of fifteen calculations accounting for sets of random orientations is large enough to provide a rather accurate distribution of the maximum normal stress. Fig. 2.8 shows also the distribution of maximum shear stress along each interface. The shear stress is almost ten times lower than the normal stress. Therefore, shear stress is expected to play a minor role in the cavity nucleation process.

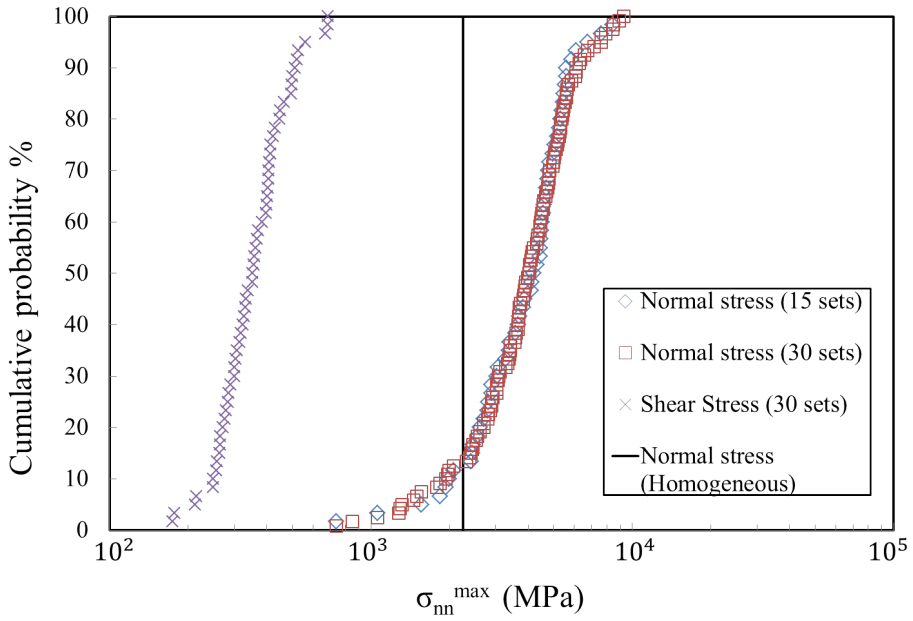

Figure 3.8: Cumulative probability curves of the maximum normal stress for fifteen and thirty couples of random orientations and of the maximum shear stress along the interface for thirty couples of random orientations $T = 600°C$, $\Sigma = 220MPa$, $E^{vp} = 4\%$.

3.4.3 Time evolution of the normal stress fields

Fig. 2.9 shows the evolution of the maximum normal stress, $\sigma_{nn}^{max}(O_1^i, O_2^i, E^{vp})$, along the interface between each inclusion and the surrounding grains, as a function of the macroscopic strain. The calculations are carried out for $600°C$, $220MPa$, for an inclusion with a shape factor equals three (mesh shown in 2.5). The results obtained for thirty couples of random crystallographic orientations are presented.

Fig. 2.9 shows that for some sets of orientations (set 1, 16...), a saturated stress is reached rather early. However, for other configurations (O_i^1, O_i^2), no significant saturation is observed. Stress relaxation is never observed.

The results show that, during creep deformation, the normal stresses computed in different microstructures reach the same value at different times (or strain levels). That could explain the continuous cavity nucleation largely reported in experimental literature.

In section 2.5, the one by one fracture of particle and neighbor grains interfaces during creep strain will be predicted based on interface normal stress evolution (Fig. 2.9) and a physically based evaluation of interface fracture stress

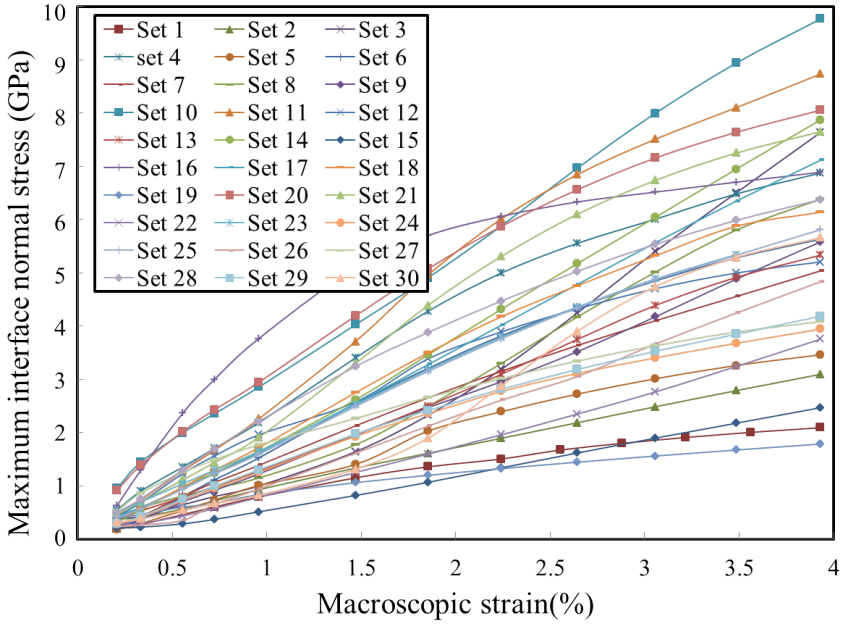

Figure 3.9: The evolution of the maximum normal stress along the interfaces of inclusions and two grains of different crystallographic orientations, depending on the macroscopic viscoplastic strain (30 sets of random crystalline orientations, Figs 2.5 and 2.6a).

3.4.4 Influence of temperature and remote stress

Based on the theory of thermally activated processes, Raj [81] found that the cavity nucleation rate, $\dot{N}_0$, increases exponentially with the increase of tensile stress ($\dot{N}_0 \propto exp(-\sigma^{-2})$). Nevertheless, the microscopic measurements [74, 76, 85, 157, 158] show that the cavity nucleation rate depends only on the strain rate for a given material, as showed bythe Dyson law ($(\dot{N}_0 \propto \dot{\varepsilon}_{min} \propto \sigma^n$, with n the exponent of the Norton law). To better understand temperature and applied stress effects, the calculations under $600°C/220$MPa, $600°C/230$MPa and $650°C/130$MPa are performed. The calculations for $600°C/230$MPa and $650°C/130$MPa are carried out with 15 couples of orientations, because the deduced distributions are shown to be statistically representative (Fig. 2.8).

Fig. 2.10 shows the distribution of maximum normal stress along interface for different temperatures and stresses. The results show that, at the same level of macroscopic strain, the maximum interfacial normal stress distribution is almost the same. We can conclude that the local interface stress evolution is almost independent on the applied stress and temperature, at least, at temperatures ranging from 600 to 650°, under 130-230MPa. This weak remote stress and temperature dependence may explained why the Dyson law prefactor, α', is weakly stress- and temperature-dependent, as shown in literature [115].

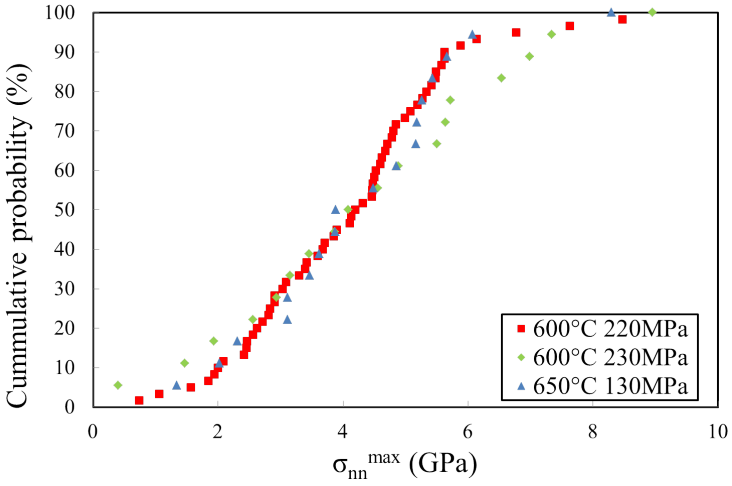

Figure 3.10: Distributions of the maximum normal stress computed along particle matrix interfaces for different temperatures and stresses for $E^{vp} = 4\%$. Each couple of T two neighbor grains have random crystalline orientations (Figs. 2.5 and 2.6a).

The previous calculations consider only grain boundaries parallel to the tensile axis. However, the second phase particles are located along all types grain boundary plans, inclined with respect to the tensile axis by an equiprobable angle $\alpha_{GB} \in [0°, 90°]$ [44].

3.4.5 Relationship between interface stresses and the orientation of each grain boundary with respect to the tensile axis.

The effect of the orientation of the grain boundary with respect to the tensile axis is investigated using similar Finite Element computations. The angle of the grain boundary with respect the tensile axis is denoted as: α_{GB} (Fig. 2.12a). Cui [44] investigated experimentally the number of the second phase particles in function of α_{GB}. In the temperature range from $600°C$ to $700°C$, the experimental measurements show that second phase particles are almost homogeneously distributed along all grain boundaries whatever the α_{GB} angle (Fig. 2.11) [44].

The calculations are carried out with α_{GB} equal to 0°, 15°, 30°, 45°, 60°, 75° and 90° (Fig. 2.12a), with $\alpha_{GB} = 0°$ corresponding to the grain boundary parallel to the tensile axis (Fig. 2.5b) and $\alpha_{GB} = 90°$ corresponding to the grain boundary perpendicular to the tensile axis. To have a large enough distribution of the set of grain orientations, the calculations are based on fifteen couples of random grain orientations, following results of section 2.4.2 (Fig. 2.8).

This grain boundary plane orientation effect is characterized by the ratio,

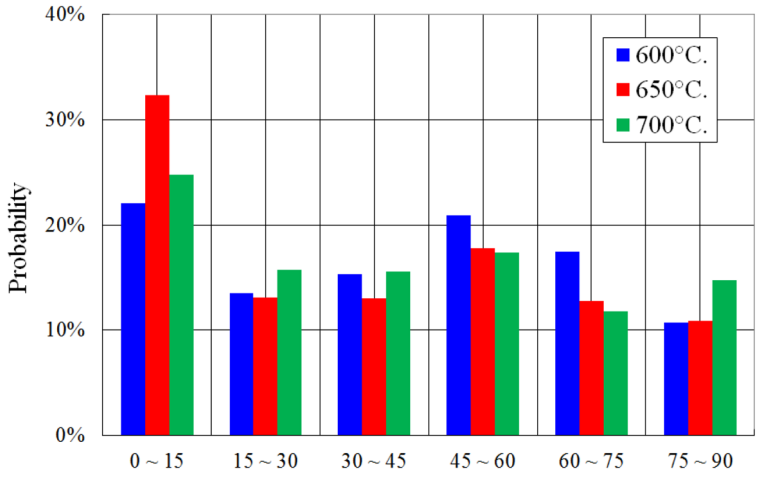

Figure 3.11: Probability of precipitates number for different grain boundary plane orientation with respect to the tensile axis [44] for 316L(N) steel at different temperatures. The microscopic measurements were carried out for creep fractured specimens. Corresponding creep tests are: $600°C$, 200MPa, 7148h; $650°C$, 130MPa, 7262h and $700°C$, 80MPa, 6756h.

$r_{GB}(\alpha_{GB}, O_i^1, O_i^2)$, of the maximum interface normal stress for a given α_{GB} angle, to the one with the grain boundary parallel to the tensile axis ($\alpha_{GB} = 0°$).

$$r_{GB}(\alpha_{GB}, O_i^1, O_i^2) = \frac{\sigma_{nn}^{max}(\alpha_{GB}, O_i^1, O_i^2)}{\sigma_{nn}^{max}(\alpha_{GB} = 0°, O_i^1, O_i^2)} \tag{3.10}$$

At a macroscopic strain of 4%, Fig. 2.12b shows that the average value of the ratio defined as, $\bar{r}_{GB}(\alpha_{GB}) =< r_{GB}(\alpha_{GB}, O_i^1, O_i^2) >_{\alpha_{GB}}$, decreases with the increase in the orientations of the grain boundary with respect to the tensile axis. The calculated maximum interface stresses are provides in Table B.1 (Appendix B). The plotted ranges of variation of the $\bar{r}_{GB}(\alpha_{GB})$ highlight the heterogeneity caused by fifteen sets of crystal orientations (shown by crosses). The average ratio computed for a grain boundary perpendicular to the tensile axis, $\bar{r}_{GB}(\alpha_{GB} = 90°)$, is equal to 0.57. This value is higher than the one found with Eshelby theory [155], which amounts is 0.46. And this value is lower than the one computed by Cui [44] for an inclusion embedded in homogeneous matrix. The calculations of Cui [44] show that the value of $r_{GB}(\alpha_{GB})$ amounts to 0.8, very close to our 'Homogeneous' evaluation (Fig. 2.12b).

It should be noticed that, even for a given set of crystalline orientations (O_i^1, O_i^2), the interface location where σ_{nn}^{max} is reached, changes in function of α_{GB}. There is a tendency that the location where σ_{nn}^{max} is reached, often on the side of the interface perpendicular to the tensile stress. For example, in case of $\alpha_{GB} = 0°$, σ_{nn}^{max} are generally obtained for θ close to 90° (Fig. 2.7). In case of $\alpha_{GB} = 90°$, σ_{nn}^{max} are mostly located for $\theta = 0$ or 180°.

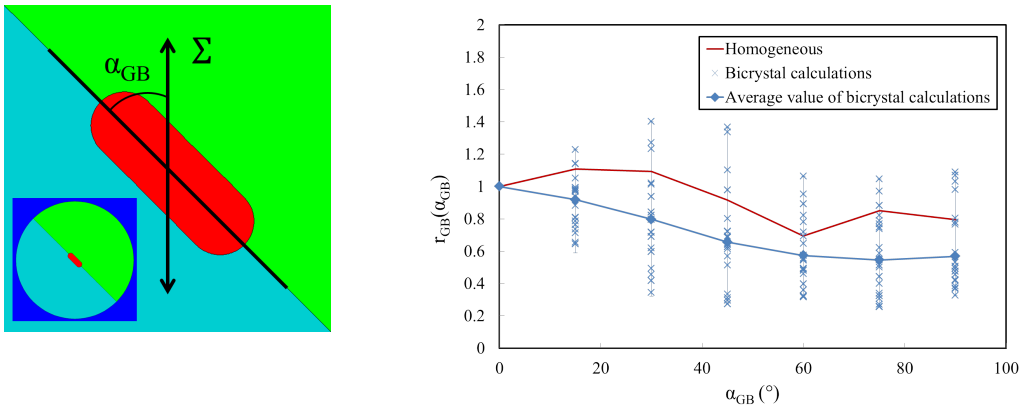

(a) (b)

Figure 3.12: a) Mesh of the inclusion (red) located at a grain boundary inclined by an angle α_{GB} with respect to the tensile axis; b) average value of $r_{GB}(\alpha_{GB})$ in function of α_{GB} for second phase particles surrounded by two grains, 15 different sets of different crystallographic orientations (blue) and for ones directly embedded in the homogeneous matrix (red), $E^{vp} = 4\%$.

3.5 Evaluation of the interface fracture evolution with the remote viscoplastic strain

3.5.1 The stress criterion

The cavity nucleation rate is now estimated using the previous interface normal stress distributions (section 2.4) and a stress criterion. The critical fracture stress is calculated by the Universal Bounding Energy Relationship (UBER, Eq. 2.11) developed by Rose et al. [159] and Rice and Wang [118]. This relationship was used by Rice and Wang [118] to predict grain boundary fracture. We apply this relationship by considering the fracture at the interface between a second phase particle and one metallic crystal:

$$\sigma_c = \frac{1}{e}\sqrt{\frac{(\gamma_{matrix} + \gamma_{second\ phase} - \gamma_{interface}) \cdot E_{interface}}{d_0}} \tag{3.11}$$

where γ_i is the free surface energy per unit area i ($i = matrix$ and $second\ phase$) and $\gamma_{interface}$ is the particle-matrix interface energy per unit area, $E_{interface}$ is Young's modulus of the interface considered as a 3D medium, and d_0 is the interface thickness.

Three types of particle-matrix interfaces are observed, as coherent, semi-coherent and incoherent interfaces. It is generally believed that the fracture of incoherent interface requires a lower stress compared to the coherent one, because of its high interface energy. The critical interface stress is now evaluated.

Several atomistic calculations [160–164] showed that the Young's modulus of general grain boundaries amounts to 70% of the one of the average polycrystal value. Further, the grain boundaries are typically incoherent interface. Therefore, the used value of interface Young's modulus is $E_{interface} = 70\% \cdot E_{metal} = 105GPa$. And the interface thickness is evaluated from High Resolution Transmission Electron Microscope (HRTEM) images on AISI 321 [165], AISI 304 [166] and AISI 316 [167, 168] stainless steels. The measurements show a value of the incoherent interface thickness as $1.5 \pm 0.5nm$ (Fig. 2.13).

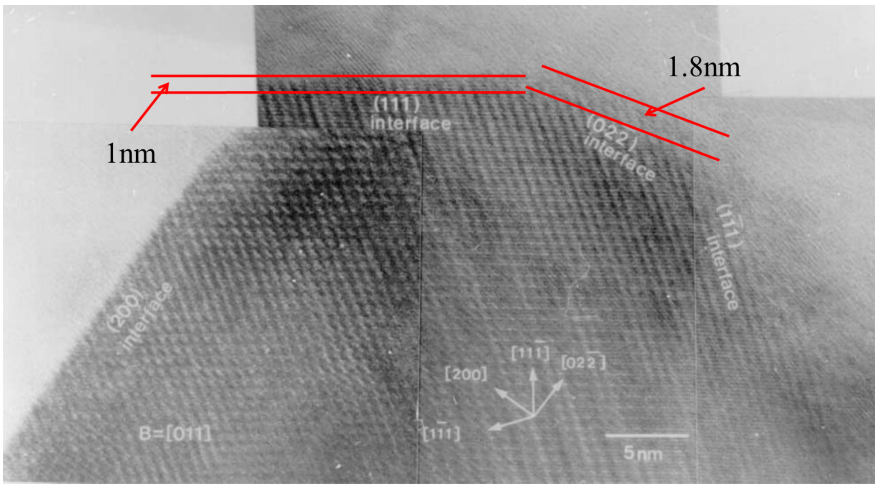

Figure 3.13: HR-TEM micrograph showing the combination of the incoherent interface of carbide and AISI 304 steel [17].

$\gamma_{matrix}\ J/m^2$		$\gamma_{interface}\ J/m^2$	
Fe-fcc	2.077-3.095 [162]	$Cr_{23}C_6$/Fe-fcc coherent	1 [169]
Fe-fcc	2.24-3.34 [170]	$Cr_{23}C_6$/Fe-fcc coherent	0.8 [171]
Fe-fcc	1.9 [172]	$Cr_{23}C_6$/Fe-fcc Incoherent	1.68-2.50 [170]
304	2.059-2.912 [162]		
316	2.09-2.25 [173]		

Table 3.4: Metal surface energies and particle-matrix interface energies

DFT calculations and the experimental measurements reported in literature were carried out to estimate the values of the energies of metal surfaces, second phase surfaces and interfaces. Some DFT and experimental results are shown in Table 2.4. Based on Table 2.4, the values used for evaluating the interface critical fracture stress, belong the following range: $\gamma_{metal} = 2 - 2.5J/m^2$ [162, 172, 173], $\gamma_{second\ phase} = 2 - 2.5J/m^2$ [171], $\gamma_{interface} = 1.5 - 2J/m^2$ (incoherent interface) [174] and $\gamma_{interface} = 0.1 - 0.2J/m^2$ (coherent interface) [175].

These parameter variations lead to a incoherent interface fracture stress of $5 \pm 1GPa$. Even taking the interface Young's modulus as the metal one, the difference in σ_c is only 20%, which is included in the variation range of σ_c. The critical fracture stress for coherent interfaces may reach $15GPa$. Such a high value is not reached as shown in Fig. 2.9. This result agree well with observations showing that cavities appear generally along the incoherent interface [175, 176]. Further, DFT calculations [162, 171] show that the interface energies depend strongly on the coherency but so much on the two considered materials. Therefore, this interface fracture stress value is adopted for both $M_{23}C_6$ and σ phase. That point will be discussed in details in Chapter 4

3.5.2 First prediction of cavity nucleation rate

Cavity nucleation is assumed to occur when the interface normal stress (Fig. 2.9) reaches the critical fracture stress. The criterion is fulfilled at different remote strain levels depending on the local microstructure (Fig. 2.5).

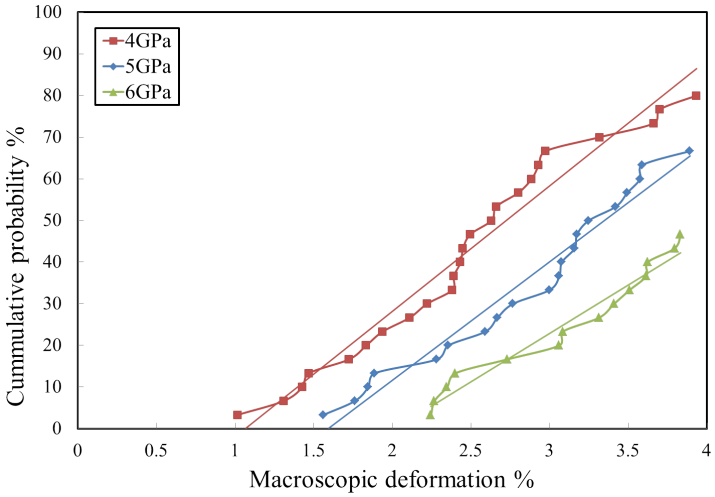

Figure 3.14: Calculated cumulative probability of fractured interfaces versus macroscopic creep strain. Only grain boundary plans parallel to the tensile axis is considered.

Fig. 2.14 shows that the probability of interface fracture increases linearly with creep remote strain. This linear dependence agrees well with the Dyson law [74]. The phenomenological is based on numerous microscopic observations in high-purity Cr-Mo-V steels [83], Nimonic 80A [74], 347 stainless steel [177], Astroloy [75, 76] and Alloy 617 [157]. Similar calculations have been carried out for different temperatures and stresses, which lead to a similar linear dependence.

The normal stresses acting on grain boundaries is only twice of the tensile stress [80]. This value is much lower than the precipitate-matrix interface one. Nevertheless, opening of grain boundary requires a stress in order of few GPa

[178]. The inclusion axial stress is much lower than the interface normal stress (3.5.2 in Chapter 3). However, the precipitate fracture requires very high inclusion axial stress ($> 10GPa$) [171]. Therefore, cavity nucleate by precipitate fracture is negligible.

However, the precipitate-matrix interface fracture criterion is fulfilled. Therefore, intergranular second phase particles are preferential cavity nucleation sites during creep deformation. Then, the combination of the density of second phase particles and our calculation results (Fig. 2.14) leads us to evaluate the prefactor of the Dyson law, α'. The Dyson law prefactor can be calculated as follows:

$$\alpha' = \frac{N_a(E^{vp})}{E^{vp} - E_c^{vp}} \tag{3.12}$$

where the $N_a(E^{vp})$ is the number of cavities per unit grain boundary area at the remote strain E^{vp}. The critical remote strain E_c^{vp}, allowing cavity nucleation to occur, corresponds to the left end of cumulative probability curves. The numerical application of Eq. 2.12 will be carried out later.

our calculations show a critical cavity nucleation strain, E_c^{vp}, of 1.5% for $\sigma_c = 5GPa$ (Fig. 2.14).

And, Fig. 2.15a highlights a value of E_c^{vp} amounts to 0.2%, the experimental measurement of Shiozawa and Weerteman [75] showed a similar value. However, the material studied by Capano et al. [76] is a Nickel-based superalloy, it may lead to some differences. For a 347 steel, the experimental measurement of Needham and Gladman [177] showed that the value of E_c^{vp} ranges between 0-8%, in function of temperature and the remote stress. However, Laha et al. [179] observed that the critical cavity nucleation strain amounts to 0.1% for a series of 347 steels. It is then difficult to draw the final conclusion. Moreover, a microscopic observation of creep test (316L(N)) stopped at 1% did not show intergranular cavities (CEA/SRMA). This leads to a E_c^{vp} higher than 1%, agrees well with our computations.

Further, as shown in Fig. 2.14, the value of E_c^{vp} depends strongly on the interface fracture stress. However, the used value of σ_c is only evaluated with UBER, which may overestimated. Because the used surface and interface energy were calculated at 0K, which may decrease at high temperature.

It should be noticed that the previous estimations of the cavity nucleation rate do not take into account the effect of the grain boundary orientation with respect the tensile axis, α_{GB}. However, the observations of Shiozawa and Weertman [75] (Fig. 2.15b), show that cavities could nucleate not only along the grain boundaries parallel to tensile stress, but along all types of grain boundaries. This may leads to a more reliable theoretical estimation of the Dyson law prefactor, α' accounting for α_{GB}.

Then, the cavity nucleation rate is reevaluated using the calculation results of the maximum interface normal stress with accounting for the random orientation of grain boundaries with respect to the tensile axis. The results show that takeing

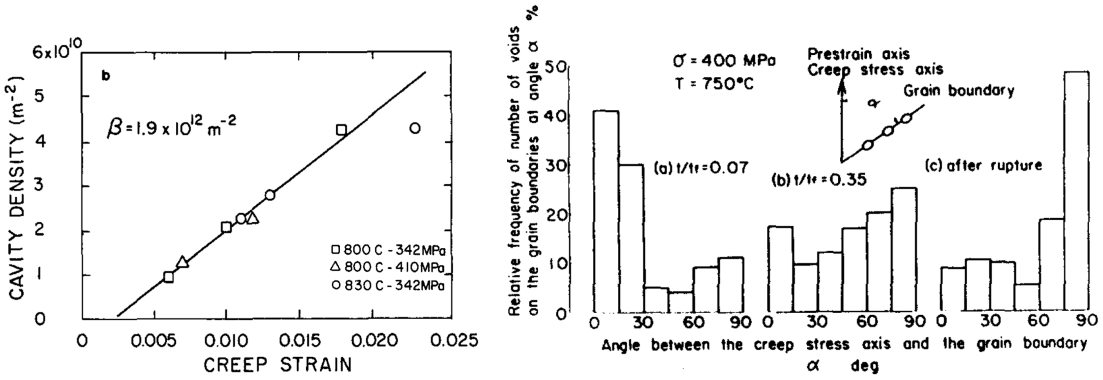

(a) (b)

Figure 3.15: a) Cavity versus creep strain in a nickel-based superalloy, Astroloy [76]; b) relative frequency of the number of cavities located along the grain boundaries inclined by an angle α_{GB}, another Astroloy batch [75].

into account the effect of α_{GB}, the cavity nucleation rate is almost constant, as shown in Fig. 2.16a. The cavity nucleation rate in this part is clearly lower than the previous one, by a factor of 2. It should be noticed that, the value of E_c^{vp} remains the same value of the one evaluated accounting only grain boundaries parallel the to tensile axis.

Moreover, the cavitation distribution in function of α_{GB} is presented in Fig. 2.16b. The results show that the cavitation occurs preferentially on the grain boundaries parallel to the tensile axis. And the relative frequency decreases in function of α_{GB} up to 75°. A small increase appear for $\alpha_{GB} = 90°$, corresponding to the grain boundary is perpendicular to the tensile axis. Fig. 2.16b agrees fairly well the qualitative observation of Dyson [74] and the quantitative experimental measurements of Shiozawa and Weertman [75] (Fig. 2.15b). It should be noticed that, only the experimental measurements carried out at the beginning of creep, $t/t_f = 0.07$ of Fig. 2.15b, should be taken into account, because only the cavity nucleation process is simulated here. For the high strain level or longer creep time, the cavity growth phenomenon should be taken into account.

The numerical application of Eq. 2.12 to evaluate the value of α' is now carried out. The cavity density per unit grain boundary area at the remote strain, E^{vp}, is used to calculate the value of α' (Eq. 2.12). This cavity density could be deduced by the multiplication of the calculated probability of fractured interface at the remote strain E^{vp}, $P(E^{vp})$, where $P(E^{vp} < E_c^{vp}) = 0$. And the intergranular particle density per unit grain boundary area N_0^{max} , as:

$$N_a(E^{vp}) = P(E^{vp}) \cdot N_0^{max} \tag{3.13}$$

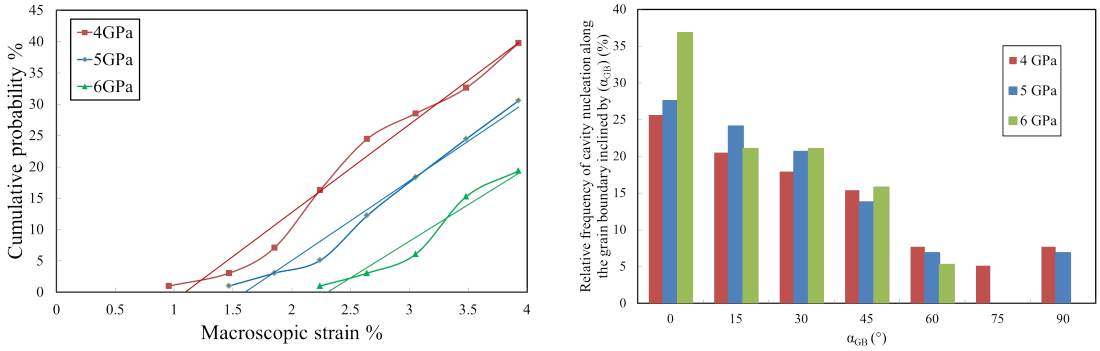

(a) (b)

Figure 3.16: a) Calculated cumulative probability of fractured interfaces versus creep strain accounting for equiprobable inclined grain boundaries ($\alpha_{GB} \in [0°, 90°]$); b) relative frequency of cavitation in function of α_{GB}, considering all grain boundary orientation as equiprobable, $E^{vp} = 4\%$.

N_0^{max} could be evaluated by:

$$N_0^{max} = \frac{d_g \cdot \rho_p}{\pi \cdot d_p} \tag{3.14}$$

where ρ_b is particle density per unit polished surface, d_p is harmonic mean of particle diameters , and d_g is the grain size measured by intercept line method. At $600°C$ under a stress of 220MPa, the experimental measurements of Cui [44] provide the following values: $\rho_b = 9.3 \cdot 10^9 m^{-2}$, $d_p = 2\mu m$ and $d_g = 37.5\mu m$. The density of second phase particles per unit surface of grain boundary is then deduced as $6.85 \cdot 10^{11}\ m^{-2}$.

Considering only inclusion along grain boundaries parallel to tensile stress, the value of α' could be evaluated using Fig. 2.9 and the measured second phase particle density. A value of the Dyson coefficient [74], α', of $1.3 \cdot 10^{13} m^{-2}$ is found. This value is much higher than the measured one, $4.6 \cdot 10^9 m^{-2}$ [44].

However, following our EBSD observations and the observations of NIMS (National Institute for Materials Science) [2], cavitation is most often observed at the interfaces of the σ phase particles and grain boundaries. Many authors [117, 180] proposed that cavitation occurs preferentially at the largest second phase particles compared to the small ones. Our observations indeed show that the σ phase particles sizes are generally larger than $1\mu m$ (Fig. 2.1) and the size of $M_{23}C_6$ particles is lower than $500nm$. This observation results agree well with literature [2, 17, 23, 37, 41, 119, 133, 135, 181, 182] (shown in Table 2.5). It should be noticed that the observations of aged specimens were carried out at different ageing duration, the ageing durations do not be presented in Table 2.5. Further, the NIMS data sheets [2, 183] are summarized from different creep loading conditions, which is not presented here.

Material	Condition	$M_{23}C_6$ (μm)	σ phase (μm)	Reference
316L	Creep $550°C$ 150MPa, 85 000h		≈ 2	[37]
316	Creep $550°C$ 245MPa, 8 300h	$\leqslant 0.3$		[41]
316	Creep $568°C$ in-service		$\geqslant 2$	[133]
316H TB	Creep	$\leqslant 0.25$	2-15	[2]
316-HP	Creep	$\leqslant 0.5$	$\geqslant 1$	[183]
316	Creep-fatigue $4 \cdot 10^{-3} s^{-1}$, $\pm 2\%$, $10 min$	$\leqslant 1$		[17]
316	Aged $685°C$		6	[135]
316	Aged $710°C$	$\leqslant 0.3$	2-5	[181]
304L	Aged $720°C$	$\leqslant 0.5$	$\geqslant 2$	[182]
304H	Aged $650°C$,	$\leqslant 0.5$	$\geqslant 4$	[119]

Table 3.5: Intergranular $M_{23}C_6$ and σ phase particle size measured form images plotted in literature [2, 17, 23, 37, 41, 119, 131, 133, 135, 181, 182].

Thereafter, it can be concluded that the size of the σ_{phase} particles is much larger than the $M_{23}C_6$ carbide one. This could explain that the cavitation occurs specifically along the interface of σ phase particles [2, 37]. However, the experimental studies of [44] did not distinguish the $M_{23}C_6$ and σ phase particles.

The cavity nucleation should be evaluated using the density of σ phase particle. The NIMS data sheet [2] show that the saturated number of σ phase per grain boundary unit surface amounts to $1.2 \cdot 10^9 m^{-2}$ in the specimen gauge portion. Using the σ phase particle density value, The Dyson law prefactor, α', is estimated to be $2.3 \cdot 10^{10} m^{-2}$, which is still five times higher than the measured value.

Thereafter, the Dyson law prefactor , α', is reevaluated taking into account the second phase particles are located along all types grain boundary plans, inclined with respect to the tensile axis by the equiprobable angle $\alpha_{GB} \in [0°, 90°]$. The value of , α', is obtained as $1.2 \cdot 10^{10} m^{-2}$, which is only 2.5 times higher than the measured value.

As shown in subsection 2.4.3, the interface stress distribution is almost independent on applied stress and temperature (Fig. 2.10). This leads to a predict α' value independent on the creep conditions, provided the density of large particles does not change much with the creep condition (long term creep). This result agrees well with quantitative measurement carried out by Capano et al. [76]. Under different temperature and stress, the cavity density increases linearly with the creep strain and the slop is almost stress and temperature independent (Fig. 2.15a).

It should be noticed that the NIMS creep data sheet [2] shows that the size and number of σ phase particle increase in function of time. This is not taken into account in the evaluation of the α' coefficient.

3.6 Discussion

Intergranular cavitation is the dominant damage mechanism for long term creep. However, the cavity nucleation mechanism has not been well established yet. Both interface fracture and thermally-activated vacancy clusters may be proposed in alloys with intergranular second phase particles. Different stress concentrations have been proposed, such as the interaction of grain boundary sliding and intergranular precipitate.

Our predictions based on the calculation results are therefore discussed with respect to both experimental observations and measurements and other modeling results.

3.6.1 Local interfacial stress

In high purity metals without second phase particles, such as 99% Al [184], creep cavities appear at grain boundaries and triple points. In alloys containing second phase particles, cavities generally appear at the interfaces of the particles located along grain boundaries [44, 51, 80, 81, 117, 121, 128, 134, 150]. We focus here on the second type of materials.

Several models [91, 155, 185, 186] were proposed based on the Eshelby inclusion theory to calculate the interfacial stresses. Using the thermo-elastic framework, an elastic elastic ellipsoidal inclusion is embedded in a homogeneous matrix. The matrix is homogeneously plastic deformed. That implies that the stress tensor is homogeneous inside the inclusion. However, these models do not take into account the heterogeneous deformation caused by the random crystallographic orientations of the two neighbor grains (Fig. 2.5). Generally, these thermo-elastic models predict that the average inclusion stress increases linearly with the macroscopic strain. Therefore, the normal stress at the inclusion tip calculated by the Eshelby theory is much higher than our value calculated by the FE method in the case of an inclusion embedded in a macroscopic matrix (Table 3.1 in Chapter 3).

Based on the use of crystal viscoplasticity, our computations take into account the effect of the random crystal orientations. This approach leads us to calculate a more statistical distribution of local interfacial stresses with effect of the crystallographic orientations.

High resolution measurement of local stress is a challenging task. Recently, Karamched and Wilkinson [187] measured the local elastic strains by HR-EBSD. Then, Finite Element simulations used the microstructure were carried out. A

monotonic tensile test weas carried out in the Ni-based alloy. The measurement and calculations for a carbide embedded in the matrix show that the stress could reach $1.5GPa$. This value is lower than our simulation ones. In fact, the measurement step size of 250nm is used the work of Karamched and Wilkinson. However, our calculations show that the maximum interface stresses may be located along an interface length in order of 100nm, considering a particle size as $2\mu m$ (Fig. 2.7). And our calculations concern an intergranular inclusion, whereas the one considered in [187] is intragranular.

3.6.2 The fracture criterion

It is generally believed that fracture can be predicted if two criteria are fulfilled the stress criterion and the energy criterion.

Pineau and Pardoen [117] published values of critical stresses in different materials from experimental results and modeling results. The interfacial fracture stress for particle decohesion are reported, as $1650MPa$ for Fe_3C in 1045 steel and $1820MPa$ TiC in Maraging steel. The critical stresses proposed are lower than the one evaluated by UBER (as $5GPa$). Further, the critical stress is generally dependent on the materials, the interface structure, the segregation, etc.

The interface fracture stress used previously is evaluated by the Universal Bounding Energy Relationship. This critical interface stress depends on fracture energy, interface thickness and interface Young's modulus. Recently, Barbé et al. [170] confirmed the validation of this relationship by DFT simulations of a complete tensile test carried out ip to interface fracture.

The surface energies used in the application of the UBER relationship were evaluated by DFT calculations, for which the temperature is generally considered as 0K. Nevertheless, the creep tests are generally carried out at temperatures higher than $0.4T_m$ (T_m is the temperature at melting point). The surface energies and elasticity constants decrease with temperature increase. This effect has not been incorporated here, because few studies focus on the surface energy variation with temperature. The decrease in surface energy may decrease the critical fracture stress. Nevertheless, our results show that the variation in σ_c influences slightly the prefactor of the Dyson law (Fig. 2.14). However, the decrease in σ_c may decrease critical remote stress to cavity nucleation. The estimated critical cavitation remote strain is $E_c^{vp} = 1\%$ for $\sigma_c = 4GPa$ and almost 2% for $\sigma_c = 6GPa$. It should be finally noticed that temperature effects on surface energies are usually considered as the temperature lower than T_m.

Several models [180, 188] derived from the energy criterion have a precipitate size effect. The energy criterion is not taken into account for this chapter. However, the size effect may be avoided because we consider only the σ phase particles, which are much lager than $M_{23}C_6$ particles. Therefore, to calculate the cavity nucleation rate, only the distribution of σ phase particles is used. Incor-

porating cohesive zone modeling is suggested to predict interface fracture using similar crystal viscoplastic FE computations. The precipitate size effect could be directly investigated and incorporated in the evaluation of α'.

3.6.3 Evaluation of the Dyson law prefactor

He and Sandstöm [114] proposed a cavity nucleation rate model based on grain boundary sliding. They assumed that cavity nucleate at the sites where the subboundaries with the second phase particles. Their predictions agree well with experimental measurements and predict also a Dyson type cavity nucleation law.

However, grain boundary sliding theory predicts often that cavitation occurs preferentially along the grain boundaries inclined by equals 45° with respect to the tensile axis. This is in contradictories with microscopic observations (Fig. 2.15b) [75]. Further, this model could not explain that cavity nucleation occurs mainly along grain boundaries parallel to the tensile axis (Fig. 2.15b). These trends are well predicted by our FE results.

Similarly to us, Neimitz and Janus [123] calculated the interfacial stresses around inclusions embedded in a homogeneous matrix. Different inclusion shapes were considered. The obtained stress values are similar to our results. However, it is difficult to get the cavity nucleation rate or a distribution of cavities from their calculations takes into account only the homogeneous matrix. Further, this may be the main reason for which the Dyson law can not be derived on a straight forward way from FE computations. The predicted continuous nucleation is, in fact, mainly based on the randomness of the local microstructure, particularly the crystal orientation of the two neighbor grains.

It is generally believed that cavities need to reach a critical size to continue to grow [189, 190]. This effect has not been investigated in present chapter. It seems probable that cavities appeared along the grain boundaries parallel to the tensile axis could hardly grow by intergranular diffusion of vacancies because the normal stress acting on grain boundary is low [80]. This is perhaps the main reason that our predicted Dyson law prefactor, α', is much higher than the experimental one. This effect will be studied in Chapter 4.

3.7 Conclusion

The SEM observations of the polished longitudinal sections of the creep samples show that the creep cavities nucleate at the interfaces of the second phase particles located along grain boundaries. The TKD observations show two types of intergranular second phase particles, $M_{23}C_6$ precipitates and σ phase particles. Cavity nucleation seems to occur mostly along the interfaces between grains and σ phase particles.

Finite Element calculations are performed to predict the distribution of matrix-particle interface stress. Ellipse-like inclusions are located along grain boundaries separating two metallic crystals. These bicrystals are embedded in a macroscopic matrix, which behavior mimics the whole polycrystal one. Thirty couples of crystal orientations are randomly chosen assuming no texture. Ellipse-like inclusion obeys isotropic elasticity. The crystals obeys crystalline constitutive laws. And the homogeneous matrix, which obeys isotropic creep flow laws. The activation volume introduced in the crystal viscoplasticity flow law is adjusted using experimental macroscopic creep curves.

For inclusion located along grain boundaries parallel to the tensile axis, the computed interface normal stress distribution shows a huge variability caused by the randomness of the couples of crystal orientations. The calculated interface normal stresses could be forty times higher than the remote tensile stress at a macroscopic strain of 4%. And these computations provide an average stress concentration factor of 1.85 compared to the configuration of an inclusion embedded directly in the homogeneous isotropic matrix. This last configuration leads to a concentration factor of 8 with respect to the remote stress.

Our calculations show that the interfacial stress distributions are almost stress and temperature independent. They depend only on the macroscopic strain, at least for temperatures ranging from 600 to 650°C and applied stresses ranging from 130 to 230MPa.

The coupling between our calculated interface normal stress distributions and the application a fracture stress criterion using a physically based critical stress value, shows that the number of cavities increases linearly with the remote creep strain in agreement with many experimental data reported in literature.

Thereafter, additional calculations are performed taking into account the effect of the angle of each grain boundary with respect to the tensile axis, α_{GB}. These results show that the average stress ratio, $\bar{r}_{GB}(\alpha_{GB})$, decreases with increase in α_{GB} up to 75°. Then, a slight increase in interface normal stress is obtained for $\alpha_{GB} = 90°$. Further, the cavity density still increase linearly with the remote strain. This effect leads to a decrease in the predicted in Dyson law prefactor.

Accounting for measured densities of the large σ phase particles, the predicted value amounts to $1.2 \cdot 10^{10} m^{-2}$, which is only two times higher than the experimental one. Further, the relative frequency of cavitation in function of the angle α_{GB} is well predicted with respect to several published observations, showing that the grain boundaries are the most affected by cavity nucleation, followed by grain boundary perpendicular to the tensile axis.

Finally, our evaluation provides a physical explanation of the well-known Dyson law. Further, the evaluated Dyson law prefactor is almost stress- and temperature-independent provided that the density of large particles tend to fracture is constant. And a critical remote strain is predicted in agreement with observations.

Finally, it should be noticed that more accurate large particle densities depending on stress, time and temperature may introduced, if available. And the particle size effect taken into account more precisely as shown in Chapter 4. Before statistical information about the particle aspect ratio and tip geometry are now introduced in Chapter 3 to evaluate their effects on interface stress, distribution and predicted cavity nucleation rate.

Chapter 4

Effect of the particle geometry on interface stress

In the previous chapter, Crystal Plasticity Finite Element computations highlight a strong heterogeneity in the interface stresses caused by the random crystallographic orientations of the two neighbor metallic crystals and the random orientation of the grain boundary with respect to the tensile axis. These calculations concern only one precipitate geometry, with an aspect ratio of three and circular tips. Nevertheless, various inclusion shapes and tip geometries are observed experimentally by SEM and TEM.

In this chapter, a similar approach is applied to compute the stress fields around second phase particles still located along grain boundaries, but accounting for new microstructure parameters. The calculations take into account various particle features, such as shape factor and symmetric/asymmetric tip geometries, based on our experimental observations. Accounting for the observed ranges of variation of these particle parameters, even higher normal interface stresses are reached. Finally, a simplified multiplication formula is proposed to calculate the statistical distribution of the maximum interfacial normal stress accounting for various statistical data characterizing the microstructure observed under creep conditions.

Finally, the assumptions used in the Finite Element calculations are discussed in order to evaluate the effect of the adopted hypotheses (lattice rotations, 3D/2D effects).

4.1 Experimental observations

The time-temperature-precipitation (TTP) diagrams of long term aged 316 stainless steels [128, 135, 136] show that the $M_{23}C_6$ carbides are generally detected after only $100h$. And the σ phase appears after $1000h$ ($750°C$), even $10000h$ ($650°C$). But, the σ phase appears earlier in the gauge portion than in the head portion (or in the purely aged specimens). In addition, the average size of σ phase particles are much higher than the one of $M_{23}C_6$ carbides (Table 2.5 in Chapter 2). And the cavity nucleation was shown to occur firstly at the large σ phase particles [2, 133].

Cui [44] carried out experimental observations and measurements on the 316L(N) under study. Fig. 3.1 shows the cumulative probability curves of shape factor and the equivalent radius of all intergranular second phase particles, which diameter is larger than $200nm$. The shape factor distribution is obtained by image processing applied to SEM pictures [44]. And the equivalent radius distribution is obtained by analyzing data from [44]. The precipitate shape factor varies from 1 to 8, and almost 99% of the precipitates have a shape factor between 1 and 5.

As mentioned in Chapter 1, microscopic observations showed two main types of second phase particles along grain boundaries, the $M_{23}C_6$ carbides and the σ phase precipitates [18, 20, 21, 24, 37, 130–133]. The crystalline structure, the lattice constant and the chemical composition differ between both second phases. However, the Cr, Fe, Mo, C and Ni elements are the main elements in the compositions of both the $M_{23}C_6$ carbides and the σ phase particles. As a consequence, it is uneasy to distinguish $M_{23}C_6$ carbides and σ phase particles by using only FEG-SEM. The second phase particle cumulative distributions plotted in Fig. 3.1 do not allow a straight-forward distinction between $M_{23}C_6$ carbides and σ phase particles. Then, TEM and TKD observations are carried out to identify the nature of the second phases and study their differences.

The thin foils prepared for the TEM (Transmission Electron Microscopy) observations, are the same for TKD observations (Chapter 3). The thin foils are taken from the longitudinal sections of the specimen, located far away from the fracture surfaces. The loading condition applied on the specimen under consideration is: $600°C$, $220MPa$, $t_f = 7148h$.

Fig. 3.2a shows some σ phase particles located along grain boundary. Three particle shapes are observed: allotriomorph, hexagonal and quadrilateral. Their schematic shapes are respectively plotted in Figs. 3.2c, 3.2d and 3.2e). According to [175], the particle shape can be explained by the particle-matrix interface coherency characteristics, respectively presented in Figs. 3.2c, 3.2d and 3.2e. This point will be explained in more details below. Nevertheless, the observations are carried out through thin foils, which means the 3D shape is unknown.

The precipitates shapes may a priori be a prolate or a oblate one. Some 3D observation results are reported in literature allowing the discussion of the

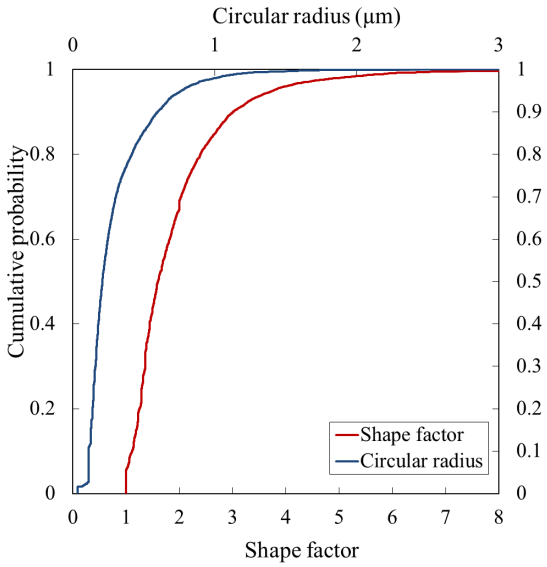

Figure 4.1: The cumulative probabilities of the shape factor and the circular radius (the intergranular second phase particles of diameter larger than $200nm$) [115]. 316L(N), $600°C$, 220MPa, t_f =7148h.

grain boundary particle shape [16, 137, 191]. By a 3D FIB (focused ion beam)-SEM image processing, Burnett et al. [137] investigated the cavitation and precipitation in a crept AISI 316H austenitic stainless steel. The creep conditions were at $T = 525°C$ and Σ =16 MPa. The material was removed from service, after 65000h (no fracture). The observations of Burnette et al. [137] show three different morphologies of the $M_{23}C_6$ carbides.

(1) The first ones are large irregular grain boundary particles that grow into the grains on both sides of the boundary (500–2000nm). This observation is similar to our observations concerning σ phase particles. However, in the study of Burnett et al. [137], the $M_{23}C_6$ particles were only determined by Energy-dispersive X-ray spectroscopy. As it was before, only this kind of chemical analysis does not allow a reliable distinction between $M_{23}C_6$ carbide and σ phase particles. The crystalline diffraction patterns are strongly required.

(2) The second ones are intermediate-size particles that also locate along the grain boundary but appear only to grow into one grain (100–300nm). This observation is close to our observations of $M_{23}C_6$ carbide particles in Incoloy 800, 316L(N) and the images presented in the NIMS data sheet [183].

(3) The third ones are small intragranular carbides (45–90 nm). We did not focus on intragranular precipitations because this does not affect directly the cavity nucleation process. These observations agree with the ones of Beckitt and Clark [16], which showed that $M_{23}C_6$ carbide particles could nucleate along the dislocations inside the metallic matrix and along incoherent twin boundary but their sizes remain small.

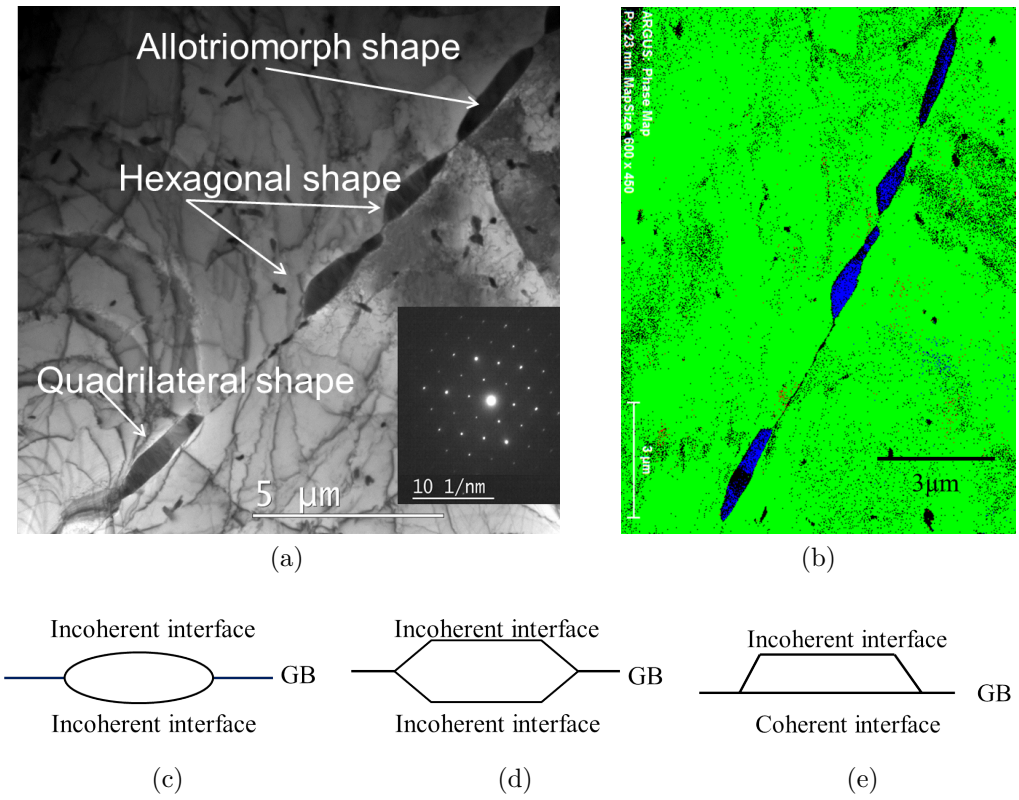

(a) (b)

(c) (d) (e)

Figure 4.2: (a) TEM image showing σ phase particles along one grain boundary and the crystalline diffraction pattern from the 'quadrilateral' σ phase particle; (b) TKD phase map with the austenitic matrix shown in green and σ phase particles in blue. And schematic presentations of (c) allotriomorph (nomenclature defined in [175]), (d) hexagonal and (e) quadrilateral particle shapes ($600°C$, 220MPa, 7147h).

By FIB tomography combined with TEM observations, Maetz [191] investigated the precipitation in an aged duplex stainless steel. Small $M_{23}C_6$ carbides (<500nm) are observed at grain boundaries. Further, their observations showed that the $M_{23}C_6$ carbides stopped growing after only $15min$ of ageing at $690°C$. These results agree well with observations reported by NIMS [2] (Fig. 1.5, Chapter 1). This leads us to assume that large second phase particles (>500nm) located at grain boundaries are generally σ phase particles in the 500-700$°C$ temperature range.

The creep induced nano-cavities are difficult to detect in the creep specimens. Fortunately, we observe a cavity at a particle-matrix interface (Fig. 3.3). The particle is quadrilateral σ phase particle shown in Fig. 3.2a. The cavity is elongated with a length of 100h and a height of 25nm, which is still much higher than the critical size (in order of 20nm evaluated as shown in chapter **??**, accounting for the remote stress but not the local interface one).

In chapter 2, the stress fields around an ellipsoidal-like precipitate are calculated by the Finite Element method. However, only one precipitate geometry is accounted, with a shape factor equal to three. According to our observations (Figs. 3.1 and 3.2), various precipitate geometries need to be considered and then additional FE calculations should be performed. Generally, the morphologies of the second phase particles are irregular. And building very representative meshes would be very time consuming. Additionally, some details of each individual precipitate geometry may ot be very influent. Then, based on our observations, it is proposed to focus on three main precipitate geometries:

1. ellipsoidal precipitate with various shape factors (allotriomorph shape);
2. angular symmetric tip precipitate with different tip angles (φ) (hexagonal shape);
3. angular asymmetric tip precipitate with different tip angles (φ) (quadrilateral shape).

The calculation results obtained based on these three main geometries are presented in the following sections.

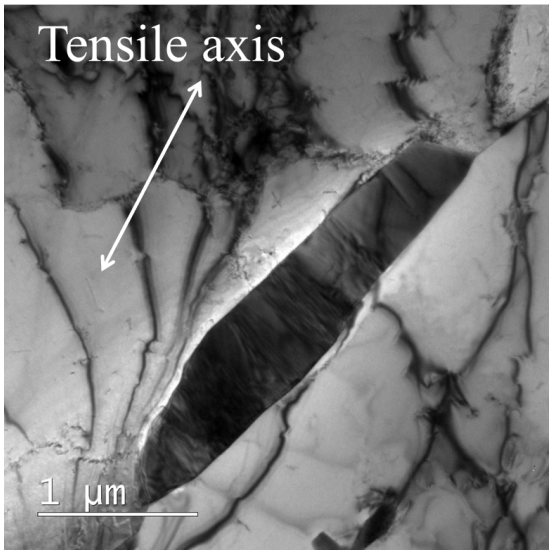

(a)

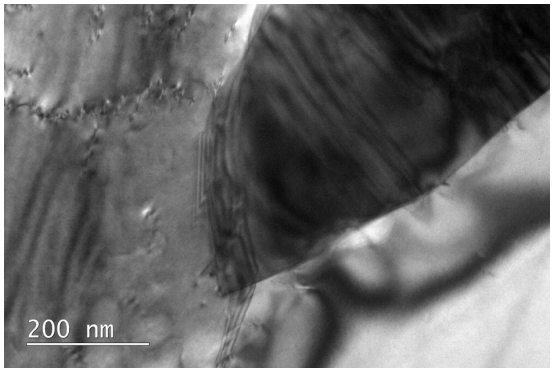

(b)

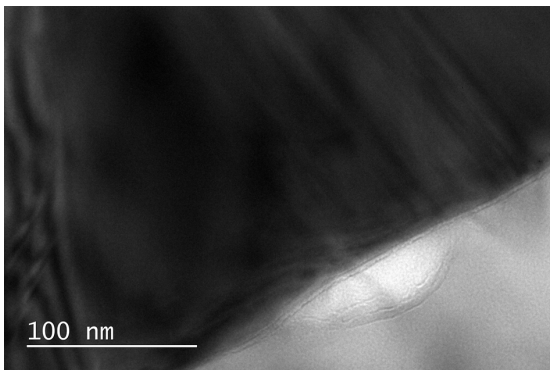

(c)

Figure 4.3: TEM images of (a) a σ phase particle (with a quadrilateral shape as shown in Fig. 3.2a); (b) the particle tip with a cavity along the interface and (c) the elongated cavity at the particle-matrix interface.

4.2 Description of the enhanced interfacial stress field calculations

Long term creep damage is characterized by intergranular intergranular cavity nucleation, growth and coalescence. As shown in Chapter 1 and section 3.1, cavities are produced at the interfaces of metallic matrix and second phase particles. Two theories were proposed to explain cavity nucleation, vacancy agglomeration [81] and interface fracture [51, 117]. However, introducing the value of the remote stress on the Raj nucleation law (Eq. 1.25), the cavity nucleation rate is lower than $1m^{-2}s^{-1}$ [82] (Fig. 1.14). This value is much lower than the measured values. A more precise numerical application will be carried out in Chapter 4, based on the computed interface stress fields instead of the remote stress. Therefore, the interface fracture seems more likely to be the mechanism inducing the observed cavity nucleation.

Interface fracture requires high local interface stress. To calculate the local interface stress, the Eshelby solution is firstly proposed. Then, some modified solutions are proposed based on Eshelby-Kröner solution. However, few studies, about the matrix and second phase interface fracture, were carried out by using continuum mechanics. Further, the solution provided using Eshelby allows only the calculation of the stress field around an inclusion embedded in a matrix which is homogeneously plastically deformed. As expected, we will show that the stress level is overestimated.

In order to evaluate the realistic stress fields at the interfaces of matrix and second phase particles, a quasi-2D plane stress analysis (Fig. 3.4a) is carried out. The homogeneous matrix (blue) obeys the isotropic creep flow rules (Eqs. 2.1 and 1.8) with the parameters given in Table 2.2. In case of bicrystals, the two grains (green and cyan) obey crystal elastoviscoplasticity laws (Eqs. 2.7 and 2.8). For each configuration, the crystal orientations of each grains is random. And the inclusion (red) obeys isotropic elasticity. Further mesh refinement or decrease of the computation time step does not affect our numerical results.

As discussed in chapter 2, the ratio between the matrix size and the grain size is equal to 7.5, to ensure that the matrix size has no effect on the inclusion stress. Then inclusions (red) are located at grain boundaries parallel to the tensile axis (Fig. 3.4). It is generally believed that a critical particle size is necessary for inerdace fracture to occur [79, 117, 180]. On the fracture point of view, larger particle size requires lower fracture stress. However, the traditional Finite Element calculation account only of length ratios as the Eshelby solution does (subsection 3.3.1). Finally, the highest measured ratio between second phase particle and grain sizes is used in our calculations ($3\mu m$ particle between two $20\mu m$ grains).

In case of interface fracture, the interfacial normal and shear stress drive interface fracture. In chapter 2, we showed that the shear stresses are lower than

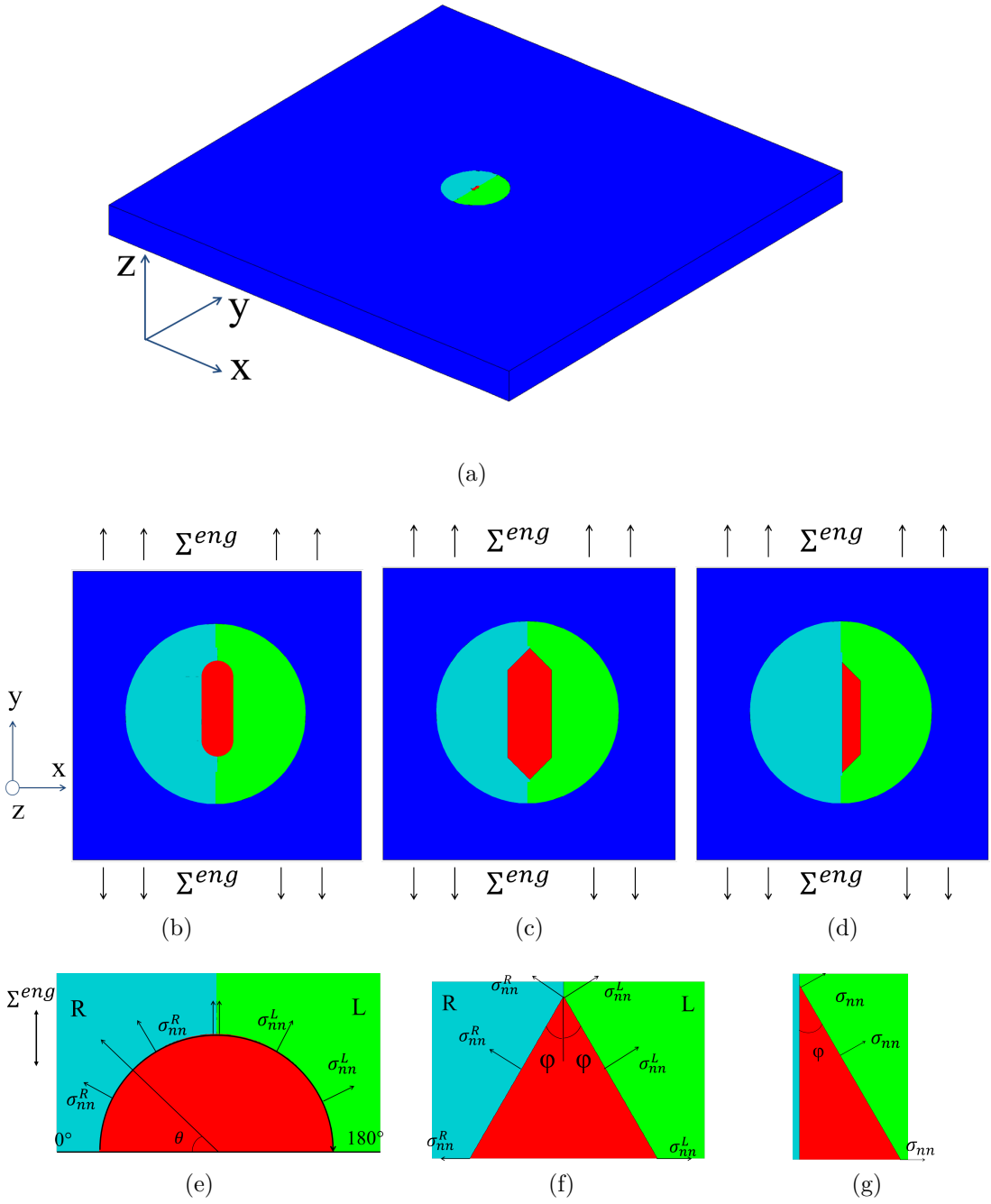

Figure 4.4: Quasi-2D mesh of the inclusion (red) located at a grain boundary, between two grains (green and cyan). The bicrystal is embedded in a homogeneous matrix (blue). (a) The ratio between second phase particles and grains is the real one. Schematic presentations using a largely increased ratio between particle and grain sizes and the definition of the interfacial normal stresses of the interest for the main geometries: (b,e) allotriomorph, (c,f) hexagonal and (d,g) quadrilateral shapes.

the normal stresses by a factor of ten (Fig. 2.8). Therefore, we focus now only on the normal stress fields. Additionally, the calculations carried out in Chapter 2 were based on thirty sets of two random crystal orientations show a strong heterogeneity in the maximum interface normal stress. And it was highlight that accounting for fifteen sets of random orientations is enough to get a reliable distribution of interface normal stress (Fig. 2.8). Therefore, only fifteen sets of orientations are taken into account in this chapter.

In the following, we calculate the normal stress fields along the interface of second phase particles located between two highly deformed crystals which are embedded in a highly deformed matrix. The Finite Element method is used, to evaluate precisely the influence of the microstructural heterogeneity. In section 3.3, shape factor effect is investigated based on the measured values plotted in Fig. 3.1.

In section 3.4, FE computations account for the three inclusion tip geometries (Figs. 3.4e, 3.4f and 3.4g]. And the corresponding stress distributions are deduced. The considered material is 316L(N) steel, loaded at $600°C$, and under $220MPa$.

4.3 Theoretical and numerical investigation of the precipitate shape factor effect

Chapter 3 investigated the effect of the random crystalline orientations on the interfacial normal stress for an inclusion with a shape factor of three. Nevertheless, according to the experimental measurements reported in section 3.1, the inclusions a shape factor range between 2.5 and 3.5 account to only less than 30% of the precipitates. This is why the effect of the shape factor is now investigated

The shape factor is characterized by the semi-major length, a, divided by the semi-minor length, b, (Figs. 3.5 and 3.8a). The calculations are carried out for shape factors ranging from 1 to 10. Three computation methods of increasing complexity are used to calculate the interfacial normal stress:

- the thermo-elastic Eshelby-Kröner solution [91];

- the Finite Element Method (FEM), accounting an elastic inclusion directly embedded in a homogeneous matrix.

- the Finite Element Method (FEM), accounting an inclusion located along a grain boundary, with two neighbor grains of random crystalline orientations (Fig. 3.4). The bicrystal is finally embedded in the same macroscopic matrix as the second method.

4.3.1 The Eshelby theory

To calculate the stress fields in an ellipsoidal inclusion in function of plastic strain, the Eshelby relationships are used.

Eshelby solution assumes that the ellipsoidal inclusion is embedded in an infinite matrix and the isotropic elasticity moduli are the same for the inclusion and the matrix. And a uniform plastic strain tensor is applied with whole inclusion but not in the matrix. Then,

$$\sigma_{ij} = \Sigma_{ij} + C_{ijkl} : (S_{ijkl} - I_{ijkl}) : \varepsilon^p_{kl} \tag{4.1}$$

where C_{ijkl} is the elasticity/rigidity tensor, S_{ijkl} are the Eshelby tensor components depending only on the inclusion geometry (Fig. 3.5) and the Poisson coefficient, ν, and ϵ^p_{kl} are the uniform inclusion plastic strain.

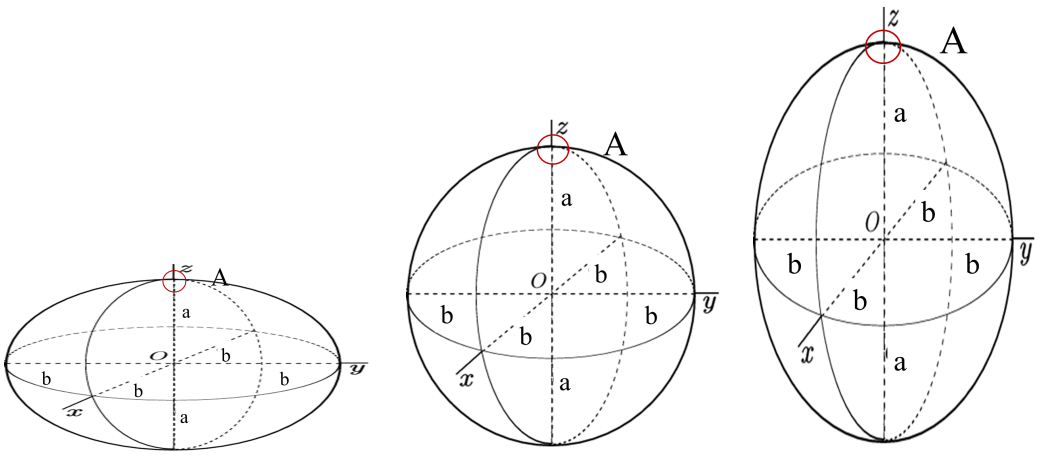

(a) Oblate (a/b<1) (b) Spherical (a/b=1) (c) Prolate (a/b>1)

Figure 4.5: Schematic presentation of inclusions with different shape factors.

Eshelby showed that the stress tensor is uniform in all the inclusion [91] and is linear dependent with the inclusion plastic strain. This linear dependence is a consequence of the thermo-elastic assumption adopted by Eshelby.

The Eshelby solution allows an easy investigation of the effect of the inclusion shape factor, a/b, compared to the Finite Element calculations results.

Based on the Eshelby solution, Kröner [192] proposed a convenient interaction law, which is readily derived from the solution of the Eshelby inclusion problem [91]. Additionally, the matrix is subjected to uniform plastic strain components, E^p_{ij}. This interaction rule assumes a thermo-elastic interaction between the matrix and the inclusion. Kröner's model provides rather accurate predictions at low plastic strain. Nevertheless, it usually leads to stress overestimations as the remote plastic strain increases [125].

So that, the modified Eshelby-Kröner problem is solved by:

$$\sigma_{ij} = \Sigma_{ij} - C_{ijkl} : (S_{ijkl} - I_{ijkl}) : (\varepsilon^p_{kl} - E^p_{kl}) \tag{4.2}$$

Assuming $\varepsilon^p_{kl} = 0$ in the elastic inclusion, the Eshelby-Kröner solution deduces that the homogeneous matrix deformed plastically. The Eshelby-Kröner

thermo-elasto theory predicts that the inclusion stress tensor is homogeneous and increases linearly with the uniform matrix plastic strain, which is not observed in elastic viscoplastic Finite Element computation results. So that, in the following, the plastic deformation is chosen as $E^p = 4\%$, in order to make comparisons with the FE calculation results. Three configurations are considered, the oblate inclusion (Fig. 3.5a), the spherical inclusion (Fig. 3.5b) and the prolate inclusion (Fig. 3.5c).

4.3.1.1 Spherical inclusions

We assume, at first, that the precipitates are spherical (Fig. 3.5b), embedded in an elastic matrix and the plastic strain tensor ε^p is uniform in the inclusion. The Eshelby relationship [193] provides the uniform inclusion stress tensor components:.

$$\sigma_{ij} = \Sigma_{ij} - 2\mu(1-\beta)\varepsilon^p_{ij} \qquad avec \qquad \beta = \frac{2(4-5\nu)}{15(1-\nu)} \tag{4.3}$$

Still in the thermo-elasticity framework and using the Kröner approach, similar formula arise considering an elastic inclusion embedded in a homogeneously plastically deformed matrix.

$$\sigma^I_{ij} = \Sigma_{ij} + 2\mu(1-\beta)E^p_{ij} \tag{4.4}$$

For 316L(N), at $600°C$, with Young's modulus equals $150GPa$ and $\nu = 0.3$, the β factor amounts to: $\beta = 0.476$. For the macroscopic plastic axial strain of $E^p = 4\%$, the average axial inclusion stress reaches $2.90GPa$. The maximum normal stress is obtained along the z-axis at point 'A' (Fig. 3.5) and is equal to the average inclusion axial stress. Assuming isotropy at the macroscale, the stresses along the transversal x- and y-axis are equal because of the axisymmetric shapes of the considered inclusions (Fig. 3.5). And the signs of these two components are negative, as the macroscopic plastic deformation is isovolumic. The magnitude of these compressive interfacial stresses is one-half of the axial internal stress magnitude.

4.3.1.2 Ellipsoidal inclusion

The microscopic observations show that the second phase particle shapes are generally irregular. To apply the Eshelby-Kröner theory, we assume that the irregular second phase particle shapes may be modeled as ellipsoidal inclusions. This allows us to evaluate specifically the influence of the shape factor on the average inclusion stress.

For an ellipsoidal inclusion embedded in an infinite homogeneous matrix, the evaluation of the Eshelby tensor components, S_{ijkl}, is not as straight-forward as the one carried out for spherical inclusions [194]. The stresses along the interface of ellipsoidal inclusions are calculated using the Eshelby tensor proposed by Piat et al [195]. The effect of the shape factor is characterized by a factor g:

$$\begin{aligned} g &= \frac{(a/b)}{((a/b)^2-1)^{3/2}}[(a/b)((a/b)^2-1)^{\frac{1}{2}} - arccosh((a/b))], \qquad (a/b) > 1 \\ g &= \frac{(a/b)}{((a/b)^2-1)^{3/2}}[arccosh((a/b))^{\frac{1}{2}} - (a/b)((a/b)^2-1)^{\frac{1}{2}}], \qquad (a/b) < 1 \end{aligned} \tag{4.5}$$

The components of the Eshelby tensor are finally [195]:

$$\begin{aligned} S_{1111} &= S_{2222} = -\frac{3(a/b)^2}{8(1-\nu)(1-(a/b)^2)} + \frac{g}{4(1-\nu)}[1-2\nu+\frac{9}{4(1-(a/b)^2)}] \\ S_{3333} &= -\frac{1}{1-\nu}[2-\nu+\frac{1}{1-(a/b)^2}] + \frac{g}{2(1-\nu)}[-4+2\nu+\frac{3}{1-(a/b)^2}] \\ S_{1122} &= S_{2211} = \frac{1}{8(1-\nu)}[1-\frac{1}{1-(a/b)^2}] + \frac{g}{16(1-\nu)}[-4(1-2\nu)+\frac{3}{1-(a/b)^2}] \\ S_{1133} &= S_{2233} = \frac{(a/b)^2}{2(1-\nu)(1-(a/b)^2)} + \frac{g}{4(1-\nu)}[1-2\nu+\frac{3(a/b)^2}{1-(a/b)^2}] \\ S_{3311} &= S_{3322} = \frac{1}{2(1-\nu)}[-(1-2\nu)+\frac{1}{1-(a/b)^2}] + \frac{g}{4(1-\nu)}[2(1-2\nu)+\frac{3}{1-(a/b)^2}] \\ S_{1212} &= \frac{(a/b)^2}{8(1-\nu)(1-(a/b)^2)} + \frac{g}{16(1-\nu)}[4(1-2\nu)+\frac{3}{1-(a/b)^2}] \\ S_{1313} &= S_{2323} = \frac{1}{4(1-\nu)}[(1-2\nu)+\frac{1+(a/b)^2}{1-(a/b)^2}] + \frac{g}{4(1-\nu)}[(1-2\nu)+3\frac{1+(a/b)^2}{1-(a/b)^2}] \end{aligned} \tag{4.6}$$

They depend only on the shape factor, a/b, and the Poisson ratio, ν. The influence of the inclusion shape factor is now studied. As reported in section 3.1, observations show that the shape factors range between 1 and 10. To investigate the aspect ratio effect, the calculations based on the Eshelby-Kröner solution are carried out for shape factors varying between 1/100 and 100. The average inclusion axial stress $< \sigma_{zz} >$ is calculated by Eq. 3.4. The calculation results are plotted in Fig. 3.6 and provided Table 3.1.

The results show that the interface stress increases with the increase in the shape factor value from 1/10 to 10. Then, the inclusion stress is almost constant in the intervals from 1/100 to 1/10 and from 10 to 100. Furthermore, the ratio of the interface normal stress computed for elongated inclusions ($a/b > 10$) (Fig. 3.5c) and the spherical inclusion stress amounts to two (Table 3.1). And the stress for inclusion with shape factor lower than 1/20 is close to $220MPa$,

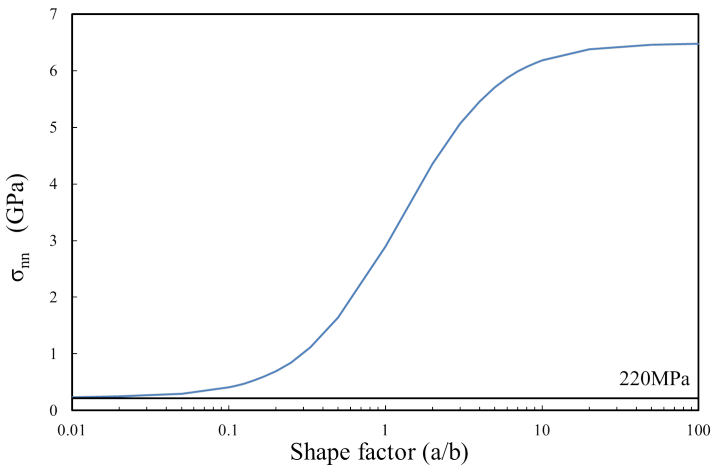

Figure 4.6: The normal stress σ_{nn} at point 'A' in function of the inclusion' shape factor, for a remote plastic deformation of 4% and a remote axial stress of 220MPa. The Eshelby-Kröner solution (Eq. 3.2).

corresponding to the remote axial the applied stress, with negligible internal stresses.

The Eshelby solution provides exact predictions in the framework of thermo-elasticity and assuming a inclusion plastic deformation through all the matrix around the inclusion (far- and close-filed). But less good ones for the case of a plastically-flowing polycrystal [196]. The Eshelby solution is based on a fully elastic interaction between each individual grain and the surrounding matrix which is a too stiff condition in the elastic-plastic regime. In fact, the matrix plastic strain fields become rapidly heterogeneous in full-field computations. The accommodation of plastic strain fields occur not only by elastic deformation but also by heterogeneous plastic deformation in the matrix. Further, Fig. 3.7 shows that, on the contrary, the interface stress increases linearly with macroscopic strain. Nevertheless, for an ellipse inclusion (a/b=3) embedded in a homogeneous matrix (Chapter 2), the curve provides by the Finite Element calculation shows is concave. Therefore, the Eshelby-Kröner solution overestimates the internal stresses and neglects the plastic accommodation processes between the inclusion and matrix which leads to a large overestimation of the macroscopic behavior [196].

Therefore, FE calculations are required to account for several parameters:

- the viscoplastic strain in the matrix which becomes quickly heterogeneous. This leads to the invalidity of the Eshelby-Kröner solution, and lower inclusion stresses than expected from this solution. A heterogeneous stress field inside the inclusion is the expected too;

- viscosity effects should be accounted, because they may affect the local stress fields;

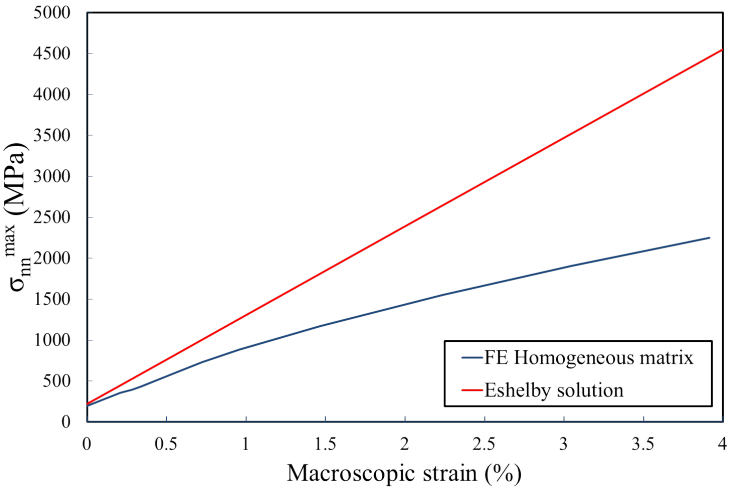

Figure 4.7: Interface stress evolution in function of the macroscopic strain, for a/b=3, calculated using the Eshelby-Kröner solution and Finite Element computation.

- the anisotropic viscoplasticity behavior of the two grains surrounding each inclusion may be influent too. The results of Chapter 2 clearly show that considering a few ten couples of crystal orientations leads to a huge scattering of the interface normal stress distribution (Fig. 2.8).

4.3.2 Finite Element calculations

The (large) inclusions are generally located along grain boundaries, and naturally the two neighbor grains have different crystalline orientations. Then, the average inclusion and the interface stresses are affected by the two grain crystalline orientations, which cannot be predicted based on Eshelby solution, even using a more advanced self-consistent homogenization schema. Therefore, crystal plasticity Finite Element computation is used. Moreover, crystal viscoplastic flow law is used at the crystal scale (Eq. 2.8), allowing us to carry out calculations valid for describing creep deformation.

Two configurations are used as inputs of the Finite Element calculations:

- the inclusion embedded directly in the homogeneous matrix;
- the inclusion along a grain boundary, between two metallic crystals, embedded in the same matrix (Figs. 3.4a and 3.4b).

The calculations are carried out for inclusion shape factors varying from 1 to 10. The interface normal stress becomes almost independent of the aspect ratio, provided, ($a/b \geqslant 8$). This saturation is in agreement with the results based on the Eshelby solution (Fig. 3.6). Further, no calculation is carried out for (a/b<1), because all observed intergranular second phase particles are elongated along grain boundaries. However, a/b<1 corresponds to the one perpendicular,

which is not exist. And only grain boundaries parallel to the tensile axis are considered here.

The shape factor effect is characterized by a stress ratio denoted as: $r_{sf}(a/b)$. This is defined as the ratio between the maximum interface normal stress computed for the shape factor a/b and the one computed for a/b=1 (circular inclusion):

$$r_{sf}(a/b) = \frac{\sigma_{nn}^{max}(a/b)}{\sigma_{nn}^{max}(a/b=1)} \tag{4.7}$$

The calculation results provided by the three approaches are shown in Table 3.1. The maximum normal stress and the shape factor ratio provided by the bicrystal calculations are the average values over fifteen couples of random crystalline orientations. The dependence of the $r_{sf}(a/b)$ ratio with the shape factor, a/b, provided by the three approaches for a macroscopic strain of 4%, are plotted in Fig. 3.8a. The ranges of variation are plotted for bicrystal calculations are the results of the randomness of the crystal orientations (fifteen couples and fifteen values of σ_{nn}^{max} for each aspect ratio value, a/b). Bicrsytal calculation values are shown in Appendix B.

Shape factor a/b	Eshelby solution		FE computations			
			Homogeneous matrix		Bicrystal environment	
	σ_{nn}^{max} (GPa)	$r_{sf}(a/b)$	σ_{nn}^{max} (GPa)	$r_{sf}(a/b)$	$\bar{\sigma}_{nn}^{max}$ (GPa)	$\bar{r}_{sf}(a/b)$
1	2.90	1.00	1.56	1.00	2.66	1.00
2	4.35	1.50	1.94	1.24	2.99	1.12
3	5.06	1.74	2.25	1.44	3.61	1.36
4	5.45	1.88	2.49	1.60	3.99	1.50
5	5.70	1.96	2.80	1.79	4.70	1.77
6	5.87	2.02	3.11	1.99	5.13	1.93
7	5.98	2.06	3.28	2.10	5.39	2.03
8	6.07	2.19	3.41	2.18	5.64	2.12
10	6.18	2.13	3.50	2.24	5.79	2.18

Table 4.1: Computed maximum interface normal stress and concentration factor, $r_{sf}(a/b)$ for the various inclusion shape factors ($600°C$, $220MPa$, remote plastic strain of 4%). Fifteen couples of random crystal orientations defining each bicrystal are accounted for as considering the bicrystal environment.

As shown in Table 3.1, the Eshelby solution provides for a maximum normal stresses higher than FE results for the inclusion embedded in a homogeneous matrix. The Eshelby solution predicts in fact that the stress increases linearly with macroscopic strain (Fig. 3.7). The higher the remote (visco-)plastic strain, the stronger the overestimation by the Eshelby-Kröner approach. The maximum normal stress computed by the FE method, for an inclusion embedded in a

homogeneous matrix is much lower than the average value obtained for inclusions along grain boundaries (fifteen couples of crystal orientations). Additionally, the neighbor grains induce a large heterogeneity in the interface normal stresses (Fig. 3.8a).

The fifteen bicrystal calculation results show that the average value of $r_{sf}(a/b)$ increases with the shape factor until the shape factor reaches seven (Fig. 3.8a). We can consider that the shape factor has no effect on the interfacial normal stress if the shape factor is higher than seven. This result is consistent with the Eshelby solution one and the one provided by Finite Element computations accounting for an inclusion embedded directly in the homogeneous matrix (Fig. 3.8a).

Then, a multiplication formula (Eq. 3.8) is proposed to calculate the whole distribution maximum interfacial normal stress accounting for random crystal orientation set, various shape factors and the macroscopic strain of E^{vp}. Such a distribution may be roughly evaluated by using:

$$\sigma_{nn}^{max}(O_i^1, O_i^2, a/b, E^{vp}) = \sigma_{nn}^{max}(O_i^1, O_i^2, a/b = 1, E^{vp}) \cdot \bar{r}_{sf}(a/b) \tag{4.8}$$

where $\sigma_{nn}^{max}(O_i^1, O_i^2, a/b = 1, E^{vp})$ is the maximum normal stress along the interface of a spherical inclusion for a given couple of crystal orientation, (O_i^1, O_i^2), at a remote strain E^{vp}.

In this sample formula, the macroscopic strain could be calculated using the macroscopic creep laws (Eqs. 2.1 and 2.5). Fig. 3.8b shows the comparison between the maximum interface normal stress σ_{nn}^{max} calculated through the fifteen bicrystal calculations carried out for $a/b = 1$ and the multiplication formula (Eq. 3.8). The comparison shows that the distributions agree well enough. Therefore, Eq. 3.8 allows a fair and straight-forward calculation of the interfacial normal stress distributions accounting different shape factors, based only on the stress distribution computed for (a/b=1). It should be noticed that this formula allows the prediction of the whole distribution accounting for random crystalline orientations, and shape factor (a/b). Nevertheless, to calculate the stress for specific crystal orientation set, it must be accounted for the ranges of variation calculated for each a/b value of the individual ratio $r_{sf}(a/b)$, as the distribution plotted in Fig. 3.8a.

Further, according to Fig. 2.10, the interface normal stress depends only on the remote strain, but not on the remote tensile stress and temperature. Therefore, Eq. 3.7 should hold for various stress and temperatures.

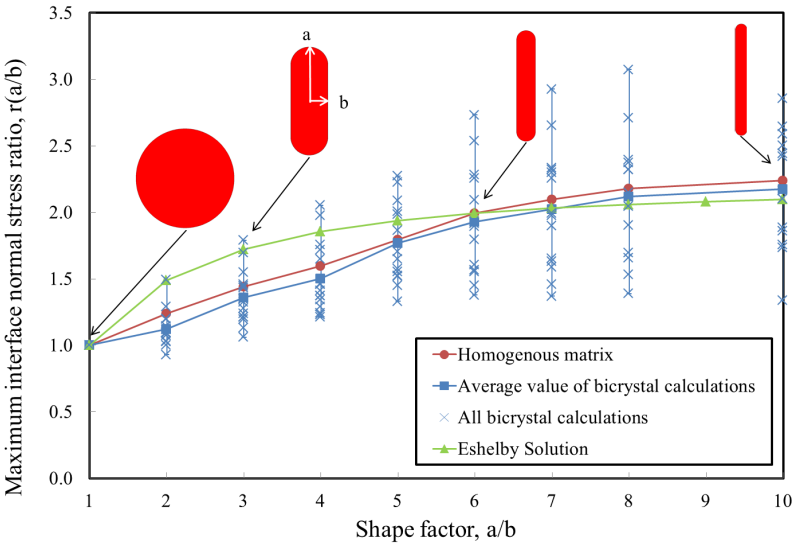

(a)

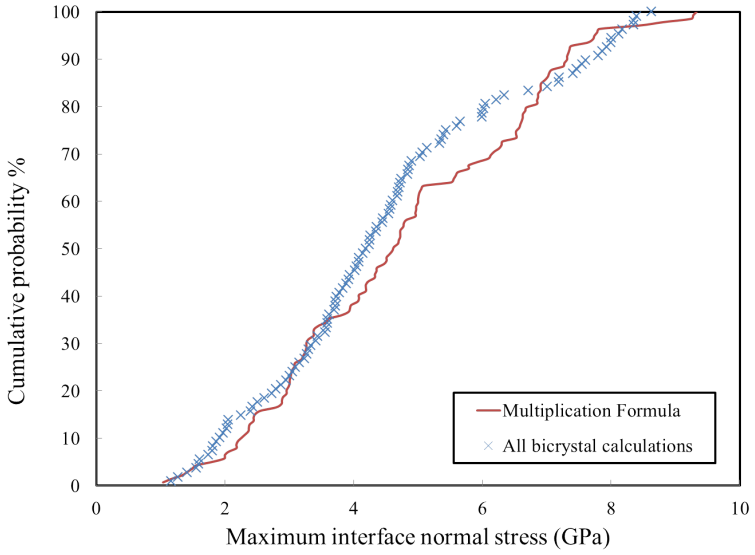

(b)

Figure 4.8: (a) the evolution of the interface stress concentration ratio, $r_{sf}(a/b)$, in function of the shape factor, a/b; (b) Cumulative probability of the maximum interfacial normal stress for shape factors between 1 and 10, and fifteen random orientations sets, (O_i^1, O_i^2), ($600°C$, $220MPa$, $E^{vp} = 4\%$). Comparison with the simplified multiplication formula (Eq. 3.8). Equiprobable shape factor values,$1 \leqslant a/b \leqslant 10$

4.4 Investigation of the effect of angular tips of the precipitates

The previous section investigates the effect of the shape factor value on the interfacial normal stress. Only a circular tip inclusion is introduced (allotriomorph shape, Fig. 3.2a). However, various inclusion tips are observed, including angular tips (hexagonal and quadrilateral shapes, Fig. 3.2a). Nevertheless, the effect of angular tip inclusion was rarely studied. Recently, Misseroni et al. [197] calculated the stress field around stiff rhombohedral inclusions embedded in a 'soft' elastic matrix. Their results show a strong stress concentration in the vicinity inclusion tip (factor 6). However, in AISI 316, the Young modulus of second phase particles (200-350GPa) are higher than the matrix one (150 GPa) at high temperature. It should be added that our FE calculations showed a negligible effect of the inclusion Young's modulus provided it belong to the [100-400GPa] range (Fig. 2.6b).

In this section, we investigate the effect of the angular inclusion tip on the interfacial normal stress by the finite element method. The angle φ is defined as shown in Fig. 3.9 and 3.11. Two tip morphologies are considered in the following, first hexagonal shape and then quadrilateral shape. The considered grain boundary plane is parallel to the tensile axis, and shape factor equals three.

4.4.1 Precipitate symmetric tip

Considering the hexagonal shape (Fig. 3.9), the interfacial free energy or surface tension equilibrium equation at the triple point (P) [175] is:

$$\cos\,\varphi = \frac{\gamma_{GB}}{2\gamma_{incoh}} \tag{4.9}$$

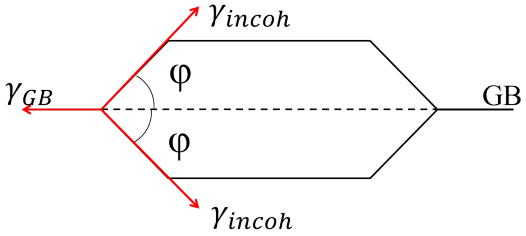

Figure 4.9: The interfacial free energy or surface tension equilibrium condition for a hexagonal precipitate, with γ_{GB} the grain boundary energy (Jm^{-2}) and γ_{incoh} the incoherent interface energy (Jm^{-2}).

Following the literature review summarized in 2 (subsection 2.5.1), the incoherent interface energies range between 2 and $2.5 J/m^2$ and the grain boundary

energy as 1.5-2J/m^2 (general grain boundary). Then, using Eq. 3.9, the half-tip angle should range between 60 and 72°. However, this result does not agree with our observations.

Therefore, to be more realistic, the FEM calculations account for φ equals 30, 45 and 60° are carried out (Fig. 3.10a). The absolute values are provided in Appendix B (Table B.3). The three inclusions respect same length in major axis and the inclined interface. The shape factor of the inclusion with $\varphi = 45°$ equals exactly three. Therefore, the ones for $\varphi = 30$ and 60° are only slightly changed.

Fig. 3.10b shows the whole calculation results (as cross markers) with fourteen crystalline orientation sets, accounted for each φ angle amounts to 30, 45 and 60°. The results show that interface stress of the inclusions with a tip angle of 30° are much higher than with tip angles of 45 and 60°, and the one for 60° is slightly higher than 45°.

The effect of the inclusion tip angle is characterized by a ratio, $r_{sym}(\varphi)$, between the maximum interfacial normal stresses computed for a symmetric angular tip, defined by φ and circular tip:

$$r_{sym}(\varphi) = \frac{\sigma_{nn}^{max}(O_i^1, O_i^2, a/b = 3, \varphi, E^{vp})}{\sigma_{nn}^{max}(O_i^1, O_i^2, a/b = 3, circular, E^{vp})} \tag{4.10}$$

The dependence of $r_{sym}(\varphi)$ with the tip angle, φ, and the bicrystal orientations, (O_i^1, O_i^2), are plotted in Fig. 3.10a. The results show that the average values $\bar{r}_{sym}(\varphi)$ ranges between 1.3 and 2.1. A large heterogeneity in the $r_{sym}(\varphi)$ ratio is also observed, as shown by the cross markers in Fig. 3.10a. Finally, we propose a simplified multiplication formula similar to Eq. 3.8, for estimating the whole distribution:

$$\sigma_{nn}^{max}(O_i^1, O_i^2, \varphi, E^{vp}) = \sigma_{nn}^{max}(O_i^1, O_i^2, circular, E^{vp}) \cdot \bar{r}_{sym}(\varphi) \tag{4.11}$$

Applying Eq. 3.11, the distribution of the maximum interfacial normal stresses for angular tip inclusions are calculated based on the one computed for circular tip inclusions only. The interface stress distribution accounting calculated using this multiplication formula for each φ value are compared with the distribution computed by the FEM for each φ value in (Fig. 3.10b). The comparison shows a fair agreement between the stress distributions calculated by these two methods. Similarly to Eq. 3.8, it should be noticed that computing the interface stress for one specific couple of crystalline orientations, it requires to take into account the range og variation of $r_{sym}(\varphi)$. The previous results holds at least for $\alpha_{GB} = 0°$ and a/b=3.

4.4.2 Precipitate asymmetric tip

In previous subsection, the effect of precipitate angular tip on the interfacial normal stress is evaluated accounting only for the symmetrical tips (hexagonal

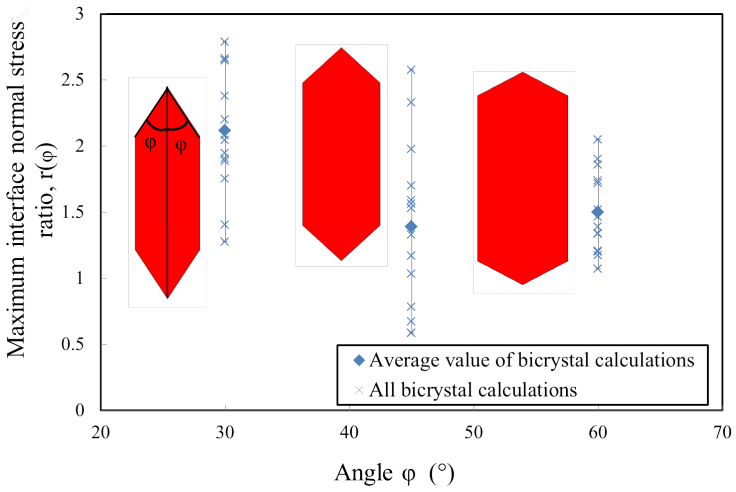

(a)

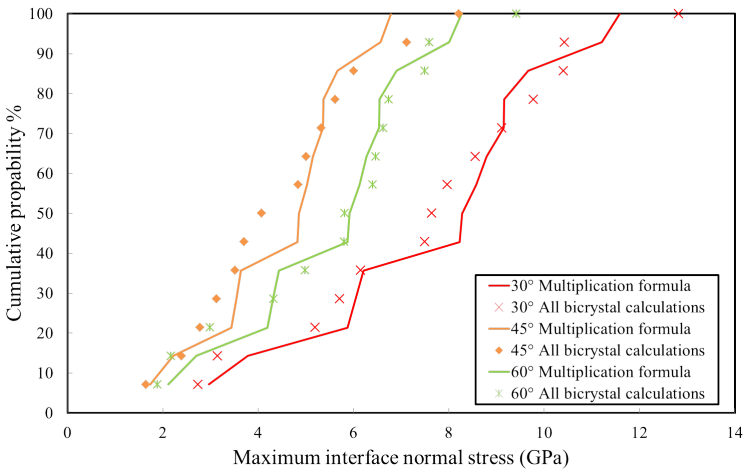

(b)

Figure 4.10: (a) Values of the maximum interface stress concentration factor, $r_{sym}(\varphi)$, calculated for 14 random couples of orientations of the bicrystals containing the inclusion; (b) cumulative probabilities of the maximum interfacial normal stresses calculated for 14 different bicrystals embedded in the homogeneous matrix. And the cumulative probability curves deduced from the multiplication formula (Eq. 3.11). Other microstructures parameters: $\alpha_{GB} = 0°$ and a/b=3 (slightly modified for $\varphi = 30°$ and 60°). $600°C$, $220MPa$, $E^{vp} = 4\%$.

shape, Figs. 3.2a, 3.2b and 3.2d). This corresponds to second phase particles which grew into both neighbor grains. However, the shapes of some of the intergranular precipitates are asymmetrical, with quadrilateral shape (Figs. 3.2a, 3.2b and 3.2e).

For the quadrilateral shape (Fig. 3.11), the interfacial free energy or surface tension equilibrium condition at point (P) leads to:

$$cos\,\varphi = \frac{\gamma_{GB} - \gamma_{coh}}{\gamma_{incoh}} \tag{4.12}$$

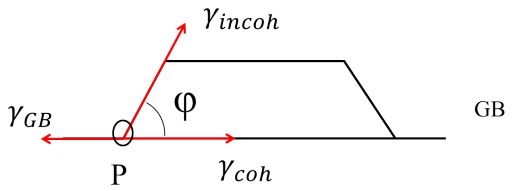

Figure 4.11: The interfacial free energy or surface tension equilibrium condition for a quadrilateral precipitate, with γ_{GB} grain boundary energy (Jm^{-2}), γ_{coh} coherent interface surface energy (Jm^{-2}) and γ_{incoh} incoherent interface energy (Jm^{-2}).

Table 2.4 reported incoherent interface energies of 2-2.5J/m^2, coherent interface energy of 0.2J/m^2 and general grain boundary energies of 1.5-2J/m^2. Then it is deduced that the angle φ should range between 25° and 60°.

Thereafter, in this subsection, the stress concentration around the intergranular quadrilateral inclusion are calculated, taking tip angle φ of 30, 45 and 60° (Fig. 3.12a). The absolute values are provided in Table B.3 in Appendix B. The bicrystal Finite Element calculations show that the maximum interfacial normal stresses generally increase with the asymmetrical tip angle decreasing (Fig. 3.12b). The distributions are in fact drifted towards higher values as φ decreases.

A new ratio, $r_{asym}(\varphi)$, is defined by dividing the maximum normal stress computed a asymmetrical inclusion by the stress computed for a symmetrical one:

$$r_{asym}(\varphi) = \frac{\sigma_{nn}^{max}(O_i^1, O_i^2, \varphi, asym, E^{vp})}{\sigma_{nn}^{max}(O_i^1, O_i^2, \varphi, sym, E^{vp})} \tag{4.13}$$

The dependence of the $r_{asym}(\varphi)$ ratio with the φ angle is plotted in Fig. 3.12a. The heterogeneity caused by the random crystalline orientations can be evaluated through the ranges of variation of $r_{asym}(\varphi)$. The average values, $\bar{r}_{asym}(\varphi)$, range between 0.85 and 1.35. Finally, Eq. 3.14 is proposed to evaluate roughly the maximum interfacial normal stress distribution of asymmetrical inclusions from

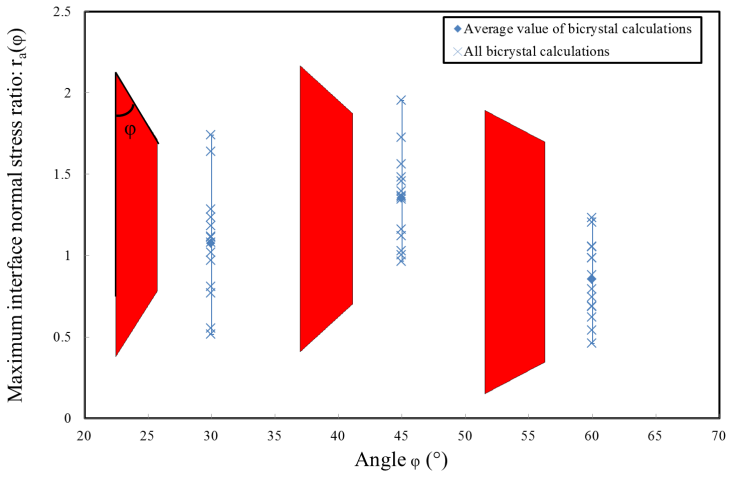

(a)

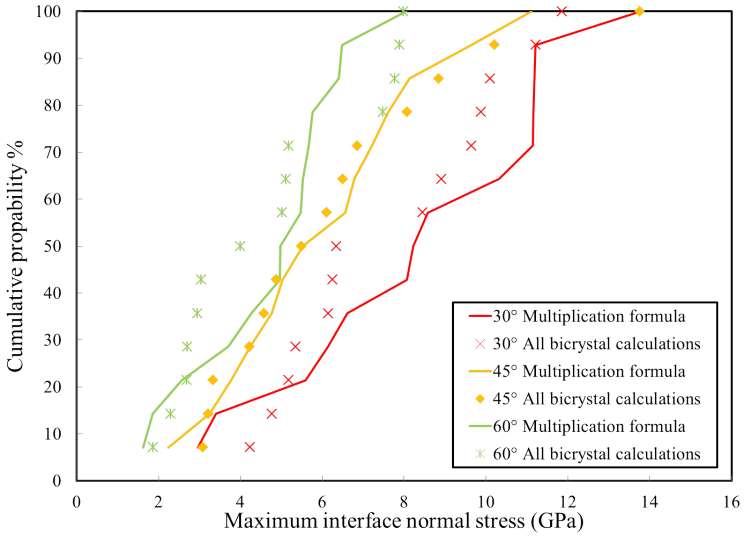

(b)

Figure 4.12: (a) Values of the maximum interface stress concentration factor, $r_{asym}(\varphi)$, calculated for 14 random bicrystal calculations; (b) cumulative probabilities of the maximum interfacial normal stresses calculated for 14 different bicrystals embedded in the homogeneous matrix. And the cumulative probability curves deduced from the multiplication formula (Eq. 3.13) ($600°C$, $220MPa$, $E^{vp} = 4\%$).

the distribution of symmetrical ones:

$$\sigma_{nn}^{max}(O_i^1, O_i^2, \varphi, asym, E^{vp}) = \sigma_{nn}^{max}(O_i^1, O_i^2, \varphi, sym, E^{vp}) \cdot \bar{r}_{asym}(\varphi) \qquad (4.14)$$

The distribution of maximum interfacial normal stress obtained from Eq. 3.14 are compared with accurate bicrystal calculation results, (Fig. 3.12b). Once more the two methods lead to close distributions. Similarly to Eq. 3.8, if we want to calculate the stress for one specific couple of crystal orientations, the range of variation of $r_{asym}(\varphi)$ should be accounted for whatever the considered φ angle (Fig. 3.12b).

All these calculations lead us propose Eq.

$$\begin{aligned}\sigma_{nn}^{max}(O_i^1, O_i^2, a/b, \varphi_{\oslash/a}, E^{vp}) = \sigma_{nn}^{max}(O_i^1, O_i^2, circular, a/b = 1, E^{vp}) \\ \cdot \bar{r}_{sf}(a/b) \cdot \bar{r}_{sym}(\phi) \cdot \bar{r}_{asym}(\phi)\end{aligned} \qquad (4.15)$$

where $\varphi_{\oslash/a}$ means symmetric ($\varphi_{\oslash}$) or asymmetric φ_a tip angle This equation allows a quick calculation of the distributions of the maximum normal stress accounting for shape factor and tip geometry variations. Only the FE calculations carried out for a circular inclusion along grain boundary with fifteen sets of random grain orientations are needed to calculate the whole stress distribution.

Unfortunately, this equation does not permit us to calculate correctly σ_{nn}^{max} for one given couple of grain orientation, various a/b and particle tip geometry. For example, $\sigma_{nn}^{max}(a/b = 4)(set24, \varphi_a = 45°, 4\%)$ calculated accurately by FEM amounts to 4.67GPa, whereas the one calculated by Eq. 3.15 amounts to 9.14GPa, which overestimates the stress. Then, the interface stress, $\sigma_{nn}^{max}(a/b = 3)(set17, \varphi_a = 30°, 4\%)$ calculated accurately by FEM reaches 11.86GPa, but the one calculated by Eq. 3.15 is only 10.21GPa, which underestimated the stress.

4.5 Discussion of the modeling assumptions

More than 200 polycrystalline calculations presented in subsections 3.3 and 3.4 provide the interfacial normal stress distribution induced by the randomness of the crystalline orientations of neighbor grains, the variability in the shape factor values and finally the detailed geometry of inclusion tips. However, the calculations are carried out with a quasi-2D mesh using plane stress boundary conditions. The plane stress typically occurs in thin flat plates, with close free surfaces. Because the plane stress condition neglects the presence of the transverse components of the stress tensor penitentially generated by the presence of the inclusion, this may leads to an underestimation of the stress fields. Therefore, a few 3D calculations are carried out to compute interfacial stress fields and then to compare with 2D plan stress calculations result.

Further, surprisingly, the evolution of the interface normal stress rarely shows a saturation with respect to the remote viscoplastic strain even at 4%. It should

be noticed that the remote creep strain rate reaches its stationary stage at about 1%. Such discrepancy is discussed in subsection 3.5.2.

Finally, our computations account for the lattice rotation occurring during viscoplastic straining. The influence of lattice rotation on the saturation of the interface stress fields with respect to the remote strain is finally investigated.

4.5.1 2D-3D comparison

3D FE calculations are performed to check if the 2D plane stress results are overestimated due to free surface effects or not. The 2D calculations using different remote stresses and temperatures show that the local interfacial stress is almost independent on tensile stress and temperature (Fig. 2.10). Therefore, we focus only on creep conditions corresponding to $600°C$ and 220MPa.

Full 3D meshes are presented in Fig. 3.13, where the external cylinder (blue) obeys the Andrade and Norton laws (Eqs. 2.1 and 2.5). The green and cyan half-spheres obey the crystal elastic and viscoplastic constitutive laws (Eq. 2.8). Finally, the red inclusion obeys isotropic elasticity. The size ratios are same as the ones of Fig. 3.4a. The explanation and used parameter values are shown in Chapter 3. The mesh refinement has a negligible effect on the interfacial normal stress. It should be noticed that the simulation of the deformation of a full 3D mesh up to 4% requires two months of computation. Therefore, only one 3D inclusion-homogeneous matrix and one 3D bicrystal calculation are carried out.

Figs. 3.14a and 3.14b show the comparison between 2D and 3D interface normal stress fields. Fig. 3.14a shows the comparison of normal stress for an inclusion directly embedded in the homogeneous matrix. The results show that the 2D/3D calculations provide the maximum normal stress, σ_{nn}^{max}, at almost the same location along the interfaces. In this case, 2D/3D stress curves display similar angle dependence. However, the angle dependence computed for the 3D bicrystal seems more chaotic than the one computed for the 2D bicrystal (Fig. 3.14b). In fact, in case of 3D bicrystal, the considered interface line is a triple junction between the two grains and the inclusion (Fig. 3.13c). On the contrary, in case of 2D bicrystal, only the point corresponding to $\theta = 90°$ is in a triple point. And triple junctions are known to trigger stress concentration because of string stress incompatibilities between three different phases.

Sauzay and Gliormini [198] studied the effect of the free surface analytically and by Finite Elements. Their results show that, if the plastic glide crosses the free surface, a decrease in elastic-plastic stress could be observed.

Further, Barbe et al. [199] and Sauzay and Gilormini [198] performed numerical simulations of the deformation of large polycrystalline aggregates. Their comparison between average bulk and surface stress-strain show a slight decrease in the surface average tensile stress, a slight increase in the surface average plastic strain, and a final light decrease in the number of activated slip systems near the free surface.

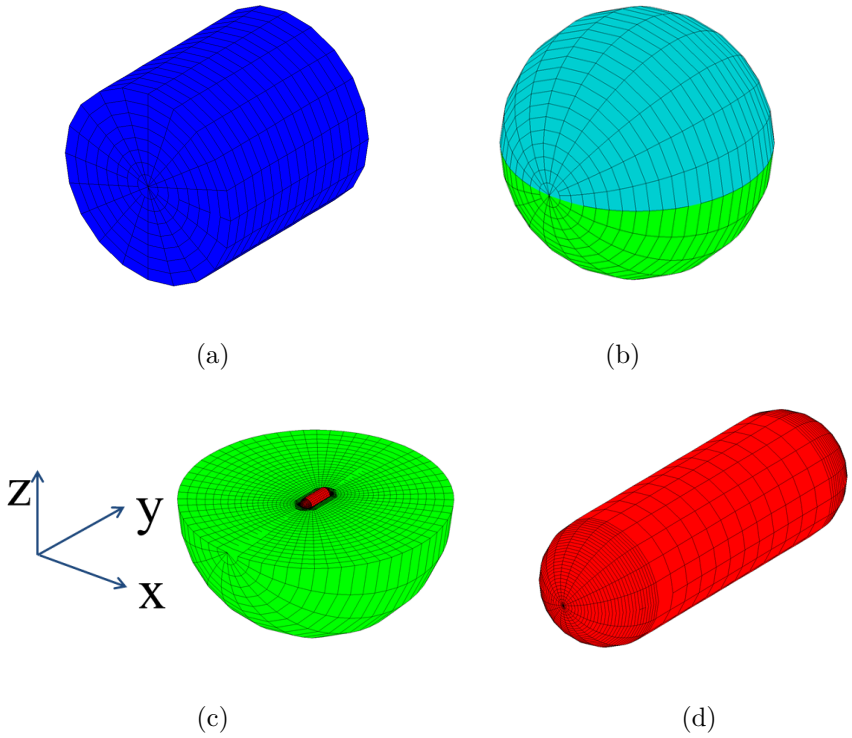

(a) (b)

(c) (d)

Figure 4.13: 3D Meshes of (a) the macroscopic cylinder (homogeneous matrix); (b) the spherical bicrystal in the center of the homogeneous matrix; (c) the ellipsoidal inclusion in the center of the bicrystal (only the green grain is shown) and (d) the ellipsoidal inclusion (a/b=3, spherical tips).

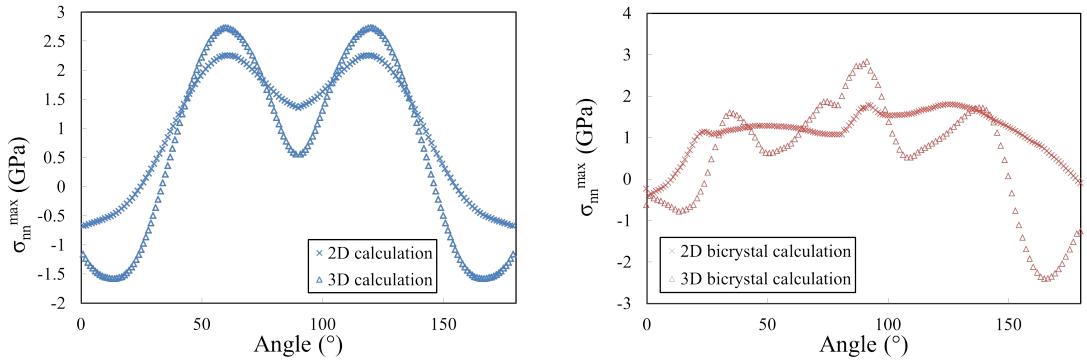

(a) (b)

Figure 4.14: Comparison between 3D and 2D normal stress distribution along the interface for an inclusion (a) directly embedded in the homogeneous matrix and (b) along the triple junction lines where the two grains and the particles are in common, $E^{vp} = 4\%$.

For both inclusion-matrix and inclusion-bicrystal configuration, the interface stresses calculated in 3D are generally higher than the ones provided by the 2D calculations. This is in line with the results of [200], which provides the comparison of 2D plane stress/strain and 3D stress fields for V-notched specimens. For an inclusion embedded in a homogeneous matrix (Fig. 3.14a), the difference in the maximum normal stress is about +20%, whereas it reaches almost 40% for the bicrystal one (Fig. 3.14b). This difference may due to the different inclusion geometries, ellipse-like geometry for 2D calculation and ellipsoid-like one for the 3D calculation. Nevertheless, free surface condition may additionally lead to stronger stress concentrations close to interface. To study the isolated effect of the inclusion geometry, the average inclusion stresses provided by 2D/3D calculations are compared in the following.

Focusing on average inclusion values will allow us

4.5.2 Evolution of the average inclusion stresses during straining

Computing inclusion average stresses with respect to the remote strain will permit us to better understand the saturation of local stress fields occurs during creep. The evolution of average inclusion and interface stress will also be discussed. The evolutions of the average inclusion stress with the macroscopic strain and creep time are now discussed for the 2D/3D calculations, and for 2D calculations accounting for eight different sets of random crystalline orientations. The inclusions obey isotropic elasticity. The main axis of the ellipse- or ellipsoid-like inclusions are parallel to the tensile axis. The shape factor is equal to three. During the creep loading, the σ_{xx} component is negative ($\sigma_{xx} = \sigma_{zz}$ in full 3D calculations), and the σ_{yy} one is positive. Therefore, only the σ_{yy} component is discussed in the following subsection.

4.5.2.1 2D/3D calculation

Fig. 3.15a shows the evolution of the average inclusion tensile stress, $< \sigma_{yy} >$, in function of the average inclusion tensile strain, $< \varepsilon_{yy} >$. The results show two separate domains for the 2D and 3D calculations. For the 2D calculations, the average inclusion strains are lower than the ones provided by the 3D calculations. For '2D/3D calculations', the separation occurs at a strain of 0.140%, and 0.125% for '2D/3D bicrystal calculations'. This may due to the difference in inclusion geometry. Fig. 3.15a shows that the $< \sigma_{yy} >$ component increases linearly with the average inclusion strain, because of isotropic elasticity.

However, the equivalent Young's modulus amounts to 335GPa, which differs the input one (350GPa). This may induces by the stress triaxiality around inclusion. And a slight discrepancy is observed between the 3D calculation and

3D bicrystal calculation results, because of the stress triaxialities in full 3D and quasi-2D calculations are different.

Figs. 3.15b and 3.15c show the average inclusion axial stress evolution in function of the macroscopic strain and the creep time, respectively. For all sets of random orientations, $< \sigma_{yy} >$ reaches a rather high magnitude (>300MPa) very quickly (after 1h and E^{vp}=0.2%). And 3D calculation values are always higher than the 2D plan stress ones. A factor of about 2 is found at $E^{vp} = 4\%$.

The for an inclusion embedded directly in the homogeneous matrix, a slight decrease in $< \sigma_{yy} >$ is observed after 250h and $E^{vp} = 1\%$, for both 2D plan stress and 3D calculations. This results agrees well with stress evolution of a single crystal during creep deformation calculated by Suquet et al. [201]. Thereafter, $< \sigma_{yy} >$ is almost constant under the 2D plane stress assumption. A slight increase is observed in 3D configuration. It may due to the difference in inclusion geometry. The decreases in $< \sigma_{yy} >$ corresponds to the 'structural' viscoplastic relaxation.

Accounting for the neighbor grains (Set $N°2$), no clear relaxation is observed. The anisotropic viscoplastic flows in each of the neighbor grain seem to overcome the structural viscoplastic relaxation. Then, similarly to the case of the homogeneous matrix, the average inclusion axial stress, $< \sigma_{yy} >$, computed for the set $N°2$ of random crystal orientations, only slightly increases under plane stress assumption, and a strong increase is observed for the 3D configuration.

These comparisons lead us to conclude that our previous calculations do not overestimate the interface stresses. The differences in the average inclusion axial stress in, $< \sigma_{yy} >$, are only due to the inclusion geometry.

4.5.2.2 Bicrystal calculations

After discussing the differences between quasi-2D and 3D calculation results, a question remains, such as: the 'structural' viscoplastic relaxation is not observed in the bicrystal calculations (Figs. 3.15b and 3.15c).

These two points lead us to carry out comparisons of the evolutions of the average inclusion axial stress, $< \sigma_{yy} >$, calculated for height different bicrystals under plane stress assumption. Then, height sets of random orientations of the neighbor grains are accounted for. Figs. 3.15b and 3.15c show similar evolutions of $< \sigma_{yy} >$ in function of the macroscopic strain and creep time. Therefore, only σ_{yy} in function of creep time is compared in this part, which is also valid for the one in function of macroscopic strain.

Fig. 3.16a presents the evolution of average inclusion axial stress versus creep time for eight sets of random crystalline sets . The results show a slight relaxation for sets 10, 15, 17 and 22. Nevertheless, the maximum stress before the relaxation could not be observed. It seems that, in the case of bicrystal calculations, the 'structural' relaxation by viscoplasticity ends reached very quickly. This may explain that, whatever the adopted full 3D or plane stress assumption, no clear

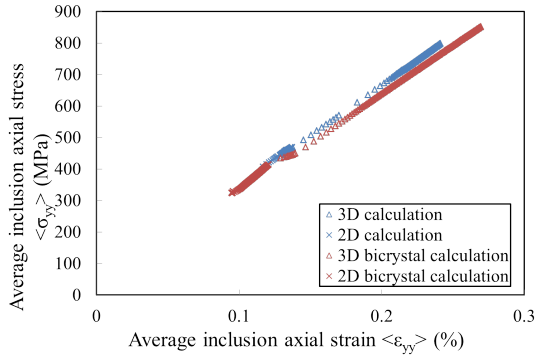

(a)

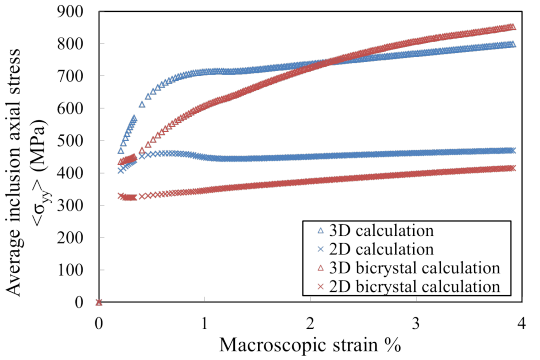

(b)

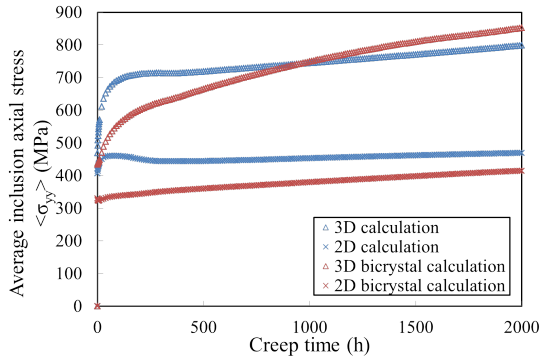

(c)

Figure 4.15: 2D/3D comparison of the average inclusion tensile stress, $< \sigma_{yy} >$, in function of (a) the average inclusion axial strain; (b) macroscopic axial strain and (c) the creep time. '2D/3D calculation' denote the calculations based on an inclusion embedded in the homogeneous matrix. '2D/3D bicrystal calculation' denote the calculations accounting for two surrounding grains (Fig. 3.13). The comparison is performed for the same couple of crystalline orientations of two neighbor grains.

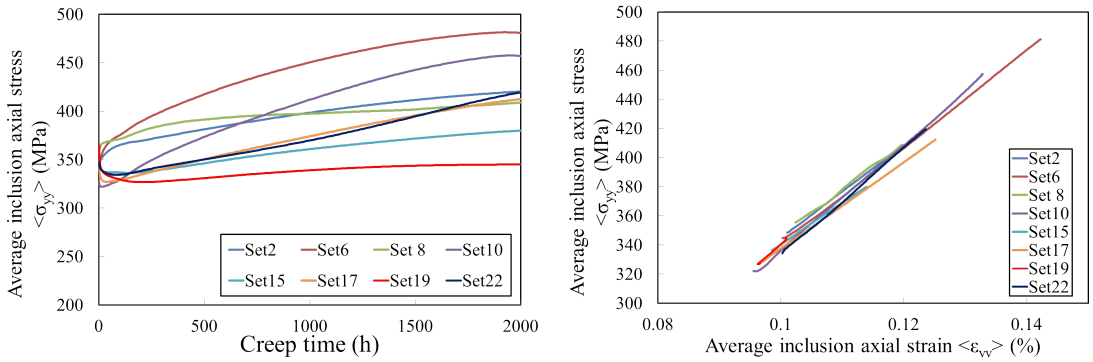

Figure 4.16: Evolution of the average inclusion axial stress in function of (a) creep time and (b) average inclusion axial strain, for eight random couple of random crystal orientations for quasi-2D calculations, (Fig. 2.5).

relaxation is observed for the bicrystal defined by Set $N°2$ (Figs. 3.15b and 3.15c.)

Fig. 3.16b presents the evolution of the average inclusion axial stress, $< \sigma_{yy} >$, versus the average inclusion strain. The curves are quite close. The variation in the triaxiality does not affect much the effective Young's modulus value. However, slight differences in the slopes could also be observed.

4.5.3 Influence of the lattice rotation

The polycrystalline calculations are based on the assumption of perfect grain cohesion during creep deformation. This assumption eliminates grain boundary sliding. Grain boundary sliding is presented in Chapter 1 and numerical applications will be presented in Chapter 5, it is not discussed in this chapter.

In polycrystalline materials, under straining, the rotation of lattice crystallographic orientations leads to the possible evolution of the wholes crystallographic texture, which may affects the mechanical properties. Such rotation occur at the local scale too, allowing increasing or decreasing local stresses. In order to simulate the most accurately as possible the stress fields, we use in our computation the finite transformation assumption. Using the kinetic model of elastoplastic transformation, the Green-Lagrange strain tensor, and the Cauchy stress tensor, the Schmid criterion is then proposed to calculate resolved shear stress on slip system (Eq. 3.16) [142]. For each slip system, $i = [1, 12]$ the resolved shear stress is computed by:

$$\tau^i = \sigma : (\overrightarrow{m}^i \otimes \overrightarrow{n}^i) \tag{4.16}$$

The effect of this lattice rotation could be highlighted in the typical shear stress slip hardening curve of a FCC single crystal oriented for single slip (Fig. 3.17).

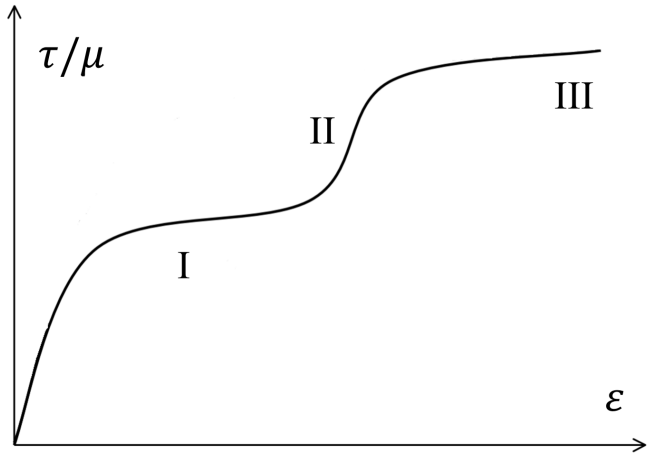

Figure 4.17: A typical hardening curve for a single slip orientated single crystal [202].

Fig. 3.17 shows three stages of work hardening:

- Stage I: the shear stress increases only slowly up to a few ten %. There is only slight work hardening. It corresponds to the activation of only one single slip system. Such behavior is observed in about 2/3 of the single crystals [124]. Dislocations do not interact much with each other, leading to this: 'easy glide' deformation stage. The active slip system is the one with the maximum Schmid factor;

- Stage II: this stage is characterized by a constant work hardening module is about ten times higher than that of stage I. The plastic activation of the single slip system leads to a progressive lattice rotation of the crystal with respect to the tensile axis. Then the primary Schimd factor decreases but the secondary one increases. This finally leads to the activation of secondary slip systems, which were initially less favorably oriented. The interaction of dislocations of the primary and secondary systems induce the formation of various junction. The stress required to deform the crystal increase much strongly (stage II). The slip lines are straight but shorter than in stage I;

- Stage III: There is a decreasing rate of work hardening. This decrease is dynamic recovery and very sensitive to temperature and strain rate.

Nevertheless, in stage II, there is a inverse effect in a polycrystal. For a polycrystal, the increase in the activated slip systems could lead to a decrease in macroscopic stress for macroscopic deformation [125], because of the accommodation of the plastic deformation in neighboring grains. To accommodate the plastic deformation incompatibilities, large elastic deformations are required inside grains and eventually along grain boundaries at high temperature. Higher elastic strains are therefore required. However, in our polycrystalline model, it is assumed that multiple slip systems could be activated. Therefore, lower elastic

strains are required to accommodate (visco-)plastic strain incompatibilities. And the necessary macroscopic stress is smaller for the same value of remote plastic strain [203].

The effect of lattice rotation on the calculated interface stresses is now investigating by comparing with the stresses calculated without. accounting for lattice rotation evolution during creep straining.

Fig. 3.18 shows the maximum interface normal stress, σ_{nn}^{max}, evolution in function of macroscopic strain, E^{vp}, for nine sets of crystalline orientations. Two types of calculations are then carried out, with and without lattice rotation evolution. For one given couple of crystal orientations of the neighbor grains, the maximum normal stress are reached at almost the same interface position along the interface ($\pm 2°$)

If no lattice rotation is accounted for, the evolution of σ_{nn}^{max} with E^{vp} is almost linear (Fig. 3.18). Lattice rotation introduces an additional a non-linearity into the viscoplastic constitutive laws. That may explain why the interface stress evolution with lattice rotation is less linear. The σ_{nn}^{max}-E^{vp} curves are generally concave, as for the majority of the cases obtained with lattice rotation. In fact, during deformation, more and more slip systems are activated, which make it easier to accommodate plastic deformation incompatibilities at the intersection of the elastic inclusion and neighbor grains. Then, lower local elastic strains are required. This may explain the concavity of the σ_{nn}^{max}-E^{vp} curves.

Figs. 3.18a and 3.18c show that the σ_{nn}^{max} stress at low remote plastic strain ($< 0.5\%$) are of the same magnitude, then, the non-linearity is observed. But only if lattice rotation are accounted for. This leads σ_{nn}^{max} stress obtained without lattice rotation higher than the other ones (Fig. 3.18a). Fig. 3.18c shows that, at low strain ($< 3\%$), σ_{nn}^{max} stress calculated with lattice rotation are higher than without ones. Once more, the evolutions of interface stress with lattice rotation are concave. Therefore, for a strain level higher than 4%, the calculated stress without lattice rotation may higher than the other ones, as Fig. 3.18a at lower remote strain.

However, Fig. 3.18b shows that the σ_{nn}^{max} stress calculated with lattice rotation may be higher than the ones computed without lattice rotation. Especially for sets 10 and 19, even at low remote strain ($< 0.5\%$), the stresses accounting for free lattice rotation are still much higher than the ones neglecting lattice rotation. As the grain viscoplastic strains in the vicinity of the interface are much higher than the remote one, such unexpectedly strong effect of lattice rotation may be qualitatively interested.

Finally, we conclude that the accounting for lattice rotation could increase and decrease the interface stress. Generally, neglecting lattice rotation leads to an interface stress dependence with the remote strain which is almost linear up to 4%. On the contrary, lattice rotation leads to more concave evaluations with the remote strain. That explains why, for the majority o f the considered sets of random orientations the interface stresses computed with lattice rotation are

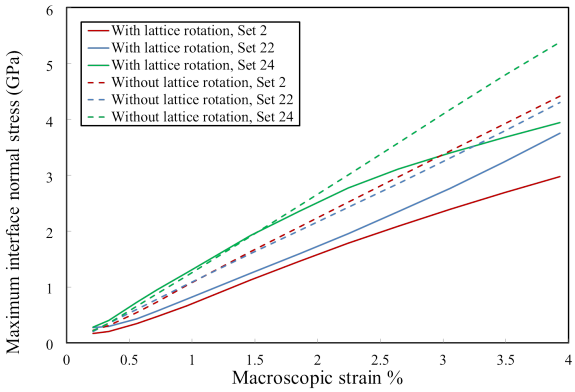

(a)

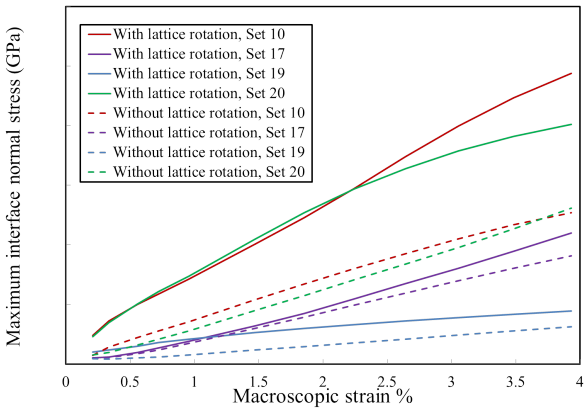

(b)

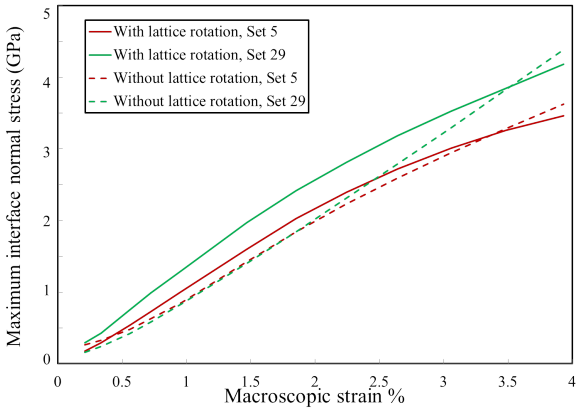

(c)

Figure 4.18: Comparison of evolutions of the maximum interface normal stress versus the macroscopic strain computed either hindering or accounting for lattice rotation. The results for nine couples of random crystal orientations of the neighbor grains are plotted. It can be observed that the maximum interface stress, σ_{nn}^{max}, computed without lattice rotation are (a) higher; (b) lower and (c) close to the ones computed accounting of lattice ration during straining.

expected to be or become lower than the ones calculated with out lattice rotation, provided the remote creep strain becomes high enough ($\approx 10\%$)

4.6 Summary and conclusion

In the present work, the maximum normal stress along the intergranular second phase particle and matrix interfaces are calculated by FE calculations.

Three families of inclusion geometries are considered:

- shape factor;
- symmetric angular tip and tip angle;
- asymmetric angular tip and tip angle.

As fifteen couples of random crystal orientations of particle neighbor grains lead to a statistic representative distribution of stress (Fig. 2.8), therefore, only fifteen couples of 2D plane stress bicrystal calculations are carried out for each inclusion geometry.

The calculation results show that the maximum normal stress increases with the shape factor up to seven, with a stress ratio. For a shape factor of seven, the interface stress is increased with an average factor of 2.03, compared to the circular inclusion. Thereafter, only slight increase is obtained. Further, the dependence of the stress ratio, $\bar{r}_{sf}$, with the shape factor is close to the on predicted by the thermo-elastic Eshelby-Kröner solution.

Symmetric angular tips lead to a large increase in maximum interface normal stress, with a average factor, $\bar{r}_{sym}(\varphi)$, of 1.67, compared to the circular tip case. The tip angle (φ) equal to 30° induces a highest average factor ($\bar{r}(\varphi = 30°) = 2.12$) compare to others ($\varphi = 45°$ and $\varphi = 60°$).

The asymmetric angular tip geometry induces only a slight increase in maximum normal stress, ($\bar{r}_{asym}(\varphi) = 1.09$), compared to the symmetric tip angle. However, in case of a asymmetric tip angle equals 60 °, a decrease is observed, $\bar{r}_a(\varphi = 60°) = 0.85$.

All these calculation results lead us to propose a simplified multiplication equation to calculate the local stresses with a large distribution of crystalline orientations. In Chapter 4, this equation will be applied to calculate the Dyson Law prefactor, α', accounting for all considered microstructure features.

Further, 2D plane stress and 3D calculations are compared for discussion of our 2D plane stress assumption. The comparisons show lower interface normal stresses under plane stress assumption. This agrees with several literature results. Therefore, the interface normal stress is not overestimated. Thereafter, the average inclusion axial stresses, $< \sigma_{yy} >$, with respect to the remote strain are compared under 2D/3D assumptions, and 2D bicrystals considering eight sets of crystalline orientations. In case of an inclusion embedded in the homogeneous matrix, slight 'structural' relaxations are observed under both 2D and 3D assumptions. Further, the stress saturation of the $< \sigma_{yy} >$ stress in function of

creep time is generally observed, which is rarely observed in in the case for the interface normal stresses for a macroscopic strain up to 4%.

The ratio between maximum and minimum average inclusion axial stresses amounts only to 1.4. The one of interface normal stress reaches 5.4, for considered eight sets of crystalline orientations. Further, there is no strong link between the $< \sigma_{yy} >$ and σ_{nn}^{max} values. For example, the maximum value of $< \sigma_{yy} >$ is obtained for Set 6, whereas, the maximum in the interface normal stress, σ_{nn}^{max}, is obtained for Set 10.

Chapter 5

Final development for lifetime prediction

From the 1980s, austenitic stainless steels, in particular the 316L(N) steel, have been widely studied concerning their creep properties, in relationship with their use in components of nuclear reactors, especially the Phénix and SuperPhénix SFR reactors built in France.

The lifetime of the nuclear reactors of Generation IV is estimated as 60 years. Therefore, the main challenge for designing reactors components in austenitic stainless steels is the demonstration of their creep resistance up to 60 years under in-service conditions. The long term creep lifetime predictions require on the one hand to carry out very long term creep tests and on the other hand to understand and model the damage mechanisms in order to propose physically–based lifetime predictions to go beyond the longest test results.

Before prediction long term creep lifetime based on the simulation of Chapters 2 and 3, it is required to check that there are really no other phenomenon influening damage initiation mechanisms.

That is why the other main mechanisms are firstly remained (subsection 4.2). Then, some existing cavity nucleation models are numerically applied, and compared to the experimental results and previous FE computations. Thereafter, the find value of prefactor of the Dyson law, α', is proposed based on our Finite Element calculation results and experimental observations of long term precipitation. Finally, long term creep lifetime predictions are performed. The Riedel model, which combines continuous cavity nucleation through the Dyson law and vacancy diffusion growth, is used to predict long term creep lifetimes. Using the evaluated value of α', our results show that lifetimes are fairly well predicted using the Riedel model. No fitting parameter has been used (subsection 4.4).

The mechanisms of deformation, precipitation and damage which may occur during very long term creep are finally discussed (subsection 4.5).

5.1 Introduction

Some experimental creep results concerning 316L(N) stainless steels are now reminded, adding some recent results concerning in particular long-term creep lifetimes. The microstructure concerning the 316L(N) is described in Chapter 1.

Experimental creep stress-lifetime data of various sheets of 316L(N) steel are plotted for temperatures ranging between 500 and 700°C (Fig. 4.1). The slope change could be clearly observed between the short and long term creep lifetime at 550, 600, 650 and 700°C. Therefore, long-term creep lifetimes cannot be correctly predicted by the extrapolations from short-term data, as the Monkman-Grant relationship [50] or Larson-Miller relationship [54].

For AISI 316L(N) SS, the main short term creep fracture mechanism is necking, which is caused by viscoplastic instability [4, 44]. Further, at high temperature and low stress, intergranular creep fracture is generally observed, as shown by Morris et al. [204], Gandhi et al. [205] and Riedel [51]. Meanwhile, intergranular cavities along grain boundaries are extensively observed in long-term creep specimens.

The first main cause of intergranular cavitation is that vacancies become mobile at elevated temperature. At the typical in-service condition temperatures, diffusion along grain boundaries is, generally, predominant compared to the bulk one. Raj [81] proposed that vacancy diffusion along grain boundaries lead to cluster and form stable cavity nuclei. Another mechanism of cavity nucleation may be second-phase interface fracture as discussed later. And, then, vacancies diffuse under the normal stress acting on grain boundary towards intergranular cavities leading to cavity growth. Intergranular cavitation is observed experimentally in 316 [44, 205]. However, the cavity nucleation mechanism has not been well established yet.

In this chapter, some numerical applications of existing cavity nucleation model are performed to be compared to our predicted ones based on interface stress distribution. And their validations are discussed with respect to experimental results. Thereafter, our Finite Element calculation results are summarized. Combining with the distribution of intergranular particles, the cavity nucleation rate are evaluated (subsection 4.4).

Similarly to Incoloy 800 (Chapter **??**), for 316L(N) SS, at low temperature and high stress, creep stain curves show an acceleration of creep deformation during the third creep stage, which corresponds to the increase in true stress and macroscopic necking (explained in chapters 1 and **??**). The modeling of necking using the Norton law [45] and the Hart criterion [67] allows lifetime predictions in agreement with experimental data up to a transition time of about 10 000 h, but which is temperature-dependent.

Experimental results show that the extrapolation of the stress-lifetime data obtained at high stress based on a power law leads to large overestimations of lifetimes at low stress (Fig. 4.1) [70]. After FEG-SEM-EBSD and TEM observa-

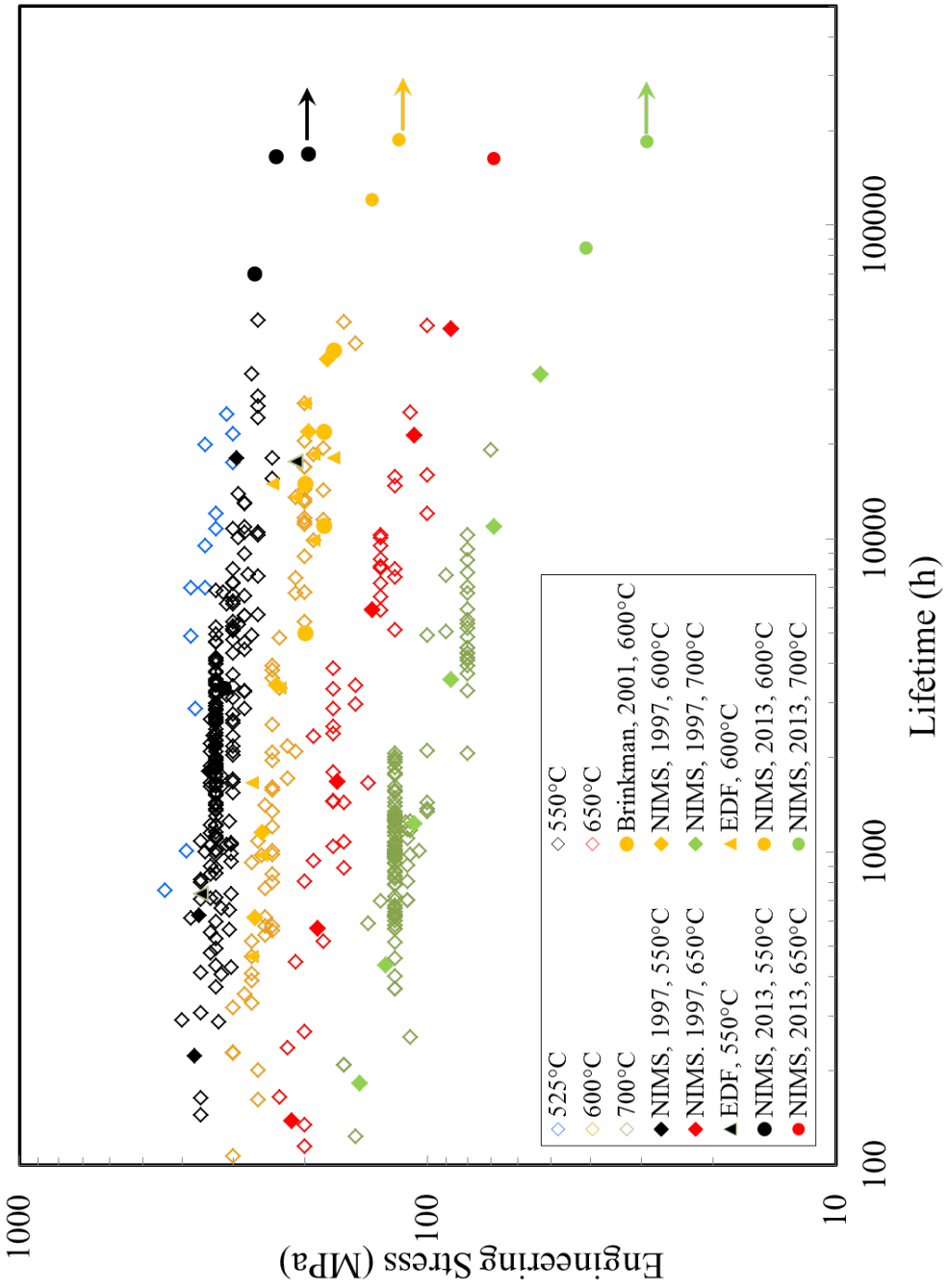

Figure 5.1: Experimental stress lifetime data of 316L(N) stainless steel (CEA, EDF, and Creusot-Loire [40], NIMS [183], ORNL [49]).

tions, these overestimates are mainly due to the fact that intergranular cavitation becomes predominant as the applied stress is decreased (chapters 2 and 3). It is generally observed in metallic materials in the long-term creep regime (Fig. 4.1). The modeling of cavity growth by vacancy diffusion along grain boundaries coupled with continuous nucleation (the Dyson law) proposed by Riedel is carried out in the following. The Riedel model, as proposed for Incoloy 800 (Chapter **??**), is used to predict long term creep lifetime of 316L(N) stainless steel for large ranges of stress and temperature. The predicted creep lifetimes are compared with numerous experimental creep results. Several creep data of 316 SS are compared with our predictions, especially the data of CEA, EDF, Creusot-Loire (316L(N)), the National Institute for Materials Science, Japan, NIMS (316-HP) [183] and others [1, 2, 44, 49, 49, 206, 207]. Cui et al. [115] carried out the experimental observations and image processing to measure experimentally the prefactor of the Dyson law, α' slightly dependent on stress and temperature. Then, using the Riedel model, these authors predicted long term creep lifetime based on these measured α' values, whereas our new long term lifetime predictions are based on predicted α' values.

In our study, the creep lifetime predictions are carried out with the calculated α', based on our Finite Element calculations and measured values of large intergranular particle densities. Experimental long term creep lifetimes are generally between well predicted by the upper and lower bound curves predicted by the Riedel model accounting for the uncertainty.

5.2 Creep damage mechanisms

5.2.1 Necking

Necking is the dominant fracture mechanism predominant in the short-term creep regime. The necking onset (Fig. **??**) is modeled, as in the case of Incoloy 800 alloys (Chapter **??**), based on the Hart criterion [67]. Lim et al. [68] deduced that necking starts when the minimum creep strain rate, $\dot{\varepsilon}_{min}$, was just been reached. By combining the Norton law, the volume conservation and the computation of the cross-section evolution of the necking part after the necking onset, Lim et al. [80] calculated the fracture time, t_f. The formula proposed by Lim et al. [68] is:

$$t_f - t_{min} = \frac{1}{\dot{\varepsilon}_{min} n}[1 - \delta D_r(2 + \varepsilon)]^n \tag{5.1}$$

The parameter variation ranges between the different 316L(N) batches was evaluated by Cui et al. [115], and is presented in Table 4.1. Taking into account the uncertainties in parameter values, Cui et al. [115] performed the lifetime predictions based on the Necking model (Eq. 4.1).

They considered the 525-700$°C$ temperature range [44, 115] The results show that creep lifetimes are well predicted for lifetimes up to about $10^4 h$ in the

Parameter	Notation	Values
ε_{min}	Strain level at which $\dot{\varepsilon}_{min}$ is reached, %	[0.8, 3.5]
t_{min}	Creep time at which ε_{min} is reached	$\frac{t_{min}}{t_f} \in$[0.1, 0.3]
δD_r	The initial variation in diameter relative to the initial average diameter $\bar{D}$, $\delta D_r = \delta D/\bar{D}$	$[10^{-4}, 5 \cdot 10^{-3}]$

Table 5.1: Parameters used in Eq. 4.1 allowing short term lifetime predictions in 316L(N) stainless steels, based on the necking mechanisms.

considered temperature range. However, it leads to large overestimations as considering long-term creep, because intergranular damage becomes dominant in this regime as extensively shown by observation in stainless steel [44, 115].

More general short term lifetimes are fairly well predicted in Incoloy 800 alloys (Chapter **??**) and in the ferritic-martensitic grade 91 steel [68] in large ranges of temperature (respectively, 500-760°C and 500-600°C).

Then, we focus only on long term lifetime predictions. We are especially interested in the cavity nucleation mechanism for which many questions seem to remain and physically-based models avoid fitting parameters.

5.2.2 Intergranular damage

At high temperature, vacancies become much more mobile. Additionally, diffusion along grain boundaries is predominant compared to the bulk one. This phenomenon leads to the intergranular damage (as discussed in Chapter 1) and particularly growth. The intergranular damage could be divided into three stage as continuous cavity nucleation, cavity growth and the cavity coalescence.

According to numerous measurements carried out on interrupted creep test specimens, Dyson suggested that cavities nucleate continuously and at a constant rate during each creep, named cavity nucleation rate $\dot{N}_0$. This phenomenological law describes well the microscopic measurement results obtained for various materials, temperature and stress, as shown in literature [74, 75, 83, 100, 208].

In Chapter 1, our literature review highlight two mechanisms for cavity growth, diffusion growth and viscoplastic growth, and the intermediate 'third mechanism' is the coupling between diffusion and viscoplastic growths. However, using the Rice length (chapters 1 and **??**) and microscopic measurements of cavity radius, Cui [44] demonstrated that, for long term 316L(N) SS test, the ratio between the average cavity radius, $\bar{r}$, (the minimum diameter of the counted cavities is $200nm$) and the Rice length, L_R, is lower than 0.2. Following the criterion proposed by Needleman and Rice [100], as $\bar{r}/L_R$ is lower than 0.2, cavity

growth is controlled essentially by vacancy diffusion. And the cavity growth by viscoplasticity is negligible except during the coalescence process. Therefore, only cavity growth by vacancy diffusion along grain boundaries is accounted in the evaluation of the intergranular damage.

Following the experimental observations in 316L(N) carried out by Cui [44] and in Incoloy 800 alloys (Fig. **??**, Chapter **??**), cracks of a few ten microns are formed by the coalescence of cavities. However, when measuring the cavity density, these cracks are split into several individual cavities based on the small remaining cavity ligaments observed along these micro cracks. Therefore, this process is neglected in our lifetime predictions using the Riedel model.

The Riedel model [51] combined continuous cavity nucleation and vacancy diffusion cavity growth mechanism. This model could lead correct long term creep lifetime predictions [68, 115]. Nevertheless, as shown in Chapter 1, the cavity nucleation mechanism has not been well established yet. Even if the Dyson law allows a fairly well description of most of the experimental data, it is still a phenomenological law. The physically-based understanding of cavity nucleation mechanism is required. Two mechanisms were proposed:

- the agglomeration of cavities leading to the continuous formation of stable nuclei under a given remote stress;

- the particle-matrix interface fracture.

Both mechanisms are explained and the corresponding equations are numerically applied in the following. Therefore, in the next two subsections, we focus only on the two cavity nucleation mechanisms. Further, the cavity nucleation rate will be modeled based on classical approaches. And the coupling with stress concentrators is next discussed in section 4.3.

5.2.3 Thermally-activated nucleation of stable vacancy nuclei

As shown in Chapter 1, the cavity nucleation mechanism based vacancy clustering agglomeration was highlighted by Raj and Ashby [77], in the framework of the theory of thermally-activated processes. They proposed Eq.4.2 to calculate the steady-state cavity nucleation rate:

$$\dot{N}_0 = \frac{4\pi\gamma_s D_{gb}\delta}{\Omega^{4/3}\sigma_n} N_0^{max} exp(-\frac{4\gamma_s^3 F_v}{\sigma_n^2 k_b T}) exp(\frac{\sigma_n \Omega}{k_b T}) \tag{5.2}$$

This equation is often called as the Raj nucleation law. Typical values of input parameters are provided in Table 4.2. The microstructure-based parameter, N_0^{max}, is the total number of the possible cavity nucleation sites per unit grain boundary area. In alloys containing intergranular second phase particles, the cavity nucleation sites are the intergranular second phase particle-matrix interfaces. Therefore, the N_0^{max} density could be considered as the density of intergranular particles per unit grain boundary area. Arnaud [82] evaluated experimentally a

particle density of $3 \cdot 10^8\ m^{-2}$ in a 316 steel at $650°C$, with an average size of $1\mu m$. The NIMS data sheet [2] provided a saturated density of σ phase particles in 316H TB as $1.25 \cdot 10^9\ m^{-2}$. Our analysis of the data of Cui [44] leads to a value of $6.85 \cdot 10^{11}\ m^{-2}$ in 316L(N), with a minimum size of 100nm. Since, the values of Arnaud [82] and NIMS data sheet [2] are in the same order of magnitude, only the values of Arnaud and Cui are used to calculate the cavity nucleation rate based the Raj model (Eq. 4.2), for getting general trends.

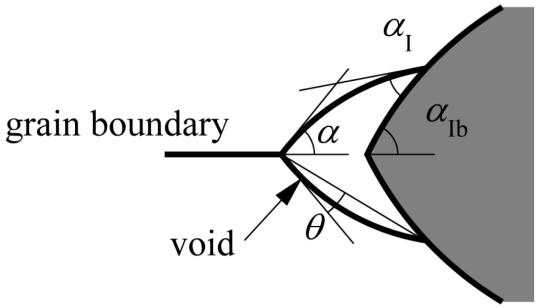

Figure 5.2: Geometry of a cavity form as by Raj and Ashby [77].

Further, assuming a cavity shape similar to the one plotted in Fig. 4.2, Raj and Ashby [77] defined a cavity geometric function, F_v:

$$F_v = \frac{2\pi}{3}(2 - 3cos\,\alpha_m + cos^3\,\alpha_m) \tag{5.3}$$

where $\alpha_m = \frac{1}{2}(\alpha + \alpha_I - \alpha_{Ib})$ (Fig. 4.2). The angles α, α_I and α_{Ib} are calculated based on surface tension equilibrium equation:

$$\begin{aligned} cos\,\alpha &= \frac{\gamma_{gb}}{2\gamma_{metal}} \\ cos\,\alpha_I &= \frac{\gamma_{interface} - \gamma_{second\ phase}}{\gamma_{metal}} \\ cos\,\alpha_{Ib} &= \frac{\gamma_{gb}}{2\gamma_{interface}} \end{aligned} \tag{5.4}$$

where, $\gamma_{interface}$ is surface energy of the particle-matrix interface, γ_{gb} is the surface energy of grain boundary, $\gamma_{second\ phase}$ is the surface free energy of metallic matrix and $\gamma_{second\ phase}$ is the surface free energy of second phase particle. Using the surface energy values shown in Table 4.2 and the ones used in Chapter 2 (Table 2.4), we deduce $F_v \approx 0.3$.

However, Raj and Ashby [77] proposed three values of F_v as 0.5, 10^{-2} and 10^{-5} to study the effect of F_v on the cavity nucleation rate.

Fig. 4.3 shows the dependence of the cavity nucleation rate in 316 stainless steel with respect to F_v and the local normal stress, σ_n, calculated using Eq. 4.2. The considered Young modulus amounts to 150GPa ($600°C$). Two values of N_0^{max} reported in [82] and [44] are used, as well as $F_v = 10^{-5}, 10^{-2}, 0.3$ and 0.5. Our results with $F_v = 10^{-5}$ is very similar to the one of Arnaud [82] (Fig. 1.14, Chapter 1). Fig. 4.3 shows that the value of N_0^{max} influences only the

Parameter	Notation	Values
Ω	Atomic volume, m^3	$1.21 \cdot 10^{-29}$ [51]
$D_{0gb}\delta$	Grain boundary self-diffusion prefactor times the grain boundary thickness δ, $m^3 s^{-1}$	$2 \cdot 10^{-13}$ [59]
Q_{gb}	Activation energy for grain boundary self-diffusion, kJ/mol	167 [59]
γ_{metal}	Surface free energy of matrix, Jm^{-2}	2.5 ± 0.5 [209]
$\gamma_{interface}$	Surface free energy of incoherent particle-matrix, Jm^{-2}	$1.5 - 2$
$\gamma_{second\ phase}$	Surface free energy of second phase particle, Jm^{-2}	$2 - 2.5$
γ_{gb}	Grain boundary surface energy, Jm^{-2}	0.75 ± 0.45 [210]
N_0^{max}	Total number of possible cavitation sites m^{-2}	$3 \cdot 10^8$ [82] $6.85 \cdot 10^{11}$ [44] $1.25 \cdot 10^9$ [2]
F_v	Geometric function describing the cavity geometry	0.5, 10^{-2}, 10^{-5} [77]

Table 5.2: Parameters used in Eq. 4.2 allowing the calculation of the cavity nucleation rate.

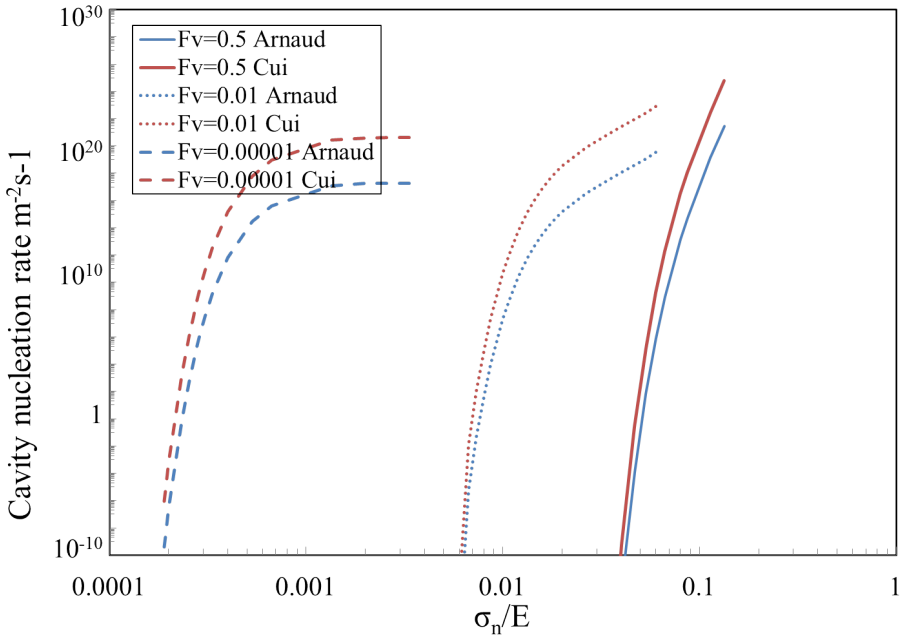

Figure 5.3: Variation of cavity nucleation rate in function of local normal stress for 316 stainless steels at $600°C$, with two values of N_0^{max} measured by Arnaud [82] and Cui [44]. Raj model, Eq. 4.2 [77].

maximum value of $\dot{N}_0$. The calculated curves assuming $F_v = 0.3$ and $F_v = 0.5$ are very similar. However, for the same level of cavity nucleation rate, the small increase in F_v from 0.3 to 0.5 requires a large increase in the normalized normal stress. Additionally, for $F_v = 10^{-2}$, the required threshold stress is 100 times higher than the one for $F_v = 10^{-5}$. Furthermore, in this model, for a given F_v value, the nucleation rate increases hugely with stress increasing due to the exponential expressions contained in Eq. 4.2. For example, for $F_v = 10^{-5}$, before the saturation, a change in stress lower than 10% leads to a huge change in nucleation rate (10^4 times) in nucleation rate. The predictions are then unstable with respect to the input parameters (Eq. 4.2).

Therefore, the Raj model could is not able to predict correctly the cavity nucleation rate. The predicted values are much lower than the measured ones. Then, the interface fracture is now considered to help to predict correctly cavity nucleation rate.

5.2.4 Interface fracture

In many alloys, the damage initiation sites are the inclusions or second-phase particles existing in the material. In case of 316L(N), both $M_{23}C_6$ and σ phase particles are harder than the surrounding matrix and generally assumed to behave elastically in the considered rage of temperature (500-700°C) (Table 2.3).

There are two modes of formation of a cavity involving an inclusion:

-the fragmentation of tjos inclusion, as observed for Ti(C,N) in Incoloy 800 (Fig. **??**);

-the decohesion of the inclusion-matrix interface (Fig. **??** and Fig. 3.3).

During creep deformation, the intergranular damage initiation consists most often in the decohesion of the intergranular precipitate-matrix interfaces. Various criteria based on theoretical models have been proposed to predict the macroscopic strain or stress. They can be classified into two main categories, based either on an energy criterion (subsection 4.2.4.1) or on a critical stress condition (subsection 4.2.4.2). The coupling between both is then discussed in subsection 4.2.4.3.

5.2.4.1 Energy criteria

A necessary condition for the formation of a cavity is that the production of the new free surface is energetically favorable. During the decohesion of precipitate-matrix interface, a dimensional analysis shows that fracture is expected to start at first along the largest inclusions [188, 211].

Indeed, the energy released by a full decohesion of the interface is a fraction of the energy stored in the inclusion and its neighborhood. This energy is proportional to the volume of the inclusion and increasing with stress and remote strain. After the interface fraction, the released energy should be equal to the

required surface energy which is proportional to the inclusion surface. The size effect thus highlighted is the one of the main characteristic of energy criteria.

The criterion proposed by Tanaka et al.
Tanaka et al. [188] proposed a energetic criterion using a solution to the problem of an elastic inclusion embedded in a homogeneously plastically deformed matrix provided by the Eshelby theory. The homogeneous plastic strain of the matrix necessary to initiate the decohesion of the inclusion in uniaxial tensile test is:

$$E_c^p = \sqrt{A_T \frac{S}{V} \frac{\gamma_{frac}}{E}} \tag{5.5}$$

where, $\gamma_{frac} = \gamma_{metal} + \gamma_{second\,phase} - \gamma_{interface}$, E_c^p is the macroscopic plastic strain necessary for the initiation of interface decohesion, A_T is a dimensionless coefficient depending on inclusion geometry and inclusion elastic constants, E, ν, E_i and ν_i the Young's moduli and Poisson's ratio of, respectively, matrix and inclusion, S and V are, respectively, the inclusion surface and volume.

Eq. 4.5 predicts that the interface decohesion occurs, at first, on the largest inclusion, following $E_c^p \propto r^{-\frac{1}{2}}$. Thus, for sufficiently large inclusion, the cavity initiation is energetically favorable, provided the remote plastic strain is large enough.

The Brown and Stobbs criterion
Brown and Stobbs [212] proposed a energy criterion for the initiation of interface fracture using an approach combining continuum mechanics and physical metallurgy. This criterion was essentially aimed to explain the effect of spherical hard particles that cannot be deformed in a metal. They introduce a new characteristic length into the problem, the Burgers vector length, b. This criterion is independent on the inclusion size, as:

$$E_c^p > \sqrt{\frac{3 \cdot \gamma_{frac}}{\mu_i b}} \tag{5.6}$$

where μ_i is the inclusion shear modulus.

The model based on Eshelby solution
Based on the Eshelby solution (subsection 3.3.1) and the hypothesis of full decohesion of inclusion-matrix interface, we propose:

For a circular inclusion, $a = b = c$:

$$E_c^p = \sqrt{\frac{2\gamma_{frac}}{(1 - \beta\mu a)}} \tag{5.7}$$

And For a prolate inclusion, $a > b = c$:

$$E_c^p = \sqrt{\frac{2\gamma_{frac}}{(1-\beta\mu a)}}\sqrt{\frac{1}{\frac{2}{3}\frac{b}{a}+\frac{1}{2}}\cdot\frac{1}{A_{SH}}} \tag{5.8}$$

where A_{SH} is a constant, depends only on inclusion shape factor, a/b. For $a/b = 1$, A_{SH} value amounts to 1 and $a/b = 3$, $A_{SH} = 1.5$. This model is denoted as 'Model_SH' in Fig. 4.4.

5.2.4.2 Stress condition

The decohesion of inclusion-matrix interface occurs if the normal stress, σ_{nn}, exceeds a critical value, σ_c. Several initiation criteria corresponding to such a condition were proposed in literature. The Universal Bounding Energy Relationship (Eq. 2.11) is presented in Chapter 2 (subsection 2.5.1), which can be used to evaluate numerically the interface fracture stress, σ_c. Or it may be predicted directly from DFT simulation of a full deformation of a bimaterial separated by the interface under stress. Finally, it could be used by careful micromechanical tests.

The Argon et al criterion
To predict the initiation of the damage by interface decohesion of an undeformable inclusion in a plastically deformed matrix, Argon et al. [213–215] proposed the stress condition as:

$$A_A\Sigma - p = \sigma_c \tag{5.9}$$

where A_A is a constant which depends on the inclusion geometry only, σ_c is the critical interface fracture stress and p is hydrostatic pressure.

In case of uniaxial tension, $p = -\Sigma/3$. Then, Eq. 4.9 can be written as:

$$\Sigma = \frac{\sigma_c}{A_A + 1/3} \tag{5.10}$$

Inclusion size effect could not be investigated by this stress criterion.

The Goods and Brown criterion
Accounting for the local dislocation density as a function of strain, Goods and Brown [180] proposed:

$$E_c^p > \frac{1}{30}\frac{\sigma_c}{\alpha\mu}\frac{r}{b} \tag{5.11}$$

where α is the Taylor law parameter depends on material.

The main difference between the decohesion criteria discussed above relates to

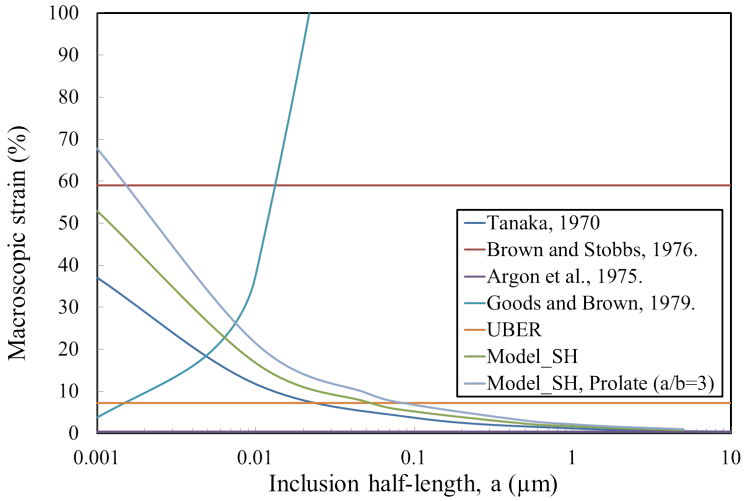

Figure 5.4: Critical macroscopic plastic strain at the initiation of inclusion-matrix interface decohesion, using the most cited energy and stress criteria, as a function of the inclusion size. The input parameters are provided in Table 4.3

the influence of the inclusion size on critical macroscopic strain. Fig. 4.4 presents the computed critical remote strain using the different models. The input parameter values are provided in Table 4.11. All the calculations are carried out for a spherical inclusion, except the 'Model_SH, Prolate (a/b=3)' one. The used value of the interface fracture stress, σ_c, in the Goods and Brown criterion amounts 5GPa, as evaluated by UBER (subsection 2.5.1). For Argon's criterion and UBER relationship, the critical remote strains are calculated using stress evolution calculated by Eshelby solution (subsection 3.3.1).

E (GPa)	E_i (GPa)	ν	ν_i	γ_{frac} (Jm^{-2})	α	σ_c (GPa)
150	350	0.3	0.3	4	0.3	5

Table 5.3: Parameters used as applying the energy or stress criteria, allowing the calculation of the critical macroscopic plastic strain at the initiation of inclusion-matrix decohesion.

Fig. 4.4 shows that the predictions based on by Brown and Stobbs [212], Argon et al. [213, 215] are independent on the inclusion size. The required strain have a large variation. The required strain predicted by the Argon et al. criterion reaches only 0.5%. However, the used interface stress evolution in function of macroscopic strain is calculated by the Eshelby theory. This may leads to an underestimation of the required strain. The model of Goods and Brown [180] predicts that the interface decohesion occurs firstly on the smallest inclusion. Such tendency is classically predicted by geometrically necessary dis-

location (GND) based model, for which the smallest inclusions are the hardest. This size effect disagrees with the one arising from the Tanaka et al. and our energy equilibrium criteria [188]. Further, microscopic observations show that the large inclusions could have interface decohesion earlier than the small ones [117]. This point is qualitatively predicted by the model proposed by Tanaka et al. [188] and our method. The energy criterion proposed by Tanaka et al. underestimate the critical remote strain compared to our method. And our method predicts that, for a higher shape factor, a/b, the required critical remote strain is higher.

In case of prolate inclusion with shape factor amounts to three, (a=3b=3c), our method predicts that for a macroscopic strain of 4%, only inclusions with half-length higher than $0.5\mu m$ could have interface fracture. This leads to a precipitate size of $1\mu m$. According Table 2.5, only σ phase particle could reach such precipitate size.

To conclude this part, for a sufficiently small inclusion radius, the stress criterion is reached before the energy criterion. And for a large enough inclusion, the energy criterion is reached before the critical stress condition [117, 211]. The two criteria must be simultaneously fulfilled, in order to predict interface fracture and corresponding remote strain. They should be determined by the energy criterion for the small inclusions and the stress criterion for the large ones.

Therefore, we focus only on the stress criterion for the evaluation of α', assuming that the energy criterion is already fulfilled for all σ phase particles. Further, the interface decohesion requires a high interface stress, about $5 \pm 1GPa$ evaluated by the UBER. Then, several stress concentrators are now discussed to understand and predict interface fracture.

5.2.4.3 Double criterion

Previous energy and stress criteria are generally based on the Eshelby solution or with questionable hypotheses. Further, it is necessary to apply both energy and stress criteria at the same time to predict more accurately interface fracture. Leguillon [216] showed that the combination of a Griffith-like energy criterion and a maximum tensile stress criterion allows predicting the failure at interface corners of assemblies subjected to mechanical loadings. The double-criterion fracture model can be related to atomistic theories which consider two layers of atoms along their separation. Sauzay et al. [90, 217] used the double-criterion to simulate intergranular microcrack initiation induced by slip bands impacting grain boundaries during tensile deformation.

This combined criterion is related to the cohesive zone model (CZM), which makes it possible to account both criteria at same time. And a further non-linear cohesive behavior could be accounted. Therefore, the cohesive zone model (CZM) is strongly suggested to be used for the interface fracture modeling and introducing more correctly of the particle.

Several CZM laws have been used in the past. Needleman [218] used polynomial and exponential functions of CZM behavior to describe the tensile-separation relationship. Tvergaard and Hutchinson [219] used a trapezoidal shape cohesive curve, applied to elastoplastic materials. Camacho and Ortiz [220] used a linear model to investigate damage impact in brittle materials.

In this part, we focus on a parabolic cohesive law (Fig. 4.5), which has already been implemented in Cast3m finite element software. This cohesive law is presented in more details in Appendix C. Liu [221] predicted fatigue microcrack initiation induced by slip band extrusion observations during fatigue loading. The application of either the double-criterion by Sauzay et al. [90, 217] or CZM modeling by Liu [221] show the validity of the predictions as compared with experimental tests.

It should be noticed that the physically based double choice of the fracture parameters is a key point in double-criterion and in cohesive zone model. Two parameters are generally used in cohesive zone models: the critical fracture stress, σ_c, and the fracture energy, γ_{frac}. Two types of particle-matrix interfaces are considered in agreement with observations (Fig. 3.2), coherent and incoherent interfaces. The ones for coherence interface were evaluated using DFT calculations by Barbé et al. [171]. Barbé et al. [171] proved that the Universal Bounding Energy Relationship allows the prediction of the critical stress with an accuracy of $\pm 10\%$ with respect to the results provided by simulation of a full tensile test run up to fracture. They showed that the Griffith criterion is almost accurate too. But simulating a full tensile test on a bimaterial containing an incoherent interface is out of the computation. The fracture energies are deduced from surface and interface energies provided by DFT computations and measurements (Table 2.4). And finally, the critical stress is deuced based on estimation of d_0 and E_{inter}.

Interface	Coherent	Incoherent
σ_c (GPa)	14.3	5 ± 1
γ_{frac} (Jm^{-2})	4.52	2-5

Table 5.4: Input parameters for cohesive zone model for coherent [171] and incoherent interfaces.

The interfacial normal stress (σ_{nn})-opening displacement (δ) relation used to simulate the interface fracture process is plotted in Fig. 4.5. The mechanical work increases with the opening displacement. The per unit area value, W, is defined by:

$$W = \int_0^{\delta} \sigma_{nn} d\delta \tag{5.12}$$

When δ reaches the critical value, δ_f, the work of opening displacement equals

fracture energy, $W = \gamma_{frac}$.

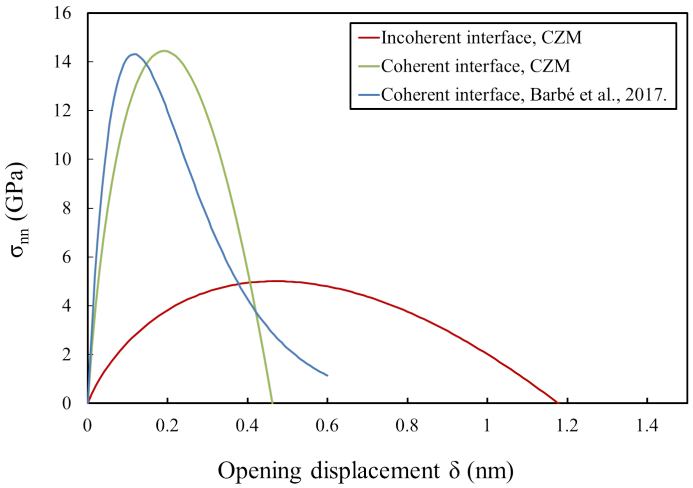

Figure 5.5: Interfacial normal stress in function of the opening displacement for incoherent and coherent interfaces provided by analytical solution of CZM, and the coherent $M_{23}C_6$-matrix interface separation law provided by DFT calculations [171].

The analytical CZM curves for incoherent and coherent interfaces with the parameters provided in Table 4.4 are plotted in Fig. 4.5. In case of coherent interface, Fig. 4.5 shows that the CZM curve describes rather well the parabolic form of σ_{nn}-δ curve, compared to the DFT one [171]. This leads us to use the parabolic cohesive behavior, but not others. From our knowledge, no such DFT calculation has yet been carried out for incoherent interface fracture. Further, our results show that incoherent interface fracture requires a opening displacement much higher than the coherent interface one.

A cohesive zone area is defined by three zones, the first one corresponds to a stress free surface, which is a fully fractured interface. The second one called interaction zone or process, where the cohesive forces are non-zero. Finally, the third one is non-damaged zone where the opening stress has not been reached yet (Fig. 4.6).

In our FE calculations in progress, the thickness of cohesive zone is chosen as being equal to the thickness of incoherent interface, $1.5nm$ (Fig. 4.7), which allows a straight-forward evaluation of the CZL curve initial slope. To investigate the influence of inclusion size on the interface fracture process, cohesive elements are meshed along the inclusion-grain interfaces (Fig. 4.7).

The cohesive zone makes it possible to investigate progressively the transition from the non-damaged zone to interface decohesion, and the size effect of inclusions. CZM calculations are in progress and the results will be compared with the ones obtained by combining FE computation of interface stress fields and a simplified energy balance (Eq. 4.8).

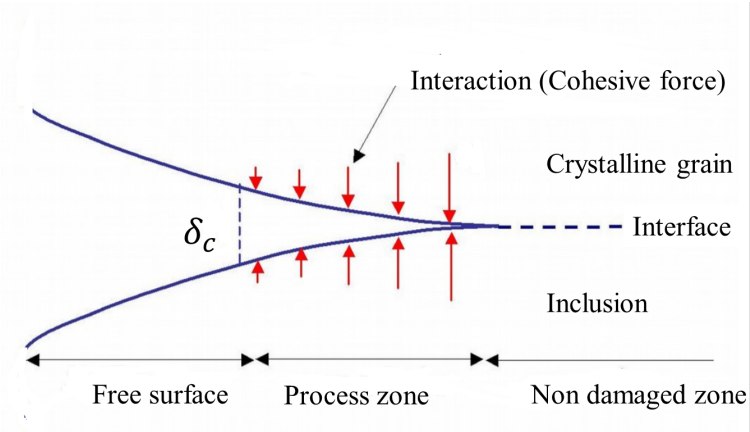

Figure 5.6: Schematic presentation of the different area along a cohesive zone

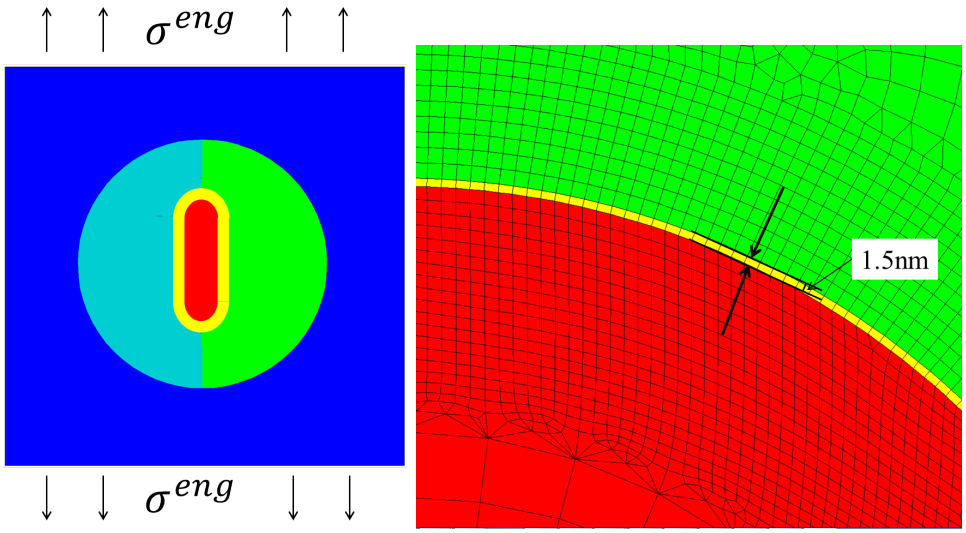

Figure 5.7: (a) Schema of a quasi-2D mesh with cohesive element (yellow) along inclusion-grain interfaces, the thickness of the cohesive zone is dilated for the sake of clarify; (b) zoom-in of the quasi-2D mesh, the cohesive element thickness is 1.5nm.

5.3 stress concentrators

As shortly discussed in Chapter 1, for reaching high interface stress, several mechanisms have been proposed, as grain boundary sliding, impact of pile-ups or slip bands, etc. In this subsection, our aim is to compare the interface stress fields we compute accounting for the viscoplastic deformation of the whole neighbor grains to the ones provided by the stress concentrators most refereed in literature in alloys with intergranular particles. Therefore, the analysis and the numerical applications based on these classical models are now carried out. Finally, our Finite Element calculation results are also discussed.

As shown in Chapter 1, the pile-up mechanism is dominant only at low temperature (as ambient temperature). Additionally, the stress fields may be overestimated using the pile-up theory, which assumes the pile-up length as grain size, and dislocations are located on the same atomic plan. Finally, our TEM observations do not show significant pile-ups close to particle matrix interfaces. Therefore, the pile-up mechanism is not be accounted in this subsection.

5.3.1 Slip bands

Watanabe and Davies [222] carried out creep tests on high purity copper bicrystal specimens. Their results show clearly slip bands and some intergranular cavities. Then, Watanabe [223] proposed that the cavity initiation caused by the interaction between grain boundary sliding and slip band impact. These lead him to propose that cavitation occurs due to both primary and secondary slip system activation (Fig. 4.8a).

Some circular shape cavities were also observed in copper by Watanabe and Davies [223]. Such a shape does not correspond to the proposed nucleation mechanism (Fig. 4.8a). It may be due to the fact that the observed cavities are very large ($25 - 100\mu m$), which meacs that they are already in the growth process. Or this mechanism could not explain correctly the cavity nucleation process. Further, interestingly, the cavities do not coalesce together into a crack, but keep the circular shapes in Watanabe's experiment.

Guo et al. [224] carried out tensile tests on a high purity Titanium (without particles). Then, by coupling EBSD measurement and crystal plasticity FE calculations, they evaluated the local stress caused by the impact of slip bands. During tensile testing, slip bands are clearly observed. The maximum measured local stresses reach only about 400MPa, which is below the typical critical stresses for the interface fracture. Such low value may be related to the rather low spatial resolution used by these authors ($0.2\mu m$).

Recently, considering a slip band of thickness from 500 μm up to $1\mu m$, embedded in an elastic matrix, Sauzay and Vor [90] carried out Finite Element computations. Their results show a strong intergranular stress singularity at the tip of slip band, may reach a factor of ten. The computed local stresses much

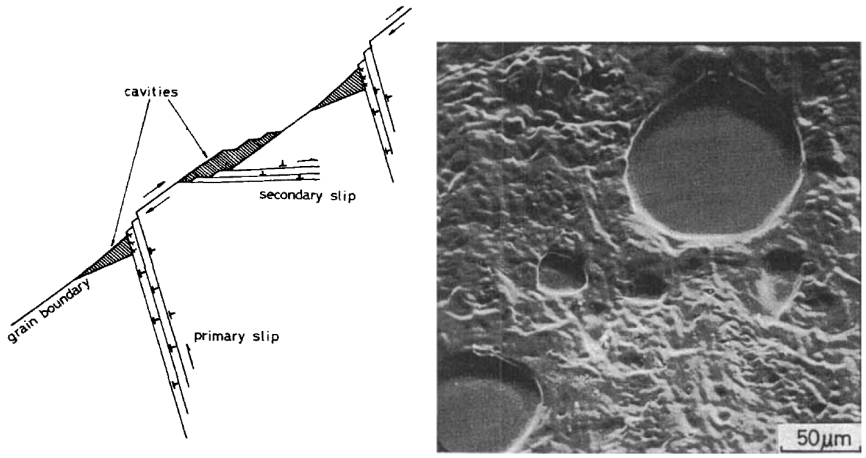

(a) (b)

Figure 5.8: (a) primary and secondary slip systems do both contribute to the formation of intergranular cavities; (b) observed circular shape cavities [223], Cooper bicrystal, $677°C$, 3.9MPa.

higher than the value measured by Guo et al. [224]. It is may because the used resolution of HR-EBSD is $0.2\mu m$. However, the computations of Sauzay and Vor [90] highlighted high stress magnitude at a smaller distance from the slip band and grain boundary impact (typically $0.02\mu m$ away from the slip band corner for a slip band thickness of 100nm).

However, slip bands are generally observed on fatigue [221, 225], tensile deformation [90, 226], creep-fatigue [165, 227] and post irradiation loading [228, 229]. It was observed for high strain rate creep test ($10^{-4}s^{-1}$) in Ti-alloys [86, 230]. But, it is not usually observed for long term creep tests, for which strain rate are low ($< 10^{-7}s^{-1}$).

5.3.2 Grain boundary sliding

For long term creep, a specific deformation mode occurring along grain boundaries is often reported [179, 231–234]. It consists in grain boundary sliding which may leads to grain boundary damage.

It is generally believed that grain boundary sliding induces stress concentrations close to the grain boundary particles, ledges and triple points. Raj [81] proposed that grain boundary sliding favors cavity nucleation because of these stress concentration. Grain boundary sliding decreases indeed the incubation time needed to nucleate stable cavities around fine intergranular precipitates by a factor of two. Therefore, Raj considered that the critical nucleation stress provided by Raj model (subsection 4.2.3) cannot be reached without grain boundary sliding.

White et al.[235] proposed that the grain boundary sliding leads two types of cavities which differ by both their location and geometry. In the case of stress concentrations induced by the geometrical heterogeneities along grain boundaries, it will facilitate the cavitation similarly to what is shown in Fig. 4.9b. The corresponding type of cavity is called round cavity (r), which is characteristic of damage at high temperature and low stress. In case of the stress concentration at triple points, cavities called wedges (w) are formed (Fig. 4.9a), which is characteristic of damage at relatively low temperatures and high stresses. The triple point cavities (w) could be modeled as microcracks. Careful observations carried out by Fields and Ashby [236] showed that in some cases wedge-like cavities result from the coalescence of round cavities of a significantly lower average size (Fig. 4.9c). Only w-type cavities are directly produced by grain boundary sliding.

In many commercial alloys, second phase particles are located along grain boundaries. After analyzing the stress field around intergranular particles, Lau et al. [237] (see reference [51]) calculated the normal stress, σ_{nn}, acting on the particle matrix interface close to the particle tip:

$$\sigma_{nn} = \tau_\infty (\frac{p}{r})^s (\frac{\lambda_p}{p})(0.572 + 0.039n) \cdot \frac{(1-s)cot\varphi}{(2cos\varphi)^s} \tag{5.13}$$

with λ_p the distance between two particles, p the particle diameter and r the distance from the particle tip (Fig. 4.10). This distance may be chosen as the stable cavity nucleus size, r_c. As usual, the Norton law exponent is denoted as n, φ is the particle tip angle (Fig. 3.9), τ_∞ is the shear stress acting on the grain boundary away from the particle. Assuming plane-strain tension, τ_∞ can be evaluated as $\Sigma/\sqrt{3}$ [51], with Σ the remote tensile stress. The exponent of the stress singularity field is denoted as s with: $\sigma_{ij} \propto r^{-s} g_{ij}$, as shown by Lau et al. [237]. The singularity exponent, s depends on both n and φ. From the values reported in [238], it can be concluded that the singularity exponent s decreases with increase in n and increase in φ. However, the evaluation of the s exponent has not been fully explained in [238]. For the 316L(N) SS under study at $600°C$, the Norton law exponent amounts to $n = 9.12$. Therefore, for the numerical application of Eq. 4.13 to 316L(N), the values $n = 7$ and $\varphi = 60°$ are selected in the parameters presented by Riedel [51]. This leads to a low stress singularity exponent of only $s = 0.101$. Then, Eq. 4.13 provides the description of the stress field close to the particles:

$$\frac{\sigma_{nn}}{\Sigma} = 0.253 (\frac{p}{r})^{0.101} (\frac{\lambda_p}{p}) \tag{5.14}$$

For the critical cavity size $r = r_c = 18nm$ evaluated by $r_c = \frac{2\gamma_s}{\Sigma}$, with $\Sigma = 220MPa$. And for the large precipitate sizes under study, $p = 3\mu m$ (Fig. 3.2a), Eq. 4.14 provides a stress concentration factor of only: $\sigma_{nn}(r_c)/\Sigma = 0.42\lambda_p/p$.

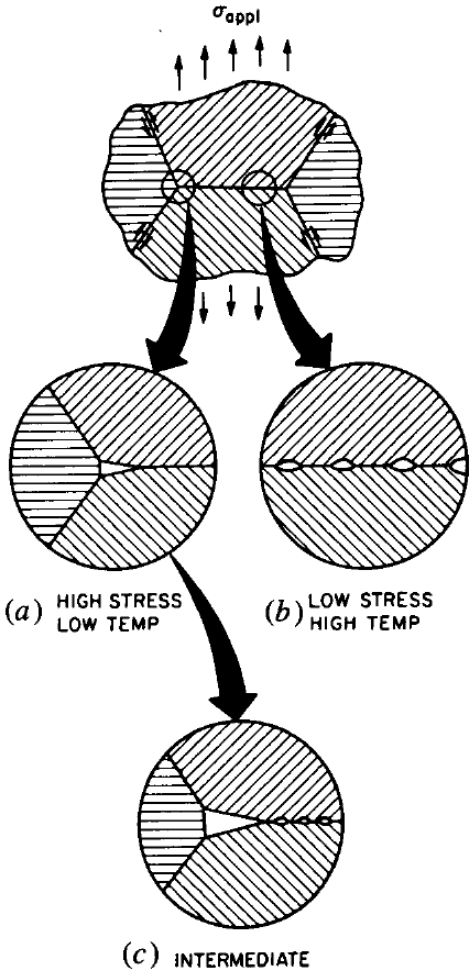

Figure 5.9: Two families of cavities and their domains of existence, as proposed by White et al. [235].

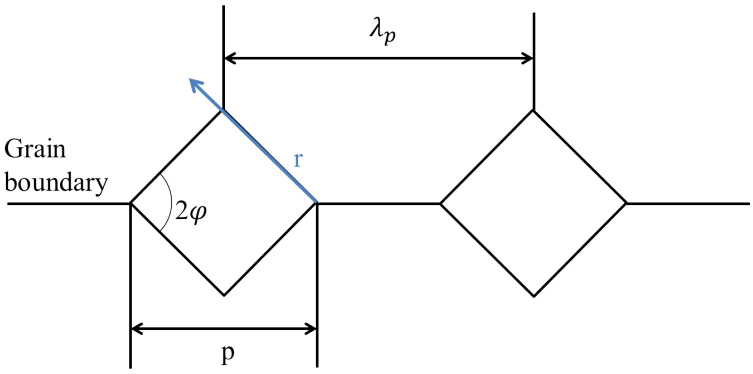

Figure 5.10: Schematic representation of the rectangular precipitates regularly located along a grain boundary [51].

Following our observations carried out on the 316 SS under study, precipitates are generally close to each other, the λ_p/p ratio is generally lower than 3, as shown by our SEM and TEM images (Figs. 2.1 and 3.2). Therefore, $\sigma_{nn}(r = r_c)/\sigma_\infty < 1.26$, in this case, the σ_{nn} value at $r = r_c$ is much below critical interface fracture stress values, which amounts to few GPa (shown in Chapter 2).

A more precise evaluation may be carried out. As the average distance between two particles could be calculate as:

$$\lambda_p = \frac{1}{\sqrt{N_0^{max}}} \tag{5.15}$$

The σ phase particle density amounts to $N_0^{max} = 1.25 \cdot 10^9 m^{-2}$ [2] (section 4.2.3). This leads to $\lambda_p = 28\mu m$. Finally, the stress concentration factor reaches $\sigma_p/\Sigma \approx 4$. This value is slightly higher than the one based on microscopic observations. In fact, only the σ phase particles are accounted for the N_0^{max} value. Still, the local interface normal stress σ_{nn} is below the typical interface critical fracture stress values, which amounts to at least few GPa. Even considering $r = b = 2.55 \cdot 10^{-10} m$, with b the Burgers vector length, Eq. 4.14 leads to $\sigma_{nn}/\Sigma = 0.65\lambda_p/p$. Then, the stress concentration reaches only $\sigma_{nn}/\Sigma \approx 6$. Even at this stress level, it seems unlikely to break the metallic bonds.

Moreover, Riedel [51] proposed Eq. 4.16 to calculate the average shear stress acting on each intergranular particle:

$$\tau_{nm} = \tau_\infty \frac{(4/\pi)(\lambda_p/p)^2}{1 + 2.65\lambda_p^2/pd_g} \tag{5.16}$$

Taking still $\tau_\infty = \Sigma/\sqrt{3}$ and the grain size as $d_g = 20\mu m$, Eq. 4.16 provides $\tau_{nm}/\sigma_\infty = 1.79$. This stress magnitude could not lead to interface fracture.

Therefore, small grains and closely-spaced particles lead to low stress concentration. It should be noticed that the FE simulations (without grain boundary

sliding) carried out by Cui [44] show that close-spaced particles aligned with the tensile axis lead to higher local stresses than individual particles.

Our numerical applications show that, for 316L(N) SS, the grain boundary sliding theories do not lead to interface stress high enough to fracture.

5.3.3 Intergranular inclusion embedded in metallic grains

As calculated interface stress by these two analytical theory based on grain boundary sliding could not reach the typical critical fracture stress, the stress fields around the intergranular inclusions deserve some interest. It shows that the crystal viscoplasticity Finite Element calculations of stress fields around the intergranular inclusion accounting for numerous microstructure heterogeneities are relevant (Chapters 2 and 3).

In Chapter 2, the Finite Element calculations taking into account the random crystal orientations of the neighbor grain (Fig. 2.5) highlighted a huge heterogeneity in interface normal stress. And the random crystal orientations leads generally to maximum interface normal stresses, σ_{nn}^{max} much higher than the one at the interface of an inclusion embedded in the homogeneous matrix (Fig. 2.7). The average interface stress is 1.85 times higher if the two crystals are introduced. Further, σ_{nn}^{max} could reach almost 20 times of the tensile stress. Calculations are also carried out for various stresses and temperatures. The results show that the local interface stress is almost independent on stress and temperature, but increases with the macroscopic strain increasing. Additionally, the increase in orientation of the grain boundary with respect the tensile stress, α_{GB}, leads to a decrease in σ_{nn}^{max}. Except for $\alpha_{GB} = 90°$, a slight increase is observed compared to the one with $\alpha_{GB} = 75°$.

Finite Element calculations reported in Chapter 2 considered only inclusions with circular tips with a shape factor of three. However, as shown in Chapter 3, our microscopic observations and others show that the shape factor varies between 1 and 5 (Fig. 3.1). And three particle tip geometries are observed, allotriomorph, hexagonal and quadrilateral (Fig. 3.2). Therefore, additional FE calculations corresponding to three types of particle shapes to investigate the effects of shape factor and tip geometry, are performed in Chapter 3. The results show that σ_{nn}^{max} increases with the shape factor increasing up to 7. The σ_{nn}^{max} computed with a hexagonal particle shape is higher than the one with an allotriomorph shape. And finally, the quadrilateral particle shape leads to a slight increase of σ_{nn}^{max} compared to the hexagonal one.

Summarizing the calculations results reported in Chapters 2 and 3 leads us to propose Eq. 4.17 to calculate the distribution of the maximum interfacial normal stress distribution accounting for all microstructure feature we have investigated.

$$\sigma_{nn}^{max}(O_i^1, O_i^2, a/b, \varphi, sym/asym, E^{vp}) = \sigma_{nn}^{max}(O_i^1, O_i^2, circular, a/b = 1, E^{vp}) \cdot \bar{r}_{sf}(a/b) \cdot \bar{r}_{sym}(\varphi) \cdot \bar{r}_{asym}(\varphi) \tag{5.17}$$

In this equation, $\sigma_{nn}^{max}(O_i^1, O_i^2, a/b = 1, circular, E^{vp})$ is the maximum interfacial normal stress around a spherical intergranular inclusion, in function of the macroscopic strain E^{vp}, with two neighbor grains of random crystalline orientations, O_i^1 and O_i^2, $\bar{r}_{GB}(\alpha_{GB})$ denotes to the orientation of grain boundary with respect to the tensile stress. And $\bar{r}_{sf}(a/b)$, $\bar{r}_{sym}(\varphi)$ and $\bar{r}_{asym}(\varphi)$ denote, respectively, the ratios of maximum interfacial normal stress with effect of the shape factor, the symmetric inclusion tip angle (as hexagonal shape) and the asymmetric inclusion tip angle (quadrilateral shape), respectively. The values of $\bar{r}_{sf}(a/b)$ are provided in Table 3.1. The values of the other factors are given in Table 4.5.

α_{GB} (°)	0	15	30	45	60	75	90
$\bar{r}_{GB}(\alpha_{GB})$	1	0.92	0.80	0.66	0.57	0.55	0.57
φ (°)	30	45	60				
$\bar{r}_{sym}(\varphi)$	2.12	1.39	1.50				
φ (°)	30	45	60				
$\bar{r}_{asym}(\varphi)$	1.07	1.35	0.85				

Table 5.5: The values of $\bar{r}(\alpha_{GB})$, $\bar{r}(\varphi)$ and $\bar{r}_a(\varphi)$ calculated by crystal viscoplasticity Finite Element computations.

Applying Eq. 4.17, the maximum value of σ_{nn}^{max} could reach:

$$\sigma_{nn}^{max}(set10, a/b = 7, \alpha_{GB} = 0°, \varphi = 30°, asym, 4\%) = 32.17GPa \tag{5.18}$$

and the minimum value is obtained as:

$$\sigma_{nn}^{max}(set19, a/b = 1, \alpha_{GB} = 75°, \varphi = 60°, asym, 4\%) = 0.91GPa \tag{5.19}$$

However, these extrema values for considered configurations are not the exact FE calculation values. As explained in subsection 3.4, Eq. 4.17 leads to a reliable calculation of the whole stress distribution. But Eq. 4.17 does not hold for each specific configuration separately.

As we consider the interface fracture occurs when the normal stress reaches the fracture stress as: 5GPa. Therefore, in some case, cavities will nucleate after at very low strain rate level (in order of few 1%). And some intergranular particles will never have interface fracture. This conclusion agrees perfectly with lots of experimental observations.

Then, α' can be calculated using our FE calculation results and the intergranular particle density. Thereafter, the Riedel model could be applied to long term creep lifetime predictions using evaluated α'.

As already mentioned in literature [51, 77], strong stress concentrations are required for reaching non negligible nucleation stress for the Raj model. Let us now consider our Finite Element calculations of interfacial stress. The evolutions of the maximum interface normal stresses along the thirty interfaces in function of macroscopic strain are plotted in Fig. 2.9, for a particle parallel to the tensile axis, with a shape factor of three, with random crystal orientations of particle neighbor grains.

Separating second phase particles in l configurations ($l = 30$, ie thirty couples of crystal orientations, O_i^1, O_i^2), therefore, the intergranular precipitate density corresponds each configuration l is $N_0^{max}/30$. For each configuration l, at time t_k, the cavity nucleation rate calculated using the Raj model is:

$$\dot{N}_0^{Raj}(l,t_k) = \frac{4\pi\gamma_s D_{gb}\delta}{\Omega^{4/3}\sigma_{nn}^{max}(l,t_k)}\frac{N_0^{max}}{30}exp(-\frac{4\gamma_s^3 F_v}{\sigma_n^2 k_b T})exp(\frac{\sigma_{nn}^{max}(l,t_k)\Omega}{k_b T}) \tag{5.20}$$

where $\sigma_{nn}^{max}(l,t_k)$ is the maximum interface normal stress of configuration l at time t_k.

Then, the total cavity number could be calculated as:

$$N_0(t_k) = \sum_{l=1}^{30}\sum_{0}^{t_k} min(\dot{N}_0^{Raj}(l,t_k); \frac{N_0^{max}}{30}) \cdot (t_k - t_{k-1}) \tag{5.21}$$

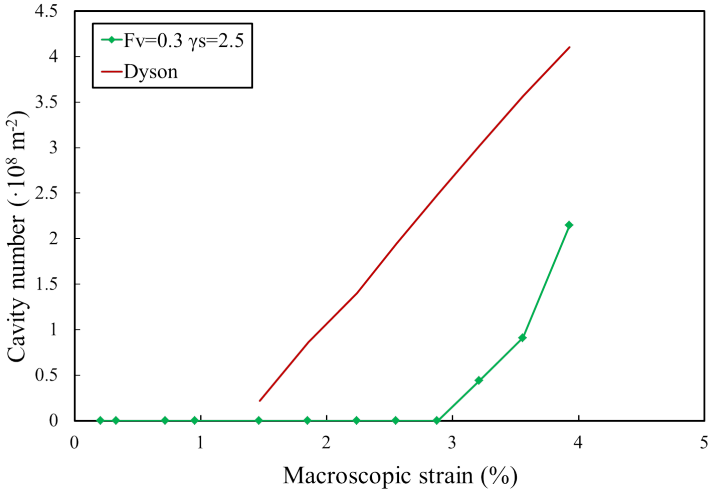

Figure 5.11: Comparison of evolution of cavity number in function of macroscopic strain E^{vp}, calculated Using the Raj model and Dyson law, $600°C$, 220MPa.

Fig. 4.11 shows the cavity nucleation rate calculated by the Raj model (Eq. 4.2), applying the maximum interface stress registered at each strain level calculated using Finite Element calculations (Fig. 2.9), for $F_v = 0.3$, $\gamma_s = 2.5J/m^{-2}$ (Table 2.4). The considered particle density is measured by NIMS at 600-750$°C$ [2].

Besides, cavity nucleation rate calculated using the Dyson law is also plotted, with the calculated α' value using stress distribution plotted in Fig. 2.9. The calculated α' value amounts to $1.2 \cdot 10^{10}\ m^{-2}$. Under 220MPa at 600$°C$, the minimum strain rate, $\dot{\varepsilon}_{min}$, amounts to $5 \cdot 10^{-9}s^{-1}$. Based on the Dyson law, this leads to a cavity nucleation rate of $60m^{-2}s^{-1}$. The predicted cavity number increases linearly with macroscopic strain E^{vp}. This result agrees well with many experimental measurements [74, 75, 85, 157].

The results show that, using the stress distribution calculated by FEM (Fig. 2.9), the Raj model predict a critical macroscopic strain, E_c^{vp}, amounts to 2.8%, which is higher than the one predicted based on interface fracture ($E_c^{vp} \approx 1.5\%$, Fig. 2.14). The Raj model requires a threshold stress of almost 8GPa for which the cavity nucleation could reach higher than $1m^{-2}s^{-1}$. Nevertheless, the evaluated interface fracture stress is only 5GPa. Further, the $N_0(t_k)$ predicted by the Raj model is lower than the one predicted based on interface fracture. Therefore, the interface fracture mechanism is dominant compared to the thermally-activated cavity nucleation mechanism.

5.4 Long term lifetime prediction

Our TEM observations (Fig. 3.3) show that intergranular creep cavities are nucleated along grain boundaries in long-term creep specimens. Dyson [74] observed that cavities nucleate continuously with a constant rate during each creep test. This phenomenon is confirmed by several experimental measurements [74, 80, 83, 185, 239, 240] and by our simulation results too, based on interface stress distribution and a fracture stress criterion.

As explained in subsection 4.2.2, only cavity growth by vacancy diffusion along grain boundaries is considered among the other cavity growth mechanisms.

Finally, the cavity growth by vacancy diffusion along grain boundaries coupled with continuous nucleation proposed by Riedel is used [51] to predict long term creep lifetime. Cui et al. [115] carried out creep lifetime predictions using the Riedel model, with parameters are in Tables 4.2 and 4.6. Fig. 4.12 shows the comparison between the experimental and the predicted lifetimes. The predictions combined both the necking and Riedel models [115]. The creep lifetimes were correctly predicted for both short and long term creep. These lifetime predictions were identical to the ones we carry out on Incoloy 800 alloys (Chapter **??**). Similar conclusions are shown for Incoloy 800 alloys (Chapter **??**) and ferritic martensitic Grade 91 steel [80].

Parameter	Notation	Values
ω_f	Critical area fraction of cavities along grain boundaries	0.04 ± 0.01 [109]
α'	Prefactor of the cavity nucleation law, m^{-2}	$[3.99 \cdot 10^9, 9.55 \cdot 10^9]$ [44]
$h(\alpha)$	cavity volume divided by a volume of a sphere of the same radius	0.826 ± 0.139 [77]

Table 5.6: Parameters used allowing the prediction of the time to fracture due to intergranular damage.

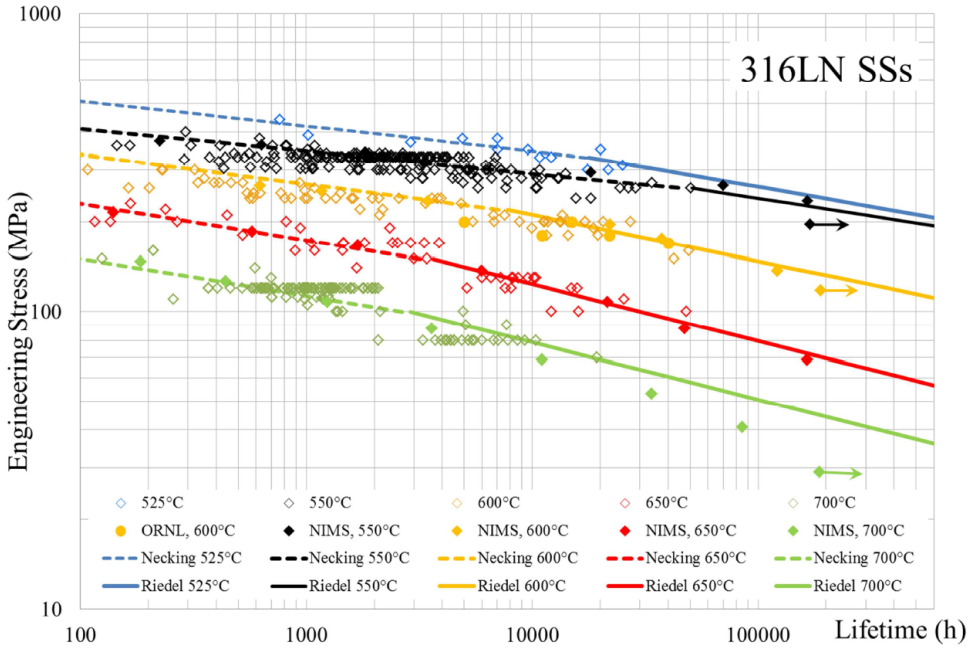

Figure 5.12: Comparison between experimental lifetimes and the lifetimes predicted by the necking and Riedel model, based on measured values of the Dyson law parameter, α' [115].

5.4.1 Final evaluation of the Dyson law prefactor α'

5.4.1.1 Evaluation of α' based on our FE calculations

In the long term creep lifetime predictions carried by Cui et al. [115], almost all parameters were found in literature (Tables 4.2 and 4.6), except that the Dyson law prefactor, α', is measured. These measurements require much work: long term creep tests at different temperatures and stresses, microscopic observations and image processing.

Further, it should be noticed that the prefactor of Dyson law, α', is not strictly a constant as used in these lifetime predictions. Cui et al. [115] provided measured values of α' varying between $3.99{\cdot}10^9$ and $9.55{\cdot}10^9 m^{-2}$ for temperatures between 525 and $700°C$ and under various stresses. This means that the cavity nucleation rate may be slightly temperature and stress dependent. However, these results do not agree with some of the published experimental measurements, which showed that α' is almost constant for a given material, and does not depend much on the stress or temperature. Further, no physical explanation of the Dyson law has been provided yet, except the recently proposal of Samdström et al. [70, 114, 241] based on the grain boundary sliding theory.

In order to provide full lifetime predictions avoiding and additional measurement, the Dyson law prefactor, α', is evaluated using our Finite Element calculation results. Following Chapters 2 and 3, the heterogeneity in the interface stresses provides a physical explanation of the Dyson law. We consider that the cavity nucleation occurs when the interface normal stress reaches the interface fracture stress, σ_c. The fracture stress is evaluated in Chapter 2, as $5 \pm 1GPa$ for an incoherent interface, using the Universal Bounding Energy Relationship (UBER).

In Chapter 2, thanks to Finite Element calculations, the Dyson law prefactor, α', is evaluated accounting for the effect of the random crystallographic orientations of the particle neighbor grains and the orientation of the grain boundary plane with respect to the tensile axis. And considering only the density of σ phase particles (experimental measurement carried out by NIMS [2]), the predicted value of α' amounts to $1.2{\cdot}10^{10} m^{-2}$. This value is about three times higher than the experimental one [44] (average value of $4.5 \cdot 10^9 m^{-2}$). As expected, all grain boundaries ($\alpha_{GB} \geqslant 0°$) are taken into account in this evaluation. Several experimental observations [74, 75] showed clearly that cavities appear at first along grain boundaries parallel to the tensile axis ($\alpha_{GB} = 0°$), then, initiate later along grain boundaries with higher α_{GB} values and finally along grain boundaries perpendicular to the tensile axis ($\alpha_{GB} = 90°$). Further, the quantitative measurements [75] show that, at low strain level, the number of cavities along grain boundaries parallel to the tensile axis is much higher than the perpendicular ones (Fig. 4.13a). However, it is believed and indeed observed that cavities along grain boundaries parallel to the tensile axis could not grow during creep (Fig. 4.13), because a very law normal stress is applied on these grain bound-

aries ($\alpha_{GB} \simeq 0°$) for driving vacancy diffusion. Further, Jazari et al. [242] show two repartitions of cavity size in a in-service fractured 316H steel. The ones with cavity sizes lower than $200nm$ may correspond to the cavities located along grain boundaries parallel (or parallel $\alpha_{GB} < 45°$) to the tensile axis observed by Shiozawa et al. [75] (Fig. 4.13). And other cavities with cavity sizes higher than $200nm$, which my correspond to the cavities along grain boundaries for which $\alpha_{GB} \geqslant 45°$. Unfortunately, diffusion growth is not straight forward to be simulated by Finite Element calculations. The FE computations coupling crystal viscoplasticity and the Fick euqtion is out of the scope of our PhD work which is focused on cavity nucleation and its consequences.

These observations lead us to proposed that only cavities along grain boundaries for which the orientation with the tensile stress axis is higher than 45° ($\alpha_{GB} \geqslant 45°$) grow by diffusion after they nucleate. And the experimental measurements of α' carried out by Cui et al. [44] considered only cavities with radius larger than $200nm$. Therefore, to evaluate the cavity nucleation rate based on our simulations, only grain boundaries with $\alpha_{GB} \geqslant 45°$ should be considered.

Further, this phenomenon could be investigated analytically through the Riedel model. The lower bound of long term lifetime prediction proposed by Riedel [51] is:

$$t_f = 0.33(\frac{h(\alpha)kT}{\Omega D_{gb}\delta\sigma})^{2/5}(\frac{\omega_f}{\dot{N}_0})^{3/5} \tag{5.22}$$

Therefore, under given creep condition (stress and temperature), Eq. 4.22 can be transformed into:

$$\omega_f = C \cdot \alpha'\Sigma^{2/3} \tag{5.23}$$

where C is a temperature and stress dependent constant.

We consider seven grain boundary planes: $\alpha_{GB} = 0, 15, 30, 45, 60, 75,$ and $90°$. The normal stress acting on each grain boundary plane, $\sigma_n(\alpha_{GB})$, amounts to, $\sigma_n(\alpha_{GB}) = \Sigma \cdot sin^2\alpha_{GB}$.

Then, the damage value, $\bar{\omega}$, is deduced:

$$\bar{\omega}[0°, 90°] \propto \sum_{\alpha_{GB}=0°}^{90°} \alpha'(\alpha_{GB}) \cdot sin^{4/3}\alpha_{GB} \cdot g(\alpha_{GB}) \tag{5.24}$$

where $g(\alpha_{GB})$ is the fraction of grain boundary corresponding to α_{GB}, $g(\alpha_{GB} = \alpha_i) = 1/7$, with $\alpha_i = 0, 15, 30, 45, 60, 75, 90°$.

And assuming that normal stress acting on grain boundary as the remote stress, as proposed by Riedel [51], we can define $\bar{\omega}_{app}$ as:

$$\bar{\omega}_{app}[\alpha_{GB}, 90°] \propto \sum_{\alpha_{GB}=0°}^{90°} \alpha'(\alpha_{GB}) f(\alpha_{GB}) \tag{5.25}$$

Further, $\alpha'(\alpha_{GB})$ is proportional to the relative frequency of fracture interface in function of α_{GB}, $P(\alpha_{GB})$, (Fig. 2.16b).

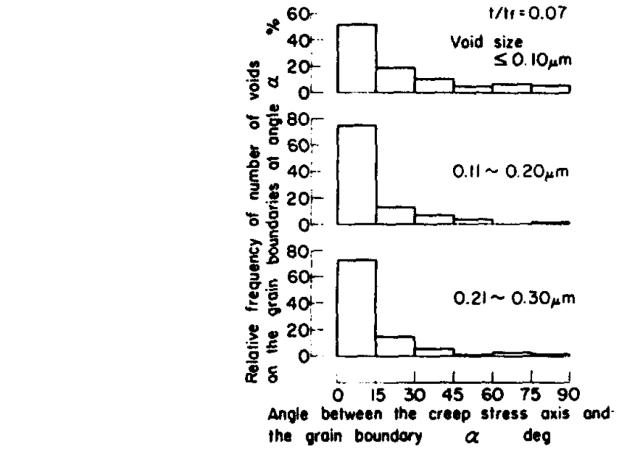

(a)

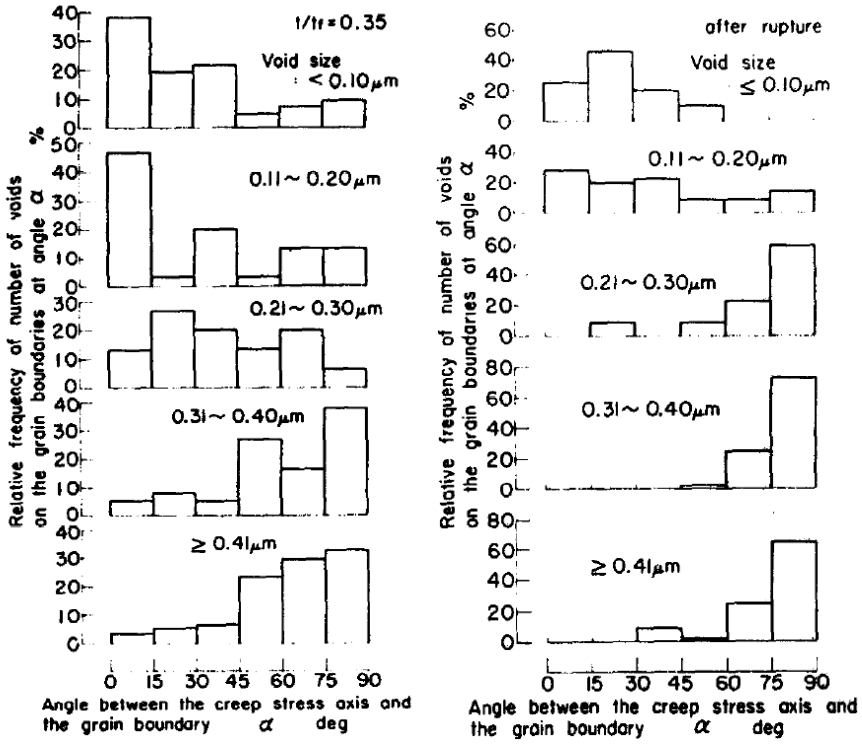

(b) (c)

Figure 5.13: Relative frequency of cavitation as a function of the orientation of the grain boundary plane with respect to the tensile axis of an astroloy. The specimens had been prestrained by 10% in the same direction as the creep loading axis, then a creep test under 400MPa at 750°C was carried out. (a) 7% of creep life; (b) 35% of creep life and (c) after fracture [75].

Finally, we define:

$$\frac{\bar{\omega}_{app}[\alpha_{GB}, 90°]}{\bar{\omega}[0°, 90°]} = \frac{\sum_{\alpha_{GB}=0°}^{90°} P(\alpha_{GB}) g(\alpha_{GB})}{\sum_{\alpha_{GB}=0°}^{90°} P(\alpha_{GB}) \cdot sin^{4/3}\alpha_{GB} \cdot g(\alpha_{GB})} \tag{5.26}$$

As shown in Table 4.7, for the α_{GB} angles ranging from 45 to 90°, the obtained $\bar{\omega}_{app}$ value is very close to the accurate $\bar{\omega}$ value. This confirms that considering $45 \leqslant \alpha_{GB} \leqslant 90$ leads to reliable predictions of both damage and lifetime.

$[\alpha_{GB}, 90°]$	$0-90°$	$15-90°$	$30-90°$	$45-90°$	$60-90°$	$75-90°$	$90°$
$\frac{\bar{\omega}_{app}[\alpha_{GB},90°]}{\bar{\omega}[0°,90°]}$	2.64	1.96	1.38	0.85	0.53	0.35	0.18

Table 5.7: Value of $\bar{\omega}_{app}[\alpha_{GB}, 90°]/\bar{\omega}[0°, 90°]$ in function of considered ranges of the α_{GB} angle.

Chapter 3 investigated the influence of two microstructure parameters: the shape factor and the tip geometry. Concerning the tip geometry, three geometries are observed, as allotriomorph, hexagonal and quadrilateral shapes. The shape factor effect is characterized by $\bar{r}_{sf}(a/b)$. The effect of hexagonal shape with reference the circular tip is characterized by $\bar{r}_{sym}(\varphi)$. And the effect of quadrilateral shape with reference the hexagonal one is characterized by $\bar{r}_{asym}(\varphi)$. However, the experimental measurement of particle tip geometry requires lots of observations and image processing. No corresponding statistical measurements have been reported in literature.

It leads us to assume, at first, that all particles are allotriomorph in our evaluation of α'. Therefore, Eq. 4.17 reduces to:

$$\begin{aligned}\sigma_{nn}^{max}(O_i^1, O_i^2, a/b, \alpha_{GB}, \varphi, E^{vp}) = \sigma_{nn}^{max}(O_i^1, O_i^2, a/b = 1, circular, E^{vp}) \\ \cdot \bar{r}_{GB}(\alpha_{GB}) \cdot \bar{r}_{sf}(a/b)\end{aligned} \tag{5.27}$$

After these computations, we reevaluate the Dyson law prefactor α' accounting for the particle shape factor distribution and random grain boundary orientation.

The shape factor distribution measured by Cui [44] is plotted in Fig. 3.1. The discretized probability of particles with shape factor, $f(a/b = i)$, could be obtained by using the shape factor continuous distribution, with $f(a/b = i) = prob(i - 1/2 \leqslant a/b \leqslant i + 1/2)$. The probability of fracture of interfaces at E^{vp} for each shape factor, $P(a/b = i, E^{vp})$, is calculated using Eq. 4.27 and the stress criterion with $\sigma_c = 5GPa$. Then, The total probability of fractured interface at E^{vp}, $P(a/b, E^{vp})$ accounting shape factor distribution is calculated as:

$$P_{sf}(E^{vp}) = \sum_{1}^{7} P(a/b = i, E^{vp}) \cdot f(a/b = i) \tag{5.28}$$

The microscopic measurement carried out by Cui [44] shows that second phase particles are distributed homogeneously along all grain boundaries whatever the α_{GB} angle. Therefore, $g(\alpha_{GB} = \alpha_i) = 1/7$, with $\alpha_i = 0, 15, 30, 45, 60, 75, 90°$. Then, the total probability of fracture ofinterface at a strain of E^{vp}, $P(\alpha_{GB}, E^{vp})$ accounting for the grain boundary plane orientations through the α_{GB} angle is:

$$P(\alpha_{GB} \geqslant \alpha_j, E^{vp}) = \sum_{\alpha_j}^{90°} P(\alpha_{GB} = \alpha_j, E^{vp}) \cdot g(\alpha_{GB} = \alpha_j) \tag{5.29}$$

Finally, α' is calculated accounting for the statistical distribution of both particle shape factor and grain boundary orientation, as:

$$\alpha' = \frac{\sum_{\alpha_j}^{90°} P_{sf}(\alpha_{GB} = \alpha_j, E^{vp}) \cdot g(\alpha_{GB} = \alpha_j) \cdot N_0^{max}}{E^{vp} - E_c^{vp}} \tag{5.30}$$

To calculate the prefactor of the Dyson law, α', we use the evaluation of the interface fracture stress ($5GPa$, UBER, subsection 2.5.1), grain boundary planes, such as with $\alpha_{GB} \geqslant 45°$, the σ phase particles density plotted by NIMS [2] (Fig. 4.14) and the distribution of particle shape factor. Combining with our Finite Element calculation results, we deduce that $\alpha' = 2.2 \cdot 10^9 m^{-2}$, which is slightly below the values measured by Cui, $[4 - 10] \cdot 10^9 m^{-2}$.

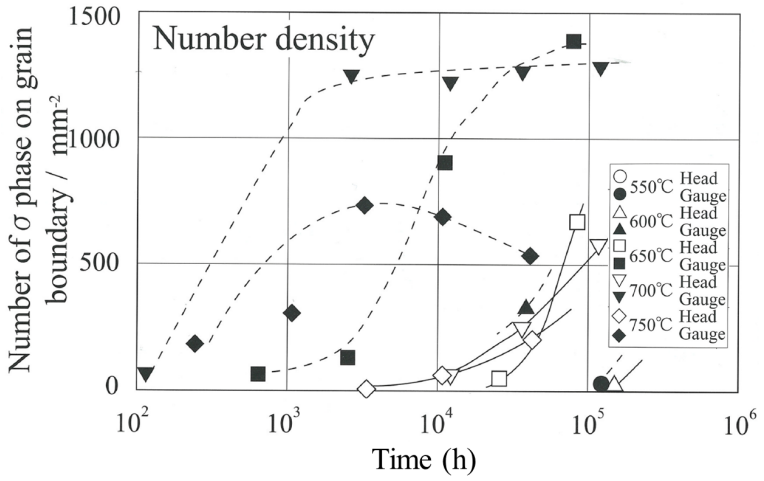

Figure 5.14: Number density of σ phase along grain boundaries in specimen head and gauge portions as a function of time for 316H TB [2].

Then, a careful TEM observations of 25 intergranular particles are carried out for a fractured specimens, ($600°C$, 220MPa, 7000h). These precise observations allow us to split the particles between three characteristic shape families (Fig. 3.2, Table 4.8). Additionally, the tip angles are measured in the hexagonal and quadrilateral particles (Fig. 4.15). This qualitative measurement could lead us

to introduce the effect of the tip geometry in the Dyson law prefactor. The measurements focus on the particle shapes (Table 4.8) and the tip angles (Fig. 4.15). The results show that the majority of the observed particles are angular ones (72%), and hexagonal and quadrilateral particles are almost equiprobable (Table 4.8). For hexagonal- and quadrilateral-like particles, the two tips of each particle could display different φ angle. And sometimes, the tip angle is difficult to measure even using TEM images. Therefore, Fig. 4.15 plots more than 18 angles (sum of observed hexagonal and quadrilateral particles number), and less than $2 \cdot 18$ angles. All the measured angles (Fig. 4.15) are finally shared between three ranges: 30°, 45° and 60°. The final results are shown in Table 4.9 and are used in combination with the interface stress values computed in Chapter 3 for these three angle values.

Allotriomorph	Hexagonal	Quadrilateral
6	10	9

Table 5.8: Number of observed particles with allotriomorph, hexagonal and quadrilateral shapes, 650°C, 130MPa, 7262h.

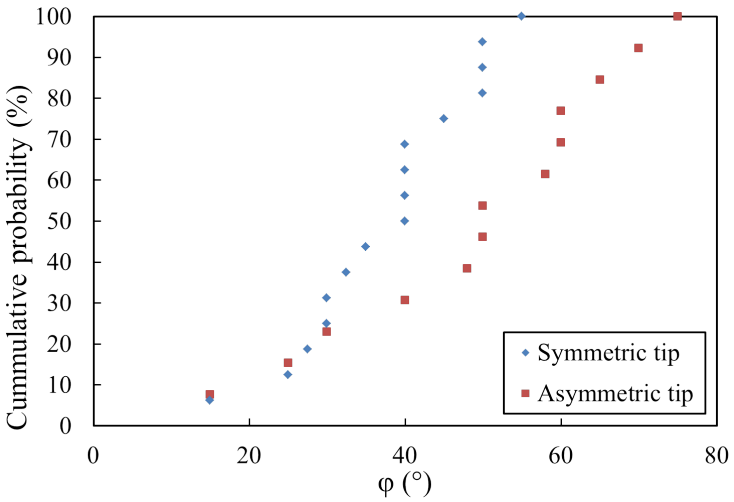

Figure 5.15: Cumulative probabilities of the tip angle of intergranular hexagonal and quadrilateral particles. 650°C, 130MPa, 7262h.

Thereafter, taking these measurement results, the Dyson law prefactor α' is reevaluated using the FE calculation results. Accounting $\alpha_{GB} \geqslant 45°$, the same shape factor distribution (Fig. 3.1) and the σ phase particle density measured at NIMS [2], we deduce the final value of α', as: $3.3 \cdot 10^9 m^{-2}$. This value is 50% higher than the previous one. And the E_c^{vp} value decreases to 0.73%. However, this evaluation is based on the qualitative measurement. The statistical

Considered φ (°)	30	45	60
Range φ (°)	< 37.5	45 ± 7.5	> 52.5
Symmetrical	7	8	1
Asymmetrical	2	5	6

Table 5.9: Number of measured angles for applying Eq. 4.27. After the analysis of the measured angle values plotted in Fig. 4.15.

measurements are required to account more accurately of the tip geometry and tip angle distribution. As the heterogeneities in inclusion geometry do not differ too much the value of α'. And this evaluation needs much more observations of particles geometry. In the following, only the evaluation taken into account the α_{GB} and shape factor is considered in the following.

5.4.1.2 Sensitivity of the predicted Dyson law prefactor, α', with respect to microstructure and fracture parameters

In the evaluation of α', severals parameters are taken into account, as

- the interface fracture stress, σ_c;
- the orientation of the grain boundary plane with respect the tensile axis, α^{GB};
- the particle shape factor, a/b;
- the intergranular large particle density, N_0^{max}.

The influence of each of these parameters on the calculated value of α' is reported in Table 4.10. The results show that the value of α' increases linearly with the increase of N_0^{max}, which agrees with the Raj model (Eq. 4.2).

N_0^{max} (m^{-2})	σ_c (GPa)	α_{GB}	α' (m^{-2})
$1.25 \cdot 10^9$ [2]	4	$\geqslant 0°$	$8.8 \cdot 10^9$
	5	$\geqslant 0°$	$8.1 \cdot 10^9$
		$\geqslant 45°$	$2.2 \cdot 10^9$
		$\geqslant 90°$	$3.3 \cdot 10^8$
	6	$\geqslant 0°$	$7.2 \cdot 10^9$

Table 5.10: The influence of the interface fracture stress σ_c, the grain boundary orientation with respect to the tensile axis (α_{GB}) and the large intergranular particle density on the prefactor of Dyson law.

In our estimation of α', we consider that the grain boundaries with $\alpha_{GB} = 0$, 15, 30, 45, 60, 75 and 90° are equiprobable. Therefore, consider only boundaries

with $\alpha_{GB} \geqslant 45°$, we take into account only 5/7 of total number grain boundaries ($\alpha_{GB} \geqslant 0°$). However, the values of α' decreases by a factor of 0.27 ($\frac{\alpha'(\alpha_{GB} \geqslant 45°)}{\alpha'(\alpha_{GB} \geqslant 0°)} \approx 0.27$), which is much lower than 5/7. This factor becomes 0.04 for the one with $\alpha_{GB} = 90°$ ($\frac{\alpha'(\alpha_{GB}=90°)}{\alpha'(\alpha_{GB} \geqslant 0°)} \approx 0.04$). Therefore, the considered grain boundary with α_{GB} higher than the chosen value influences significantly the value of α'.

It should be noticed that, in subsection 2.5.2, the α' value was calculated considering all grain boundaries, without effect of particle shape factor. This is the main reason that the α' value was overestimated in subsection 2.5.2.

The critical interface fracture stress, σ_c, affects only slightly the value of α', as already shown in Figs. 2.14 and 2.16a. The relative decrease in the α' value calculated with 4GPa and 6GPa reaches only to 20%. Nevertheless, the interface fracture stress affects more strongly to the onset of cavity nucleation (Figs. 2.14 and 2.16a). The critical viscoplastic strain, E_c^{vp}, corresponds to the onset of cavity nucleation. Such a critical strain is generally observed experimentally on metallic materials (Nimonic 80A (room temperature) [74], Astroloy [75], Alloy 617 [157], 347 steel [177, 179], and Copper alloy [85]).

The critical cavity nucleation strain, E_c^{vp}, is independent on the particle density, N_0^{max}. Nevertheless, this parameter depends strongly on α_{GB} and σ_c. The values of E_c^{vp} in function of σ_c and α_{GB} are presented in Table 4.11.

σ_c (GPa)	E_c^{vp} (%)		
	$\alpha_{GB} \geqslant 0°$	$\alpha_{GB} \geqslant 45°$	$\alpha_{GB} = 90°$
4	1.02	1.82	2.96
5	1.56	2.21	3.72
6	2.27	2.58	4.18

Table 5.11: Influence of the interface fracture stress, σ_c, and the grain boundary plane orientation with respect to the tensile stress (α_{GB}) on the critical cavity nucleation strain, E_c^{vp}.

The study of Table 4.11 shows that cavities appear at first along the grain boundaries parallel to the tensile axis ($\alpha_{GB} = 0°$), then the ones such as $\alpha_{GB} = 45°$ and finally the ones perpendicular to the tensile axis ($\alpha_{GB} = 90°$). The results agree well with microscopic observations in [74, 80, 83, 185, 239, 240]. Further, such grain boundary plane orientation dependence could not be correctly predicted by the interaction of grain boundary sliding with elastic particles.

Therefore, following all our calculations and as generally the stationary stage is reaches as $E^{vp} > E_c^{vp}$, we can deduce the general dependence of the number of cavities par unit area of grain boundary with respect to the remote viscoplastic strain E^{vp}:

$$N_0(E^{vp}) = \dot{N}_0 \cdot (E^{vp} - E_c^{vp}) = \alpha' \cdot \dot{\varepsilon}_{min} \cdot (E^{vp} - E_c^{vp}) \tag{5.31}$$

In Eq. 4.31, α', E_c^{vp} and $\dot{\varepsilon}_{min}$ are all material dependent. E_c^{vp} may slightly depends on the stress and temperature [76]. The minimum strain rate, $\dot{\varepsilon}_{min}$, depends strongly on the temperature and tensile stress, as usually observed in creep.

5.4.1.3 Conclusion

In this section, a final estimation of the prefactor of the Dyson law, α', based on our Finite Element calculations is proposed. Assuming $\sigma_c = 5GPa$, $\alpha_{GB} \geqslant 45°$ and the nucleation sites density as the number of σ phase particles per unit grain boundary area, N_0^{max} (316H TB [2]), the calculated Dyson law prefactor is lower than the measured values by factors between 0.23 and 0.55. However, several microstructure details are not take into account, as the tip geometries. Further, the interface fracture stress σ_c is only evaluated by a simple formula (UBER) proposed by Rice and Wang [118]. Density Functional Theory (DFT) calculations may be required to calculate more accurately the interface fracture stress by simulating the full fracture of bimaterials.

Our coupling between Finite Element calculations and a interface fracture criterion, provide first a theoretical framework justifying the Dyson law. And this coupling predicts a Dyson law prefactor and a critical remote strain which are close to experimental data. Accounting for more or less informations about the microstructure induces changes in the α' value. But the order of magnitude remain the same (Table 4.10).

Further, our theoretical results show that α' depends slightly on the temperature and stress (Fig. 2.10), similarly to what was measured in literature [74–76]. This result agree well with microscopic observations [76, 93]. Thereafter, the calculated value of α' is used to predict the long term creep lifetime for various temperatures temperature and stresses.

5.4.2 lifetime predictions in 316 SSs

As explained in chapters 1 and **??**, the Riedel model assumes that cavity growth by vacancy diffusion along grain boundaries coupled with continuous nucleation. However, the set of equations cannot be solved analytically. Then, the upper and lower bounds were proposed to help to predict lifetime. Lim [80] improved the bounds proposed by Riedel. The upper and lower bounds proposed by Lim [80] is applied to predict the long term creep lifetime. It has been proved in 316L(N) [115] and Incoloy 800 alloy (subsection **??**) that the unconstrained diffusion gorwth law is valid [61].

Now, we recall the main laws used for the lifetime predictions.

The Dyson law predicts the cavity nucleation rate. For the sake of simplicity, it is assumed that $E^{vp} - E_c^{vp} \approx E^{vp}$: [74]:

$$\dot{N}_0 = \alpha' \cdot \dot{\varepsilon}_{min} \tag{5.32}$$

Considering only the grain boundaries with α_{GB} higher than 45° for allowing diffusion growth to occur, the α' value is deduced as $2.2 \cdot 10^9 m^{-2}$.

The upper and lower bound functions proposed by Lim [80] are:

$$0.301 \cdot (\frac{h(\alpha)k_bT}{\Omega D_{gb/v}\delta\sigma})^{2/5}\frac{\omega_f^{0.5164}}{\dot{N}_0^{3/5}} \leqslant t_f \leqslant 0.354 \cdot (\frac{h(\alpha)k_bT}{\Omega D_{gb/v}\delta\sigma})^{2/5}\frac{\omega_f^{2/5}}{\dot{N}_0^{3/5}} \tag{5.33}$$

The used parameters are reported in Tables 4.2 and 4.6.

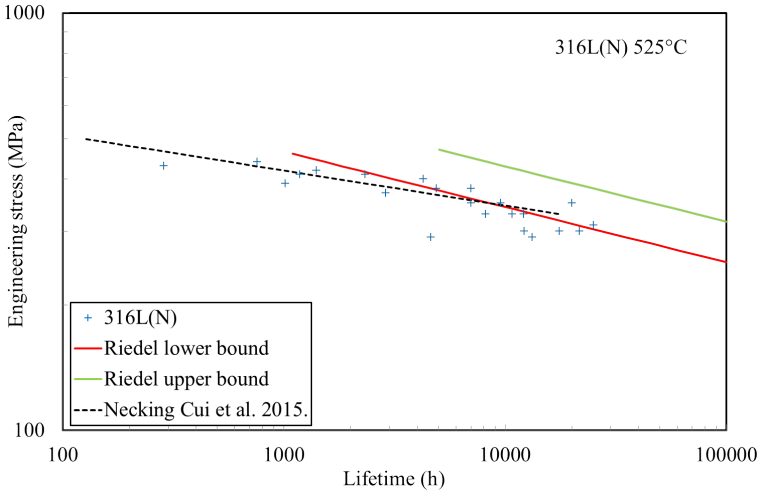

Figure 5.16: Experimental data and predicted lifetimes based on the Riedel model (Eq. 4.33) compared with experimental data provided by CEA, EDF &Creusot-Loire (316L(N)), 525°C.

The experimental data and predicted lifetime curves are compared at 525°C (Fig. 4.16), 550, 600°C (Fig. 4.17), 650 and 700°C (Fig. 4.18) for 316L(N) SS. Experimental data from literature [2, 49, 183] are also compared.

The used minimum strain rates, $\dot{\varepsilon}_{min}$, are calculated with the Norton power law parameters adjusted for different temperatures and stresses using the CEA &EDF Data. However, no such information was reported in NIMS data sheets [2, 183]. It should be noticed that, at 700°C, to predict very long term creep lifetime under very low stress (29-100MPa), the used Norton law parameters are evaluated using experimental data from Kloc et al. [243]. The corresponding values are: $n = 7.25$ and $C = 1.03 \cdot 10^{-19} MPa^{-n}s^{-1}$.

The calculated α' value is used in our lifetime predictions, amounts to $2.2 \cdot 10^9 m^{-2}$. This value is lower than the ones measured by Cui et al. ($[3.99 \cdot 10^9; 9.55 \cdot 10^9 m^{-2}]$) [115]. As $t_f \propto (\alpha')^{-3/5}$, it may lead to that our predicted lifetimes are overestimated compared to the ones predicted by Cui et al. [115].

It should be noticed that, at 525°C (Fig. 4.16), the slope change can be hardly be defined using the available experimental data. Experimental data obtained at lower stresses are required to validate our predictions. For temperatures ranging

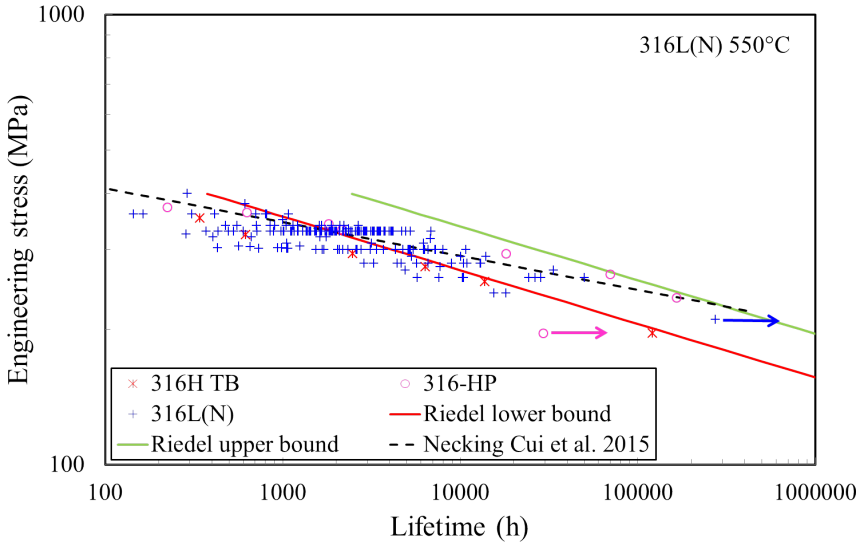

(a)

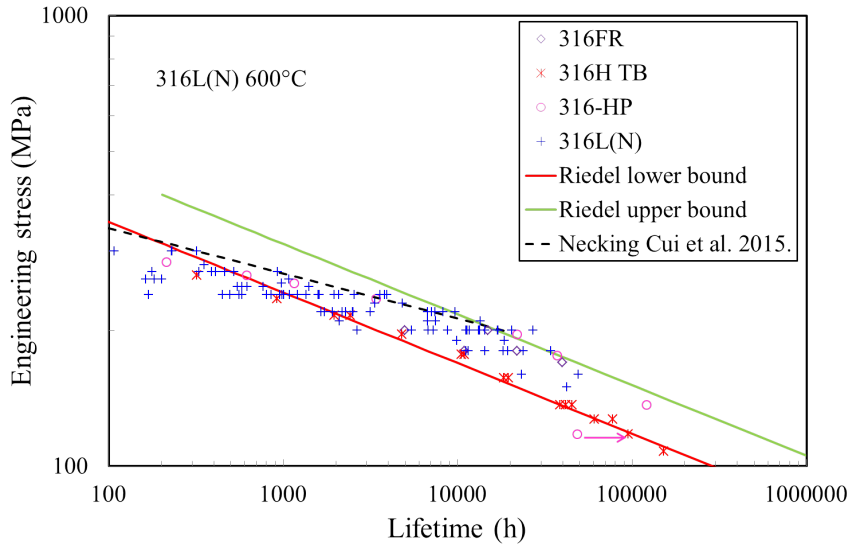

(b)

Figure 5.17: Experimental data and predicted lifetimes based on the Riedel model (Eq. 4.33) compared compared with experimental data at (a) 550°C and (b) 600°C, data provided by CEA&EDF (316L(N)), ORNL (316FR [49]) (ORNL) and NIMS (316H TB [183], 316-HP [2]).

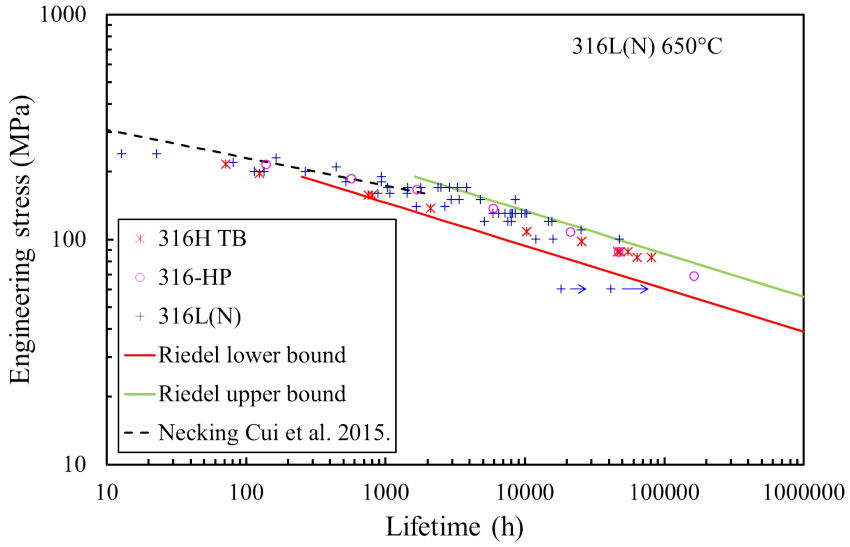

(a)

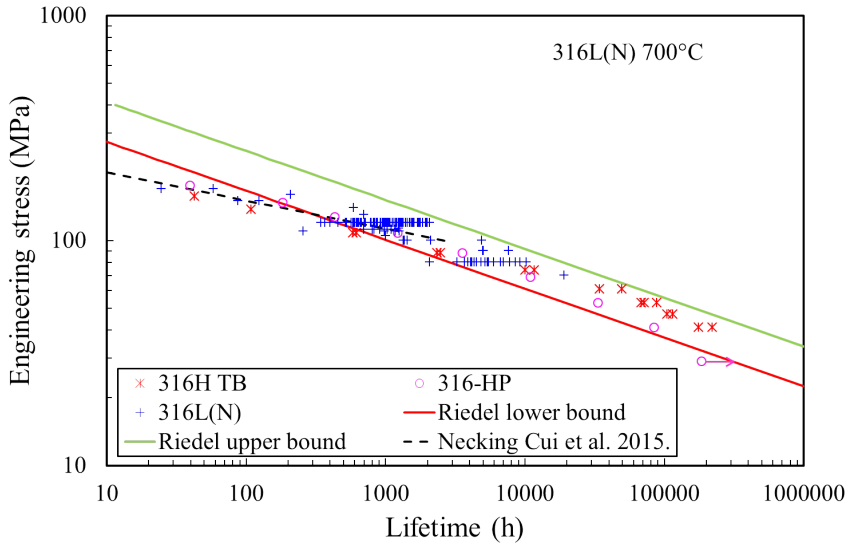

(b)

Figure 5.18: Experimental data and predicted lifetimes based on the Riedel model (Eq. 4.33) compared with experimental data provided at (a) 650°C and (b) 700°C, data provided by CEA&EDF (316L(N)) and NIMS (316H TB [183], 316-HP [2]).

from 500 to 700°C (Figs. 4.17 and 4.18), the combination of the short term prediction provided by Cui et al. [115] and our predictions describe well the slope change in stress-lifetime curves. Further, the lifetimes are fairly well predicted for long term creep regime.

5.5 Discussion and conclusion

5.5.1 Cavity nucleation model

Two cavity nucleation models are proposed in literature, either vacancy condensation or interface fracture. The vacancy condensation mechanism is modeled by Raj and Ashby [77].

As the Raj model, interface fracture requires high local stress concentration. Several mechanisms were proposed to be responsible for such local stress concentrations: especially grain boundary sliding. Using the formulas reported in [51], the normal and shear stresses acting on the particle-matrix interface induced by grain boundary sliding are estimated using characteristic microstructure measured in 316SS for σ phase particles. It was shown that such local stresses are below the interface fracture stress, even at a distance of the Burgers length, $1b$, with respect to the particle tip.

Sandström et al. [70, 112, 113, 241] proposed a cavity nucleation rate based on grain boundary sliding. They proposed that the cavitation locations are the ones where particles meet subboundaries during grain boundary sliding. Further, their results provide a cavity nucleation law similar to the Dyson law, which means that $\dot{N}_0$ varies linearly with the minimum strain rate.

5.5.2 Evaluation of cavity nucleation rate

5.5.2.1 Finite Element calculations

The numerous Finite Element calculation results lead us to propose Eq. 4.17 to predict interface stress distribution depending on the statistical data defining each microstructure. Once dislocation density, ρ, and activated volume, V^* are adjusted to get correct creep curves. Using Eq. 4.17, only 15 Finite Element calculations, accounting the effect of the random crystalline orientations of the neighbor grains, are needed to calculate the stress distribution accounting for the grain boundary plane angle, α_{GB}, shape factor and tip geometry (circular tip, and symmetric/asymmetric tip defined by the tip angle, φ). Then, the value of prefactor of the Dyson law, α' is evaluated based on an interface fracture stress value and second phase particle density.

The considered grain boundaries with orientation respect the tensile stress α_{GB} affect both the Dyson law prefactor value, α', and E_c^{vp}. Following microscopic observations [75], we restrict the angle range to $\alpha_{GB} \geqslant 45°$. These

assumptions drive that: $\alpha' \approx 2.2 \cdot 10^9 m^{-2}$, which is lower than the experimental values by factors from 0.23 to 0.55 [115]. Accounting for the effect of inclusion tip geometry, a higher value of α' is obtained, as $3.3 \cdot 10^9 m^{-2}$, close to the measured values.

Further, the Finite Element calculations carried out for various stresses and temperatures (Fig. 2.10) show that the stress distribution is almost independent on stress and temperature. Therefore, our theoretical estimations show that the value of α' is almost independent on temperature and stress provided the change in the particle density and size is negligible. And the α' value depends only slightly on the critical interface fracture stress. However, the interface fracture stress affects more strongly the cavity initiation threshold strain, E_c^{vp}.

5.5.2.2 Fracture criteria

The interface fracture stress is evaluated using the Universal Bounding Energy Relationship (Eq. 2.11). The input parameters of the UBER formula are free surface and interface energies, interface thickness and the interface Young's modulus. In fact, all the selected free surface and interface energies values are computed by DFT reported in literature (Table 2.4 in Chapter 2). Few DFT studies focus on incoherent surface energy calculations, especially for σ phase and austenitic matrix interface. Generally, DFT calculations are performed at $0K$. However, the surface energies decrease with increase in temperature. Further, chemical segregation [44, 150] and appearance of dislocations [175] at the interface could also decrease surface energies. These decreases in surface energies may lead to decrease in σ_c. However, these phenomena are uneasy to be calculated by DFT computations because of the huge required computation time.

In this evaluation, the energy criterion is not taken into account. The energy criterion allows accounting for the effect of particle size on cavity nucleation rate. In fact, Pineau and Pardoen [117] and Tanaka et al. [188] studied that interface fracture occurs at first on large second phase particles (Fig. 4.4). The σ phase particles are generally longer than $1\mu m$ whatever the temperature because of quick growth once the nucleation has been reached [2, 37, 133, 181]. Therefore, we used the saturated density of σ phase particles in 316H TB [2]. Further, our microscopic observations of 316L(N) and the NIMS data sheet [2] show that cavity nucleation is generally occurs at the interface of σ phase particle and matrix interfaces. Therefore, it was assumed that the σ phase particles (generally larger than $1\mu m$) as the cavity nucleation site. It should be noticed that the value of α' increases linearly with the density of the intergranular particles. Therefore, it will be better if we can take the σ phase density for the material under study. Further, the use of a cohesive zone model is under the way to introduce the effect of particle size.

5.5.2.3 Intergranular particle density

Further, it is assumed that the density of σ phase particles is almost saturated since the beginning of cavitation, at E_c^{vp}. And NIMS data sheet [2] shows that the density of σ phase particle is almost saturated after respectively 10 000h and a few 1000h, respectively at 650 and 700-750°C (Fig. 4.14). The saturated σ phase density amounts to $1.25 \cdot 10^9 m^{m-2}$, which is the N_0^{max} value used in our evaluation of the α' prefactor.

However, as shown in Fig. 4.14, the σ phase particles do not preexist in specimens. They nucleate and then grow during creep. And the value of N_0^{max} varies with temperature, tensile stress and time. Therefore, it may be more accurate to use a $N_0^{max}(\sigma, T)$ density. This will induce a stress and temperature dependence of the Dyson law prefactor, $\alpha'(\sigma, T)$.

Nevertheless, if we assume that the precipitates larger than $2\mu m$ are *sigma* phase particles, the SEM images reported in [44] show a slight difference in the σ phase density. And considered that all σ phase particles diameters are larger than $2\mu m$ at 600°C, the number of *sigma* phase particles amounts to only 2% of total precipitate number (Fig. 3.1). This leads to a N_0^{max} density of $1.37 \cdot 10^{10} m^{-2}$, which is ten times of the one measured by NIMS.

Fig. 4.14 shows that the nucleation of σ phase in specimen gauge portion is promoted by stress and/or deformation as referred to the heads of the specimens (negligible strain and stress). The experimental investigations of the σ phase precipitation kinetic require many creep tests under various stresses at various temperatures.

At least, it seems clear from experimental investigation that many intergranular participles of $\sim 2\mu m$ are observed after 80 000h of creep deformation [20, 37, 133]. More precisely, Chastell and Flewitt [133] conclued that after 85 000h of creep at 568°C, most of the large intergranular particles are σ phase ones. Interestingly, their large-scale observations make us thick that the σ phase particles are as dense as shown in the SEM pictures of Cui [44] (about 7000h of creep at 600°C, 650°C and 700°C).

5.5.2.4 Conclusion about cavity nucleation rate

Knowing the parameters of the macroscopic Andrade and Norton laws, the parameters of crystal viscoplasticity laws can be easily adjusted (Fig. 2.3). Then, the interface normal stress distributions can be calculated by crystal viscoplasticity Finite Element computations. Thereafter, combining the time dependence of the fraction of fractured interfaces with the distribution of intergranular particles, it may be possible to check the validity of the Dyson law, and calculate the prefactor of the Dyson law, α', under any creep condition for perhaps all polycrystalline alloys with intergranular particles.

A similar Finite Element calculation was performed to calculate the stress field at triple points [80]. The stress obtained is only 1.5 times higher than the

tensile stress, which is not enough for inducing the grain boundary decohesion. However, cavities at triple points are often observed. This may be due to the fact that second phase particles at triple points may induce even higher stress concentration than the ones along grain boundaries. Similarly, we found very high interface stress close to the particle tip, which could be considered as the triple points enhanced by participles, aligned with the tensile axis and two neighbor grains ($\alpha_{GB} = 0°$). But lower interface stress we found along the interfaces of particles and one grain only ($\alpha_{GB} = 90°$).

It is then recommended to perform similar Finite Element calculations with inclusions at triple points. Random crystallographic orientations of the neighbor grains should of cause be accounted for. It should nevertheless be noticed that particles at triple point are much less than intergranular ones, even if they are larger. Therefore, accounting triple point particles may impact more the predicted cavity nucleation threshold strain, E_c^{vp}, the α' prefactor. Further, the effect of grain boundary sliding should become more dominant at triple points than the one along grain boundary full of particles. This phenomenon may also increase the stress concentration.

5.5.3 Lifetime predictions

Finally, long term creep lifetimes predictions are performed using the Riedel model, with the predicted α' prefactor value, at temperatures ranging from 525 to 700°C. The results show that the long term creep lifetimes at temperatures ranging from 525 to 700°C are well predicted.

Even the evaluated α' is lower than the experimental ones [115] by factors between two and three. It could still lead to largely validated lifetime predictions. Because, the differences in creep lifetimes caused by the difference of α' is only 41-70% (Eq. 4.34), which is much lower than the scatter in experimental data.

$$t_f \propto \dot{N}_0^{-3/5} \propto {\alpha'}^{-3/5} \tag{5.34}$$

Further, our predictions valid well for the creep data of 316H TP steel [2] and 316-HP steel[183]. This leads us to proposed that the Norton law parameters of 316H TP, 316-HP and 316L(N) steels under study are very similar. Further, the intergranular particle densities do not differ too much for both materials.

No fitted parameter is used for performing the long term creep lifetime predictions based on which the Riedel model. The Riedel model uses the phenomenological Dyson law, which becomes a fully physically-based model through our modeling.

5.5.4 Comparison of the long term creep resistance in Incoloy 800, 316L(N) and Grade 91 steel

Despite the differences in chemical composition, precipitation evolution, microstructure, etc. , similarities in the creep behavior of 316L(N) stainless steel ([44, 69, 128] and present work), Incoloy 800 (present work) and Grade 91 [80] should be noticed such as:

(1) Necking fracture occurs generally at high stress and low temperature, intergranular fracture is predominant at low stress and high temperature;

(2) The change in damage mechanism leads to a slope change in stress-lifetime curves;

(3) The combination of the necking and Riedel models allows lifetime predictions in fair agreement with experimental data.

Fig. 4.19 allows us to discuss the predicted creep lifetime in these three materials in the stress range of 50-500MPa, at 500, 550 and 600°C. The predictions are performed by the combination of the necking and Riedel models. It should be noticed that the transition in damage mechanisms is neither observed or predicted in Grade 91 steel at 500°C, 200kh and 600°C, 94kh [68]. And the longest experimental test duration of Incoloy 800 is only 30 000h, which is shorter than the ones in other materials. Then, additional long term creep data may be required. For the necking regime in 316L(N), the lifetimes were predicted by Cui et al. [115]. And for the intergranular damage regime of 316L(N), the creep lifetimes are predicted through the Riedel model, taken into account our predicted value of the Dyson law prefactor, $\alpha' = 2.2 \cdot 10^9 m^{-2}$.

Fig. 4.19 shows that generally, the 316L(N) steel have the strongest creep strength compared to the others. At 500°C, under high tensile stress ($> 250MPa$), Incoloy 800 has better creep strength than Grade 91. We can conclude from Fig. 4.19 that the change in damage mechanisms is firstly predicted in Incoloy 800, then, 316L(N) and finally, Grade 91.

Two families of steels could be distinguished here. For ferritic-martensitic steel, dislocation densities decrease during creep. Therefore, the strain rate accelerates after the minimum strain rate is reached. On the contrary, 316L(N) and Incoloy 800 are subjected to hardening during creep due to the production of dislocations. The microscopic observations carried out on Grade 91 [80, 147] highlighted a low intergranular precipitates density compared to the Incoloy 800 and 316L(N) ones. Nevertheless, this is only a qualitative conclusion, because we have not performed statistical measurements concerning intergranular particles in Incoloy 800 and Grade 91. As intergranular second phase particles provide the cavity nucleation site, then, less cavities could be nucleated in Grade 91 steel. This may explain why the intergranular damage is not dominant compared to the necking one up to 10 years at 600°C. In Incoloy 800, no σ phase particle is observed. The $M_{23}C_6$ particles are generally observed along grain boundaries with sizes about $500nm$. There seems to be a higher density intergranular particles

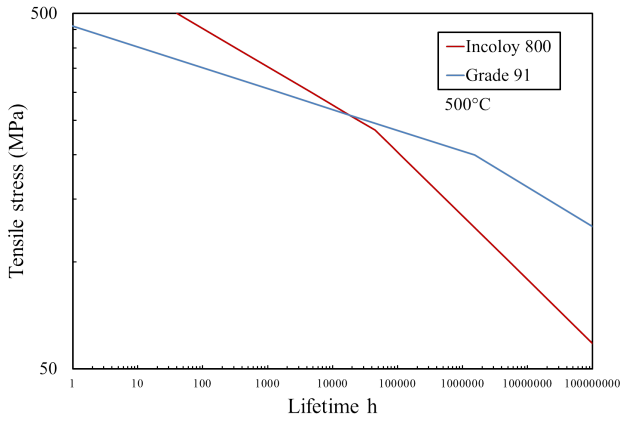

(a)

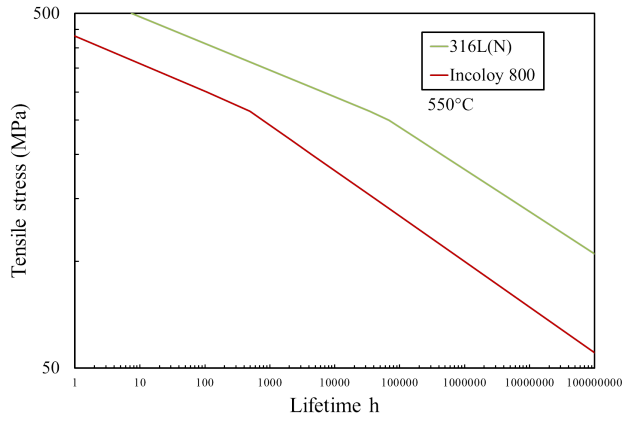

(b)

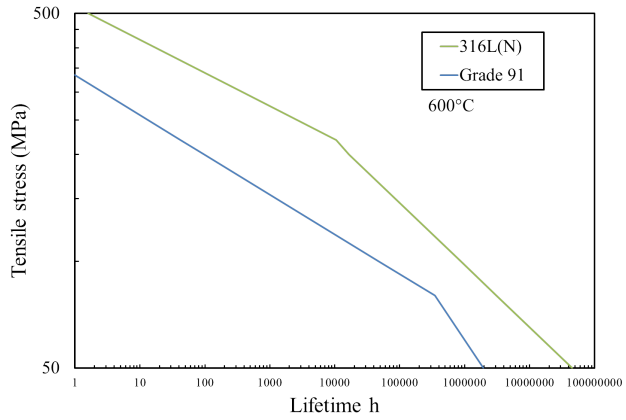

(c)

Figure 5.19: Comparison between predicted lifetimes in Incoloy 800, 316L(N) and Grade 91 at (a) 500, (b) 550 and (c) 600°C.

in Incoloy 800 than in 316L(N). This may explain that the Dyson law prefactor, α', in Incoloy 800 is 100 times higher than in 316L(N). However, further statistical measurements of particle densities and sizes are definitively required to draw definitive conclusions. And computations similar to the ones presented in this manuscript may allow the prediction of the Dyson law prefactor in Incoloy 800 and Grade 91 steels, accounting for their viscoplastic behavior and intergranular particle kind, size and density.

Chapter 6

Conclusions, work in progress and perspectives

6.1 Conclusions

The generation IV of nuclear reactors under development in France large research efforts in relationship with the design of the ASTRID (Advanced Sodium Technological Reactor for Industrial Demonstration), a sodium-cooled fast reactor (SFR). The 316L(N) stainless steel will be used in circuit components. And Incoloy 800 was proposed to be used in steam generator tubes. The corresponding components will operate at high temperature and low stress and for a long duration, up to 60 years. The extrapolation of short term experimental data obtained at high tensile stress, high or low temperature, generally lead to large overestimations of long term creep lifetimes with respect to the existing experimental data.

Short and long creep damages of Incoloy 800 and austenitic stainless steel 316L(N) are investigated both experimentally and theoretically, which leads us to finally predict creep lifetime based on the involved physical mechanisms.

We focus on three main tasks:

- experimental investigations of damage mechanisms showing that cavity nucleation occurs along the interfaces of intergranular particle and matrix;

- the Finite Element calculations of particle-matrix interface stress fields combined with cavity nucleation criteria;

- short and long term creep lifetime predictions and careful comparisons with experimental data.

6.1.1 Experimental investigation of damage mechanisms

During this thesis, various observation techniques are used to characterize the damage mechanisms, including SEM-FEG, TKD and TEM.

Considering Incoloy 800, SEM-FEG observations show two main fracture mechanisms: necking fracture and intergranular fracture. The observations of fracture surfaces show that:

- necking fracture surfaces are covered by voids and dimples at high stress;

- on the intergranular fracture surface, grain boundaries and grains are clearly observed at the stress.

Then, the relationship between the fracture mechanism and the reduction in cross-section is highlighted. Necking fracture leads to generally high reduction in cross-section ($Z\% > 40\%$), and intergranular fracture leads to a lower reduction in cross-section ($Z\% < 30\%$).

The observations of the polished longitudinal sections by FEG-SEM in long term specimens show intragranular microcracks, intergranular cavities and intergranular cracks. Intragranular microcracks are generally observed along intragranular $Ti(C,N)$ precipitates-matrix interfaces and inside $Ti(C,N)$ precipitates. However, the size of microcracks is limited by the precipitates size. Intergranular cavities are generally observed along intergranular $M_{23}C_6$ carbide-matrix interfaces. During creep, intergranular cavities grow and finally coalesce to from intergranular cracks.

Similarly, in 316L(N) steel and more generally in austenitic stainless steels, necking and intergranular fractures were generally observed at respectively high and low stress.

Two types precipitates are generally observed along grain boundaries: $M_{23}C_6$ carbide and σ phase particles. The main chemical element of these two second phase particles are very similar, however their crystallographic structures are different. Therefore, the main observation techniques used to characterize these particles are: TKD and TEM. Microscopic observations show that the typical σ phase particle size ($> 1\mu m$) is much larger than the $M_{23}C_6$ carbide one ($200 - 500\mu m$). And cavities are generally located along intergranular σ phase particle-matrix interfaces. Therefore, we focus only on the characterization of precipitation and cavitation.

Even it has been widely observed, the cavity nucleation mechanism has not been well established yet. It is generally believed that cavities nucleate due to high local stress. This leads us to perform FE computations to investigate the stress fields around intergranular second phase particles in agreement with our as well as literature observation.

6.1.2 Crystal viscoplasticity Finite element calculations of stress fields around intergranular second phase particles and effect on cavity nucleation

A crystalline viscoplasticity law is used in the Finite Element calculations (Cast3M). Only on crystal viscoplasticity parameters are adjusted by predicting macroscopic

creep strain curves of polycrystalline aggregates as close as possible to experimental curves. The parameter adjustment is performed, at $600°C$ (220MPa and 230MPa) and $650°C$ (130MPa).

The stress fields around intergranular inclusions are calculated using Finite Element simulations assuming quasi 2D plane stress. The microstructur meshes are base on the analysis of our SEM/TEM images. The main microstructure features are accounted for step by step in our FE simulations: the random crystalline orientations of the two neighbor grains, the orientation of the grain boundary with respect to the tensile axis, the intergranular particle shape factor and the particle tip geometry and angle in case of angular tip.

The crystalline orientations of the neighbor grains lead to a large heterogeneity in the normal and shear stress fields along particle-matrix interface compared to the one of one isolated particle embedded in a homogeneous matrix. And the average ratio between the maximum normal stress computed along the interface of a particle surrounded by two grains and the one embedded in the homogeneous matrix amounts to 1.85. And the maximum and minimum ratio are respectively 4.14 and 0.33 Surprisingly, fifteen couples of crystalline orientations only allow the prediction of an accurate enough distribution of interface stresses. Furthermore, three creep conditions are considered, at $600°C$ under 220MPa, $600°C$ under 230MPa and $650°C$ under 130MPa. And the results show that the various interface stress distributions are almost independent on stress and temperature. In the considered range of loading parameter variation, the interface stresses depend only on the macroscopic creep strain.

By varying the angle between grain boundary plane and the tensile axis, α_{GB}, calculation results show that the increase in α_{GB} angle leads to a continuous decrease in the interface normal stress for α_{GB} up to 75°, by a factor of 0.55, and a slight final increase up to $\alpha_{GB} = 90°$.

The particle geometry, itself includes the shape factor, the tip geometry (circular, symmetrical angular and the asymmetrical angular features) and finally the tip angle of the angular tip. Our results show that the maximum interface normal stresses increase generally the shape factor varying from one to seven. Thereafter, the maximum interface normal stress is almost constant. The average stress ratio between elongated and circular particles amounts to 2.2, very close to the value predicted by the thermo-elastic Eshelby-Kröner solution. Symmetrical angular tip leads an increase in the interface normal stress by an average factor of 1.66, referring to circular tips. And this average factor reaches 1.09 for the asymmetrical angular tip compare to the symmetrical one. The effect of the angle of these angular tip is investigated too.

Finally, a simplified multiplication equation is proposed to calculate the distribution of interface normal stress accounting for the considered microstructure feature details.

Then, a stress criterion and an energy criterion are used to predict interface fracture. The required interface fracture stress value is evaluated by applying

the Universal Bounding Energy Relationship [118, 159]. An interface fracture stress of $5 \pm 1GPa$ is found using parameters reported in literature. The size effect is highlighted by the simplified energy criterion. The results show that large precipitates $> 1\mu m$ are favorite for cavity nucleation. Therefore, only the density of σ phase particles is accounted, deduce the cavity nucleation rate.

Combining the computed interface stress distribution with the interface fracture stress criterion allows the prediction of the fraction of fractured interfaces and threshold remote strain, E_c^{vp}. The fraction of fractured interfaces increases linearly with the difference between the remote strain and the threshold strain, $E^{vp} - E_c^{vp}$. Assuming that the number of particle is constant during each test for $E^{vp} > E_c^{vp}$, our results permits us to provide a theoretical explanation of the phenomenological cavity nucleation law proposed by Dyson. This well-known law was proved by numerous observations and measurements carried out in various materials. Further, the distribution of cavities in function of the α_{GB} angle is well predicted compared to experimental observations [75], which means that at the beginning of creep, much more cavities are observed along grain boundaries parallel to the tensile axis than along the perpendicular ones.

Finally, the use of measured σ phase particle density reported in literature, permits us predict the Dyson law prefactor, α', value. Considering only the grain boundaries with the α_{GB} angle higher than 45° for allowing stress-induced diffusion growth to occur along grain boundaries. The deduced value of the Dyson law prefactor amounts to $2.2 \cdot 10^9 m^{-2}$. This calculated prefactor differs from the experimental values by a factor ranging between 2 and 4. However, only crystalline orientations, shape factor and grain boundary planes such as: $\alpha_{GB} \geqslant 45°$ are considered. This may underestimate the stress distribution. The values of Dyson law prefactor, α', depending on the assumptions describing the microstructure are provided in Table 5.1.

α_{GB} (°)	shape factor (a/b)	particle tip angle (φ)	α' (m^{-2})
0-90	3		$1.2 \cdot 10^{10}$
0-90	measured distribution$^{(1)}$		$8.1 \cdot 10^9$
45-90	measured distribution$^{(1)}$		$2.2 \cdot 10^9$
45-90	measured distribution$^{(1)}$	measured distribution$^{(2)}$	$3.3 \cdot 10^9$

Table 6.1: Effect of the considered microstructure features on the predicted Dyson law prefactor, α', value. $^{(1)}$ statistically representative, $^{(2)}$ only 25 particles are accounted for.

6.1.3 Enhanced prediction of creep lifetimes

The final predictions of creep lifetimes are deduced by combination of two models: the necking model and the Riedel model.

For the short term creep, the viscoplastic instability is dominant. This leads to a local unstable reduction of cross-section, named necking. The evolution of necking leads to short term creep fracture. Based on the Hart criterion, a necking model is proposed to predict short creep lifetimes.

For long term creep, intergranular damage is dominant, which can be separated into three parts: cavity nucleation, intergranular vacancy diffusion growth and coalescence. Assuming that cavity nucleates continuously (the Dyson law) and cavity growth by vacancy diffusion along grain boundaries, the Riedel model is applied.

The predictions of creep lifetime using this combination of two models are applied to many creep conditions in Incoloy 800 alloys and 316L(N) stainless steels.

Concerning Incoloy 800, the parameters are experimentally measured or reported in literature. The combined model leads to predictions at temperatures ranging between 500 and 760°C and lifetimes up to 35 000h. And time and stress at which the slope change in the stress-lifetime curves is correctly predicted. Further, the comparisons between different batches of Incoloy 800 show that high Ti+Al content leads to enhanced creep resistance. This effect is qualitatively well predicted by the combined model.

Concerning austenitic stainless steels (316L(N), 316H TB and 316 TB), the prefactor of the Dyson law is deduced from our Finite Element calculations and measured density and size of intergranular particles. The short term creep lifetime predictions were evaluated. The long term lifetimes using the computed Dyson law prefactor are well predicted for temperature ranging in 550 and 700°C and lifetime up to 166 000h.

6.2 Work in progress

At the end of this thesis, some works are still in progress, including CZM computations and SEM *in situ* tensile tests.

Information concerning CZM are presented in subsection 4.2.4.3. The final computation using various precipitate sizes should allow us to introduce direly the size effect and the energy balance equation.

In our context, SEM *in situ* tensile tests is aimed to visualize and quantify surface damage of the specimen. These tests require the careful preparation of the surface of the samples, which is essential for the image processing for the measurement of a fracture criterion (critical remote strain) at which cavities are initiated along some of the precipitate interface. Thereafter, it is possible to evaluate the viscoplastic cavity growth kinetics. The SEM *in situ* tensile tests will be carried out at the SRMA/LA2M laboratory.

The material used is a 316L(N) steel aged at 550°C during 130 000h (at EDF, les Renardières). Rather long σ phase and/or carbide particles are located along

grain boundaries. On specimen surface, a deposit of micro-grids of gold could be made by micro-electrolithography. Then, the field of local deformations could thus be determined by image correlation. Further, the lattice rotation could be determined by the evolution of EBSD patterns during straining. Then, Finite Element simulations based on the local microstructure data will be carried out to determine the critical interface stress and to compare with the DFT simulations.

The tensile tests will be carried out at ambient temperature. Therefore, thermally-activated cavity nucleation is avoided. That allows us to focus only on interface fracture. The specimens of aged material are ready to be used in the *in situ* tensile testing and using a planning with many interruptions at various strains

6.3 Perspectives

6.3.1 Local stress concentration

Microscopic observations [231] show that cavities nucleate at first at triple points, and then along grain boundaries. In this thesis, we focus only on the stress concentrations around the intergranular precipitates. Previous FE calculations of the stress concentration at triple point showed a local stress higher than the tensile stress by a factor of two [80]. Nevertheless, these last calculations did not take into account particles located at triple junctions. It may be necessary to carry out simulations with particles located at triple junction.

Further, in Incoloy 800, fracture inside intragranular $Ti(C,N)$ particles is often observed. The fracture could be observed at the interface of $Ti(C,N)$ and matrix, or in the $Ti(C,N)$ particles. Using the same crystalline viscoplastic law but readjusting the activation volume and evaluating the dislocation density, it is possible to calculate the interface stress and the stress inside the particle to understand such a competition. DFT computations predicting the fracture of $Ti(C,N)$ particles and $Ti(C,N)$-matrix interface to predict the corresponding fracture stress and energies, or cohesive laws. These works will be carried out in collaborating with E.Barbé (CEA, SRMP&SRMA)

6.3.2 Intergranular Diffusion

In our Finite Element calculations, the viscoplastic relaxation is only slightly observed in some of the curves of interface stress evolution with remote creep strain. Nevertheless, several authors [72, 73, 244] proposed that the interfacial diffusion may lead to another type of local stress relaxation.

Further, intergranular vacancy diffusion controls the cavity growth process for these materials and under the considered conditions. In this thesis, we consider the grain boundary planes such that $\alpha_{GB} \geqslant 45°$, based on experimental

observations, to avoid cavities which do not grow after nucleation because of the low normal stress acting on grain boundary planes. However, taken into account the intergranular diffusion mechanism, it is possible to quantify this dependence with respect to α_{GB} by recomputing the intergranular damage accounting for both $\alpha'(\alpha_{GB})$ and the normal stress acting on grain boundary inclined with respect to the tensile axis.

6.3.3 Precipitation

The cavity nucleation rate affects the prediction of long term creep lifetimes. And cavities are usually observed close to intergranular precipitates. In our evaluation of the Dyson law prefactor, α', the precipitate density used as an input parameter is based on numerous measurements at high temperature, but only in fractured specimens. Then, we assume in our FE computation that the precipitates are preexisting. However, precipitation is a continuous process occurring during creep. Further, these experimental observations and measurements require very long term creep tests and careful observations and measurements, which are rarely performed.

Therefore, the predictions of precipitation may be very helpful to predict long term creep lifetimes. Some numerical tools, as THERMOCALC, CALPHAD [42], DICTRA [34] or MATCALC, could give several precipitation information (at equilibrium or in kinetic conditions). Furthermore, it is observed that the precipitation in the head and gauge portions of specimens may differ strongly. Then, DICTRA or MATCALC may better to be used compared to THERMOCALC or CALPHAD.

Bibliography

[1] Association française pour les règles de conception et de construction des matériels des chaudières électro-nucléaires, RCC-MR 2007 Design and Construction Rules for Mechanical components of nuclear installations, AFCEN, 2007.

[2] NIMS, Creep data sheet, No. M-2, Micrographs and microstructural characteristics of crept specimens of 18cr-12ni-Mo stainless steel for boiler and heat exchanger seamless tubes (SUS 316h TB), Tech. rep., Japan (2003).

[3] American Society for Testing Material (ASTM), Specification for nickel-iron-chromium alloy seamless pipe and tube, B407-04 Standard, 2004.

[4] F. Abe, T.-U. Kern, R. Viswanathan (Eds.), Creep-Resistant Steels, Woodhead Publishing, Boca Raton, Fla., 2008.

[5] J. E. Harris, Nucleation of Creep Cavities in Magnesium, Trans. Met. Soc. AIME 233.

[6] Sof'in M.V, Kerimov E.Y., Slyusarenko E.M., Isotermal section of the phase diagram of te Fe-Ni-Cr system at 1373 K (1997) 46–49.

[7] J. C. Lippold, D. J. Kotecki, Welding Metallurgy and Weldability of Stainless Steels, 1st Edition, Wiley-Interscience, Hoboken, NJ, 2005.

[8] P. Lacombe, B. Baroux, G. Béranger, Les aciers inoxydables, les editions de physique Edition, EDP Sciences, Les Ulis, 1990.

[9] A. F. Padilha, P. R. Rios, Decomposition of Austenite in Austenitic Stainless Steels, ISIJ International 42 (4) (2002) 325–327. doi:10.2355/isijinternational.42.325.

[10] E. M. Westin, Microstructure and properties of welds in the lean duplex stainless steel LDX 2101, PhD Thesis, Royal Institute of Technology, Stockholm, oCLC: 704529656 (2010).

[11] S. Hertzman, J. Charles, On the effect of nitrogen on duplex stainless steels, in: Revue de Métallurgie, Vol. 108, EDP Science, 2011, pp. 413–425. doi:10.1051/metal/2011071.

[12] H. Berns, V. Gavriljuk, S. Riedner, High Interstitial Stainless Austenitic Steels, Springer Science & Business Media, 2012, google-Books-ID: 9sQTk-CiVrnkC.

[13] R. L. Coble, A Model for Boundary Diffusion Controlled Creep in Polycrystalline Materials, Journal of Applied Physics 34 (6) (1963) 1679–1682. doi:10.1063/1.1702656.

[14] F. R. N. Nabarro, Deformation of Crystals by the Motion of Single Lonsin, Physical Society, U.K, 1948, pp. 75–90.

[15] A. Bougault, Private Communication, CEA.

[16] F. R. Beckitt, B. R. Clark, The shape and mechanism of formation of M23c6 carbide in austenite, Acta Metallurgica 15 (1) (1967) 113–129. doi:10.1016/0001-6160(67)90159-9.

[17] H. U. Hong, B. S. Rho, S. W. Nam, Correlation of the M23c6 precipitation morphology with grain boundary characteristics in austenitic stainless steel, Materials Science and Engineering: A 318 (1–2) (2001) 285–292. doi:10.1016/S0921-5093(01)01254-0.

[18] T. Sourmail, Precipitation in creep resistant austenitic stainless steels, Materials science and technology 17 (1) (2001) 1–14.

[19] C.-C. Hsieh, W. Wu, C.-C. Hsieh, W. Wu, Overview of Intermetallic Sigma Phase Precipitation in Stainless Steels, International Scholarly Research Notices, International Scholarly Research Notices 2012, 2012 (2012) e732471. doi:10.5402/2012/732471,10.5402/2012/732471.

[20] A. Padilha, D. Escriba, E. Materna-Morris, M. Rieth, M. Klimenkov, Precipitation in AISI 316l(N) during creep tests at 550 and 600c up to 10 years, Journal of Nuclear Materials 362 (1) (2007) 132–138.

[21] K. H. Lo, C. H. Shek, J. K. L. Lai, Recent developments in stainless steels, Materials Science and Engineering: R: Reports 65 (4–6) (2009) 39–104. doi:10.1016/j.mser.2009.03.001.

[22] J. Pavlu, Ab initio and semiempirical modelling of intermetallic phases, PhD Thesis, Masaryk University (2016).

[23] G. F. Slattery, P. O'Riordan, M. E. Lambert, S. M. Green, An integrated electron and optical metallographic procedure for the identification of precipitate phases in type 316 stainless steel, Journal of Microscopy 122 (2) (1981) 109–130. doi:10.1111/j.1365-2818.1981.tb01251.x.

[24] W. E. White, I. Le May, Metallographic observations on the formation and occurrence of ferrite, sigma phase, and carbides in austenitic stainless steels: Part II: Studies of AISI Type 316 Stainless Steel, Metallography 3 (1) (1970) 51–60. doi:10.1016/0026-0800(70)90004-2.

[25] A. D. Warren, I. J. Griffiths, R. L. Harniman, P. E. J. Flewitt, T. B. Scott, The role of ferrite in Type 316h austenitic stainless steels on the susceptibility to creep cavitation, Materials Science and Engineering: A 635 (2015) 59–69. doi:10.1016/j.msea.2015.03.048.

[26] R. Cozar, M. Rouby, The influence of microstructure on the mechanical properties of alloy 800, in: Alloy 800, North-Holland Publishing Company, Amsterdam, 1978, pp. 77–82.

[27] C. Smithells, Metals reference book . 4th Edition, Journal of Molecular Structure 1 (1968) 256–256. doi:10.1016/0022-2860(68)87010-3.

[28] W. E. White, I. Le May, Metallographic observations on the formation and occurrence of ferrite, sigma phase and carbides in austenitic stainless steels. Part III. Electron microscopy studies, Metallography 5 (4) (1972) 333–345. doi:10.1016/0026-0800(72)90014-6.

[29] E. A. Trillo, L. E. Murr, A TEM investigation of M23c6 carbide precipitation behaviour on varying grain boundary misorientations in 304 stainless steels, Journal of Materials Science 33 (5) (1998) 1263–1271. doi:10.1023/A:1004390029071.

[30] J. Y. Maetz, T. Douillard, S. Cazottes, C. Verdu, X. Kléber, M23c6 carbides and Cr2n nitrides in aged duplex stainless steel: A SEM, TEM and FIB tomography investigation, Micron 84 (2016) 43–53. doi:10.1016/j.micron.2016.01.007.

[31] J. K. L. Lai, D. J. Chastell, P. E. J. Flewitt, Precipitate phases in type 316 austenitic stainless steel resulting from long-term high temperature service, Materials Science and Engineering 49 (1) (1981) 19–29. doi:10.1016/0025-5416(81)90129-4.

[32] F. Danoix, P. Auger, Atom Probe Studies of the Fe?Cr System and Stainless Steels Aged at Intermediate Temperature, Materials Characterization 44 (1-2) (2000) 177–201. doi:10.1016/S1044-5803(99)00048-0.

[33] J.-O. Nilsson, Super duplex stainless steels, Materials Science and Technology 8 (8) (1992) 685–700. doi:10.1179/mst.1992.8.8.685.

[34] M. Schwind, J. Källqvist, J. O. Nilsson, J. Agren, H. O. Andrén, Sigma phase precipitation in stabilized austenitic stainless steels, Acta Materialia 48 (10) (2000) 2473–2481.

[35] J. M. Vitek, S. A. David, The sigma phase transformation in austenitic stainless steels, welding Journal 65 (4) (1986) 106s–111s.

[36] T. H. Chen, K. L. Weng, J. R. Yang, The effect of high-temperature exposure on the microstructural stability and toughness property in a 2205 duplex stainless steel, Materials Science and Engineering: A 338 (1) (2002) 259–270. doi:10.1016/S0921-5093(02)00093-X.

[37] D. M. E. Villanueva, F. C. P. Junior, R. L. Plaut, A. F. Padilha, Comparative study on sigma phase precipitation of three types of stainless steels: austenitic, superferritic and duplex, Materials Science and Technology 22 (9) (2006) 1098–1104.

[38] M. Rieth, A. Falkenstein, P. Graf, S. Heger, U. Jaentsch, M. Klimiankou, E. Materna-Morris, H. Zimmermann, Creep of the austenitic steel AISI 316 L(N). Experiments and models, Tech. Rep. FZKA–7065, Forschungszentrum Karlsruhe GmbH Technik und Umwelt (Germany). Inst. fuer Materialforschung - Programm Kernfusion (2004).

[39] M. Odnobokova, A. Kipelova, A. Belyakov, R. Kaibyshev, Microstructure evolution in a 316l stainless steel subjected to multidirectional forging and unidirectional bar rolling, IOP Conference Series: Materials Science and Engineering 63 (1) (2014) 012060. doi:10.1088/1757-899X/63/1/012060.

[40] EDF, CEA, Etude des caractéristiques méchaniques à chaud de quatre tôles en acier inoxydable austénitique 17-12 au molybdène, à très bas carbone et awote contôlé, nuance ICL 167 SPH de Creusot-Loire, référencées SP, SQ, SR et ST., Tech. rep. (1987).

[41] M. D. Mathew, M. Sundararaman, S. L. Mannan, Dislocation Substructure and Precipitation in Type 316 Stainless Steel Deformed in Creep, Materials Transactions, JIM 38 (1) (1997) 37–42. doi:10.2320/matertrans1989.38.37.

[42] Y. Yang, J. T. Busby, Thermodynamic modeling and kinetics simulation of precipitate phases in AISI 316 stainless steels, Journal of Nuclear Materials 448 (1–3) (2014) 282–293. doi:10.1016/j.jnucmat.2014.02.008.

[43] J. Lemaitre, J.-L. Chaboche, A. Benallal, R. Desmorat, Mécanique des matériaux solides - 3ème édition, 3rd Edition, Dunod, Paris, 2009.

[44] Y. Cui, Etude numérique et expérimentale de l'endommagement de fluage à long terme dans les aciers inoxydables austénitiques, PhD Thesis, Paris 6 (2015).

[45] F. H. Norton, The creep of steel at high temperatures, 1st Edition, McGraw-Hill book company, inc., New York [etc.], 1929.

[46] O. D. Sherby, P. M. Burke, Mechanical behavior of crystalline solids at elevated temperature, Progress in Materials Science 13 (1968) 323–390. doi:10.1016/0079-6425(68)90024-8.

[47] G. A. Webster, R. A. Ainsworth, High Temperature Component Life Assessment, 1994th Edition, Springer Netherlands, London u.a.: Chapman & Hall, 1994.

[48] M. K. Booker, Analytical representation of the creep and creep-rupture behavior of Alloy 800h, ONRL.

[49] C. R. Brinkman, Elevated-Temperature Mechanical Properties of an Advanced-Type 316 Stainless Steel, Journal of Pressure Vessel Technology 123 (1) (2000) 75–80. doi:10.1115/1.1343911.

[50] F. J. Monkman, N. J. Grant, An empirical relationship between rupture life and minimum creep rate in creep-rupture tests, Proc. Am. Soc. Test Mater. (1956) 593–620.

[51] H. Riedel, Fracture at High Temperatures, Springer-Verlag, Berlin ; New York, 1987.

[52] M. E. Kassner, M.-T. Perez-Prado, Fundamentals of Creep in Metals and Alloys, Elsevier, 2004.

[53] P. Feltham, J. D. Meakin, Creep in face-centred cubic metals with special reference to copper, Acta Metallurgica 7 (9) (1959) 614–627. doi:10.1016/0001-6160(59)90131-2.

[54] F. R. Larson, J. Miller, A Time-Temperature Relationship for Rupture and Creep Stresses, Trans. ASME 74 (1952) 765–771.

[55] A. K. Mukherjee, J. E. Bird, J. E. Dorn, Experimental Correlations for High-Temperature. Creep, Transactions of the American Society for Metals 62 (1969) 155–179.

[56] W. R. Cannon, T. G. Langdon, Creep of ceramics, Journal of Materials Science 23 (1) (1988) 1–20. doi:10.1007/BF01174028.

[57] D. Francois, A. Pineau, A. Zaoui, Comportement mecanique des materiaux : viscoplasticite, endommagement, mecanique de la rupture, mecanique du contact, Hermes, 1993.

[58] C. Herring, Diffusional Viscosity of a Polycrystalline Solid, Journal of Applied Physics 21 (5) (1950) 437–445. doi:10.1063/1.1699681.

[59] H. J. Frost, M. F. Ashby, Deformation-Mechanism Maps: The Plasticity and Creep of Metals and Ceramics, 1st Edition, Pergamon Press, Oxford Oxfordshire ; New York, 1982.

[60] H. Park, B. C. D. Cooman, Creep Deformation of Type 2205 Duplex Stainless Steel and its Constituent Phases, ISIJ International 54 (4) (2014) 945–954. doi:10.2355/isijinternational.54.945.

[61] R. Raj, M. F. Ashby, On grain boundary sliding and diffusional creep, Metallurgical Transactions 2 (4) (1971) 1113–1127. doi:10.1007/BF02664244.

[62] J. Weertman, Theory of Steady State Creep Based on Dislocation Climb, Journal of Applied Physics 26 (10) (1955) 1213–1217. doi:10.1063/1.1721875.

[63] O. D. Sherby, J. Weertman, Diffusion-controlled dislocation creep: a defense, Acta Metallurgica 27 (3) (1979) 387–400. doi:10.1016/0001-6160(79)90031-2.

[64] A. Tavassoli, Private Communication, CEA.

[65] N. HofF, The necking and the rupture of rods subjected to constant tensile loads, J. Appl. Mech. 20 (No. 1) (1953) 105–108.

[66] R. Westlund, A qualitative evaluation of phenomenological creep rupture theories, J. Mechanical Engineering Science 18 (1976) 175–178.

[67] E. W. Hart, Theory of the tensile test, Acta Metallurgica 15 (2) (1967) 351–355. doi:10.1016/0001-6160(67)90211-8.

[68] R. Lim, M. Sauzay, F. Dalle, I. Tournié, A.-F. Gourgues-Lorenzon, Modelling of necking during creep of grade 91 steel, International Journal of Fracture 169 (2011) 213–228.

[69] J. He, R. Sandström, Basic modelling of creep rupture in austenitic stainless steels, Theoretical and Applied Fracture Mechanics 89 (2017) 139–146. doi:10.1016/j.tafmec.2017.02.004.

[70] R. Sandström, Fundamental Models for Creep Properties of Steels and Copper, Transactions of the Indian Institute of Metals 69 (2) (2016) 197–202. doi:10.1007/s12666-015-0762-y.

[71] R. Sandström, H. C. M. Andersson, Creep in phosphorus alloyed copper during power-law breakdown, Journal of Nuclear Materials 372 (1) (2008) 76–88. doi:10.1016/j.jnucmat.2007.02.005.

[72] R. C. Koeller, R. Raj, Diffusional relaxation of stress concentration at second phase particles, Acta Metallurgica 26 (10) (1978) 1551–1558. doi:10.1016/0001-6160(78)90064-0.

[73] T. Mori, M. Okabe, T. Mura, Diffusional relaxation around a second phase particle, Acta Metallurgica 28 (3) (1980) 319–325. doi:10.1016/0001-6160(80)90167-4.

[74] B. F. Dyson, Continuous cavity nucleation and creep fracture, Scripta Metallurgica 17 (1) (1983) 31–37. doi:10.1016/0036-9748(83)90065-0.

[75] K. Shiozawa, J. R. Weertman, Studies of nucleation mechanisms and the role of residual stresses in the grain boundary cavitation of a superalloy, Acta Metallurgica 31 (7) (1983) 993–1004. doi:10.1016/0001-6160(83)90194-3.

[76] M. A. Capano, A. S. Argon, I.-W. Chen, Intergranular cavitation during creep in astroloy, Acta Metallurgica 37 (12) (1989) 3195–3204. doi:10.1016/0001-6160(89)90191-0.

[77] R. Raj, M. F. Ashby, Intergranular fracture at elevated temperature, Acta Metallurgica 23 (6) (1975) 653–666. doi:10.1016/0001-6160(75)90047-4.

[78] J. N. Greenwood, D. R. Miller, J. W. Suiter, Intergranular cavitation in stressed metals, Acta Metallurgica 2 (2) (1954) 250–258. doi:10.1016/0001-6160(54)90166-2.

[79] M. H. Yoo, H. Trinkaus, Crack and cavity nucleation at interfaces during creep, Metallurgical Transactions A 14 (3) (1983) 547–561. doi:10.1007/BF02643772.

[80] R. Lim, Numerical and experimental study of creep of Grade 91 steel at high temperature, PhD Thesis, MINES ParisTech, Paris (2012).

[81] R. Raj, Nucleation of cavities at second phase particles in grain boundaries, Acta Metallurgica 26 (6) (1978) 995–1006. doi:10.1016/0001-6160(78)90050-0.

[82] J.-C. Arnaud, Etude de l'endommagement par fluage des aciers inoxydables austenitiques entre 550 degre c et 650 degre c, PhD Thesis, Ecole Nationale Supérieure des Mines de Saint-Etienne, (1987).

[83] H. R. Tipler, B. E. Hopkins, The creep cavitation of commercial and high-purity Cr-Mo-V steels, Metal Science 10 (2) (1976) 47–56.

[84] C. W. Chen, E. S. Machlin, On the mechanism of intelcrystalline cracking, Acta Metallurgica 4 (6) (1956) 655–656. doi:10.1016/0001-6160(56)90171-7.

[85] R. G. Fleck, D. M. R. Taplin, C. J. Beevers, An investigation of the nucleation of creep cavities by 1 MV electron microscopy, Acta Metallurgica 23 (4) (1975) 415–424. doi:10.1016/0001-6160(75)90081-4.

[86] B. Barkia, V. Doquet, J. P. Couzinié, I. Guillot, E. Héripré, In situ monitoring of the deformation mechanisms in titanium with different oxygen contents, Materials Science and Engineering: A 636 (2015) 91–102. doi:10.1016/j.msea.2015.03.044.

[87] B. F. Dyson, M. S. Loveday, M. J. Rodgers, Grain Boundary Cavitation Under Various States of Applied Stress, Proceedings of the Royal Society of London A: Mathematical, Physical and Engineering Sciences 349 (1657) (1976) 245–259. doi:10.1098/rspa.1976.0071.

[88] A. N. Stroh, A theory of the fracture of metals, Advances in Physics 6 (24) (1957) 418–465. doi:10.1080/00018735700101406.

[89] M. E. Kassner, T. C. Kennedy, K. K. Schrems, The mechanism of ductile fracture in constrained thin silver films, Acta Materialia 46 (18) (1998) 6445–6457. doi:10.1016/S1359-6454(98)00299-7.

[90] M. Sauzay, K. Vor, Influence of plastic slip localization on grain boundary stress fields and microcrack nucleation, Engineering Fracture Mechanics 110 (Supplement C) (2013) 330–349. doi:10.1016/j.engfracmech.2013.04.019.

[91] J. D. Eshelby, The Determination of the Elastic Field of an Ellipsoidal Inclusion, and Related Problems, Proceedings of the Royal Society of London A: Mathematical, Physical and Engineering Sciences 241 (1226) (1957) 376–396. doi:10.1098/rspa.1957.0133.

[92] D. Hull, D. E. Rimmer, The growth of grain-boundary voids under stress, Philosophical Magazine 4 (42) (1959) 673–687. doi:10.1080/14786435908243264.

[93] B. F. Dyson, Constraints on diffusional cavity growth rates, Metal Science 10 (10) (1976) 349–353. doi:10.1179/030634576790431417.

[94] J. R. Rice, Constraints on the diffusive cavitation of isolated grain boundary facets in creeping polycrystals, Acta Metallurgica 29 (4) (1981) 675–681. doi:10.1016/0001-6160(81)90150-4.

[95] W. D. Nix, K. S. Yu, J. S. Wang, The effects of segregation on the kinetics of irrtergranular cavity growth under creep conditions, Metallurgical Transactions A 14 (3) (1983) 563–570. doi:10.1007/BF02643773.

[96] I.-W. Chen, A. S. Argon, Diffusive growth of grain-boundary cavities, Acta Metallurgica 29 (10) (1981) 1759–1768. doi:10.1016/0001-6160(81)90009-2.

[97] J. W. Hancock, Creep cavitation without a vacancy flux, Metal Science 10 (9) (1976) 319–325. doi:10.1179/msc.1976.10.9.319.

[98] W. Beere, M. V. Speight, Creep cavitation by vacancy diffusion in plastically deforming solid, Metal Science 12 (4) (1978) 172–176. doi:10.1179/msc.1978.12.4.172.

[99] A. C. F. Cocks, M. F. Ashby, On creep fracture by void growth, Progress in Materials Science 27 (3–4) (1982) 189–244. doi:10.1016/0079-6425(82)90001-9.

[100] A. Needleman, J. R. Rice, Plastic creep flow effects in the diffusive cavitation of grain boundaries, Acta Metallurgica 28 (1980) 1315–1332. doi:10.1016/0001-6160(80)90001-2.

[101] A. Weck, D. S. Wilkinson, Experimental investigation of void coalescence in metallic sheets containing laser drilled holes, Acta Materialia 56 (8) (2008) 1774–1784. doi:10.1016/j.actamat.2007.12.035.

[102] R. D. Thomson, J. W. Hancock, Local stress and strain fields near a spherical elastic inclusion in a plastically deforming matrix, International Journal of Fracture 24 (3) (1984) 209–228. doi:10.1007/BF00032684.

[103] P. F. Thomason, Three-dimensional models for the plastic limit-loads at incipient failure of the intervoid matrix in ductile porous solids, Acta Metallurgica 33 (6) (1985) 1079–1085. doi:10.1016/0001-6160(85)90201-9.

[104] V. Tvergaard, Material Failure by Void Growth to Coalescence, Advances in Applied Mechanics 27 (1989) 83–151. doi:10.1016/S0065-2156(08)70195-9.

[105] A. L. Gurson, Plastic Flow and Fracture Behavior of Ductile Materials Incorporating Void Nucleation, Growth, and Interaction, PhD Thesis, Brown University, google-Books-ID: xtrnHgAACAAJ (1975).

[106] S. Shima, M. Oyane, Plasticity theory for porous metals, International Journal of Mechanical Sciences 18 (6) (1976) 285–291. doi:10.1016/0020-7403(76)90030-8.

[107] K. Guan, H. Xu, Z. Wang, Quantitative study of creep cavity area of HP40 furnace tubes, Nuclear Engineering and Design 235 (14) (2005) 1447–1456. doi:10.1016/j.nucengdes.2005.01.009.

[108] K. Ankit, Remaining Creep Life Assessment Techniques Based on Creep Cavitation Modeling, Metallurgical and Materials Transactions A 40 (2009) 1013–1018. doi:10.1007/s11661-009-9781-9.

[109] Q. Auzoux, Fissuration en relaxation des aciers inoxydables austenitiques - Influence de l'écrouissage sur l'endommagement intergranulaire, PhD Thesis, Ecole Nationale Superieure des Mines de Paris (2004).

[110] R. Sandström, M. Farooq, J. Zurek, Basic creep models for 25cr20ninbn austenitic stainless steels, Materials Research Innovations 17 (5) (2013) 355–359. doi:10.1179/1433075X13Y.0000000120.

[111] R. Sandström, R. Wu, Influence of phosphorus on the creep ductility of copper, Journal of Nuclear Materials 441 (1–3) (2013) 364–371. doi:10.1016/j.jnucmat.2013.06.020.

[112] R. Wu, R. Sandström, Strain dependence of creep cavity nucleation in low alloy and 12%Cr steels, Materials Science and Technology 12 (5) (1996) 405–415. doi:10.1179/026708396790165858.

[113] J. He, R. Sandström, Brittle rupture of austenitic stainless steels due to creep cavitation, Procedia Structural Integrity 2 (2016) 863–870. doi:10.1016/j.prostr.2016.06.111.

[114] J. He, R. Sandström, Formation of creep cavities in austenitic stainless steels, Journal of Materials Science 51 (14) (2016) 6674–6685. doi:10.1007/s10853-016-9954-z.

[115] Y. Cui, M. Sauzay, C. Caes, P. Bonnaillie, B. Arnal, C. Cabet, M. Blat-Yrieix, S. Dubiez-Legoff, Modeling and experimental study of long term creep damage in austenitic stainless steels, Engineering Failure Analysis 58 (2015) 452–464. doi:10.1016/j.engfailanal.2015.08.009.

[116] A. S. Argon, I. W. Chen, C. W. Lau, Creep-fatigue-environmental interactions, AIME (1980) 46–69.

[117] A. Pineau, T. Pardoen, 2.06 - Failure of Metals A2 - Milne, I., in: R. O. Ritchie, B. Karihaloo (Eds.), Comprehensive Structural Integrity, Pergamon, Oxford, 2007, pp. 684–797.

[118] J. R. Rice, J.-S. Wang, Embrittlement of interfaces by solute segregation, Materials Science and Engineering A 107 (1989) 23–40. doi:10.1016/0921-5093(89)90372-9.

[119] H. Tanaka, M. Murata, F. Abe, H. Irie, Microstructural evolution and change in hardness in type 304h stainless steel during long-term creep, Materials Science and Engineering: A 319–321 (2001) 788–791. doi:10.1016/S0921-5093(01)01012-7.

[120] F. W. Crossman, M. F. Ashby, The non-uniform flow of polycrystals by grain-boundary sliding accommodated by power-law creep, Acta Metallurgica 23 (4) (1975) 425–440. doi:10.1016/0001-6160(75)90082-6.

[121] J. He, High temperature performance of materials for future power plants, PhD Thesis, KTH Royal Institute of Technology (2016).

[122] E. Smith, J. T. Barnby, Crack Nucleation in Crystalline Solids, Metal Science Journal 1 (1) (1967) 56–64. doi:10.1179/msc.1967.1.1.56.

[123] A. Neimitz, U. Janus, Analysis of Stress and Strain Fields in and around Inclusions of Various Shapes in a Cylindrical Specimen Loaded in Tension, Archives of Metallurgy and Materials 61 (2) (2016) 569–576. doi:http://dx.doi.org/10.1515/amm-2016-0097.

[124] M. Sauzay, L. Kubin, Scaling laws for dislocation microstructures in monotonic and cyclic deformation of fcc metals, Progress in Materials Science 56 (6) (2011) 725–784. doi:10.1016/j.pmatsci.2011.01.006.

[125] F. Hajjaji Rachdi, Modélisation du comportement mécanique des aciers austénitiques inoxydables en fatigue pure et en fatigue-relaxation, PhD Thesis, Paris 6 (2015).

[126] J. Cadek, Creep in Metallic Materials, 1st Edition, Elsevier Science Ltd, Amsterdam ; New York, 1989.

[127] D. Francois, A. Pineau, A. Zaoui, Viscoplasticite, endommagement, mecanique de la rupture et mecanique du contact, Hermes Science Publications, Paris, 2009.

[128] K. Kimura, M. Murata, K. Kamihira, H. Tanaka, Creep strength and microstructural evolution of Type 316l(N) stainless steel, National Institute for Materials Science.

[129] R. Lombard, H. Vehoff, Nucleation and growth of cavities at defined grain boundaries in bicrystals, Scripta Metallurgica et Materialia 24 (3) (1990) 581–586. doi:10.1016/0956-716X(90)90205-U.

[130] E. J. Chun, H. Baba, K. Nishimoto, K. Saida, Precipitation of sigma and chi phases in delta-ferrite of Type 316fr weld metals, Materials Characterization 86 (2013) 152–166. doi:10.1016/j.matchar.2013.10.003.

[131] D. N. Wasnik, G. K. Dey, V. Kain, I. Samajdar, Precipitation stages in a 316l austenitic stainless steel, Scripta Materialia 49 (2) (2003) 135–141. doi:10.1016/S1359-6462(03)00220-3.

[132] J. K. L. Lai, A review of precipitation behaviour in AISI type 316 stainless steel, Materials Science and Engineering 61 (2) (1983) 101–109. doi:10.1016/0025-5416(83)90191-X.

[133] D. J. Chastell, P. E. J. Flewitt, The formation of the sigma phase during long term high temperature creep of type 316 austenitic stainless steel, Materials Science and Engineering 38 (2) (1979) 153–162.

[134] J. K. Shin, S. W. Nam, S. C. Lee, A Study of Nitrogen Effect on the Characteristics of Creep-Rupture in 18cr-9ni Austenitic Steels, Key Engineering Materials 297-300 (2005) 409–414. doi:10.4028/www.scientific.net/KEM.297-300.409.

[135] J. K. L. Lai, A study of precipitation in AISI type 316 stainless steel, Materials Science and Engineering 58 (2) (1983) 195–209. doi:10.1016/0025-5416(83)90046-0.

[136] T. Sourmail, H. K. D. H. Bhadeshia, Modelling simultaneous precipitation reactions in austenitic stainless steels, Calphad 27 (2) (2003) 169–175. doi:10.1016/j.calphad.2003.08.002.

[137] T. L. Burnett, R. Geurts, H. Jazaeri, S. M. Northover, S. A. McDonald, S. J. Haigh, P. J. Bouchard, P. J. Withers, Multiscale 3d analysis of creep cavities in AISI type 316 stainless steel, Materials Science and Technology 31 (5) (2014) 522–534. doi:10.1179/1743284714Y.0000000639.

[138] J. R. Saithala, S. Mahajanam, H. Rincon, J. Clapp, H. S. Ubhi, J. D. Atkinson, Effect of sigma phase on the environmental assisted cracking of super duplex stainless steel in oil field environments, ResearchGate 3 (2012) 2066–2077.

[139] A. Perron, C. Toffolon-Masclet, X. Ledoux, F. Buy, T. Guilbert, S. Urvoy, S. Bosonnet, B. Marini, F. Cortial, G. Texier, C. Harder, V. Vignal, P. Petit, J. Farré, E. Suzon, Understanding sigma-phase precipitation in a stabilized austenitic stainless steel (316nb) through complementary CALPHAD-based and experimental investigations, Acta Materialia 79 (2014) 16–29.

[140] D. Caillard, J. L. Martin, Thermally Activated Mechanisms in Crystal Plasticity, Elsevier, 2003.

[141] P. F. Giroux, F. Dalle, M. Sauzay, C. Caes, B. Fournier, T. Morgeneyer, A. F. Gourgues-Lorenzon, Influence of strain rate on P92 microstructural

stability during fatigue tests at high temperature, Procedia Engineering 2 (2010) 2141–2150. doi:10.1016/j.proeng.2010.03.230.

[142] S. Heraud, Du polycristal au multicristal : élaboration d'un mésoscope numérique pour une analyse locale en élastoviscoplasticité, PhD Thesis, Palaiseau, Ecole polytechnique (1998).

[143] D. Gentet, Compréhension et modélisation du comportement mécanique cyclique anisotherme de l'acier austénitique AISI 316l (N), PhD Thesis, CEA Saclay, Direction des systèmes d'information (2010).

[144] Y. Liu, Y. Jiang, J. Xing, R. Zhou, J. Feng, Mechanical properties and electronic structures of M23c6 (M = Fe, Cr, Mn)-type multicomponent carbides, Journal of Alloys and Compounds 648 (2015) 874–880. doi:10.1016/j.jallcom.2015.07.048.

[145] S. Osterstock, Vers la prediction de l'apparition de reseaux de fissures : influence des parametres microstructuraux sur la dispersion a l'amorcage., PhD Thesis, Ecole Centrale de Lille (2008).

[146] S. Catalao, Etude de l'interaction plasticité/fluage d'un acier austénitique par une approche micro-mécanique, PhD Thesis, Ecole Centrale Paris (2005).

[147] B. Fournier, Fatigue-fluage des aciers martensitique à 9-12%Cr: comportement et endommagement, PhD Thesis, l'Ecole des Mines de Paris (2007).

[148] L. J. Cuddy, Internal stresses and structures developed during creep, Metallurgical and Materials Transactions B 1 (2) (1970) 395–401. doi:10.1007/BF02811548.

[149] K. D. Challenger, J. Moteff, Quantitative characterization of the substructure of AISI 316 stainless steel resulting from creep, Metallurgical Transactions 4 (3) (1973) 749–755. doi:10.1007/BF02643084.

[150] J. H. Hong, S. W. Nam, S. P. Choi, The influences of sulphur and phosphorus additions on the creep cavitation characteristics in type 304 stainless steels, Journal of Materials Science 21 (11) (1986) 3966–3976. doi:10.1007/PL00020267.

[151] Y. Li, Y. Gao, B. Xiao, T. Min, Y. Yang, S. Ma, D. Yi, The electronic, mechanical properties and theoretical hardness of chromium carbides by first-principles calculations, Journal of Alloys and Compounds 509 (17) (2011) 5242–5249. doi:10.1016/j.jallcom.2011.02.009.

[152] J. J. Han, C. P. Wang, X. J. Liu, Y. Wang, Z.-K. Liu, First-principles calculation of structural, mechanical, magnetic and thermodynamic properties for gamma-M 23 C 6 (M = Fe, Cr) compounds, Journal of Physics: Condensed Matter 24 (50) (2012) 505503. doi:10.1088/0953-8984/24/50/505503.

[153] V. F. Degtyareva, L. Dubrovinsky, A. Kurnosov, Structural stability of the sigma phase FeCr under pressure up to 77 GPa, Journal of Physics: Condensed Matter 21 (7) (2009) 075706. doi:10.1088/0953-8984/21/7/075706.

[154] C. Jiang, First-principles study of structural, elastic, and electronic properties of chromium carbides, Applied Physics Letters 92 (4) (2008) 041909. doi:10.1063/1.2838345.

[155] G. P. Tandon, G. J. Weng, Stress distribution in and around spheroidal inclusions and Voids at Finite concentration, Journal of Applied Mechanics 53 (3) (1986) 511–518. doi:10.1115/1.3171804.

[156] B. J. Lee, M. e. Mear, Stress concentration induced by an elastic spheroidal particle in a plastically deforming solid, Journal of the Mechanics and Physics of Solids 47 (6) (1999) 1301–1336. doi:10.1016/S0022-5096(98)00104-5.

[157] T. Lillo, J. Cole, M. Frary, S. Schlegel, Influence of Grain Boundary Character on Creep Void Formation in Alloy 617, Metallurgical and Materials Transactions A 40 (12) (2009) 2803. doi:10.1007/s11661-009-0051-7.

[158] C. Schlacher, T. Pelzmann, C. Béal, C. Sommitsch, C. Gupta, H. Toda, P. Mayr, Investigation of creep damage in advanced martensitic chromium steel weldments using synchrotron X-ray micro-tomography and EBSD, Materials Science and Technology 31 (5) (2014) 516–521. doi:10.1179/1743284714Y.0000000621.

[159] J. H. Rose, J. R. Smith, F. Guinea, J. Ferrante, Universal features of the equation of state of metals, Physical Review B 29 (6) (1984) 2963–2969. doi:10.1103/PhysRevB.29.2963.

[160] E. Bonetti, E. G. Campari, L. Del Bianco, G. Scipione, Anelasticity and structural stability of nanostructured metals and compounds, Nanostructured Materials 6 (5) (1995) 639–642. doi:10.1016/0965-9773(95)00139-5.

[161] M. D. Kluge, D. Wolf, J. F. Lutsko, S. R. Phillpot, Formalism for the calculation of local elastic constants at grain boundaries by means of atomistic simulation, Journal of Applied Physics 67 (5) (1990) 2370–2379. doi:10.1063/1.345533.

[162] J. Yu, X. Lin, J. Wang, J. Chen, W. Huang, First-principles study of the relaxation and energy of bcc-Fe, fcc-Fe and AISI-304 stainless steel surfaces, Applied Surface Science 255 (22) (2009) 9032–9039. doi:10.1016/j.apsusc.2009.06.087.

[163] T. D. Shen, C. C. Koch, T. Y. Tsui, G. M. Pharr, On the elastic moduli of nanocrystalline Fe, Cu, Ni, and Cu–Ni alloys prepared by mechanical milling/alloying, ResearchGate 10 (11). doi:10.1557/JMR.1995.2892.

[164] A. Latapie, D. Farkas, Effect of grain size on the elastic properties of nanocrystalline alpha-iron, Scripta Materialia 48 (5) (2003) 611–615. doi:10.1016/S1359-6462(02)00467-0.

[165] K. S. Min, S. W. Nam, Correlation between characteristics of grain boundary carbides and creep–fatigue properties in AISI 321 stainless steel, Journal of Nuclear Materials 322 (2–3) (2003) 91–97. doi:10.1016/S0022-3115(03)00274-5.

[166] K. J. Kim, H. U. Hong, K. S. Min, S. W. Nam, Correlation between the carbide morphology and cavity nucleation in an austenitic stainless steels under creep-fatigue, Materials Science and Engineering: A 387–389 (2004) 531–535. doi:10.1016/j.msea.2004.01.126.

[167] H. U. Hong, S. W. Nam, The occurrence of grain boundary serration and its effect on the M23c6 carbide characteristics in an AISI 316 stainless steel, Materials Science and Engineering: A 332 (1–2) (2002) 255–261. doi:10.1016/S0921-5093(01)01754-3.

[168] R. Soulas, Effet de la cristallographie sur les premiers stades de l'oxydation des aciers austénitiques 316 L, Ph.D. thesis, Université de Grenoble (2012).

[169] H.-J. Jou, Microstructure modeling of third generation disk alloys.

[170] E. Barbe, Simulation multi-echelles du comportement mecanique de l'interface carbure-metal a partir des structures electronique, Internship report, CEA (2015).

[171] E. Barbe, C.-C. Fu, M. Sauzay, Prediction of the mechanical properties of carbide-metal interfaces from first principles (2017).

[172] J. P. Hirth, J. Lothe, Theory of Dislocations, reprint edition Edition, Krieger Pub Co, Malabar, FL, 1992.

[173] H. Pitkänen, M. Alatalo, A. Puisto, M. Ropo, K. Kokko, L. Vitos, Ab initio study of the surface properties of austenitic stainless steel alloys, Surface Science 609 (2013) 190–194. doi:10.1016/j.susc.2012.12.007.

[174] M. H. Biglari, C. M. Brakman, E. J. Mittemeijer, S. V. D. Zwaag, The kinetics of the internal nitriding of Fe-2 at. pct Al alloy, Metallurgical and Materials Transactions A 26 (4) (1995) 765–776. doi:10.1007/BF02649075.

[175] L. Priester, Grain Boundaries, Vol. 172 of Springer Series in Materials Science, Springer Netherlands, Dordrecht, 2013, dOI: 10.1007/978-94-007-4969-6.

[176] A. A. Wahab, M. V. Kral, 3d analysis of creep voids in hydrogen reformer tubes, Materials Science and Engineering: A 412 (1–2) (2005) 222–229. doi:10.1016/j.msea.2005.08.223.

[177] N. G. Needham, T. Gladman, Nucleation and Growth of Creep Cavities in a Type 347 Steel, Metal Science 14 (1980) 64–72. doi:10.1179/030634580790426300.

[178] V. Yamakov, E. Saether, D. R. Phillips, E. H. Glaessgen, Molecular-dynamics simulation-based cohesive zone representation of intergranular fracture processes in aluminum, Journal of the Mechanics and Physics of Solids 54 (9) (2006) 1899–1928. doi:10.1016/j.jmps.2006.03.004.

[179] K. Laha, J. Kyono, N. Shinya, Copper, Boron, and Cerium Additions in Type 347 Austenitic Steel to Improve Creep Rupture Strength, Metallurgical and Materials Transactions A 43 (4) (2012) 1187–1197. doi:10.1007/s11661-011-0953-z.

[180] S. H. Goods, L. M. Brown, Overview No. 1: The nucleation of cavities by plastic deformation, Acta Metallurgica 27 (1) (1979) 1–15. doi:10.1016/0001-6160(79)90051-8.

[181] J. E. Spruiell, J. A. Scott, C. S. Ary, R. L. Hardin, Microstructural stability of thermal-mechanically pretreated type 316 austenitic stainless steel, Metallurgical Transactions 4 (6) (1973) 1533–1544. doi:10.1007/BF02668005.

[182] C. C. Tseng, Y. Shen, S. W. Thompson, M. C. Mataya, G. Krauss, Fracture and the formation of sigma phase, M23c6, and austenite from delta-ferrite in an AlSl 304l stainless steel, Metallurgical and Materials Transactions A 25 (6) (1994) 1147–1158. doi:10.1007/BF02652290.

[183] NIMS, Creep data sheet, No. M-10, Micrographs and microstructural characteristics of crept specimens of 18cr-12ni-Mo-middle N-low C hot rolled stainless steel plate (SUS 316hp), Tech. rep., Japan (2013).

[184] P. Yavari, T. G. Langdon, An experimental investigation of the orthogonal (diamond) grain configuration in high temperature fatigue, Journal of Materials Science 18 (11) (1983) 3219–3229. doi:10.1007/BF00544146.

[185] K. Shiozawa, J. R. Weertman, The nucleation of grain boundary voids in a nickel-base superalloy during high temperature creep, Scripta Metallurgica 16 (6) (1982) 735–739. doi:10.1016/0036-9748(82)90332-5.

[186] M. Shibata, K. Ono, Stress concentration due to an prolate spheroidal inclusion, Journal of Composite Materials 12 (2) (1978) 132–138. doi:10.1177/002199837801200202.

[187] P. S. Karamched, A. J. Wilkinson, High resolution electron back-scatter diffraction analysis of thermally and mechanically induced strains near carbide inclusions in a superalloy, Acta Materialia 59 (1) (2011) 263–272.

[188] K. Tanaka, T. Mori, T. Nakamura, Cavity formation at the interface of a spherical inclusion in a plastically deformed matrix, Philosophical Magazine 21 (170) (1970) 267–279. doi:10.1080/14786437008238415.

[189] S. V. Raj, Apparent activation volume for creep of copper and alpha brass at intermediate temperatures, Journal of Materials Science 24 (9) (1989) 3196–3204. doi:10.1007/BF01139041.

[190] M. E. Kassner, T. A. Hayes, Creep cavitation in metals, International Journal of Plasticity 19 (10) (2003) 1715–1748. doi:10.1016/S0749-6419(02)00111-0.

[191] J.-Y. Maetz, Évolution de la microstructure d'un acier inoxydable lean duplex lors du vieillissement, Ph.D. thesis, Lyon, INSA (2014).

[192] E. Kröner, Zur plastischen verformung des vielkristalls, Acta Metallurgica 9 (2) (1961) 155–161. doi:10.1016/0001-6160(61)90060-8.

[193] M. Sauzay, Effets de surface et d'anisotropie en fatigue multiaxiale, Paris 6, 2000.

[194] C. Weinberger, W. Cai, D. Barnett, Lecture Notes–Elasticity of Microscopic Structures, ME340–Stanford University.

[195] R. Piat, I. Tsukrov, N. Mladenov, V. Verijenko, M. Guellali, E. Schnack, M. J. Hoffmann, Material modeling of the CVI-infiltrated carbon felt I: Basic formulae, theory and numerical experiments, Composites Science and Technology 66 (15) (2006) 2997–3003. doi:10.1016/j.compscitech.2006.02.008.

[196] M. Berveiller, A. Zaoui, An extension of the self-consistent scheme to plastically-flowing polycrystals, Journal of the Mechanics and Physics of Solids 26 (5) (1978) 325–344. doi:10.1016/0022-5096(78)90003-0.

[197] D. Misseroni, F. Dal Corso, S. Shahzad, D. Bigoni, Stress concentration near stiff inclusions: Validation of rigid inclusion model and boundary layers by means of photoelasticity, Engineering Fracture Mechanics 121–122 (2014) 87–97. doi:10.1016/j.engfracmech.2014.03.004.

[198] M. Sauzay, P. Gilormini, Surface and cyclic microplasticity, Fatigue & Fracture of Engineering Materials & Structures 23 (7) (2000) 573–579. doi:10.1046/j.1460-2695.2000.00307.x.

[199] F. Barbe, S. Forest, G. Cailletaud, Intergranular and intragranular behavior of polycrystalline aggregates.Part 2: Results, International Journal of Plasticity 17 (4) (2001) 537–563. doi:10.1016/S0749-6419(00)00062-0.

[200] I. Dlouhy (Ed.), Transferability of Fracture Mechanical Characteristics, Springer Netherlands, Dordrecht, 2002, dOI: 10.1007/978-94-010-0608-8.

[201] P. Suquet, H. Moulinec, O. Castelnau, M. Montagnat, N. Lahellec, F. Grennerat, P. Duval, R. Brenner, Multi-scale modeling of the mechanical behavior of polycrystalline ice under transient creep., Procedia IUTAM 3 (2012) 76–90. doi:10.1016/j.piutam.2012.03.006.

[202] D. Francois, A. Pineau, A. Zaoui, Comportement mecanique des matériaux: elasticite et plasticite, Hermes, 1992.

[203] R. A. Lebensohn, R. Brenner, O. Castelnau, A. D. Rollett, Orientation image-based micromechanical modelling of subgrain texture evolution in polycrystalline copper, Acta Materialia 56 (15) (2008) 3914–3926. doi:10.1016/j.actamat.2008.04.016.

[204] D. G. Morris, D. R. Harries, Creep and rupture in Type 316 stainless steel at temperatures between 525 and 900 C Part III: Precipitation behaviour, Metal Science 12 (11) (1978) 542–549. doi:10.1179/msc.1978.12.11.542.

[205] C. Gandhi, R. Raj, Intergranular fracture in bicrystals—II, Acta Metallurgica 30 (2) (1982) 505–511. doi:10.1016/0001-6160(82)90231-0.

[206] F. Abe, Stress to produce a minimum creep rate of 10ˆ-5%/h and stress to cause rupture at 105h for ferritic and austenitic steels and superalloys, International Journal of Pressure Vessels and Piping 85 (1) (2008) 99–107. doi:10.1016/j.ijpvp.2007.06.005.

[207] NIMS, Creep data sheet, No. M-1, Micrographs and microstructural characteristics of crept specimens of 18cr-8ni stainless steel for boiler and heat exchanger seamless tubes (SUS 304h TB), Tech. rep., Japan (1999).

[208] L. Babout, E. Maire, R. Fougères, Damage initiation in model metallic materials: X-ray tomography and modelling, Acta Materialia 52 (8) (2004) 2475–2487. doi:10.1016/j.actamat.2004.02.001.

[209] L. Vitos, A. V. Ruban, H. L. Skriver, J. Kollár, The surface energy of metals, Surface Science 411 (1–2) (1998) 186–202. doi:10.1016/S0039-6028(98)00363-X.

[210] M. Caul, J. Fiedler, V. Randle, Grain-boundary plane crystallography and energy in austenitic steel, Scripta Materialia 35 (7) (1996) 831–836. doi:10.1016/1359-6462(96)00234-5.

[211] F. Montheillet, F. Moussy, Physique et mécanique de l'endommagement, EDP Sciences, 1986.

[212] L. M. Brown, W. M. Stobbs, The work-hardening of copper-silica v. equilibrium plastic relaxation by secondary dislocations, Philosophical Magazine 34 (3) (1976) 351–372. doi:10.1080/14786437608222028.

[213] A. S. Argon, J. Im, R. Safoglu, Cavity formation from inclusions in ductile fracture, Metallurgical Transactions A 6 (4) (1975) 825. doi:10.1007/BF02672306.

[214] A. S. Argon, Formation of Cavities From Nondeformable Second-Phase Particles in Low Temperature Ductile Fracture, Journal of Engineering Materials and Technology 98 (1) (1976) 60–68. doi:10.1115/1.3443338.

[215] A. S. Argon, J. Im, Separation of second phase particles in spheroidized 1045 steel, Cu-0.6pct Cr alloy, and maraging steel in plastic straining, Metallurgical Transactions A 6 (4) (1975) 839. doi:10.1007/BF02672307.

[216] D. Leguillon, Strength or toughness? A criterion for crack onset at a notch, European Journal of Mechanics - A/Solids 21 (1) (2002) 61–72. doi:10.1016/S0997-7538(01)01184-6.

[217] M. Sauzay, M. Ould Moussa, Prediction of grain boundary stress fields and microcrack initiation induced by slip band impingement, International Journal of Fracture 184 (2013) 215–240. doi:10.1007/s10704-013-9878-4.

[218] A. Needleman, An analysis of tensile decohesion along an interface, Journal of the Mechanics and Physics of Solids 38 (3) (1990) 289–324. doi:10.1016/0022-5096(90)90001-K.

[219] V. Tvergaard, J. W. Hutchinson, The relation between crack growth resistance and fracture process parameters in elastic-plastic solids, Journal of the Mechanics and Physics of Solids 40 (6) (1992) 1377–1397. doi:10.1016/0022-5096(92)90020-3.

[220] G. T. Camacho, M. Ortiz, Computational modelling of impact damage in brittle materials, International Journal of Solids and Structures 33 (20) (1996) 2899–2938. doi:10.1016/0020-7683(95)00255-3.

[221] J. Liu, Prédictions multi-échelles de l'initiation des microfissures de fatigue, PhD Thesis, Paris 6 (2013).

[222] T. Watanabe, P. W. Davies, Grain boundary sliding and intergranular fracture behaviour of copper bicrystals, Philosophical Magazine A 37 (5) (1978) 649–681. doi:10.1080/01418617808239197.

[223] T. Watanabe, Grain boundary sliding and stress concentration during creep, Metallurgical Transactions A 14 (3) (1983) 531–545. doi:10.1007/BF02643771.

[224] Y. Guo, D. M. Collins, E. Tarleton, F. Hofmann, J. Tischler, W. Liu, R. Xu, A. J. Wilkinson, T. B. Britton, Measurements of stress fields near a grain boundary: Exploring blocked arrays of dislocations in 3d, Acta Materialia 96 (2015) 229–236. doi:10.1016/j.actamat.2015.05.041.

[225] H. Mughrabi, F. Pschenitzka, Constrained glide and interaction of bowed-out screw dislocations in confined channels, Philosophical Magazine 85 (26-27) (2005) 3029–3045. doi:10.1080/14786430500079975.

[226] J. C. Stinville, N. Vanderesse, F. Bridier, P. Bocher, T. M. Pollock, High resolution mapping of strain localization near twin boundaries in a nickel-based superalloy, Acta Materialia 98 (Supplement C) (2015) 29–42. doi:10.1016/j.actamat.2015.07.016.

[227] M. Carroll, L. Carroll, Influence of Hold Time on Creep-Fatigue Behavior of an Advanced Austenitic Alloy, Tech. rep., Idaho National Laboratory (United States). Funding organisation: DOE-NE (United States) (2011).

[228] J. V. Sharp, Deformation of neutron-irradiated copper single crystals, Philosophical Magazine 16 (139) (1967) 77–96. doi:10.1080/14786436708229258.

[229] G. S. Was, D. Farkas, I. M. Robertson, Micromechanics of dislocation channeling in intergranular stress corrosion crack nucleation, Current Opinion in Solid State and Materials Science 16 (3) (2012) 134–142. doi:10.1016/j.cossms.2012.03.003.

[230] M. Kikuchi, K. Shiozawa, J. R. Weertman, Void nucleation in astroloy: theory and experiments, Acta Metallurgica 29 (10) (1981) 1747–1758. doi:10.1016/0001-6160(81)90008-0.

[231] R. Abbasi, K. Dzieciol, A. Borbély, Three-dimensional analysis of creep voids in copper by serial sectioning combined with large field EBSD, Materials Science and Technology 31 (5) (2015) 540–546. doi:10.1179/1743284714Y.0000000593.

[232] E. Van Der Giessen, P. R. Onck, M. W. D. Van Der Burg, Some effects of random microstructural variations on creep rupture, Engineering Fracture Mechanics 57 (2) (1997) 205–226. doi:10.1016/S0013-7944(97)00009-X.

[233] K. J. Hsia, D. M. Parks, A. S. Argon, Effects of grain boundary sliding on creep-constrained boundary cavitation and creep deformation, Mechanics of Materials 11 (1) (1991) 43–62.

[234] W. Beere, Stress redistribution due to grain-boundary sliding during creep, Metal Science 16 (5) (1982) 223–228. doi:10.1179/030634582790427280.

[235] C. L. White, J. H. Schneibel, R. A. Padgett, High temperature embrittlement of NI and Ni-Cr alloys by trace elements, Metallurgical Transactions A 14 (3) (1983) 595–610. doi:10.1007/BF02643776.

[236] R. J. Fields, M. F. Ashby, Observation of wedge cavities in the S.E.M., Scripta Metallurgica 14 (7) (1980) 791–795. doi:10.1016/0036-9748(80)90290-2.

[237] C. W. Lau, A. S. Argon, F. A. McClintock, Stress Concentrations Due to Sliding Grain Boundaries in Creeping Alloysdoi:10.1520/STP37315S.

[238] D. H. Riedel, Cavity Nucleation by Stress Concentrations During Creep, in: Fracture at High Temperatures, Materials Research and Engineering, Springer Berlin Heidelberg, 1987, pp. 85–115, dOI: 10.1007/978-3-642-82961-1_7.

[239] M. Sauzay, 6 - Mechanical behavior of structural materials for Generation IV reactors, in: P. Yvon (Ed.), Structural Materials for Generation IV Nuclear Reactors, Woodhead Publishing, 2017, pp. 191–252, dOI: 10.1016/B978-0-08-100906-2.00006-9.

[240] I.-W. Chen, A. S. Argon, Creep cavitation in 304 stainless steel, Acta Metallurgica 29 (7) (1981) 1321–1333. doi:10.1016/0001-6160(81)90023-7.

[241] R. Sandström, J. He, Survey of Creep Cavitation in fcc Metals, in: Study of Grain Boundary Character, InTech, 2017, pp. 19–42, dOI: 10.5772/66592.

[242] H. Jazaeri, P. J. Bouchard, M. T. Hutchings, A. A. Mamun, R. K. Heenan, Application of small angle neutron scattering to study creep cavitation in stainless steel weldments, Materials Science and Technology 31 (2014) 535–539. doi:10.1179/1743284714Y.0000000577.

[243] L. Kloc, V. Skieničkа, J. Ventruba, Comparison of low stress creep properties of ferritic and austenitic creep resistant steels, Materials Science and Engineering: A 319 (Supplement C) (2001) 774–778. doi:10.1016/S0921-5093(01)00943-1.

[244] R. S. Mishra, T. R. Bieler, A. K. Mukherjee, Mechanism of high strain rate superplasticity in aluminium alloy composites, Acta Materialia 45 (2) (1997) 561–568. doi:10.1016/S1359-6454(96)00194-2.

Appendix A

Evaluation of the experimental uncertainty in the measurement of the Dyson law prefactor, α'

As shown in chapter **??**, The Dyson law prefactor α' factor is evaluated using the following equations:

$$\alpha' = \frac{N_a}{\varepsilon_f} \tag{A.1}$$

$$N_a = \frac{d_g \cdot N_m}{\pi \cdot d_H} \tag{A.2}$$

where

- N_a is the number of cavities per unit grain boundary area (m^{-2})

- N_m is the number of cavities per unit area of polished longitudinal section (m^{-2})

- ε_f is the axial strain in the homogeneous parts of the specimen (away from the necking volume), measured after fracture

- d_g is the grain size measured by the intercept line method (μm)

- d_H is the harmonic average of intersected cavity diameters (μm).

The Dyson law prefactor, α', is determined by experimental measurements and using Visilog software. Fifteen FEG-SEM images are analyzed for each specimen with a magnification of 1000X.

The CEA/EDF document [15] provides the harmonic mean value of grain size, d_g. This parameter was determined by Average Grain Intercept (AGI) method. For a given material, draw a set of random positioned line segments on the microscopic images. Then, the number of times each line segment intersects a grain boundary is counted, and the ratio of intercepts to line length is measured. Then the grain size could be calculated as:

$$d_g = \frac{number\ of\ intercepts}{line\ length} \tag{A.3}$$

Then the harmonic mean value of d_g and the corresponding standard deviation Δd_g is obtained.

The cavity number per unit surface is evaluated with fifteen FEG-SEM images for each specimen. The cavities with size larger than $0.4\mu m$ are considered, the cavity number per each image is labeled as x. The observation uncertainty is induced by the counted number of cavities. The average value of the cavity number per each image, denoted as $\bar{x}$ is calculated as:

$$\bar{x} = \frac{1}{n}\Sigma_{i=1}^{n}[\frac{x_{max,i} + x_{min,i}}{2}] = \frac{1}{n}\Sigma_{i=1}^{n}x_i \tag{A.4}$$

where n is the number of images.

Then, the corresponding mean deviation, Δx, is:

$$\Delta x = \sqrt{\frac{1}{n-1}\Sigma_{i=1}^{n}(x_i - \bar{x})^2} \tag{A.5}$$

The uncertainty induced by the microscopic observations in the measurement of N_m, Δe, is:

$$\Delta e = \frac{\Delta x/x}{\sqrt{n}} \tag{A.6}$$

The cavity sizes are measured using the Visilog software, which leads to an uncertainty in the cavity diameter d_H. This uncertainty Δd_H is evaluated $0.01\mu m$, which is the software accuracy.

Thereafter, the uncertainty in N_a could be deduced as:

$$\mid \frac{\Delta N_a}{N_a} \mid = \mid \frac{\Delta d_g}{d_g} \mid + \mid \Delta e \mid + \mid \frac{\Delta d_H}{d_H} \mid \tag{A.7}$$

Summarizing all previous stage, we can deduce the uncertainty in measured the Dyson law prefactor, α', as:

$$\mid \frac{\Delta \alpha'}{\alpha'} \mid = \mid \frac{\Delta N_a}{N_a} \mid + \mid \frac{\Delta \varepsilon_f}{\varepsilon_f} \mid \tag{A.8}$$

The relative uncertainties in all parameters, and the deduced relative uncertainty in the measured valuers o f α' are given in Table A.1.

$\frac{\Delta d_g}{d_g}(\%)$	$\frac{\Delta d_H}{d_H}(\%)$	$\frac{\Delta \varepsilon_f}{\varepsilon_f}$ $(\%)$	$\frac{\Delta x}{x}(\%)$	$\Delta e(\%)$	$\frac{\Delta \alpha'}{\alpha'}(\%)$
20	3	0.1	27	7	$\approx$30

Table A.1: Uncertainties in d_g, d_H, ε_f, N_a and α' (relative amplitudes).

Finally, it is deduced that $\Delta\alpha'/\alpha' = \pm 30\%$.

Appendix B

Interface normal stresses calculated by Crystal Plastic Finite Element Method

α_{GB} (°)	0	15	30	45	60	75	90
σ_{nn}^{max} (GPa)	2.80	2.26	1.67	0.77	1.38	1.44	1.28
	2.88	2.81	2.29	1.97	1.15	1.58	1.22
	6.71	4.32	5.65	4.20	3.86	1.71	3.56
	8.45	8.40	7.93	8.28	7.54	7.47	4.28
	9.77	*	4.81	6.78	5.37	2.65	3.64
	5.42	5.70	5.53	3.34	3.51	4.00	1.99
	7.87	7.37	3.28	2.33	2.50	2.56	3.88
	4.36	4.29	3.58	3.15	1.57	1.93	3.40
	5.00	4.68	2.09	1.48	1.59	1.63	2.47
	6.89	6.78	5.66	4.98	2.49	3.05	5.37
	3.37	*	5.72	4.51	2.34	3.27	3.48
	6.14	6.99	8.61	*	2.96	*	1.26
	3.06	2.18	2.11	1.96	0.98	0.79	1.00
	3.76	3.03	1.29	*	1.22	1.15	*
	2.96	2.32	2.12	1.52	1.45	1.74	1.41
	4.08	2.67	2.82	3.27	2.27	1.39	1.70
	1.41	2.67	*	*	1.34	0.88	1.13
	1.80	1.38	1.29	1.30	1.41	1.42	1.38
	3.94	3.82	2.45	2.25	1.81	1.58	1.88
	4.60	5.65	5.68	5.07	4.90	3.45	5.02
	3.38	2.49	1.54	1.05	2.77	2.77	2.00
	5.22	3.99	*	1.75	2.84	2.62	2.01
	4.18	2.70	3.52	2.62	2.41	1.07	2.22
	3.92	3.89	3.68	3.84	3.50	3.46	1.98

6.38	5.16	3.81	1.75	3.15	3.28	2.91
5.34	5.21	4.25	3.66	2.13	2.93	2.26
4.73	5.40	6.01	6.47	*	3.64	5.06
4.73	4.17	4.79	3.06	3.40	4.95	4.64

Table B.1: Maximum interface normal stresses calculated for circular tip inclusion with a/b=3. The inclusions are located along grain boundaries of a bicrystal, with different grain boundary plan orientations with respect to the tensile axis. The bicrystal is embedded in a homogeneous matrix. For each α' angle value, 28 coupes of random crystal orientations of the bicrystals. Only fifteen random couples are used in Fig. 3.8a. *: the corresponding calculations do not converge numerically.

a/b	1	2	3	4	5	6	7	8	10
	2.25	2.42	2.80	3.09	3.84	4.05	4.45	4.84	4.87
	1.61	2.40	2.88	3.30	3.58	4.08	4.26	4.35	4.25
	2.02	2.62	2.96	3.34	4.02	4.24	4.72	4.85	4.90
	3.41	3.73	4.08	4.14	4.54	4.71	4.68	4.74	4.56
	1.59	1.75	1.80	2.06	2.51	3.05	3.59	3.78	3.89
σ_{nn}^{max}	1.16	1.27	1.41	1.56	1.81	1.87	1.92	1.97	2.04
(GPa)	3.72	3.72	3.94	4.58	5.66	7.18	7.41	7.60	7.01
	3.60	3.70	4.60	5.07	6.71	8.12	8.35	8.36	7.55
	3.16	3.62	4.18	5.43	6.34	5.99	6.00	6.02	8.18
	2.73	3.27	3.92	5.40	6.22	7.47	8.00	8.40	7.80
	3.23	3.01	4.36	4.44	4.69	5.03	5.14	5.37	5.61
	3.45	3.56	5.34	6.05	7.20	7.86	7.93	8.00	8.63

Table B.2: Maximum interface normal stresses calculated for circular tip inclusion with various shape factors, a/b. Inclusion locates along grain boundary of a bicrystal, with grain boundary plan parallel to the tensile axis. The bicrystal is embedded in a homogeneous matrix.

Circular tip	Symmetric angular φ (°)			Asymmetric angular tip φ (°)		
	30	45	60	30	45	60
2.80	5.72	4.76	3.00	6.36	6.52	2.96
2.96	6.16	4.71	4.33	6.27	6.86	2.70
1.80	3.16	2.40	2.18	5.19	3.35	2.31
3.94	10.44	4.08	7.50	8.46	4.58	5.19
4.18	7.98	2.45	5.82	8.93	4.24	5.13
4.36	10.38	8.62	5.83	11.23	8.86	4.01
4.36	9.61	7.12	6.63	11.87	10.22	3.06
2.88	7.66	4.50	5.00	4.24	6.12	2.71
4.08	5.21	3.20	7.60	6.16	3.09	8.00
1.41	2.75	1.65	1.89	4.78	3.22	1.87
4.60	12.84	8.22	9.43	9.89	13.77	7.50
3.92	10.38	6.00	6.75	5.36	8.08	5.03
5.34	7.51	3.13	6.41	9.66	4.89	7.90
5.52	10.41	3.71	6.47	10.11	5.50	7.79

Table B.3: Maximum interface normal stresses (GPa) calculated for circular tip, symmetric angular tip, and a asymmetric angular tip inclusions (Fig. 3.2). The inclusions are located along grain boundaries of a bicrystal, with the grain boundary plane parallels to the tensile axis ($\alpha_{GB} = 0°$). The bicrystal is embedded in a homogeneous matrix.

Appendix C

Cohesive law: HINTE

The cohesive law 'HINTE' has already been implemented in the Cast3m finite element software. Two damage mechanisms are considered in this cohesive law, damage induced by shear stress, and crack opening damage induced by normal stress. This model assumes that both damages are time-independent.

Several parameters are used in the HINTE cohesive law:

Y_0	:	threshold damage energy
Y_C	:	critical damage energy, equivalent to γ_{frac}
$GAM1$	:	coupling parameter between shear and opening energies
AL	:	govern shape and location of fracture in mixed mode
NN	:	characterizes the interface brittleness (the interface is more brittle, the NN exponent is higher)
$DCRI$	:	allows to simulate a brittle fracture (by default DCRI = 1)
KS	:	interface stiffness in shear mode
KN	:	interface stiffness in open mode

The displacements of the cohesive zone are defined by 'U_1' in shear mode and 'U_2' in open mode.

$$U_1 = \frac{\tau_{nm}}{KS(1-d_1)} \qquad KS = \frac{\mu}{d_0} \tag{C.1}$$

$$U_2 = \frac{\sigma_{nn}}{KN(1-d_1)} \qquad KN = \frac{E_{inter}}{d_0} \tag{C.2}$$

where:

τ_{nm}	:	shear stress acting on cohesive element
σ_{nn}	:	normal stress acting on cohesive element
d_0	:	interface thickness
E_{inter}	:	Young's modulus of the interface
μ	:	elastic shear modulus

Issuing isotropic damage, the internal damage variables, d_1 and d_2, are defined as:

$$d_1 = d_2 = [\frac{NN}{NN+1}(\frac{Y - Y_0}{Y_c - Y_0})]^{NN} \tag{C.3}$$

where the total energy release rate, Y, induced by shear mode and open mode is defined by:

$$Y = (Y_2^{AL} + GAM1 * Y_1^{AL})^{\frac{1}{AL}} \tag{C.4}$$

with the share mode and opening mode energy releases rates:

$$Y_1 = \frac{1}{2}KS(U_1)^2 \quad Y_2 = \tfrac{1}{2}KN(U_2)^2 \tag{C.5}$$

Our FE calculations show that the interface shear stresses are much lower than interface normal stresses (subsection 2.4.2). Therefore, the shear damage mode considered as negligible and $GAM1$ is chosen as 0. Then, $Y = Y_2$. This means that we focus only on the open damage mode.

Then, combination of Eqs. C.1-C.5 leads to:

$$\sigma_{nn} = KN[1 - [\frac{NN}{NN+1}(\frac{Y - Y_0}{Y_c - Y_0})]^{NN}]U_2 \tag{C.6}$$

And we assume that cohesive zone damage begins at the beginning of the loading, which means that the value of Y_0 is zero. According to Eqs. C.4-C.6, σ_{nn} is obtained:

$$\sigma_{nn} = KN[1 - [\frac{NN}{NN+1}(\frac{\frac{1}{2}KN(U_2)^2}{Y_c})]^{NN}]U_2 \tag{C.7}$$

When

$$\frac{\partial \sigma_{nn}}{\partial U_2} = 0 \tag{C.8}$$

We obtain $\sigma_{nn} = \sigma_c$. This corresponds the unstable equilibrium (Fig. 4.5). KN and Y_C are the constants which value are known. Therefore, only one parameter need to be adjusted is the NN exponent. Once σ_c is known (UBER relationship, DFT computations), NN could be adjusted by inversely identification. The values of NN for coherent and incoherent interfaces amount to, respectively, 0.14 and 0.09.

The two CZM curves plotted in Fig. 4.5 are evaluated using the parameters provided in Table C.2.

Interface	E_{inter} (GPa)	d_0 (nm)	$Y_c = \gamma_{frac}$ (Jm^{-2})	σ_c (GPa)	NN
Coherent	162 [171]	0.46[171]	4.52 [171]	14.3 [171]	0.14
Incoherent	105	1.5	4	5	0.09

Table C.2: Input parameters of the 'HINTE' cohesive laws, for coherent and incoherent interfaces.